Baby MIND Detector Construction and Commissioning

Parsa, Saba

UNIVERSITÉ DE GENÈVE **FACULTÉ DES SCIENCES**
Département de Physique Nucléaire et Corpusculaire Prof. F. Sanchez
Prof. A. Blondel
Dr. E. Noah

Baby MIND Detector Construction and Commissioning

THÈSE

Présentée à la Faculté des sciences de l'Université de Genève
pour obtenir le grade de Docteur ès science, mention physique

par

Saba Parsa

de
Tehran, (Iran)

THÈSE N° 5552

Genève

Atelier d'impression ReproMail

2021

UNIVERSITÉ DE GENÈVE
FACULTÉ DES SCIENCES

DOCTORAT ÈS SCIENCES, MENTION PHYSIQUE

Thèse de Madame Saba PARSA

intitulée :

«Baby MIND Detector Construction and Commissioning»

La Faculté des sciences, sur le préavis de Monsieur F. SANCHEZ NIETO, professeur ordinaire et directeur de thèse (Département de physique nucléaire et corpusculaire), Monsieur A. BLONDEL, professeur ordinaire et codirecteur de thèse (Département de physique nucléaire et corpusculaire), Monsieur E. NOAH, collaborateur scientifique II et codirecteur de thèse (Département de physique nucléaire et corpusculaire), Madame A. SFYRLA, professeure associée (Département de physique nucléaire et corpusculaire), Monsieur C. GIGANTI, (Chargé de recherche, Laboratoire de Physique Nucléaire et de Hautes Énergies (LPNHE), Sorbonne Université, Paris, France), autorise l'impression de la présente thèse, sans exprimer d'opinion sur les propositions qui y sont énoncées.

Genève, le 30 mars 2021

Thèse - 5552 -

Le Doyen

N.B. - La thèse doit porter la déclaration précédente et remplir les conditions énumérées dans les "Informations relatives aux thèses de doctorat à l'Université de Genève".

Abstract

Baby MIND is a Magnetized Iron Neutrino Detector, serving as a downstream magnetized muon range detector for the WAGASCI experiment on the T2K beam line in Japan.
WAGASCI experiment aims to conduct neutrino cross-section measurements on water and hydrocarbon at a slightly different off-axis angle (1.5 degrees) than that of ND280 (2.5 degrees), and improve the systematic uncertainties related to neutrino oscillation studies.
This thesis covers the description of Baby MIND detector systems in detail and reports on the activities carried out in different stages of the project in which I was involved.
After an intense period of prototyping and validation, the Baby MIND detector systems were constructed at CERN and the full detector setup was tested in a beam test at T9 beamline at CERN in summer 2017, before the detector was shipped to Japan.
The installation and commissioning of the detector at J-PARC took place in the first quarter of 2018 and the first physics run of Baby MIND together with other WAGASCI sub-detectors took place in the period from November 2019 to February 2020 (T2K run10), where a total of 4.8×10^{20} POT (Protons on Target) were delivered.
Detector performance studies such as the detector light yield measurements, timing studies, electronics noise investigations and data corruption instances are reported. The data processing flow from raw binary data to event creation and the scheme of event pre-selection, based on the topology criteria are discussed and some examples of neutrino interactions events on iron are presented.
A sample of clean single track neutrino events was analyzed and the distributions of the reconstructed muons momentum and scattering angle are presented.

Résumé

Baby MIND est un détecteur de neutrinos en fer magnétisé, servant comme un détecteur de muons situés en aval de l'expérience WAGASCI sur la ligne de faisceau de T2K au Japon.
L'expérience WAGASCI vise à effectuer des mesures de section efficace des neutrinos sur l'eau et les hydrocarbures à un angle hors-axe légèrement différent (1.5°) de celui du détecteur proche appelé ND280 (2.5°), et à réduire les incertitudes systématiques liées aux études d'oscillation des neutrinos.
Cette thése couvre la description des systèmes du détecteur Baby MIND en détail et rend compte des activités menées leur des différentes étapes du projet dans lequel l'auteure était impliquée.
Après une période intense de prototypage et de validation, les systèmes du détecteur Baby MIND ont été construits au CERN et la configuration complète du détecteur a été éprouvée lors d'un test de faisceau sur la ligne T9 au CERN l'été 2017, avant que le détecteur ne soit expédié au Japon.
L'installation et la mise en service du détecteur au J-PARC ont eu lieu en février 2018 et le premier cycle de physique de Baby MIND avec d'autres sous-détecteurs de WAGASCI a eu lieu entre novembre 2019 et février 2020 (T2K run 10), où un total de 4.8×10^{20} POT (Protons on Target: protons sur cible) ont été livrés.
La thèse rapporte les études de performance du détecteur en ce qui concerne le rendement lumineux du détecteur, les études de synchronisation, les enquêtes sur le bruit électronique, ainsi que les cas de corruption de données. Le flux de traitement des données depuis les données binaires brutes jusqu'à la création d'événements et le schéma de pré-sélection d'événements basé sur les critères de topologie sont discutés et quelques exemples d'événements illustrant les interactions des neutrinos sur le fer sont présentés.
Enfin, la thèse présente l'analyse d'un échantillon d'événements neutrinos purs d'une seule trajectoire comprenant la distributions d'impulsion et la distribution de l'angles d'ouverture reconstruits des muons.

Acknowledgments

This thesis work would not have been possible without the support, help, collaboration and encouragement of all and everyone around me. Specially I would like to express, in these lines, my deep gratitude to following people.

I express my sincere gratitude to my thesis advisers. Firstly, to my primary supervisor, Prof. Alain Blondel, for giving me the opportunity to start my PhD at University of Geneva on the Baby MIND project, and for his support and encouragements during the first two years of my PhD. This period covered the construction and assembly of the detector, CERN beam test in summer 2017 and installation of the detector at J-PARC in the first quarter of 2018.

Similarly, I am thankful to Prof. Federico Sanchez for accepting the official supervisory role for my PhD after the retirement of prof. Blondel and for his support during the last two years of my PhD, which covered the period of development of the DAQ system and the first physics run of Baby MIND with the T2K neutrino beam in 2019-2020 as well as the data analysis works. I am grateful to Prof. Sanchez for reviewing my thesis with attention and providing me with valuable and insightful comments.

To Dr. Etam Noah, my co-supervisor, I owe particular gratefulness. He led the Baby MIND project from the conceptual stage to the delivery of the detector to Japan and its first physics run with great amount of dedication. He provided day-to-day supervision of my PhD work during all the stages of the project which were carried out in various locations, at labs at University of Geneva, at CERN, and at J-PARC. He continued to reach out, and to provide me with essential advice during the writing of my thesis, to this date.

I like to express my gratitude towards the engineering teams of DPNC at Unige, particularly to Yannick Favre, the head of the electronics engineering group, to Franck Cadoux, the head of the mechanical engineering group, and to Laurent Nicola from the mechanical engineering group for their expertise shared and support throughout the project.

My sincere appreciation also goes to Prof. Minamino-san for hosting me during the three months stay in Japan under the JSPS Switzerland-Japan exchange program. To me It was a remarkable and enriching experience to work with our Japanese scholar colleagues, and get to know the Japanese culture and discover their beautiful country.

I would like to thank this thesis jury committee: Prof. Anna Sfyrla and Dr. Claudio Giganti, for agreeing to review and evaluate my work.

I thank my fellow colleagues and friends in the neutrino group at Unige: Mark Rayner, Yordan Karadzhov, Antoaneta Damayanova, Leila Haegel, Ruslan Asfandiyarov, Lucie Maret, Stephanie Bron, Dana Douqa and Robert Amarinei, with whom I shared parts of this path in the last four years. Let these lines bring to life the memory of the time well spent together.

I am deeply indebted to Solange and Claude Demole, who helped me to pursue my studies for Master's in Geneva by unlocking the immigration obstacles I was facing as an Iranian student visa applicant. Had it not been for their kindness and care, I would have a very different life trajectory as science is concerned and beyond.

Finally, the very inconceivable happened in the final period of my PhD, imposing an almost unsocial public order, due to COVID-19 pandemic. It is my wish to thank my family and dear friends for their constant encouragements and support that helped me to take the final steps in this journey.

Funding Acknowledgment:

This project has received funding from the European Union's Horizon 2020 Research and Innovation programme under Grant Agreement no. 654168.

Contents

Chapter 1

Introduction

Neutrinos might be referred to as the most intriguing and elusive breed of all fundamental particles. Lightweight, constantly switching identities on the fly and exceedingly difficult to detect. Nevertheless these ghost particles have played a fascinating role in the evolution of the universe, from leptogenesis to primordial nucleosynthesis, the cosmic microwave background (CMB) and structure formation. Neutrinos are the most abundant type of massive particles in nature. Understanding neutrino properties has brought new insights into the field of fundamental interactions.

Today we know rather accurately how to describe neutrino interactions with matter, formulated by the successful standard model of electroweak interactions. Many pieces of information have been collected in reactor and accelerator experiments, but the main breakthrough in neutrino physics over the last decades came from astrophysics. The solar neutrino problem, an observed deficit of neutrino flux from the sun, along with the atmospheric neutrino anomaly, has led to the discovery of neutrino oscillations and the fact that neutrinos have mass. This is believed to be the first and so far only concrete evidence for physics beyond the realm of the standard model of particle physics which does not account for neutrino masses.

Despite the progress made in the last two decades in the field of neutrino physics, some fundamental properties of neutrinos remain up for debate. Some of the key questions are related to their mass spectrum and the origin of their light masses, the nature of neutrino antimatter, the number of neutrino species in existence and the asymmetry between particles and anti-particles in neutrino oscillations known as CP-violating phase.

Around the world, at particle colliders, at nuclear reactors, in abandoned mine shafts, ever bigger and more accurate experiments are coming online: signs that the neutrino

physics is occupying the limelight for the years to come.
The work presented in this thesis is aligned with these efforts and consists in developing a new particle detector to serve along with many other detectors in the T2K experiment complex. The topics of this thesis are organized as follows:

- The rest of this chapter summarizes the historical background and our present understanding of neutrino physics.
- Chapter two presents a brief description of the T2K experiment, its main detectors and upgrade plans, followed by the description of the WAGASCI experiment, the new member of the T2K Near Detector complex and its physics goals.
- Chapter three describes the Baby MIND detector, its design concepts, prototyping and validation tests of the detector systems and the construction stages.
- Chapter four discusses Baby MIND beam test at T9 beam line at CERN. It covers operational aspects and challenges that were overcome, electronics parameter studies and brief summary of the collected data.
- Chapter five is dedicated to Baby MIND performance at J-PARC. It covers the installation and commissioning of the detector with the T2K neutrino beam, data taking campaign during Baby MIND and WAGASCI first physics run, and detector response studies.
- Chapter six focuses on analysis of single track neutrino events in Baby MIND. The data processing scheme, event selection strategy and a simple track reconstruction algorithm is described and the reconstructed momentum and angle of the muon tracks is presented.
- Chapter seven presents a brief conclusion of this thesis.

1.1 Historical review of neutrino physics

1.1.1 The path to neutrino observation

To trace back the story of the neutrinos, we have to go back in time much further than its discovery or even its postulation. The radioactivity of uranium was a known phenomenon since its discovery in 1896 by H. Becquerel. While studying its radioactivity, E. Rutherford understood that three different radiation types exist: α, β and γ. Questions arose in 1914, when the measurements of J. Chadwick showed a continuous energy spectrum for the emitted electron in nuclear β-decay, while the α energy spectrum was monochromatic [1]. Many more measurements followed this work for a decade and more accurate measurements of the β spectrum were obtained (Figure 1-1). One would expect fixed, mono-chromatic energies in a two body decay. Ex-

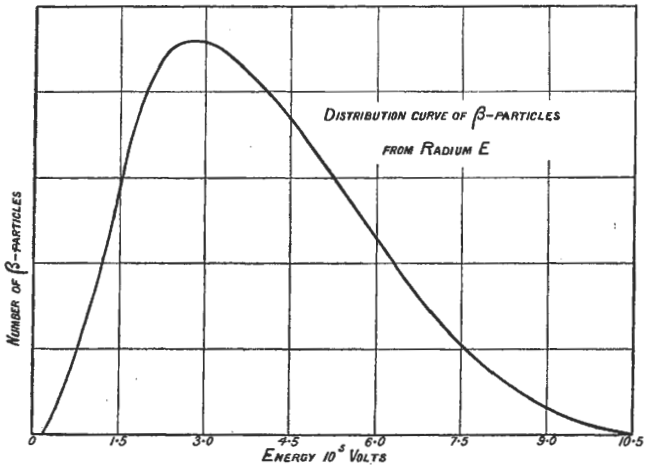

Figure 1-1: Distribution of Beta decay from Radium E, measured by C. D. Ellis and W. A. Wooster in 1927.

tended distributions are suggestive of three or more particles. In 1930, Wolfgang Pauli proposed the existence of a new weakly interacting particle, as *'a desperate remedy'* to reslove the energy crisis in β decay [2], and he called it *neutron*. After the discovery of neutrons in 1932 by J. Chadwick, E. Fermi renamed Pauli's particle to *neutrino* and proposed the first theory of weak interactions in 1934 [3], which could describe the experimental results of the β-decay. Soon afterwards, H. Bethe and R. Peierls calculated the cross section for the inverse reaction in which a neutrino is absorbed, but when they found a value of about 10^{-44} cm^2, they concluded that the *'Neutrino is undetectable'* [4]. After the discovery of nuclear fission and the self-sustaining nuclear chain reaction (see figure 1-2), an intense source of neutrinos was available for making a direct detection of neutrinos. A few years after the end of the Second World War,

Figure 1-2: World's first self-sustaining nuclear chain reaction, Chicago Pile No.1, led by E. Fermi, December 1942. Painting by Gary Sheehan, 1957.

F. Reines and C. Cowan proposed to place a detector close to a bomb-test tower and detect antineutrinos from the fireball with a liquid scintillation detector dug below the ground. They were urged to use the more practical idea of using a nuclear reactor. This was challenging because the antineutrino flux from a reactor would be thousands of times smaller than that from a nuclear explosion, thus the separation of signal from background needed another ingenious idea to detect neutron capture. In 1956, neutrinos were detected at last by F. Reines and C. Cowan [5](Nobel 1995). Their experiment, shown in figure1-3, used a nuclear reactor as an intense source of an-

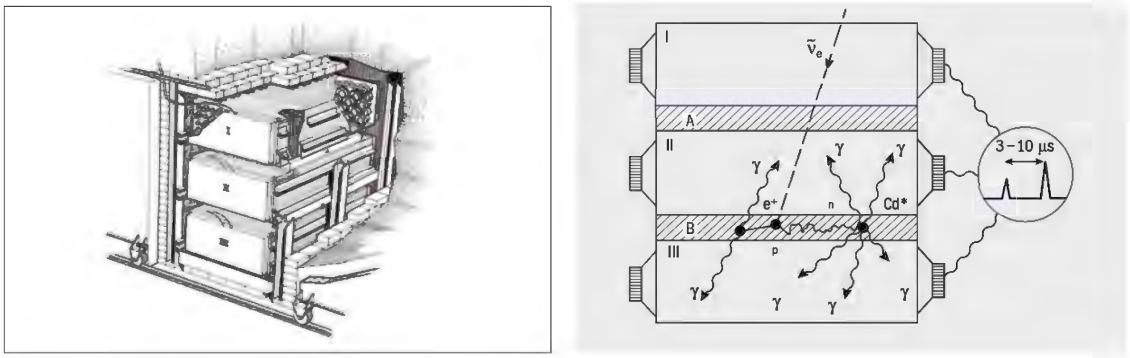

(a) The detector used at Savannah River. (b) The detection method

Figure 1-3: Neutrino discovery. Detection of electron antineutrino in the experiment at Savannah River. Reproduction of the original plots by [6].

tineutrinos. The target was a water tank with additional cadmium. The antineutrinos would interact with the protons, creating a neutron and a positron. Cadmium would capture the neutron and emit a gamma ray. The signal for a antineutrino interaction was the detection of the cadmium gamma ray 5 μs after the detection of a gamma ray from positron annihilation.

The next important step was taken in the same year. T. D. Lee and C. N. Yang

published a paper questioning parity conservation in weak interactions [7], and C. S. Wu demonstrated in an experiment of ^{60}Co that parity was indeed violated in β-decays [8]. In 1958, M. Goldhaber determined the helicity of neutrinos to be consistent with a left-handed massless particle [9]. Thus far it was not yet known that neutrinos have flavours. The muon-neutrino, ν_μ, was discovered at Brookhaven National Laboratory in 1962 by L. Lederman, M. Schwartz and J. Steinberger [10](Nobel 1988). All these are the ingredients upon which the Standard Model of particle physics has been built.

1.1.2 Solar neutrinos

The mechanism of energy production in the Sun was a major puzzle until the 20th centuary. In 1939 H. A. Bethe gave a complete picture of the thermonuclear reactions that power the Sun and the stars [4]. The basic process consists of four protons combining into a helium nucleus and releasing two positrons, two neutrinos and 26.7 MeV energy.

$$p + p + p + p \rightarrow He^4 + e^+ + e^+ + \nu_e + \nu_e \tag{1.1}$$

Detection of solar neutrinos is the only way to provide direct evidence of specific nuclear reactions occurring in the interior of the Sun. By 1964 J. Bahcall had made a prediction of the solar neutrino fluxes reaching the earth [11]. R. Davis with the Homestake Chlorine experiment aimed to confirm this prediction. In the process of neutrino capture Cholrine-37 atoms would convert to Argon-37 atoms, which were then counted by means of their radioactive decay. In the end he could count only one third

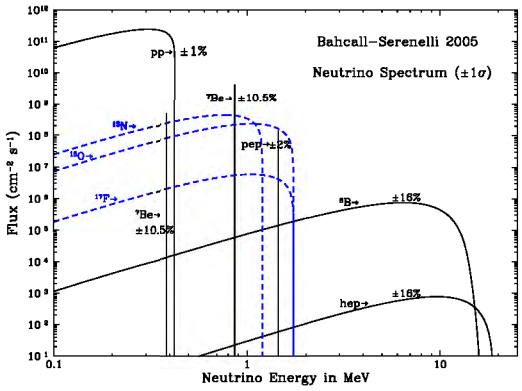

(a) Solar neutrino fluxes.

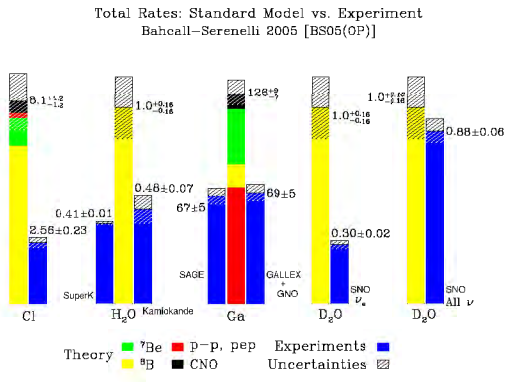

(b) Solar neutrino experiment results.

Figure 1-4: The solar neutrino problem lasted 30 years until a clear picture of neutrino oscillations explained the observations.

of the number of neutrinos predicted by Bahcall [12] [13]. He continued to measure solar neutrinos for 30 years and eventually other experiments joined the effort. In 1989 the Kamiokande experiment which utilised a real time water Cherenkov detection technology reported directional observation of the solar neutrinos with a deficit of one half with respect to predictions [14]. The deficit in detected neutrinos, as is shown in figure 1-4 for some experimental results, became known as the solar-neutrino problem.

1.1.3 Atmospheric neutrinos

Cosmic rays were discovered in 1911 by V. Hess during a series of ascents with a hydrogen balloon to measure the levels of ionizing radiation in the atmosphere with an electroscope [15]. Cosmic rays are mostly energetic protons that collide on Nitrogen and Oxygen nuclei in the atmosphere and create showers of different particle types. Many elementry particles such as muon (μ), kaon (K) and pion (π) were originally discovered in cosmic ray research. All of these particles can decay and give rise to the atmospheric neutrinos (figure 1-5-a). The first detection of these neutrinos happened in 1965 by two experiments, installed in deep mines in India [16] and in South Africa [17]. The gradual awareness that the observations of atmospheric neutrinos were not as expected took place in the 80s when experiments looking for proton decay started studying atmospheric neutrinos as their principal background. The water cherenkov detectors IMB (Irvine-Michigan-Brookhaven) and consequently Kamiokande reported

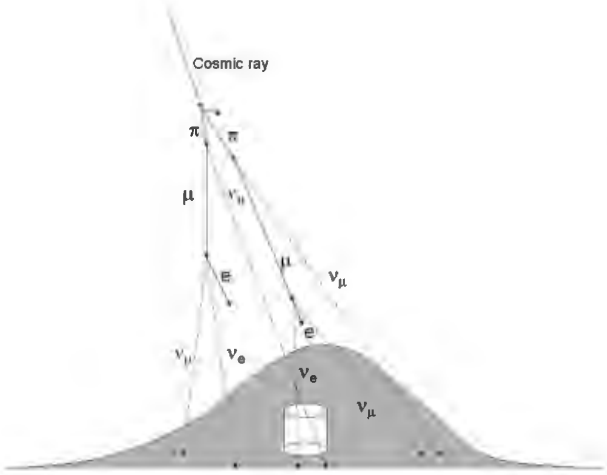

(a) Atmospheric neutrinos from cosmic rays

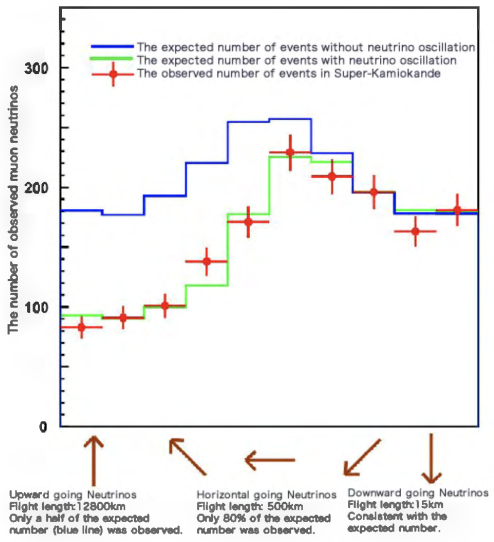

(b) Super Kamiokande result of directional deficit of ν_μ [18].

Figure 1-5: The discovery of atmospheric neutrino oscillation in Super-Kamiokande.

that the ratio of ν_μ to ν_e was smaller than the predicted ratio [18] [19]. This was a first observation of atmospheric neutrino anomaly, however the statistical significance was not sufficient to support any conclusion.

1.1.4 Solution to neutrino anomalies

The solution was eventually explained by neutrino oscillations. The concept of oscillations in the neutrino sector had actually been around for quite some time. B. Pontecorvo was the first to mention neutrino oscillations by analogy with the oscillations of neutral kaons $K^0 \rightleftharpoons \overline{K^0}$. He proposed the possible oscillation of $\nu \rightleftharpoons \overline{\nu}$ for neutrinos back in 1957 [20]. The motivation for this proposition was a statistical fluctuation in an experimental result, pointing to the existence of neutrinos in a reactor antineutrino flux, which vanished shortly after. In 1962 a possible mixing theory for two kinds of neutrinos, $\nu_e \rightleftharpoons \nu_\mu$, was proposed by Z. Maki, M. Nakagawa and S. Sakata [21] [22]. It was based on the idea that the *weak neutrinos*, can be related to the *true neutrinos* (propagating states of definite mass), through some orthogonal transformations, characterized by a mixing angle, implying that a neutrino created with a specific lepton flavour, can later be measured to have a different flavour and this probability is governed by the mass squared difference of the *true neutrino* states. The ultimate experiments which laid to rest the decades old problem and confirmed neutrino oscillations were the Super-Kamiokande and SNO experiment for which they were awarded the 2015 Nobel prize in physics. In 1998, Super-Kamiokande published a clear deficit of atmospheric muon-neutrinos from the other side of the planet which was infered to have oscillated to tau-neutrinos, since no excess of electron-neutrinos was observed in the experiment (figure 1-5-b) [23] [24]. Two years later in 2001 the SNO experiment which used heavy water D_2O as the target, explained the solar neutrino deficit by a two in one experiment where both the CC and NC interactions were detected. In the CC interactions only electron-neutrinos participated while in the NC interactions all neutrino types could be observed. The oscillation between three flavour eigenstates was confirmed [25]. In section 1.2.3 a more complete picture of three neutrino mixing is presented.

1.1.5 Era of neutrino oscillation precision

The first two decades of the 21st century witnessed the launch of many experiments with artificial neutrino sources to study neutrino oscillation parameters which consist

of three mixing angles θ_{12}, θ_{23} and θ_{13}, a charge-parity (CP) violating phase and two mass squared differences (figure 1-6).

KEK to Kamioka (K2K) was the first accelerator long baseline experiment operating

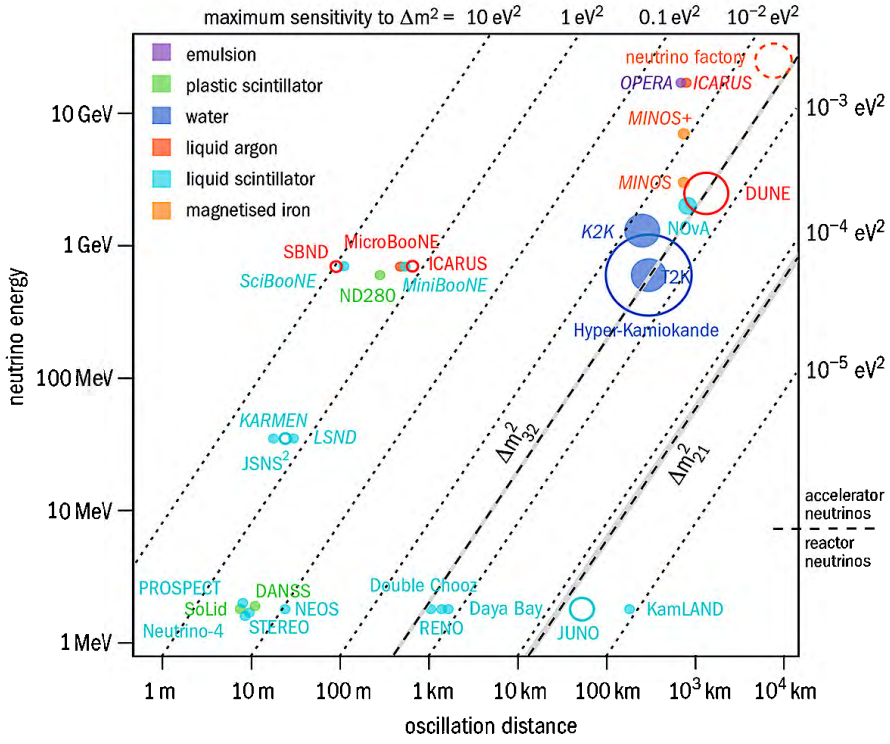

Figure 1-6: Neutrino-oscillation experiments using neutrinos from nuclear reactors or accelerator beams, as a function of the distance from source to detector and the peak energy of the neutrinos. Taken from [26].

from 1999 to 2006. K2K confirmed muon-neutrino disappearance, though could not detect the tau-neutrinos directly which was out of reach for K2K, given their low energies. It was the CERN Neutrinos to Gran Sasso (CNGS) experiment from 2006 to 2012 that had sufficient beam energies to confirm oscillation to tau-neutrinos by directly observing the tau leptons. These experiments were joined by MINOS, T2K and Nova to determine the atmospheric parameters $|\Delta m_{23}|$ and θ_{23}. The Solar experiments combined with KamLand, a long baseline reactor neutrino experiment, measured the solar parameters Δm_{12} and θ_{12}. The θ_{13} which is the smallest of the mixing angles was measured using electron antineutrinos from nuclear reactors by experiments such as Daya Bay, Double Chooz and RENO.

One of the remaining ambiguities in oscillation parameters is the mass ordering of the third neutrino mass eigenstate ν_3 [27]. The two possible mass ordering scenarios are shown in figure 1-7, where *normal* refers to ν_3 being the heaviest and *inverted* refers to ν_3 being the lightest. This question will soon be adressed by the JUNO (Jiangmen

Underground Neutrino Observatory) experiment in China, currently under construction. JUNO is a medium range reactor neutrino experiment and plans to distinguish the mass ordering through exquisite energy resolution which enables it to observe a fast oscillation within a slower and deeper oscillation.

Other remaining piece of the oscillation parameters is the CP violating phase, which

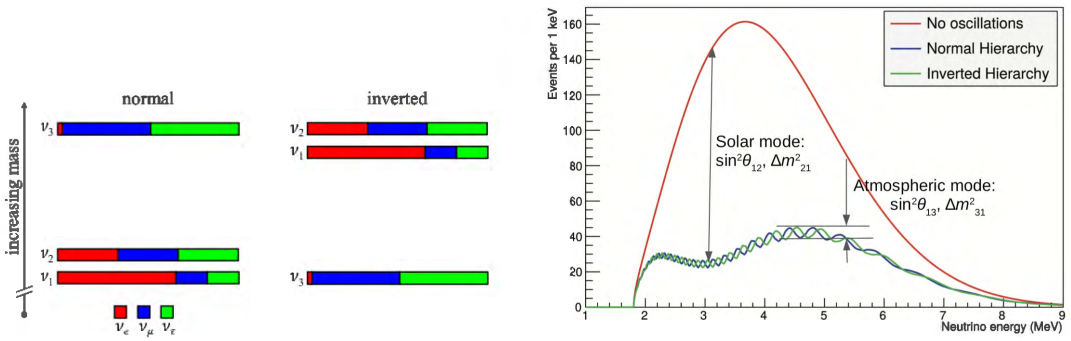

(a) Two possible normal and inverted mass ordering.

(b) JUNO plans to resolve the mass ordering through exquisite energy resolution.

Figure 1-7: Neutrino mass ordering problem.

has not yet been precisely measured. The accelerator based experiments are perfect candidates for this analysis since by switching the polarity of the magnetic horns they can compare the probabilities for the CP-mirror oscillations $\nu_\mu \rightarrow \nu_e$ and $\overline{\nu_\mu} \rightarrow \overline{\nu_e}$. The T2K experiment has recently published an evidence for non-zero values for the CP phase, favouring near maximal CP violation in the vicinity of $\delta_{CP} = -\pi/2$ [28]. Future long baseline neutrino experiments Hyper-Kamiokande in Japan, with water Cherenkov detection technology and the Deep Underground Neutrino Experiment (DUNE) in the US with liquid argon technology have their goals set to measure the exact degree of CP violation in neutrino sector.

Current values of the neutrino mixing parameters from the global best fit analysis of oscillation data for normal and inverted mass ordering are summarized in the table 1.1.

1.1.6 In search of neutrino mass

Measuring the neutrino mass and understanding the mechanism through which neutrinos acquire this mass is a key to physics beyond the standard model. It is also of great importance to cosmological models since cosmological data provide restrictive limits on the sum of neutrino masses $\Sigma\, m_{\nu_i}$ in the range of $[0.11 - 0.68]$ eV [30]. Direct neutrino

Table 1.1: Neutrino mixing parameters [29].

	Normal	Inverted	Units
θ_{12}	$33.82^{+0.78}_{-0.76}$	$33.82^{+0.78}_{-0.76}$	$^\circ$
θ_{23}	$48.3^{+1.2}_{-1.9}$	$48.6^{+1.1}_{-1.5}$	$^\circ$
θ_{13}	$8.61^{+0.13}_{-0.13}$	$8.65^{+0.13}_{-0.12}$	$^\circ$
Δm^2_{21}	$7.39^{+0.21}_{-0.20}$	$7.39^{+0.21}_{-0.20}$	10^{-5}eV^2
Δm^2_{32}	$2.499^{+0.032}_{-0.030}$	$-2.509^{+0.032}_{-0.032}$	10^{-3}eV^2
δ_{CP}	$-1.89^{+0.70}_{-0.58}$	$-1.38^{+0.48}_{-0.54}$	rad

mass determination is based purely on kinematics without further assumptions. Precision investigation of weak decays provide this kinematics information, often referred to as β endpoint measurements. The shape of the β-distribution near the endpoint as

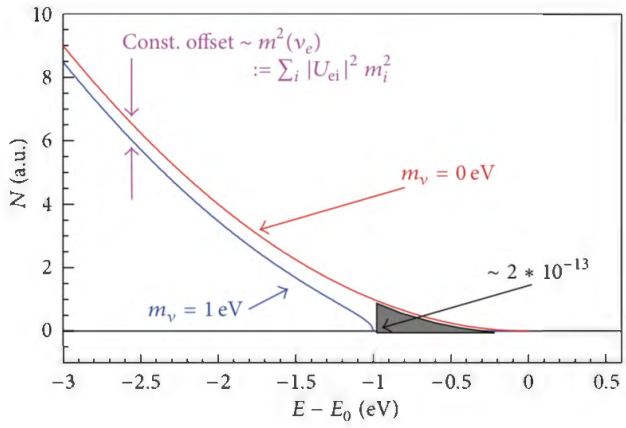

Figure 1-8: β-spectrum around its endpoint E_0 for $m(\nu_e) = 0$ (red line) and $m(\nu_e) = 1$ eV (blue line). The gray area corresponds to $2 \cdot 10^{-13}$ of all tritium β-decays.

seen in figure 1-8 reveals the neutrino mass.

To date the strongest upper limit for the electron-neutrino mass from direct measurements has been put by the KATRIN experiment to be 1.1 eV [31], which has improved the measurements of its predecessor, Troitsk nu-mass experiment, by a factor 2 [32]. KATRIN experiment (figure 1-9) examines the energy spectrum of the electrons emitted from beta decay by a high resolution MAC-E filter. KATRIN aims to advance the experimental sensitivity on m_μ down to 0.2 eV after five years.

Currently there are alternative approaches that aim for comparable performance and better scalability in the study of weak decay endpoints. One aproach is being pursued by the Project 8 experiment through Cyclotron Radiation Emission Spectroscopy (CRES) [33]. This technique uses frequency information from a cyclotron motion of an

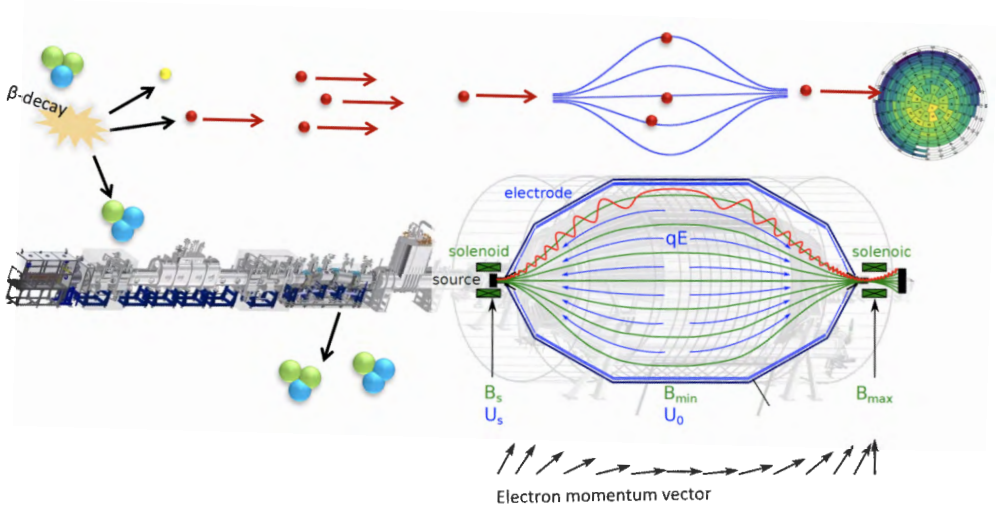

Figure 1-9: KATRIN tritium spectrometer.

electron in a magnetic bottle to infer its kinetic energy. Several other groups explore micro-calorimetric techniques to measure all the de-excitation energy available in rhenium β- decays [34] or holmium electron capture decays [35]. These novel techniques are currently in the R&D phase.

In order to shed light on the nature of neutrino mass, experimental research is focused on neutrinoless double β-decay, a process that is forbidden in the SM and can only occur if the neutrino is its own antiparticle. Discovering such a Majorana nature for neutrino would be in favour of theorists seeking to explain the tininess of neutrino masses by balancing them against still to be discovered heavy neutral leptons (see section 1.2.2).

1.1.7 Neutrino astronomy

The first ideas for large neutrino detectors to look for astrophysical sources of high energy neutrinos were brought forward during the 1976 DUMAND summer workshop in Hawai. It was understood that detection of high energy neutrinos in TeV range, as expected in galactic and extra galactic objects need detectors of gigaton class. The DUMAND project (Deep Underwater Muon and Neutrino Detector), *'a Neutrino eye watching violent remote cosmological epochs'*, envisioned an array of bottom moored strings carrying 22000 optical detectors distributed in a volume of over one cubic kilometer. DUMAND was canceled in 1995 by the US department of energy but the proposed technology was used for smaller water filled detectors such as IMB and Kamiokande. The first accidental astrophysical neutrino observation took place in 1987 during 15 seconds when neutrinos from a supernova collapse in the Large Magellanic

cloud passed through the Earth. The operational neutrino detectors around the world -IMB, Kamiokande and Baskan detectors- observed a burst of neutrinos [36] [37] [38]. Such bursting neutrino sources are expected to occur a few times per century. The original idea of a cubic kilometer neutrino telescope was finally realized years later by the IceCube experiment in the South Pole, and at smaller scales by ANTARES in Mediterranean Sea and GVD in Lake Baikal. In 2013 IceCube reported observation of

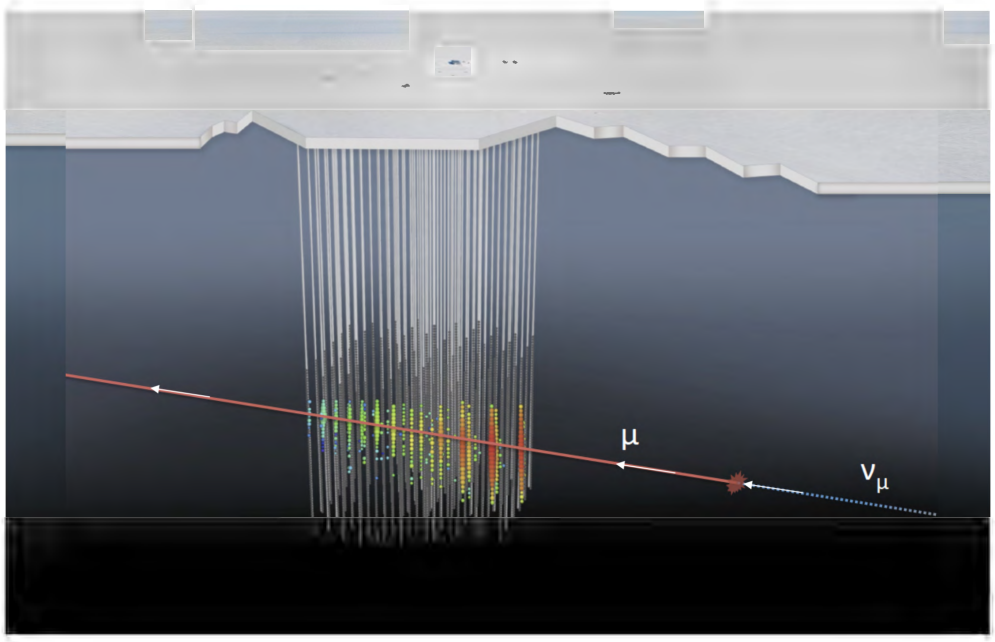

Figure 1-10: Icecube instrument 1 cubic kilometer of natural ice below 1.45 km depth in Antarctica.

high energy astrophysical neutrinos of TeV-PeV energy range [39], paving the way for the new field of multi-messenger astronomy, aiming to study the astronomical sources using photons, neutrinos, cosmic rays and gravitational waves. To date the origins of such ultrahigh energy neutrinos remain an open question. A recent study suggest that radio-bright AGNs (Active galactic nuclei) with parsec-scale cores might be an important population of neutrino sources see figure 1-11 [40].

1.1.8 Cosmic neutrino background

Neutrinos play several roles in the story of the expanding universe. They couple to gravity and contribute to the expansion dynamics, they interact in the primordial plasma with charged leptons and hadrons via electroweak interactions, until the rate of these processes become so slow compared to the expansion rate that they decouple and start to propagate freely, forming the cosmic neutrino background (CNB). Even

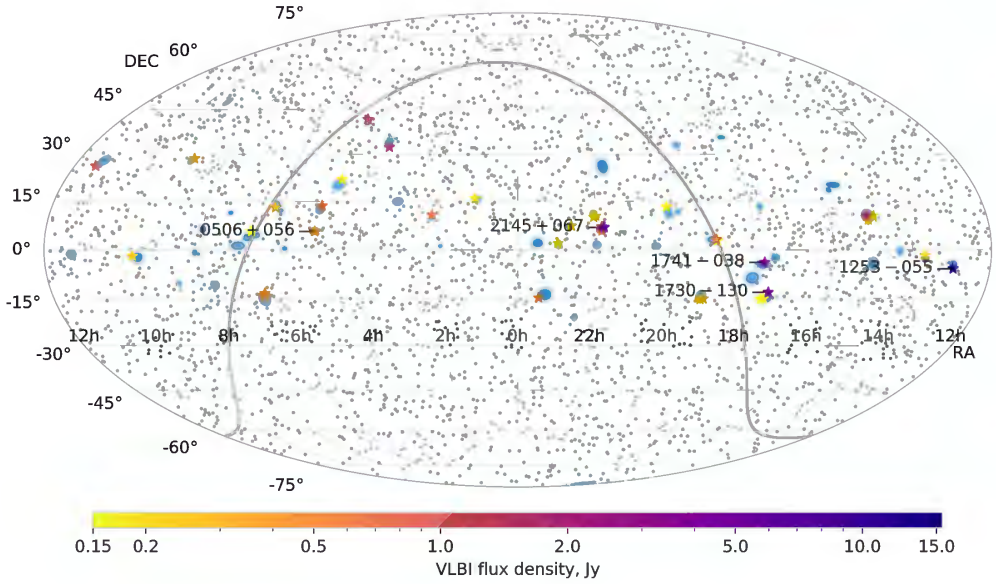

Figure 1-11: IceCube high energy neutrinos represented in blue elipses. Stars represent all AGNs within the neutrino error region, taken from [40].

after that point they continue to silently influence the evolution of the universe. They are perhaps responsible for the production of the baryon density which we see today. They were involved in primordial nucleosynthesis and affected the nuclear abundances and have left their mark in the Cosmic Microwave Background (CMB) anisotropies and in structure formation. The relic neutrinos today are quite cold particles with energies of order 0.1 meV and despite their large number densities of $336/\text{cm}^3$ on Earth they have not yet been detected. For comparison refer to the plot of neutrino flux from different sources on earth, shown in figure 1-12. Perhaps the most realistic

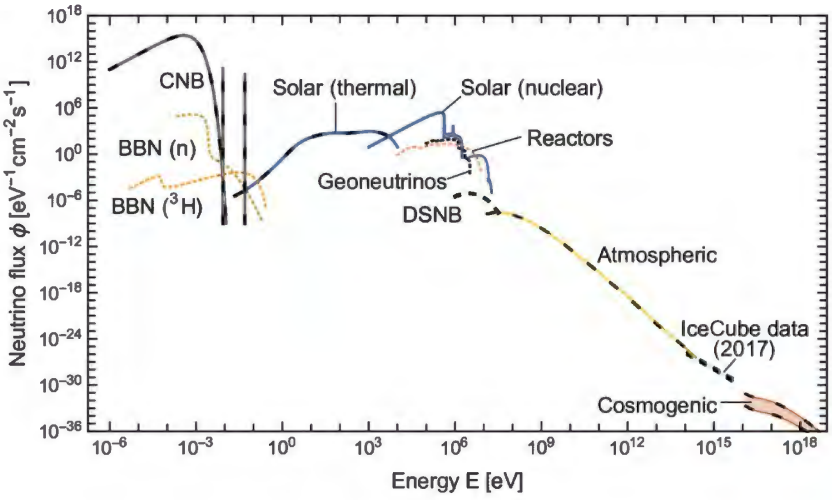

Figure 1-12: Unified Neutrino spectrum at Earth. Taken from [41]

approach to detect CNB neutrinos is neutrino capture on β-unstable nuclei such as

^{3}H. This is the same technique that is used for neutrino mass detection. If the Q-value is the energy available for a specific β decay, the electron energy spectrum has an endpoint at $E_e = Q - m_\nu$, while the CNB neutrino capture process produces a signal at $E_e = Q + m_\nu$. If the neutrino capture rate is not too low and the energy resolution of the apparatus is of the order of m_ν, the capture peak might be visible. The PTOLEMY project in the US aims to develop a conceptual design for a CNB detector [42].

1.2 Theoretical formulation of neutrino physics

According to the standard model (SM), all the matter we know is composed of elementary fermions with spin 1/2. Neutrinos are neutral leptons (fermions with no strong interactions) that come in three generations or flavours, electron-neutrino (ν_e), muon-neutrino(ν_μ) and tau-neutrino (ν_τ), and they participate only in weak interactions. Remarkably, all the known fermions except neutrinos have been observed as left-handed and right-handed chirality. Neutrinos so far have only been observed as left-handed particles. The notion of fermion chirality refers to two types of spin-1/2 representations of the Poincare group. The SM assumes all neutrinos have exactly zero mass and lepton flavour is conserved. This is where the SM fails to explain neutrino oscillations. Minimal extensions of SM, such as νMSM, proposed by T. Asaka and M. Shaposhnikov in 2005 [43], describe non-zero masses of neutrinos by adding three right-handed neutrinos to the particles table (see figure 1-13).

The irreducible representation of fermions in the electroweak gauge group and their

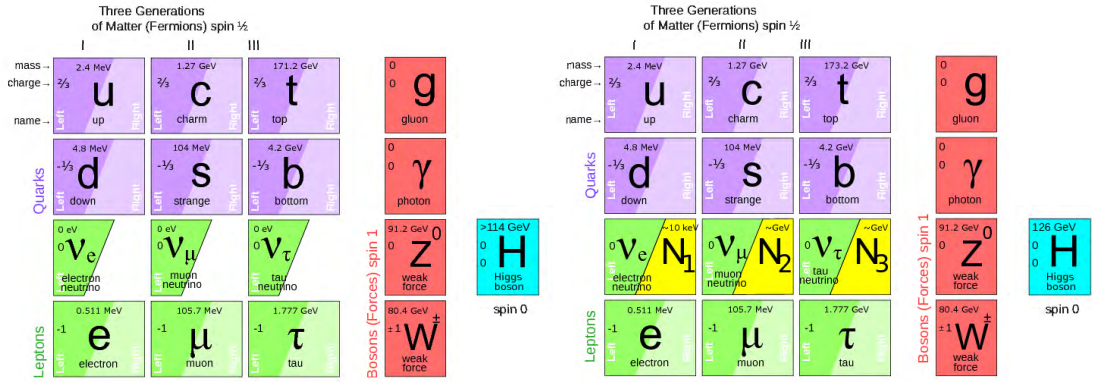

(a) SM (b) νMSM

Figure 1-13: The particle content of the Standard model (left) and the extended SM with right-handed neutrinos

associated charges are shown in table 1.2, where Q , T_3 and Y_W represent electric charge, third component of weak isospin and weak hypercharge respectively. All the fermions represented in table 1.2, have corresponding opposite-handed anti-particle CP partners, with opposite sign charges. The left-handed neutrinos are electrically and color neutral but they have non-zero weak charges and therefore participate in weak interactions whereas the right-handed neutrinos are singlet under all gauge interactions. Such particles are referred to as sterile neutrinos.

Table 1.2: Electroweak quantum numbers of fermions.

Fermion family	Left-chiral fermions				Right-chiral fermions			
	doublets	Q	T_3	Y_W	singlets	Q	T_3	Y_W
Leptons	$\begin{pmatrix}\nu_{eL}\\ e_L\end{pmatrix}, \begin{pmatrix}\nu_{\mu L}\\ \mu_L\end{pmatrix}, \begin{pmatrix}\nu_{\tau L}\\ \tau_L\end{pmatrix}$	0 -1	$+\frac{1}{2}$ $-\frac{1}{2}$	-1 -1	ν_{eR}, $\nu_{\mu R}$, $\nu_{\tau R}$ e_R , μ_R , τ_R	0 -1	0 0	0 -2
Quarks	$\begin{pmatrix}u_L\\ d_L\end{pmatrix}, \begin{pmatrix}c_L\\ s_L\end{pmatrix}, \begin{pmatrix}t_L\\ b_L\end{pmatrix}$	$+\frac{2}{3}$ $-\frac{1}{3}$	$+\frac{1}{2}$ $-\frac{1}{2}$	$+\frac{1}{3}$ $+\frac{1}{3}$	u_R, c_R, t_R d_R , s_R ,b_R	$+\frac{2}{3}$ $-\frac{1}{3}$	0 0	$+\frac{4}{3}$ $-\frac{2}{3}$

1.2.1 Electroweak theory for neutrinos

The electroweak interactions at very high energies are described by a relativistic quantum field theory based on gauge symmetry for the group $SU(2)_L \times U(1)Y$. The fields are mediated by four massless bosons $W^{0,\pm}$ and B^0. However at low energies this gauge symmetry is spontaneously broken to $U(1)_Q$ via the Higgs mechanism. As the Higgs field acquires a vacuum expectation value, three massive bosons of the weak interactions $W^{\pm}$ and Z^0 alongside the massless photon for electromagnetism are produced.

In physical cosmology, this transition occurs as the universe expands and cools below the critical temperature for electroweak symmetry breaking, at ∼160 GeV, which has happened in the early universe shortly after the Big Bang. The electroweak lagrangian density before the symmetry breaking, shown in equation 1.2, consists of kinetic terms for the fermions and the gauge bosons, the Higgs self-interaction terms responsible for symmetry breaking and the Yukawa terms responsible for the charged leptons and quarks masses.

$$\begin{aligned}\mathcal{L}_{\text{EW}} =& i\overline{\psi}\not{D}\psi - \frac{1}{4}\vec{F}_{\mu\nu}\vec{F}^{\mu\nu} - \frac{1}{4}B_{\mu\nu}B^{\mu\nu} \\ &+ (D_\rho\Phi)^\dagger(D^\rho\Phi) + \mu^2\Phi^\dagger\Phi - \lambda(\Phi^\dagger\Phi)^2 + y\overline{\psi_L}\Phi\psi_R + h.c.\ ,\end{aligned} \tag{1.2}$$

where the fermion field ψ can be separated into left-chiral and right-chiral components with P_L and P_R projection operators.

$$\begin{aligned}\psi_L &= P_L\psi = \frac{1-\gamma^5}{2}\psi \\ \psi_R &= P_R\psi = \frac{1+\gamma^5}{2}\psi\end{aligned} \tag{1.3}$$

After electroweak symmetry breaking, the lagrangian reorganizes itself. In equation 1.4, the kinetic terms and the mass terms as well as the electromagnetic, neutral current and charged current interaction terms of the lagrangian are expressed. Here, g is the weak coupling constant and θ_w is the Weinberg angle.

$$\begin{aligned}
\mathcal{L}_{\text{EW}} &= \overline{\psi}(i\partial\!\!\!/ - m_\psi)\psi - \frac{1}{4}A_{\mu\nu}A^{\mu\nu} - \frac{1}{2}W^{+}_{\mu\nu}W^{-\mu\nu} + m_W^2 W^{+}_{\mu}W^{-\mu} \\
&\quad - \frac{1}{4}Z_{\mu\nu}Z^{\mu\nu} + \frac{1}{2}m_Z^2 Z_\mu Z^\mu + \frac{1}{2}(\partial^\mu\phi)(\partial_\mu\phi) - \frac{1}{2}m_\phi^2\phi^2 \\
\mathcal{L}^{(EM)} &= - eQ\overline{\psi}\gamma^\mu\psi A^\mu \\
\mathcal{L}^{(NC)} &= - \frac{g}{2\cos\theta_w}J^\mu_Z Z_\mu + h.c. \\
\mathcal{L}^{(CC)} &= - \frac{g}{2\sqrt{2}}J^\mu_W W_\mu + h.c.
\end{aligned} \tag{1.4}$$

where J^μ_W represents leptonic and quark charge currents, relating the elements in the left-handed doublets:

$$J^\mu_W = 2(\overline{u_i}\gamma_\mu\frac{1-\gamma^5}{2}M^{CKM}_{ij}d_j + \overline{\nu_i}\gamma_\mu\frac{1-\gamma^5}{2}e_i) \tag{1.5}$$

and J^μ_Z represents leptonic and quark neutral current, relating each fermion to itself. Both right-handed and left-handed fermions participate in this reaction but with different strengths.

$$J^\mu_Z = 2(T_3^f\overline{\psi_f}\gamma_\mu\frac{1-\gamma^5}{2}\psi_f - \sin^2\theta_w Q_f\overline{\psi_f}\gamma_\mu\psi_f) \tag{1.6}$$

Bringing back our focus on the neutrinos and inserting the charge values for neutrinos from table 1.2 into equation 1.6, one can see that only left-handed neutrinos couple to the weak gauge bosons $W^\pm$ and Z, and for right-handed neutrinos both terms vanish. The two charged current and neutral current interaction terms can be expressed in Feynman diagrams, figure 1-14.

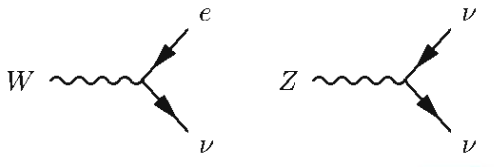

Figure 1-14: Charged current and neutral current for the left-handed neutrinos

1.2.2 Mass terms for neutrinos

Dirac mass term

The Yukawa coupling terms in equation 1.2 give rise to Dirac masses for the fermions in SM. Here we expand in details the leptonic term with the assumption of the right-handed sterile neutirnos:

$$\mathcal{L}_{H,L} = - Y^{l}_{\alpha\beta}\overline{L_{\alpha L}}\Phi l_{\beta R} - Y^{\nu}_{\alpha\beta}\overline{L_{\alpha L}}(i\sigma\Phi^{*})\nu_{\beta R} + h.c \tag{1.7}$$

In this equation the $L = \begin{pmatrix} e_\alpha \\ \nu_\alpha \end{pmatrix}$ is the left-handed lepton doublet, $\Phi = \begin{pmatrix} \phi_+ \\ \phi_0 \end{pmatrix}$ is the Higgs doublet, and the matrices $Y_{\alpha\beta}$ represent the complex couplings. These matrices are generally not diagonal in the three flavours space. This means that the flavour eigenstates or interaction eigenstates $|\nu_\alpha\rangle_{(\alpha=e,\mu,\tau)}$ do not have a definite mass. Once the Higgs field is developed around its minimum and the $Y_{\alpha\beta}$ matrices are diagonalized through bi-unitary transformations we get:

$$\mathcal{L}_{H,L} = - \frac{v + H(x)}{\sqrt{2}} \left(y^{l}_{\alpha}\overline{l_{\alpha L}} l_{\alpha R} + y^{\nu}_{k}\overline{\nu_{kL}}\nu_{kR} + h.c \right) \tag{1.8}$$

The neutrino masses for the mass eignestates are then given by $m_k = y^{\nu}_{k} v/\sqrt{2}$, whereas the contribution proportional to $H(x)$ accounts for tri-linear coupling between the leptons and the scalar boson H. We can rewrite the Dirac mass term for neutrinos in a simple form:

$$\mathcal{L}_{\text{Dirac mass term}} = -m_k\overline{\nu_{kL}}\nu_{kR} + h.c\,, \tag{1.9}$$

Majorana mass term

One other possible mass term that we could add to the Lagrangian is the Majorana mass term. Since the antiparticle of a left-handed neutrino behaves as a right-handed field, we could ask the question whether the ν_R in the mass term could be replaced with the ${\nu_L}^c$. This scenario was introduced by Majorana, working on neutrino masses in 1937 [45]. A Majorana spinor is identical to its antiparticle $\psi = \psi^c$ if it is written in the following form:

$$\psi_{\text{Majorana}} = \psi_L + \psi^{c}_{L}\,. \tag{1.10}$$

Of course an analogous term holds for ψ_R . A proper Majorana mass term with only one left-handed neutrino type can then be written as:

$$\mathcal{L}_{\text{Majorana mass term}} = -\frac{1}{2} m \overline{(\nu_L)^c} \nu_L + h.c\,. \tag{1.11}$$

The Majorana mass term cannot be added for any other SM fields because it would violate the electric charge conservation (for a charged fermion, f_L and $(f_L)^c$ carry opposite charges, so $\overline{(f_L)^c}$ carry the same charge as f_L, which indicate pair production of the same charge). Since the left-handed neutrinos are in the same $SU(2)$ doublet as the charged leptons, any mass term for the left-handed neutrinos, has to be obtained from an $SU(2)$ invariant theory. The Dirac mass term is consistent with $SU(2)$-invariance, while a Majorana mass term for ν_L would not be. A Majorana mass term for ν_R, on the other hand is allowed, and is in fact one of the main ideas behind the see-saw mechanism [46].

See-saw mechanism

The seesaw mechanism is often considered the most natural way to explain the extremely small masses of neutrinos compared with charged fermions. The see-saw lagrangian, equation 1.12, accommodates the Dirac mass term together with a Majorana mass term for ν_R.

$$\begin{aligned} \mathcal{L}_{see-saw} =& - m_D \overline{\nu_L} \nu_R - \frac{1}{2} m_M \overline{(\nu_R)^c} \nu_R + h.c \\ =& - \frac{1}{2} \overline{n^c} M n + h.c\,, \end{aligned}$$

where m_D is a Dirac mass, m_M is a Majorana mass and we have defined:

$$n = \begin{pmatrix} \nu_L \\ (\nu_R)^c \end{pmatrix}, M = \begin{pmatrix} 0 & m_D \\ m_D & m_M \end{pmatrix}, \tag{1.12}$$

we can find the eigenvalues of M to be

$$m_{1,2} = \frac{m_M}{2} \pm \sqrt{\frac{m_M^2}{4} + m_D^2}\,. \tag{1.13}$$

Now looking at the case in which $m_M = 0$, we recover the Dirac eigenvalues $\pm m_D$ (pure Dirac mass). More interesting is the case where $m_M > m_D$ which results in one

Majorana neutrino to have a very small mass.

$$m_1 = \frac{m_D^2}{m_M}\,, \tag{1.14}$$

and one very heavy Majorana neutrino with the mass of order m_M. The light Majorana neutrino

$$n_{1L} = \nu_L + \frac{m_D}{m_M}(\nu_R)^c\,, \tag{1.15}$$

is almost identical to the SM neutrinos (The small admixture of ν_R is not relevant experimentally). As an example we can assume that $m_D = 100$ GeV since this mass comes from the Higgs mechanism. m_M on the other hand can be chosen arbitrarily large $= 10^{14}$GeV, we then find $m_1 = 0.1$ eV, which would be consistent with the experimental upper limits on the value of neutrino mass.

1.2.3 Neutrino mixing and oscillation

In section 1.2.2, we saw that the mass eigenstates $|\nu_i\rangle$ are not exactly the same as the flavour eigenstates $|\nu_\alpha\rangle_{(\alpha=e,\mu,\tau)}$. We can relate these two sets of eigenstates with a unitary matrix called the Pontecorvo-Maki-Nakagawa-Sakata (PMNS) matrix [21] [22],

$$|\,\nu_\alpha\rangle = \sum_i U^*_{\alpha i}\,|\,\nu_i\rangle\,. \tag{1.16}$$

The PMNS matrix can be expressed as 3 rotation and a CP-violating phase.

$$\begin{aligned} U &= \begin{pmatrix} 1 & 0 & 0 \\ 0 & c_{23} & s_{23} \\ 0 & -s_{23} & c_{23} \end{pmatrix} \begin{pmatrix} c_{13} & 0 & s_{13}e^{i\delta_{\rm CP}} \\ 0 & 1 & 0 \\ -s_{13}e^{i\delta_{\rm CP}} & 0 & c_{13} \end{pmatrix} \begin{pmatrix} c_{12} & s_{12} & 0 \\ -s_{12} & c_{12} & 0 \\ 0 & 0 & 1 \end{pmatrix} \qquad (1.17) \\ &= \begin{pmatrix} c_{12}c_{13} & s_{12}c_{13} & s_{13}e^{i\delta} \\ -s_{12}c_{23} - c_{12}s_{13}s_{23}e^{i\delta} & c_{12}c_{23} - s_{12}s_{13}s_{23}e^{i\delta} & c_{13}s_{23} \\ s_{12}s_{23} - c_{12}s_{13}c_{23}e^{i\delta} & c_{12}s_{23} - s_{12}s_{13}c_{23}e^{i\delta} & c_{13}c_{23} \end{pmatrix}, \qquad (1.18) \end{aligned}$$

where $c_{ij} = \cos\theta_{ij}$, $s_{ij} = \sin\theta_{ij}$ and $\delta_{\rm CP}$ is a CP-violating phase.

Flavour oscillation in vacuum

To express the probability of neutrino oscillations in vacuum we assume the scenario in which ν_α with energy E is generated through a charged current weak interaction, propagated for a time t, and then detected as a ν_β through another charged current interaction:

$$P_{\nu_\alpha \to \nu_\beta} = \left| \left\langle \nu_\beta \middle| \nu_\alpha(t) \right\rangle \right|^2 . \tag{1.19}$$

Assuming plain wave solutions for free neutrinos, the evolution of the mass eigenstates in the vacuum is described by the free Hamiltonian H:

$$\left| \nu_i(t) \right\rangle = e^{-iHt} \left| \nu_i(0) \right\rangle , \tag{1.20}$$

and a generic $|\nu_\alpha\rangle$ produced at time $t = 0$ evolves in time as:

$$\left| \nu_\alpha(t) \right\rangle = \sum_k U^*_{\alpha k} e^{-iE_k t} \left| \nu_k(0) \right\rangle . \tag{1.21}$$

The coefficient proportional to $\left| \nu_\beta \right\rangle$ is given by

$$\begin{aligned} \left\langle \nu_\beta \middle| \nu_\alpha(t) \right\rangle &= \sum_k U^*_{\alpha k} e^{-iE_k t} \left\langle \nu_\beta \middle| \nu_k(0) \right\rangle \\ &= \sum_\gamma \sum_k U^*_{\alpha k} e^{-iE_k t} U_{\gamma k} \left\langle \nu_\beta \middle| \nu_\gamma \right\rangle \\ &= \sum_k U^*_{\alpha k} e^{-iE_k t} U_{\beta k} , \end{aligned} \tag{1.22}$$

where we used the orthogonality of eigenstates $\left\langle \nu_\beta \middle| \nu_\gamma \right\rangle = \delta_{\beta\gamma}$. From this expression we can rewrite equation 1.19:

$$P_{\nu_\alpha \to \nu_\beta} = \left| \left\langle \nu_\beta \middle| \nu_\alpha(t) \right\rangle \right|^2 = \textstyle\sum_{k,j} U^*_{\alpha k} U_{\beta k} U_{\alpha j} U^*_{\beta j} e^{-i(E_k - E_j)t} . \tag{1.23}$$

For relativistic neutrinos

$$E_i = \sqrt{|\vec{p}|^2 + m_i^2} \approx |\vec{p}| + \frac{m_i^2}{2|\vec{p}|} \tag{1.24}$$

by substituting this expression into equation 1.23 we get:

$$P_{\nu_\alpha \to \nu_\beta} = \left| \left\langle \nu_\beta \middle| \nu_\alpha(t) \right\rangle \right|^2 = \textstyle\sum_{k,j} U^*_{\alpha k} U_{\beta k} U_{\alpha j} U^*_{\beta j} \exp\left\{ \frac{\Delta m^2_{kj}}{2|\vec{p}|} t \right\} . \tag{1.25}$$

where $\Delta m^2_{kj} = m^2_k - m^2_j$ is the mass square difference of the mass eigenstates. It is customary to replace the time dependence with variable L/c, since in a neutrino experiment the time dependence of the flavour transition cannot be followed, but rather one can measure the distance of the detection point from the origin of the neutrino beam. equation 1.25 in natural units becomes

$$P_{\nu_\alpha \to \nu_\beta}(L) \;=\; \sum_{k,j} U^*_{\alpha k} U_{\beta k} U_{\alpha j} U^*_{\beta j} \exp\left\{ \frac{\Delta m^2_{kj}}{2|\vec{p}|} L \right\}. \tag{1.26}$$

One can split the summation $\sum_{k,j} = \sum_{k>j} + \sum_{j>k} + \sum_{k=j}$ and rewrite 1.26 in this form

$$\begin{aligned} P(\nu_\alpha \to \nu_\beta) \;=\; & \delta_{\alpha\beta} - 4 \sum_{k>j} Re(U^*_{\alpha k} U_{\beta k} U_{\alpha j} U^*_{\beta j}) \sin^2 \left(\frac{\Delta m^2_{kj} L}{4|\vec{p}|} \right) \\ & + 2 \sum_{k>j} Im(U^*_{\alpha k} U_{\beta k} U_{\alpha j} U^*_{\beta j}) \sin \left(\frac{\Delta m^2_{kj} L}{2|\vec{p}|} \right), \end{aligned} \tag{1.27}$$

Figure 1-15 shows the vacuum oscillation probabilities for electron-neutrino, muon-neutrino and tau-neutrino with energy of 1 GeV. The oscillation parameters used to generate these plots are the global best fit values reported in table 1.1.

The charge, parity, time reversal (CPT) and the charge, parity (CP) transformations relate transition amplitudes between neutrinos and antineutrinos in the following way

$$|\nu_\alpha\rangle \to \left|\nu_\beta\right\rangle \overset{CPT}{\longleftrightarrow} \left|\overline{\nu_\beta}\right\rangle \to |\overline{\nu_\alpha}\rangle \tag{1.28}$$

$$|\nu_\alpha\rangle \to \left|\nu_\beta\right\rangle \overset{CP}{\longleftrightarrow} |\overline{\nu_\alpha}\rangle \to \left|\overline{\nu_\beta}\right\rangle . \tag{1.29}$$

The CPT symmetry is always obeyed in electroweak transitions, which is confirmed by all present data. Observation of a difference between the two oscillation probabilities $P_{\nu_\alpha \to \nu_\beta} - P_{\overline{\nu_\alpha} \to \overline{\nu_\beta}}$ implies the discovery of CP-violation in neutrinos. By using the same steps we went through for neutrinos one can write the antineutrino oscillation probability and thus the difference in the probabilities reads:

$$P_{\nu_\alpha \to \nu_\beta}(L) - P_{\overline{\nu_\alpha} \to \overline{\nu_\beta}}(L) \;=\; 4 \sum_{k>j} Im(U^*_{\alpha k} U_{\beta k} U_{\alpha j} U^*_{\beta j}) \sin \left(\frac{\Delta m^2_{kj} L}{2|\vec{p}|} \right). \tag{1.30}$$

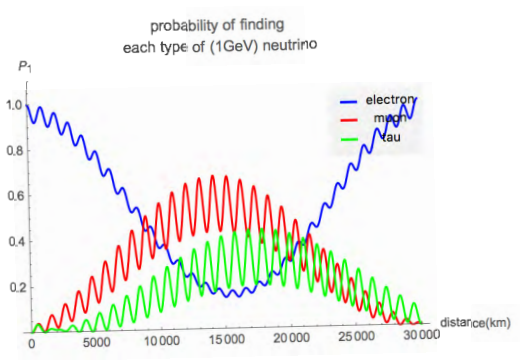

(a) electron-neutrino oscillations

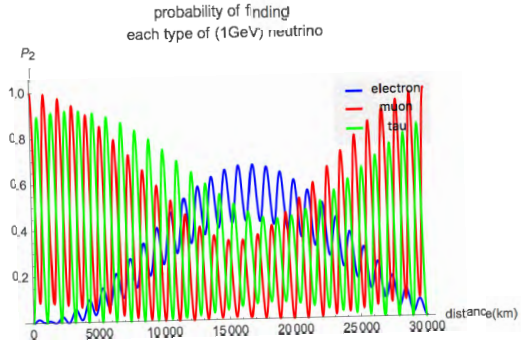

(b) muon-neutrino oscillations

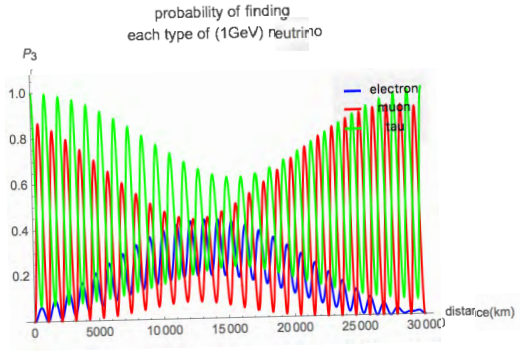

(c) tau-neutrino oscillations

Figure 1-15: Vacuum oscillation probabilities for the electron-neutrino (blue), muon-neutrino (red) and tau neutrino (green). The plots are generated by Mathematica [47].

The CP-violation term for the $(\nu_\mu \to \nu_e)$ appearance probability is:

$$\begin{aligned} &\pm \cos\theta_{13}\ \sin(2\theta_{13})\ \sin(2\theta_{12})\ \sin(2\theta_{23})\ \sin\delta_{CP} \\ &\times \sin\left(\frac{\Delta m^2_{32} L}{4E_\nu}\right) \sin\left(\frac{\Delta m^2_{31} L}{4E_\nu}\right) \sin\left(\frac{\Delta m^2_{21} L}{4E_\nu}\right), \end{aligned} \tag{1.31}$$

with the + and - sign for ν_e and $\overline{\nu_e}$ respectively. Inserting the parameters for the T2K experiment, the CP-violation term for the appearance probability will have a peak around 600 MeV, indicating the most important energy region to explore for evidence of δ_{CP}.

Flavour oscillation in matter

As shown earlier, flavour oscillation is a consequence of the different velocities of propagation of neutrino mass eigenstates. This is a pure quantum phenomenon where the oscillation frequencies f_i are related to the energy of the states $E_i = hf_i$. In

a medium different from vacuum the electron-neutrinos receive an additional phase caused by the potential of a gas of unpolarized electrons existing in the medium, as first remarked by Wolfenstein and later by Mikheev and Smirnov [48] [49]. It is commonly known as the MSW matter effect. Similar charge current scatterings are absent for other neutrino types since ordinary matter does not contain μ or τ. Neutral current scatterings of neutrinos with any particle X of the medium can also generate additional phases, however this contribution is the same for all types of neutrinos. The hamiltonian density of the Fermi interaction between electrons and electron-neutrino is the following

$$H^{CC} = \frac{G_f}{\sqrt{2}}[\overline{\nu_e}\gamma_\mu(1-\gamma_5)e][\overline{e}\gamma^\mu(1-\gamma_5)\nu_e] \tag{1.32}$$

A gas of unpolarized electrons with a statistical distribution function $f(E_e)$ can be described by the density matrix

$$\rho_e = \int \frac{d^3p_e}{(2\pi)^3 2E_e} f(E_e)\frac{1}{2}\sum \left|e^-\right\rangle \left\langle e^-\right| . \tag{1.33}$$

The effective potential due to charged current interactions, V_{CC}, is obtained by averaging 1.32 over the background particle distribution

$$\overline{H^{CC}_{eff}} = Tr[\rho_e H^{CC}_{eff}(x)] = V_{CC}\overline{\nu_{eL}}(x)\gamma^0\nu_{eL}(x) \tag{1.34}$$

$$V_{CC} = \sqrt{2}G_F n_e . \tag{1.35}$$

The same approach can be applied to neutral current interactions of neutrinos of any flavour α in a background of unpolarized fermions, including electrons, protons and neutrons. The Neutral current effective potential V_{NC} is

$$V^f_{NC} = \sqrt{2}G_F[n_e g^e_V + n_p g^p_V + n_n g^n_V] , \tag{1.36}$$

and after inserting the g_V values for fermions, we get

$$V^f_{NC} = -\frac{1}{2}\sqrt{2}G_F n_n . \tag{1.37}$$

Now we can write an effective potential for a generic ν_α

$$V_\alpha = \sqrt{2}G_F(n_e\delta_{e\alpha} - \frac{1}{2}n_n) . \tag{1.38}$$

In the Schrödinger picture, a neutrino initially in the α state evolves according to

$$i\frac{d}{dt}\left|\nu_\alpha(t)\right\rangle = (H_0 + H_I)\left|\nu_\alpha(t)\right\rangle \,, \tag{1.39}$$

such that $H_0\left|\nu_k\right\rangle = E_k\left|\nu_k\right\rangle$ and $H_I\left|\nu_\alpha\right\rangle = V_\alpha\left|\nu_\alpha\right\rangle$. The matrix element of the flavour transition $\alpha \to \beta$ will get the following evolution equation

$$i\frac{d}{dL}\left\langle\nu_\beta\middle|\nu_\alpha(L)\right\rangle = (U^k_\beta E_k U^{\dagger\gamma}_k + \delta^\gamma_\beta V_\gamma)\left\langle\nu_\gamma\middle|\nu_\alpha(L)\right\rangle \,. \tag{1.40}$$

If we consider the electron and muon bi-dimensional space the hamiltonian reduces to a 2 hermitian matrix:

$$H_{\text{eff}} = \frac{1}{4|\vec{p}|}\begin{pmatrix} -\Delta m^2\cos(2\theta) + 2|\vec{p}|\,V_{CC} & \Delta m^2\sin(2\theta) \\ \Delta m^2\sin(2\theta) & \Delta m^2\cos(2\theta) - 2|\vec{p}|\,V_{CC}\end{pmatrix} \tag{1.41}$$

$$\tag{1.42}$$

which can be diagonalized via an orthogonal transformation, $O(\theta_M)$:

$$H_M = \begin{pmatrix}\Delta m^2_M & 0 \\ 0 & \Delta m^2_M\end{pmatrix} = O^T(\theta_M)H_{\text{eff}}O(\theta_M) \tag{1.43}$$

The mixing angle in matter, θ_M becomes

$$\tan(2\theta_M) = \tan(2\theta)[1 - \frac{2|\vec{p}|\,V_{CC}}{\Delta m^2\cos(2\theta)}]^{-1} \tag{1.44}$$

This evolution equation shows a resonance for

$$\Delta m^2\cos(2\theta) = 2|\vec{p}|\,V_{CC}\,, \tag{1.45}$$

which can be expressed in terms of electron number density

$$n_e^{\text{res}} = \frac{\Delta m^2\cos(2\theta)}{2\sqrt{2}G_F|\vec{p}|}\,. \tag{1.46}$$

When this condition is satisfied, $\theta_M = \pi/4$ and the largest transition from one flavour to the other occurs. In astrophysical environments such as the sun and supernovae the matter density can provide the condition for a resonant conversion which is the mechanism behind the solar neutrino problem.

1.2.4 Neutrino interactions

Neutrinos interact weakly with matter through charged current (CC) processes mediated by a $W^{\pm}$ boson, or through neutral current (NC) processes mediated by a Z boson, whose masses are of the order of 100 GeV. As long as energies carried by leptons and quarks are much smaller than this value, the gauge bosons can only propagate as virtual particles and we can use the effective lagrangian described in 1.4. The general form of a two body scattering process is encoded in the matrix element $\mathcal{M}$, and the phase space available in the interaction.

Neutrino-electron interaction We can consider a simple case where a muon-neutrino with 4-momentum p_ν scatters with an atomic electron at rest in the lab frame with 4-momentum p_e, producing an outgoing muon with 4-momentum k_μ and a scattered electron-neutrino with 4-momentum k_e.

$$\nu_\mu + e^- \to \mu^- + \nu_e \tag{1.47}$$

The Lorentz invariant kinematic variables s, Q^2 and y are

$$\begin{aligned} s &= (p_\nu + p_e)^2 \quad (\text{center of mass energy}) , && (1.48)\\ Q^2 &= -q^2 = (p_\nu - k_\mu)^2 \quad (\text{momentum transfer}) , && (1.49)\\ y &= \frac{p_e \cdot q}{p_\nu \cdot p_e} \quad (\text{inelasticity}) . && (1.50) \end{aligned}$$

for a two body collision with a stationary target, the cross-section is given by the general formula

$$\frac{d\sigma}{dq^2} = \frac{1}{16\pi} \frac{\left|\mathcal{M}^2\right|}{(s - m_e^2)^2} . \tag{1.51}$$

In order to express the differential cross-section as a function of the muon scattering angle, θ_μ, or the fraction of neutrino energy transferred to the lepton, y, one can use the proper Jacobian:

$$\begin{aligned} \frac{dq^2}{d\cos\theta_\mu} &= 2|\vec{p}_\nu|\left|\vec{k}_\mu\right| , && (1.52)\\ \frac{dq^2}{dy} &= 2m_e E_\nu . && (1.53) \end{aligned}$$

The tree level amplitude for this scattering is

$$\mathcal{M}_{\nu_\mu e^- \to \mu^- \nu_e} = -\frac{G_F}{\sqrt{2}}\{[\overline{\mu}\gamma^\mu(1-\gamma^5)\nu_\mu][\overline{\nu}_e\gamma_\mu(1-\gamma^5)e]\} \tag{1.54}$$

By summing over all polarization and spin states, and integrating over all unobserved momenta, one gets the differential cross-section:

$$\frac{d\sigma_{(\nu_\mu e^- \to \mu^- \nu_e)}}{dy} = \frac{2m_e G_F^2 E_\nu}{\pi}\left(1 - \frac{(m_\mu^2 - m_e^2)}{2m_e E_\nu}\right), \tag{1.55}$$

This cross-section has an energy threshold imposed by kinematics of the system, $E_\nu \geq \frac{m_\mu^2 - m_e^2}{2m_e}$, which reflects the fact that the center of mass energy of the collision needs to be greater than the squared mass of the generated lepton, in this case a muon, $s > m_\mu^2$. By inserting the numerical values, we can find the energy threshold of neutrinos interacting with the atomic electrons to be $E_\nu > 11$ GeV. Integration of the above expression yields the total neutrino cross-section as a function of neutrino energy:

$$\sigma_{\nu_\mu + e^- \to \mu^- + \nu_e} \simeq \frac{2m_e G_F^2 E_\nu}{\pi} = \frac{G_F^2 s}{\pi}. \tag{1.56}$$

We can see that the neutrino cross-section grows linearly with energy.

Neutrino-nucleus interaction: The simplest nuclear interaction that we can consider is the inverse beta decay:

$$\overline{\nu}_e + p \to e^+ + n \tag{1.57}$$

The threshold for this process is given by $E_\nu \geq \frac{(m_n + m_e)^2 - m_p^2}{2m_p} = 1.806$ MeV. The relevant matrix element is given by:

$$\mathcal{M} = \frac{G_F V_{ud}}{\sqrt{2}}\left[\langle \overline{n}|\, \overline{u}_d(\gamma_\mu(1-\gamma^5)u_u\,|p\rangle\, \langle \overline{\nu}_e|\, \gamma_\mu(1-\gamma^5)\,|e\rangle\right]. \tag{1.58}$$

In principle the hadronic currents should be computed using quantum chromodynamics (QCD), but unfortunately it is still hardly treatable. Typically to study the hadronic current, one exploits the symmetry constraints and expresses it in terms of complex

form factors:

$$\mathcal{M} = \frac{G_F V_{ud}}{\sqrt{2}} \left[\langle \overline{n} | \left(\gamma_\mu f_V(0) - \gamma_\mu \gamma^5 f_A(0) - \frac{i f_P(0)}{2M_n} \sigma_{\mu\nu} q^\nu \right) | p \rangle \langle \overline{\nu}_e | \gamma_\mu (1 - \gamma^5) | e \rangle \right] , \quad (1.59)$$

where f_V, f_A and f_P are the nuclear vector, axial and Pauli (weak magnetism) form factors evaluated at zero momentum transfer. With this recipe, the differential cross-section with respect ot scattering angular becomes:

$$\frac{d\sigma_{(\overline{\nu}_e p \to e^+ n)}}{d\cos\theta} = \frac{G_F^2 |V_{ud}|\, E_e p_e}{2\pi} \left[f_V^2(0)(1 + \beta_e \cos\theta) + 3 f_A^2(0)(1 - \frac{\beta_e}{3} \cos\theta) \right] , \quad (1.60)$$

where E_e, p_e, β_e, and $\cos\theta$ refer to the electrons energy, momentum, velocity and scattering angle respectively.

Descriptions of the low energy neutrino cross-sections are based on a variety of model-building scenarios. Yet, the number of direct experimental measurements of these cross-sections is remarkably few, making the ability to test the robustness of theoretical models and techniques somewhat limited. As we move up to intermediate energies $E_\nu \sim 0.1 - 20$ GeV, the description of neutrino scattering becomes more diverse and complicated. We can name several distinct scattering mechanisms:

- ***Elastic and quasi-elastic scattering:*** For neutrino energies less than $\sim$ 2 GeV, the interactions are predominantly quasi-elastic (QE) where the neutrino can elastically scatter off an entire nucleon liberating a nucleon (or multiple nucleons) from the target while converting a neutron to a proton or vice versa.

$$\nu_\mu + n \to \mu^- + p \quad (1.61)$$

$$\overline{\nu}_\mu + p \to \mu^+ + n \,, \quad (1.62)$$

  Based on the Llewellyn Smith formulation [51], the QE differential cross-section can be expressed as:

$$\frac{d\sigma}{dQ^2} = \frac{G_F^2 M^2 |V_{ud}|^2}{8\pi E_\nu^2} \left[A(Q^2) \pm \frac{s-u}{M^2} B(Q^2) + \frac{s-u}{M^4} C(Q^2) \right] , \quad (1.63)$$

  where M is the nucleon mass, m is the lepton mass, $(s-u) = 4ME_\nu - Q^2 - m^2$ and the factors A, B and C are functions of the F_V, F_A and F_P form factors of the nucleon. This formalism was used for neutrino scattering on deuterium, whereas modern day neutrino experiments use complex nuclei as their neutrino target. As a result nuclear effects introduce sizable modifications to 1.63. Since

the QE events form the largest contribution of signal samples in many oscillation experiments like T2K, increasing efforts have been put in measurement and modeling of nuclear effects. An example used by most experiments is the relaticvistic Fermi Gas model [52].

- ***Resonance production:*** At energies above ~ 200 MeV, neutrinos can excite the target nucleon to a resonance state (Δ, N) which decays to a variety of mesonic final states. We can consider the case of a single pion production:

$$\nu_\mu N \to \mu^- \quad N^* \tag{1.64}$$

$$N^* \quad \to \pi N' \tag{1.65}$$

For single pion production the transition amplitude for CC and NC interactions can be written as:

$$\mathcal{M}_{CC} = \frac{G_F \cos\theta_C}{\sqrt{2}} [\bar{l}\gamma^\mu(1-\gamma^5)\nu] \langle N^*| J_\mu |N\rangle \ , \tag{1.66}$$

$$\mathcal{M}_{NC} = \frac{G_F}{\sqrt{2}} [\overline{\nu}\gamma^\mu(1-\gamma^5)\nu] \langle N^*| J_\mu |N\rangle \ . \tag{1.67}$$

Based on Rein and Sehgal's model [53], the double differential cross-section of a single resonance with mass M_{N^*} in narrow width approximation is given by:

$$\frac{d^2\sigma}{dQ^2 dE_q} = \frac{1}{64\pi M_N E_\nu^2} \sum_{\text{spins}} |\mathcal{M}|^2 \, \delta(W^2 - M_{N^*}^2) \, . \tag{1.68}$$

where W is the observed resonant mass. For a resonance of finite width we can replace the δ-function by a Breit-Wigner factor:

$$\delta(W^2 - M_{N^*}^2) \to \frac{1}{2\pi} \frac{\Gamma}{(W - M_{N^*})^2 + \Gamma^2/4} \, . \tag{1.69}$$

where Γ is the decay width of N^*. For other resonances such as single photon, K and η productions, one needs to change the decay probability of the resonance. figure 1-16 shows the contributions of different scattering mechanisms alongside existing measurements for charged current neutrino and antineutrino processes.

- ***Deep inelastic scattering:*** Above a neutrino energy of $\sim 20-30$ GeV, neutrinos can resolve the individual quark constituent of the nucleon which manifests

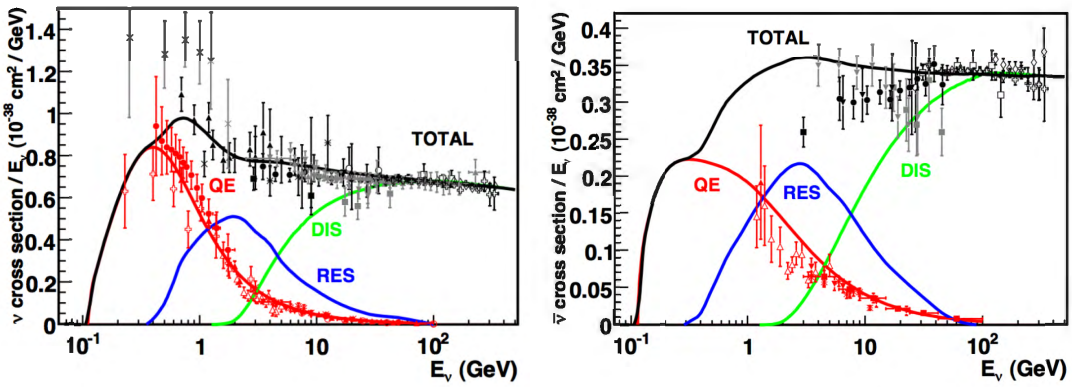

(a) ν_μ CC cross-section (b) $\overline{\nu}_\mu$ CC cross-section

Figure 1-16: Contribution of different scattering mechanisms for intermediate energies of muon-neutrino and muon antineutrino. The plot shows charged current cross-sections per nucleon divided by neutrino energy as a function of energy [54].

in the creation of a hadronic shower:

$$\nu_\mu N \to \mu^- X \quad \overline{\nu}_\mu N \to \mu^+ X \tag{1.70}$$

$$\nu_\mu N \to \nu_\mu X \quad \overline{\nu}_\mu N \to \overline{\nu}_\mu X\,. \tag{1.71}$$

DIS processes can be described by three kinematic invariants, the 4-momentum

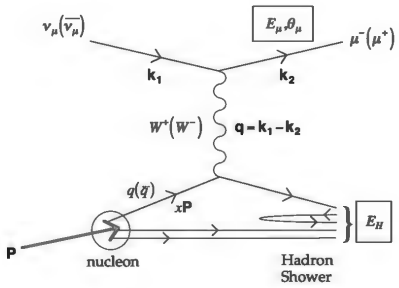

Figure 1-17: Diagram for a CC-DIS process.

transfer ($Q^2 = -q^2$), the inelasticity y, and the Bjorken scaling variable x:

$$Q^2 = -m_\mu^2 + 2E_\nu(E_\mu - p_\mu \cos\theta_\mu) \tag{1.72}$$

$$y = E_H/E_\nu \tag{1.73}$$

$$x = \frac{Q^2}{2M_N E_H}\,. \tag{1.74}$$

where E_H is the energy of the hadronic system. Using these variables, the cross-section for DIS scattering can be written as:

$$\frac{d^2\sigma^{\nu,\bar{\nu}}}{dx\ dy} = \frac{G_F^2 M_N E_\nu}{\pi(1+Q^2/M_{W,Z}^2)^2}\Big[y^2 x F_1(x,Q^2) + (1-y-\frac{M_N x y}{2E_\nu})F_2(x,Q^2) \pm y(1-\frac{y}{2})xF_3(x,Q^2)\Big], \tag{1.75}$$

where $F_i(x,Q^2)$ are the nucleon structure functions and can be expressed in terms of parton distribution functions (PDFs). DIS has long been used to validate the standard model and probe nucleon structure.

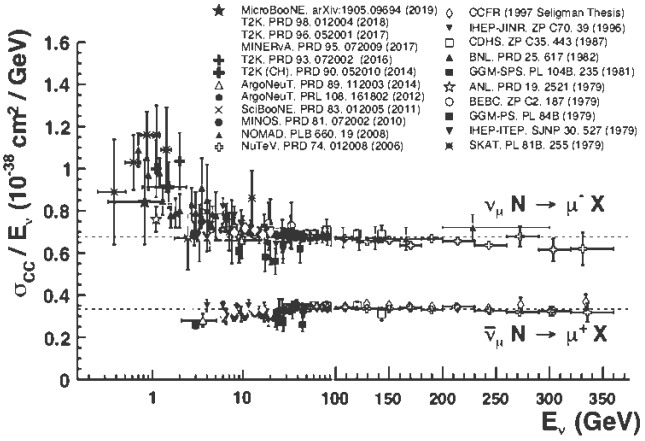

Figure 1-18: Inclusive neutrino and antineutrino CC cross-sections devided by neutrino energy. world averaged cross-sections for neutrinos and antineutrinos are indicated by dotted lines.

Looking at the figure 1-18, the charged current cross-sections for neutrinos are typically twice as large as that for antineutrinos for high energies and about three times larger at energies around 1 GeV. For experiments like T2K, this difference enhances the contamination of neutrino background events in the antineutrino beam mode. Therefore the discrimination of neutrino events is very important for precise measurements of the antineutrino cross-sections. The difference also implies that the antineutrino cross section measurements requires higher beam fluxes to obtain the same statistics as in the neutrino measurements.

Chapter 2

The T2K Experiment

The T2K (Tokai to Kamioka) experiment [55] is a long baseline accelerator neutrino experiment which was launched in 2006, in order to use the already existing Super-Kamiokande detector (see section 2.4) with an accelerator neutrino beam, to seek the observation of the appearance of a neutrino flavour, $\nu_\mu \rightarrow \nu_e$. Figure 2-1 shows an

(a) T2K location in Japan.

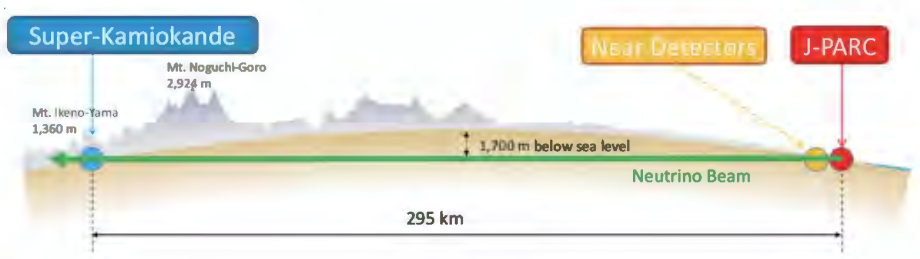

(b) T2K beam.

Figure 2-1: A schematic layout of T2K experiment.

overview of the T2K experiment. The neutrino beam is generated at Japan Proton Accelerator Research Complex (J-PARC) in Tokai, located on the east coast of Japan, and is sent towards Kamioka in western Japan. The beam is first sampled by a near detector (ND280) located 280 m downstream of the beam target, and is measured again by Super-Kamiokande (SK) after traveling a distance of 295 km. The ND280 and SK are both located at 2.5° off-axis angle with respect to the beam direction. Figure 2-2 shows the beam energy spectrum at different off-axis angles. The off-axis method has the advantage that the beam flux has a narrower band in energies with a peak shifted to lower energy values around 600 MeV. This specific energy region is

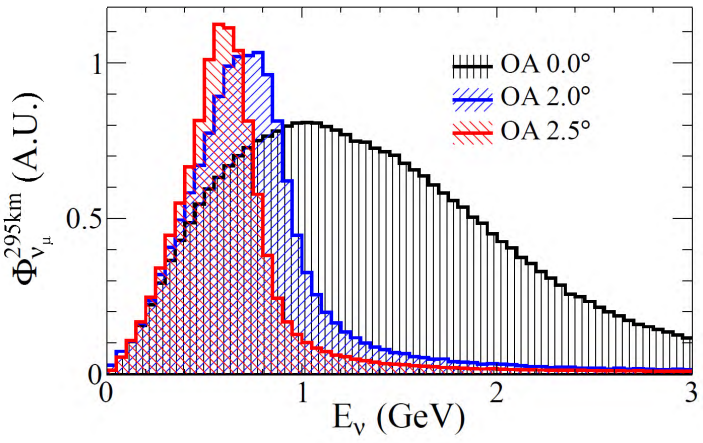

Figure 2-2: Off-axis neutrino beam method.

where the maximum oscillation for ν_μ disappearance and $\nu_\mu \rightarrow \nu_e$ transition happens, and therefore observation of the CP violation becomes accessible for T2K. Since the beginning of operation in 2010, T2K has achieved a number of milestones by studying two modes of neutrino oscillations, electron-neutrino appearance and muon-neutrino disappearance [56] [57]. T2K has accumulated a total of 31.97×10^{20} protons on target (POT) in the ν_μ mode and 16.3×10^{20} POT in the $\overline{\nu}_\mu$ mode by February 2020, which is 30% of the original T2K target POT.

2.1 T2K extended run

The T2K collaboration has recently approved to extend the data taking for a five or six years period to reach 20×10^{21} POT [58], in order to explore CP violation with sensitivity greater than 3σ (if $\delta_{CP} \sim -\frac{\pi}{2}$ and the mass hierarchy is normal), and improve the precision of neutrino oscillation parameters, θ_{23} and Δm^2_{32}. Figure 2-3 shows the target data accumulation scenario where six months operation of the

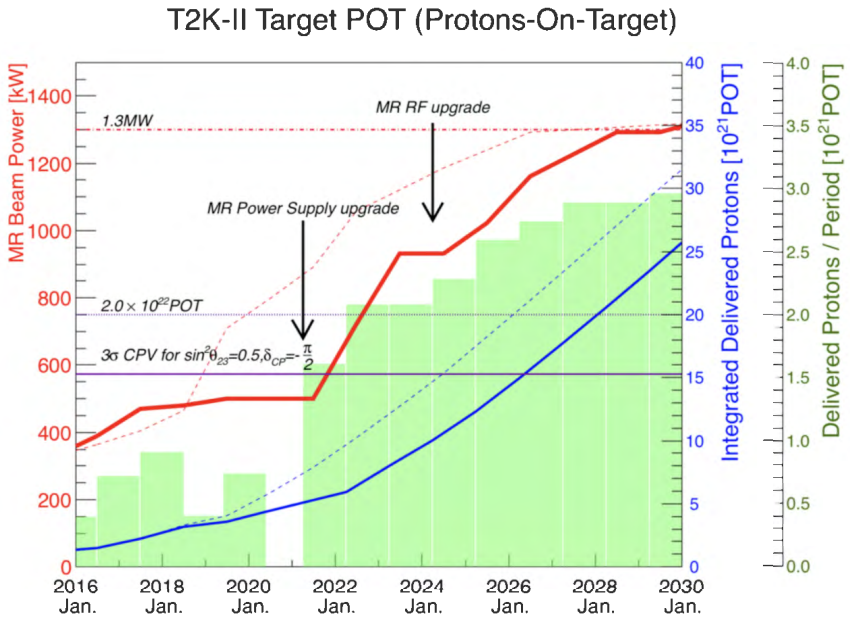

Figure 2-3: The target main ring beam power and accumulated POT for the T2K extended run (T2K-II).

accelerator each year and the running time efficiency of 90% is assumed. The next generation neutrino oscillation projects, Hyper-Kamiokande and DUNE aim to study CP violation with greater sensitivity across a wide range of parameter space, on the time scale of 2026 and beyond. Dune experiment in addition looks for the order of mass hierarchy.

2.2 The T2K neutrino beam

The T2K neutrino beam is obtained from acceleration of protons. J-PARC hosts three accelerators, a linear accelerator (LINAC), a rapid-cycling synchrotron (RCS) and a main ring (MR) synchrotron (see figure 2-4-a). The protons injected into MR form eight bunches in a cycle and are accelerated up to 30 GeV. The circulating proton bunches are then extracted within one turn (fast extraction) into the neutrino primary beamline. Spills with a width of 5.6 μs are repeated every 2.48 s. Each bunch has a width of 58 ns and bunches are separated from each other by 580 ns. The design parameters of the MR for the neutrino beamline extraction are listed in table 2.1. The primary beamline directs the extracted proton bunches towards the neutrino production target. The intensity, profile and position of the protons are monitored by various beam instruments. The target is a graphite rod, 90 cm in length and 2.6 cm in diameter, enclosed by a titanium container. It is designed to withstand thermal

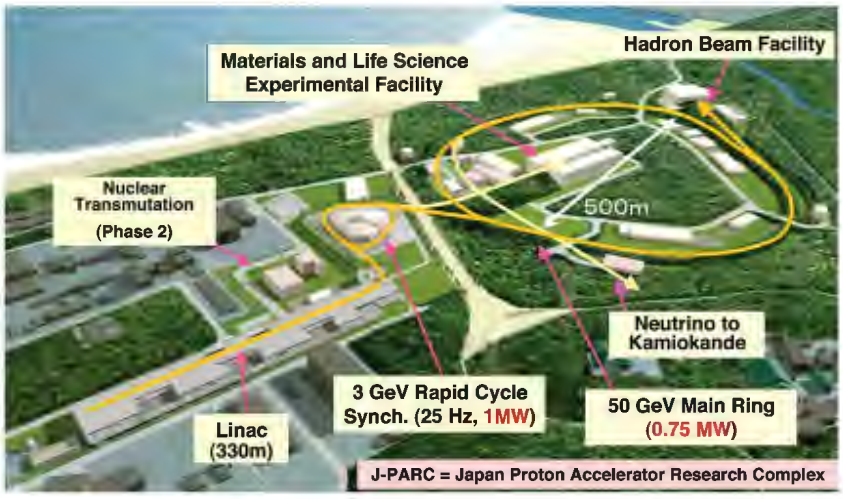

(a) J-PARC facility overview.

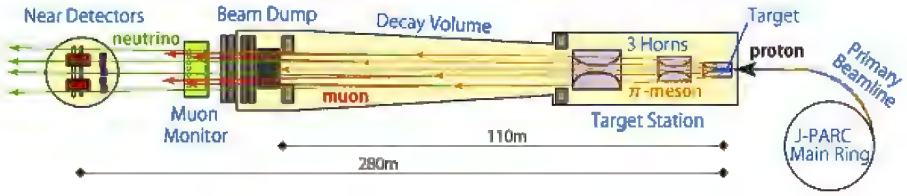

(b) Secondary beamline overview.

Figure 2-4: Neutrino beam creation at J-PARC facility.

Table 2.1: Design parameters of the J-PARC Main Ring synchrotron .

Max. Beam power	~ 750 kW
Beam kinetic energy	30 GeV
Beam intensity	$\sim 3 \times 10^{14}$ p/spill
Spill cycle	~ 0.4 Hz
RF frequency	$1.67 - 1.72$ MHz

shocks from a beam delivery with up to 3.3×10^{14} protons per pulse (ppp). The impact of protons on the target generates secondary pions. Three magnetic horns focus the pions of one charge and scatter the opposite charge. The focused pions enter the decay volume of 94 m long, where they decay in flight into muons and moun-neutrinos. An overview of the secondary beamline is shown in figure 2-4-b. Changing the polarity of the magnetic horns current (from 250 kA to -250 kA), makes a switch between neutrino mode (equation 2.1) and antineutrino mode (equation 2.2) beams:

$$\pi^+ \to \mu^+ + \nu_\mu \quad , \quad \mu^+ \to e^+ + \nu_e + \overline{\nu}_\mu \tag{2.1}$$

$$\pi^- \to \mu^- + \overline{\nu}_\mu \quad , \quad \mu^- \to e^- + \overline{\nu}_e + \nu_\mu \,, \tag{2.2}$$

The muons further decay into electrons, and two other unwanted neutrino types, which constitute the main flux contamination in each beam mode. Figure 2-5 shows the amount of contamination in the flux of neutrino mode and anti-neutrino mode beams at ND280.

All the hadrons, as well as muons below $\sim$ 5GeV are stopped by a beam dump

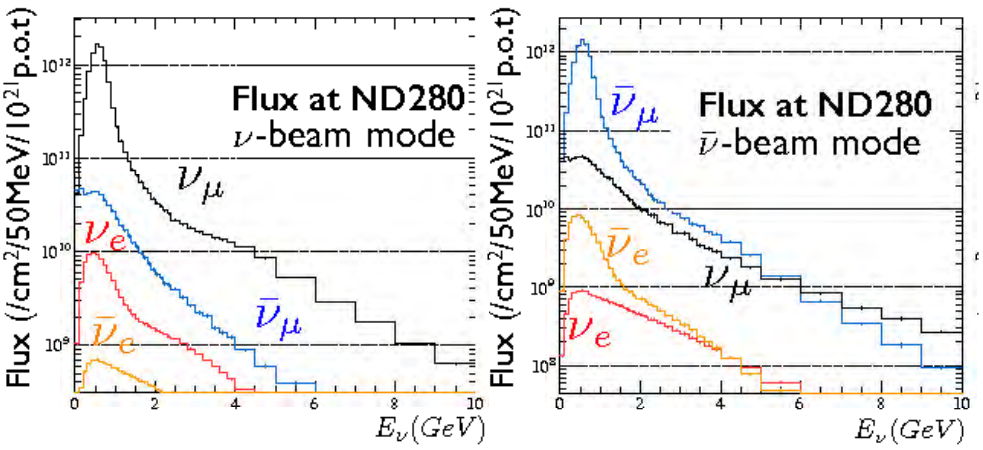

Figure 2-5: T2K flux and the amount of contamination of other neutrino types in neutrino mode (left) and antineutrino mode (right) beams [59].

graphite block behind the pions decay volume (see figure 2-4-b). Neutrinos penetrate through the graphite block and continue their travel towards Super-Kamiokande.

2.2.1 Flux monitoring

The neutrino beam flux, direction and its angular distribution are monitored by the MUMON [60] and INGRID detectors [61].

MUMON sits right after the beam dump chamber, and measures high energy muons ($>$ 5 GeV) which do not stop in the graphite block.

The Interactive Neutrino Grid Detector (INGRID), is an on-axis neutrino detector located in the same building as ND280 (figure 2-6). It is composed of 16 identical modules, made of plastic scintillator interleaved with iron layers. These modules form a cross configuration, with its arms stretched along the horizontal and vertical axis to sample the beam. This detector provides monitoring of the beam intensity, direction, profile and bunch stability, by means of neutrino interactions in iron.

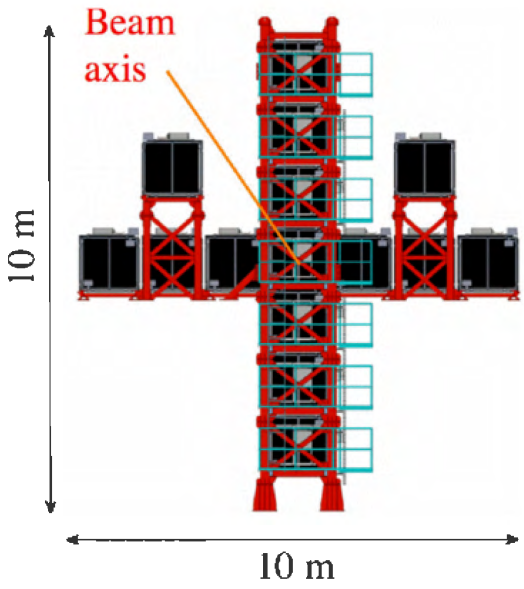

Figure 2-6: INGRID on-axis detector

2.2.2 Beam power

Since the beginning of operations in 2010, the T2K beam power has constantly increased. Figure 2-7 shows the beam power and accumulated Protons On Target (POT) during 10 years operation of T2K experiment. A record high beam power of 515 kW

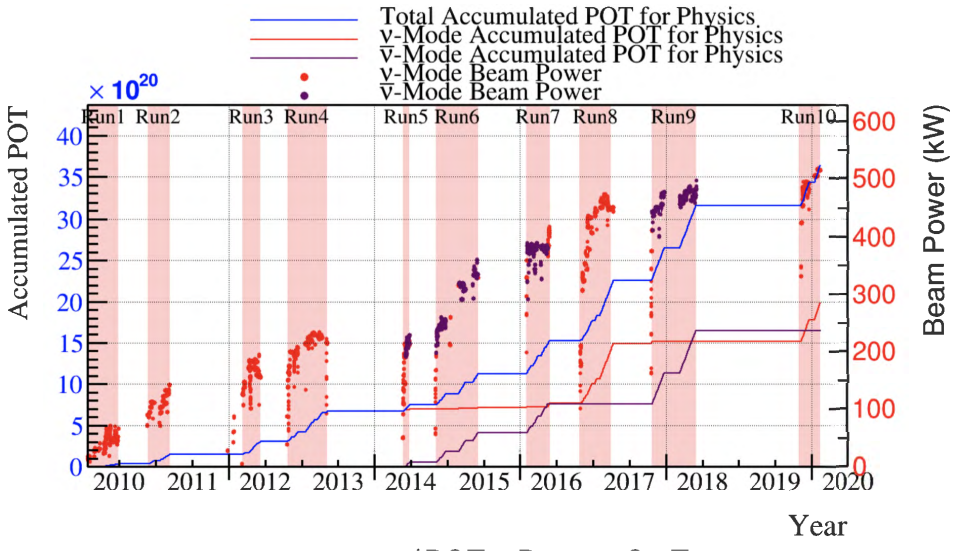

Figure 2-7: Gradual increase of the beam power and accumulated POT. T2K has accumulated a total of 31.97×10^{20} POT in ν_μ mode and 16.3×10^{20} POT in $\overline{\nu}_\mu$ mode.

was reached, with 2.5^{14} protons per pulse (ppp) at 2.48 s cycle, in February 2020. Currently, series of beamline upgrades are under way, to accommodate higher beam power for the extended T2K run [62]. The aim is to achieve 1.3 MW with 3.2×10^{14} ppp at 1.16 s cycle by 2026.

2.3 The T2K near detector: ND280

The off-axis near detector, ND280, located 280 m downstream from the neutrino beam target, is designed to provide constraints on the neutrino flux which is directed towards the far detector. ND280 samples the neutrino energy, flavour content and interaction rates of the unoscillated beam. One main source of uncertainty in oscillation searches comes from the lack of confidence in the existing neutrino interaction models used to interpret the far detector data. An efficient way to suppress the uncertainty is to use the data from an independent but similar detector on the same beamline, this is the role of the near detector.

The current ND280 is composed of several sub-detectors visible in figure 2-8, in-

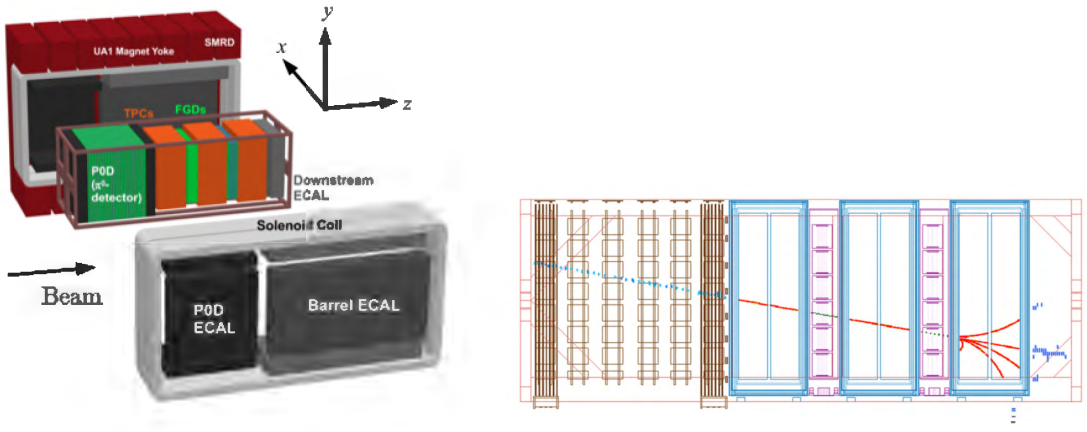

(a) (b)

Figure 2-8: An exploded view of the near detector ND280.

cluding a π_0 detector (P0D) [63], the tracker which consist of three Time Projection Chambers (TPCs) [64] and two Fine-Grained Detectors (FGDs) [65], electromagnetic calorimeters (ECal) [66] surrounding the inner sub-detectors, and side muon range detectors (SMRD) [67] which are attached to the inner side of the UA1 magnet yoke operating at 0.2 T. The FGDs are currently the active targets for neutrino interactions and combined with the TPCs, provide measurements of the charged particles generated in neutrino interactions. The target material is mainly hydrocarbon and consist of plastic scintillating bars aligned in alternating x or y direction perpendicular to the beam direction z, with limited angular acceptance only suitable for forward-going secondaries. Currently, detector related systematic uncertainties of $\sim 2\%$ have been achieved in the charged current samples selected in ND280 [68]. Figure 2-9 shows the muon momentum and angular distribution of the T2K beam at an off-axis angle of 2.5°.

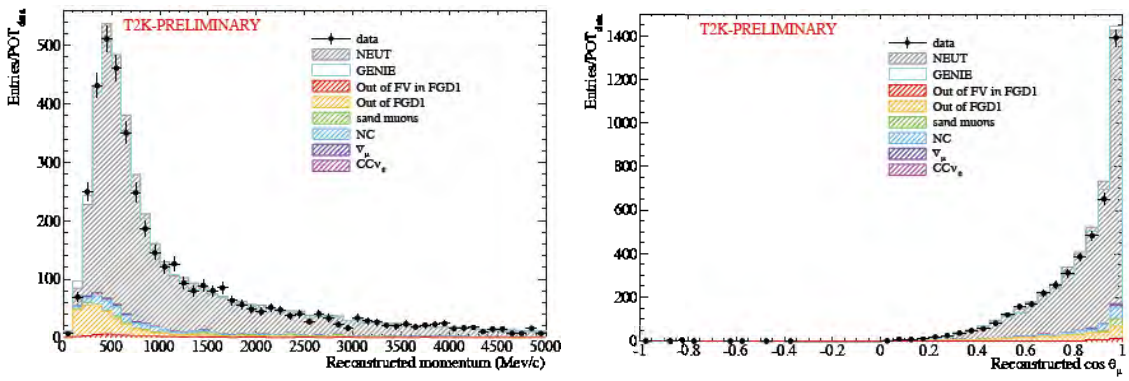

Figure 2-9: Muons momentum and angular distribution measured by ND280 [69].

2.3.1 Cross-section measurement program

Neutrino cross sections are an essential ingredient in all neutrino experiments. They represent the interaction probability of a particle, in a given initial state, with a target, to produce a specified final state. Interest in neutrino scattering has recently increased due to the need for such information in the interpretation of neutrino oscillation data and a renewed appreciation for nuclear effects. The T2K near detector has thus an extensive program for measuring neutrino cross sections on CH, H_2O and Fe targets. Table 2.2 summarizes the published measurements of neutrino and antineutrino cross

Table 2.2: Cross section measurements by T2K experiment

	Measurement	Target	Reference
CC-Inclusive	σ_{ν_μ}	CH, H_2O, Fe	[71] [72][73][74][75]
	σ_{ν_e}	CH, H_2O	[76] [77]
	$\sigma_{\overline{\nu_\mu}}/\sigma_{\nu_\mu}$	CH, H_2O	[78]
CC-0π	$\frac{d\sigma^2}{dp_\mu d\theta_\mu}$	CH, H_2O	[79] [80] [81]
	$\frac{d\sigma}{dE_\nu}$	CH	[82]
	$\sigma_{\nu_\mu}, M_A^{QE}$	CH	[83]
	$\frac{d\sigma_{\nu_\mu}}{d\delta_{p_T}}, \frac{d\sigma_{\nu_\mu}}{d\delta_{\alpha_T}}$	CH	[84]
NC-QE	σ_{ν_μ}	H_2O	[85]
CC-1π	$\frac{d\sigma_{\nu_\mu}}{dp_\mu}, \frac{d\sigma_{\nu_\mu}}{d\theta_\mu}$	H_2O	[86]
	σ_{ν_μ}	CH	[87]

sections conducted by T2K collaboration [70]. The measurements include total inclusive charged current cross sections for muon-neutrinos and electron-neutrino as well as the muon-antineutrino. Since at low neutrino energy, relevant for T2K, the inclusive cross section is an additionally complex combination of quasi-elastic (QE) scattering and pion production processes, these interaction types are in the focus of separate measurements. For the case of QE interactions on heavy nuclear targets, the nuclear effect can impact the final state composition, kinematics and topology, hence the modern experiments tend to instead report cross sections for pionless final states processes, CC-0π. T2K has been increasingly active in reporting single and double differential cross sections as a function of the final state particles kinematics, which is much less model-dependent and is crucial for getting a better handle on the underlying nuclear physics impacting neutrino-nucleus interactions. T2K has also measured neutral current (NC) elastic scattering cross section on water, and CC-1π cross sections on water and hydrocarbon.

2.3.2 ND280 upgrade

After years of studying and understanding the advantages and limitations of the current ND280 design, the T2K collaboration has launched an upgrade project for the ND280 detector to enhance its performance [88], in particular to increase the angular acceptance for the charged particle tracks, and increase the granularity of the target-tracker section for the extended T2K run.
The configuration of the new components for the ND280 upgrade project is shown in figure 2-10. The upstream part of the ND280 basket will be replaced by a 3D high granularity scintillator detector, SuperFGD, in the center, sandwiched by two horizontal TPCs, one above and one below. This central block of detectors will be surrounded by a thin layer of Time Of Flight (TOF) detectors, based on SHiP technology [89]. The downstream part of the ND280 remains unchanged.

SuperFGD detector design

The highly granular target-tracker scintillating detector, SuperFGD, has a novel design made of optically isolated 1 cm^3 cubes of scintillating plastic, which are read out by wavelength shifting (WLS) fibers from three orthogonal directions (figure 2-11). The dimensions of the SuperFGD detector will be $192 \times 192 \times 56$ cm^3, with 2,060,384 cubes and 58,368 readout channels in total.

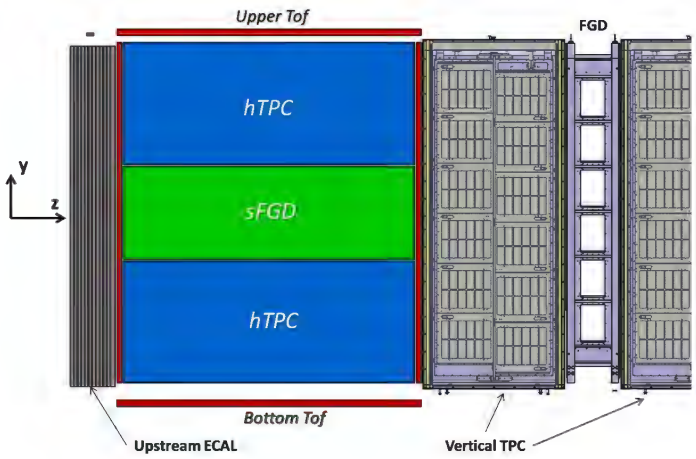

Figure 2-10: Envelopes for the new detectors of the T2K ND280 upgrade. SuperFGD in the center in green, sandwiched by two horizontal TPCs in blue and surrounded by a thin layer of TOF detectors in red.

The expected performance of SuperFGD, compared to that of the current FGDs is

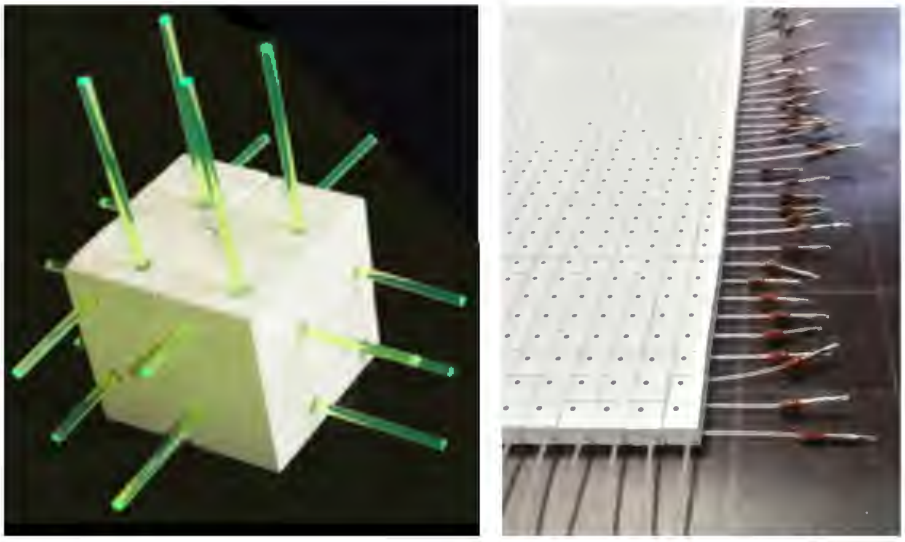

(a) (b)

Figure 2-11: Plastic scintillator cubes with the WLS fibers (left). Assembly of a cubic plane, threaded by fishing lines (right).

studied using simulations. The track reconstruction efficiency in SuperFGD is evaluated for muons and protons using GENIE event generator and the T2K neutrino flux and is shown in figure 2-12. The reconstruction efficiency for muons is higher than 90% for the entire angular spectrum (4π) (left), and the energy threshold for detection of protons is lower than that of the current FGDs (right).

The production and assembly of the scintillating cubes and design of the integration solutions are currently ongoing and the readout electronics which is a evolved version

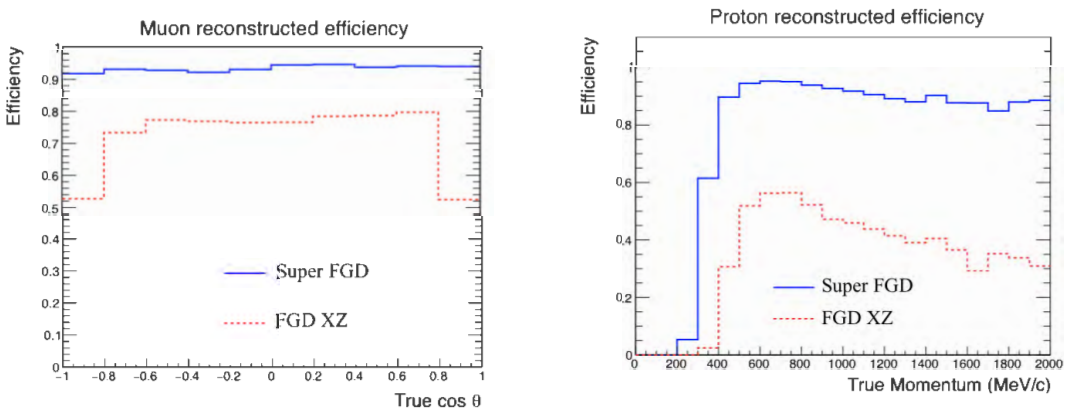

(a) Muon reconstruction efficiency as a function of scattering angle.

(b) Proton reconstruction efficiency as a function of proton true momentum.

Figure 2-12: Simulations show comparison of SuperFGD and current FGDs performances.

of the Baby MIND electronics (section 3.7), with a more compact layout and a higher grade FPGA is under development. The installation of the new sub-detectors of the ND280 are foreseen to take place in late 2021.

SuperFGD beam test at CERN, 2018

In 2018, a superFGD prototype with dimensions $8 \times 24 \times 48$ cm^3 was constructed at INR and tested at CERN beamtest in the T9 beamline. The prototype was instrumented by Hamamatsu MPPCs and equipped by BabyMIND cabling and electronics readout systems which are described in sections 3.5 and 3.7.

During the 2018 beam tests at CERN, good quality data was collected with different beam configurations of muons and hadrons with momentum of 0.5 to 5 GeV/c. Figure 2-13 shows three event displays from top view. The curvature of the tracks is due to 0.2 T magnetic field provided by the MNP17 magnet. The middle plot demonstrates the ability of this detector to identify gamma conversions. In particular it can resolve two particles in one cube from energy deposition.

The results from the SuperFGD prototype beamtest at CERN showed a very promising performance [91]. The Light Yield per cube readout view was measured to be ~ 50 p.e. for minimum ionizing particles and ~ 500 p.e. for the last cube of a stopping proton tracks. The hit time resolution for a sample of 2 GeV muons was found to be 0.9 ns.

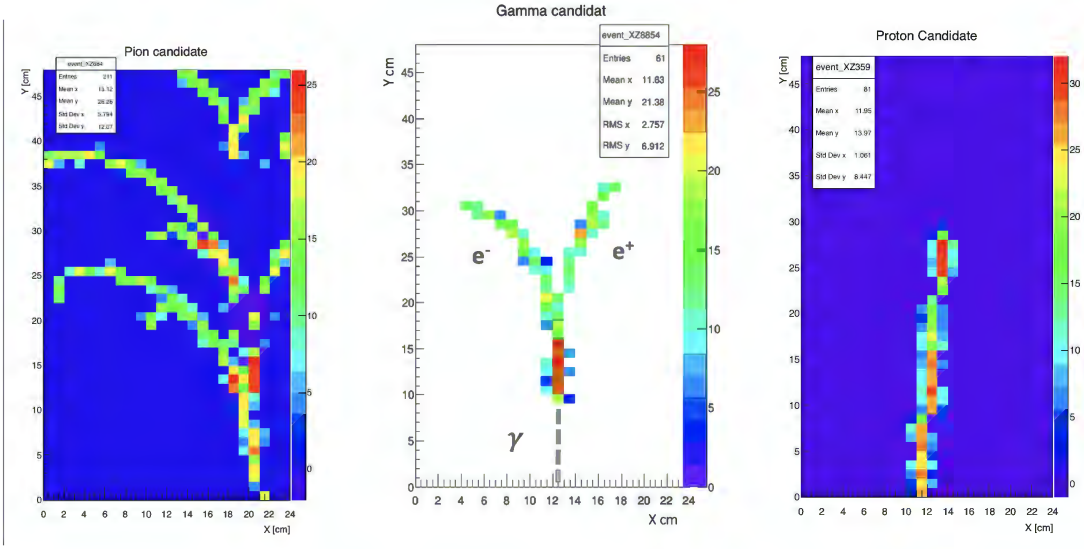

(a) A pion candidate. (b) A gamma conversion. (c) A stopping proton.

Figure 2-13: Event displays from the data collected at CERN beam test, 2018 [90].

2.4 The far detector: Super-Kamiokande

The far detector, Super-Kamiokande (SK) [92] is a 50 kton cylindrical pure water Cherenkov neutrino detector, 1 km deep in the heart of Mt. Ikenoyama (figure 2-14). It was designed to study solar and atmospheric neutrinos, and keep watch for

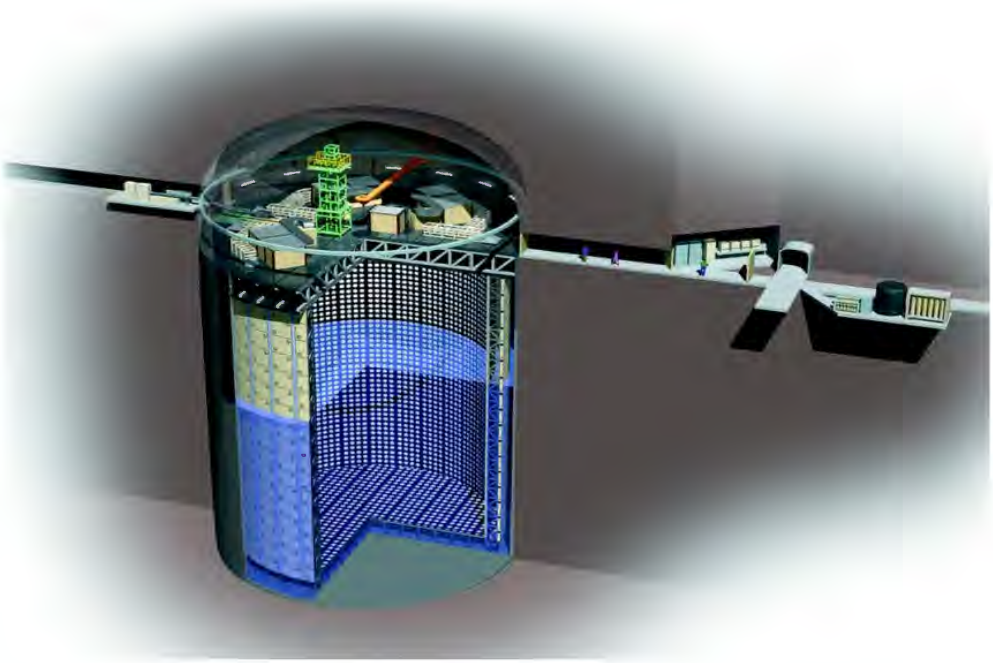

Figure 2-14: Super-Kamiokande (SK) water Cherenkov detector.

supernovae in the Milky Way galaxy or nearby galaxies such as Large Magellanic could. The experiment began in 1996, and apart from three shut down intervals for

maintenance and upgrade has been running up to this day. The detector has two optically separated layers, the inner detector (ID) and the outer detector (OD). About 13000 Hamamatsu photo-multiplier tubes (PMT) of 20" (facing the ID) and 8" (facing the OD) are instrumenting the inner walls of the detector. PMTs are very sensitive light detectors and can detect single photons. The OD serves as an active and passive background veto.

2.4.1 Detection principle

As the charged particles above an energy threshold travel through a dielectric medium such as water at a speed greater than the phase velocity of light in that medium, a cone of Cherenkov photons is produced [93]. The neutrino interactions with H_2O in the ID, are detected by observing the Cherenkov light emitted by the final state charged leptons, projected onto the detector walls as ring shape hit patterns. The topology, timing and rate of the rings are used to infer the location and properties of the particles produced in the interactions. The goal of the far detector is to measure the flavour composition of the oscillated neutrino beam. To do so, an efficient particle identification (PID) strategy is needed. Muons, counted to measure ν_μ disappearance, produce a clear, sharp ring due to their relatively large mass and little deviation, while the electrons, used to search for ν_e appearance, scatter more often and leave behind a fuzzy ring pattern. Figure 2-14-b shows the reconstructed ring induced by a muon event. The external background events can be identified and discriminated by the OD veto. The acceptance for detecting the charged leptons in ID is 4π.

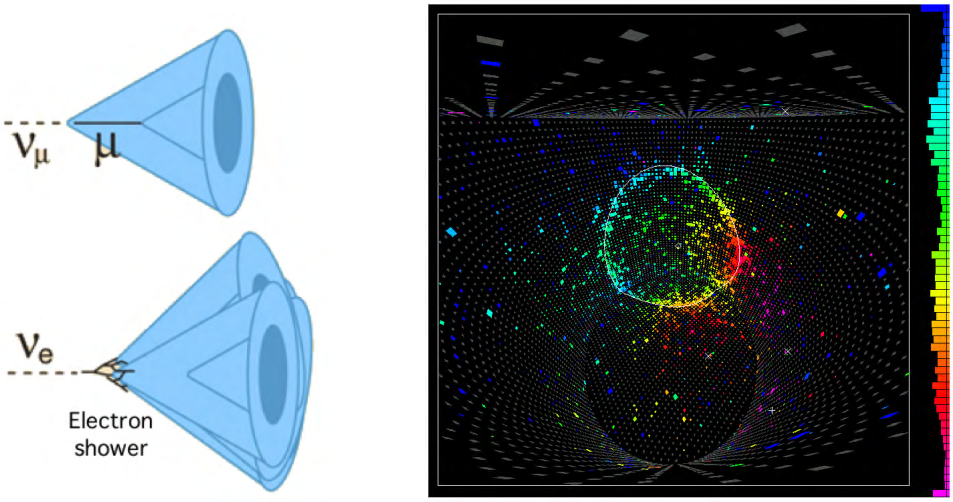

(a) Cherenkov cone created by a muon and an electron.

(b) Example of an electron ring at SK.

Figure 2-15: The Cherenkov radiation and its detection in the SK detector.

2.4.2 Gadolinium upgrade

Gadolinium (Gd) is a rare earth element and has the highest affinity for capturing neutrons among all elements in nature. The idea of adding a soluble Gd compound to a large water Cherenkov detector was first proposed by John Beacom and Mark Vagins, back in 2004 [94], in order to see antineutrinos interacting via inverse beta decays. With addition of Gd to the SK pure water, neutrons generated by the neutrino interactions are captured by Gd, producing observable gamma rays, as shown in figure 2-16. This characteristic signal can be used to identify supernovae relic neutrino events

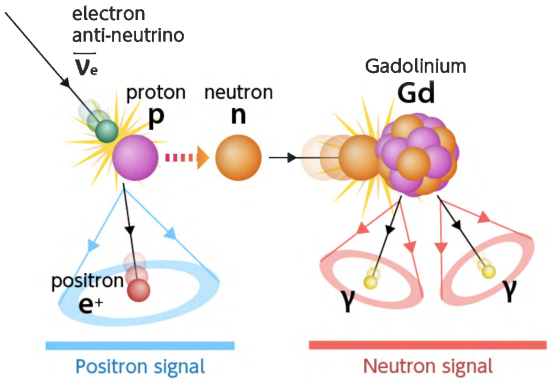

Figure 2-16: Anti-electron neutrino interaction and the expected signals produced by Gadolinium.

in the SK.

In summer 2020, the first stage of the upgrade project, with the introduction of 13 tons of Gadolinium Sulfate ($Gd_2(SO_4)_3$) into the SK tank was carried out. This corresponds to a 0.01% concentration of Gd by weight and a neutron capture efficiency of 50%. Over the next few years the Gd concentration will be increased to 0.2%, enabling the first ever observation of supernova relic neutrinos within seven or eight years.

2.5 The WAGASCI Experiment

The WAGASCI (WAter Grid And SCIntillator) experiment [96] is a new member of the near detector experimental hall. It is located at the B2 floor of the ND280 building at slightly different off-axis angle (1.5°) compared to that of ND280 (2.5°). Figure 2-17 shows the location of WAGASCI detectors in the near detector complex building.

The main purpose of WAGASCI experiment is to measure charged current neutrino interaction coss-sections in water (H_2O) and hydrocarbon (CH) at a slightly different neutrino spectra than ND280. The neutrino flux spectrum for WAGASCI and ND280

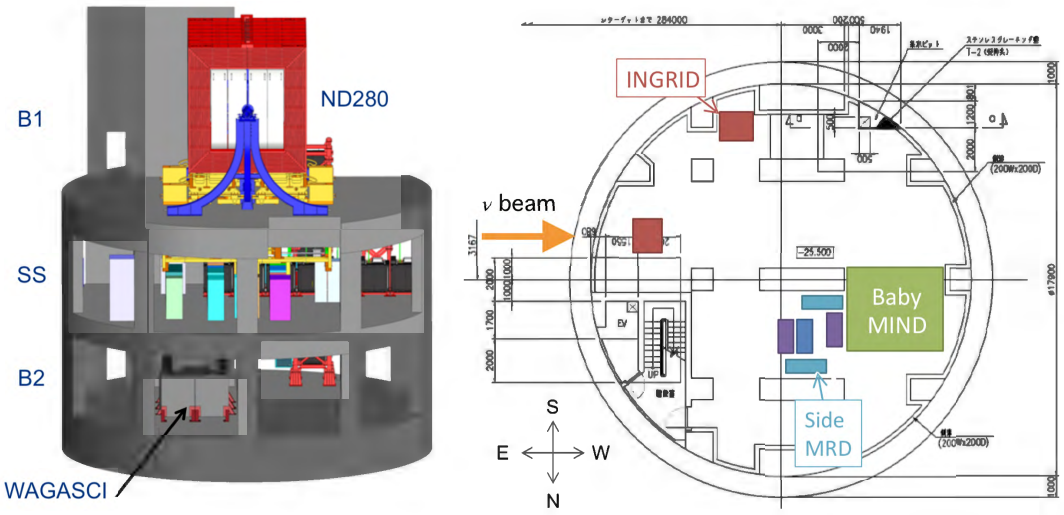

(a) ND280 pit overview. (b) B2 floor plan.

Figure 2-17: The WAGASCI experiment is located at the B2 floor of the ND280 building.

is shown in figure 2-18.

WAGASCI took its first neutrino data with the full setup during T2K run 10, between

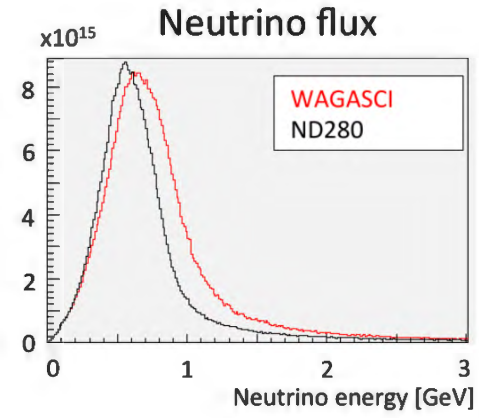

Figure 2-18: Neutrino flux reaching WAGASCI detector compared to ND280.

Nov 2019 and Feb 2020.

The experimental setup, shown in figure 2-19, consist of two hollow cuboid lattice WAGASCI target modules, two non-magnetized Muon Range Detectors, called Wall MRDs and the Baby MIND detector serving as the magnetized downstream MRD. One of the WAGASCI target modules is filled with water while the other module is empty, they are referred to as water-in and water-out modules, combined together they can provide measurement of neutrino cross-section on water with high purity. The INGRID proton module which is fully made of scintillating plastic, is added to the setup to provide a high statistics sample of neutrino interactions on hydrocarbon used

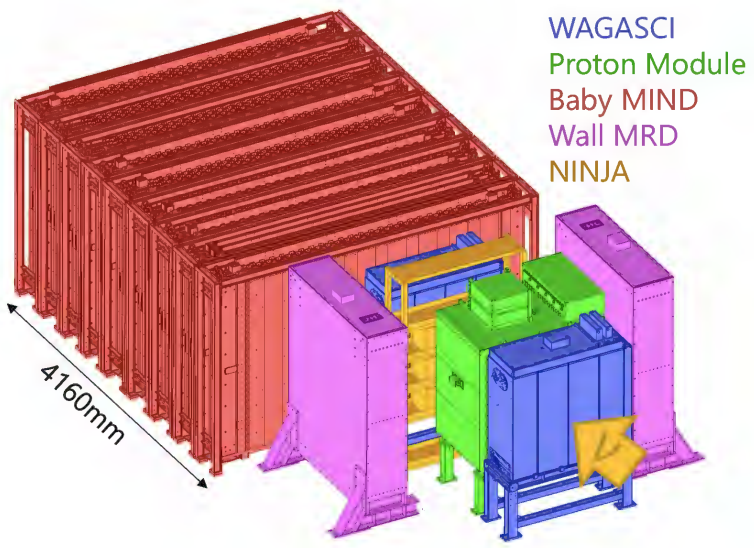

Figure 2-19: WAGASCI experimental setup.

for comparison of cross-sections between water and hydrocarbon and also comparison with ND280 measurements.

The original proposed layout of the WAGASCI sub-detectors is shown in figure 2-20-a, where the WAGASCI modules, proton module and Baby MIND were centered on the same axis and the two Wall MRDs were symmetrically positioned on both sides of the WAGASCI modules. In this proposed configuration, two gaps were envisioned between the stacks of Baby MIND modules, which would serve as lever-arms for determination of particle charge in case of low momentum tracks. The final layout of the installed detectors is shown in figure 2-20-b. The Baby MIND modules were moved away from the central axis and the gaps were eliminated due to the access requirement for the maintenance of the pit walls. upstream detectors were readjusted to provide complementary angular coverage for the water-in WAGASCI module.

2.5.1 WAGASCI target modules

The main target modules of the experiment are the two WAGASCI modules. Each module has a dimension of $1 \times 1 \times 0.5$ m^3 and is composed of a three dimensional grid structure made of scintillating bars and can be filled with 0.6 tons of water. A total of 1280 scintillating bars of dimension $1020 \times 25 \times 3$ mm^3, make up each WAGASCI module. The bars have a groove with a wavelength shifting fiber (Kuraray, Y-11), which collects the deposited light generated in the scintillating bar by passage of a particle, and transmits the signal to a Hamamatsu MPPC. Figure 2-21 shows the grid

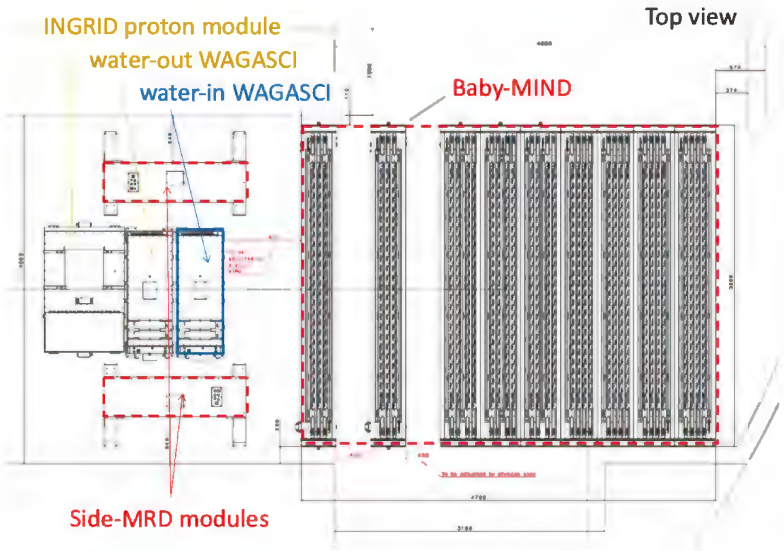

(a) Original proposed layout of the subdetectors.

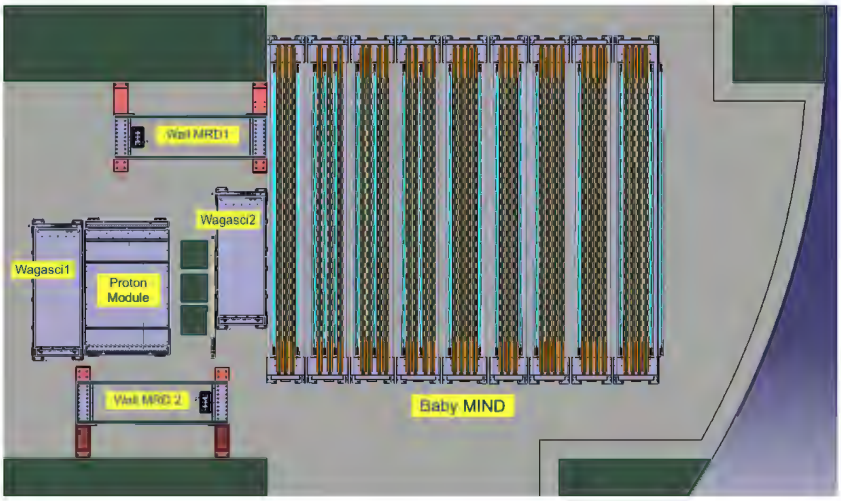

(b) Final layout imposed by building maintanance requirement.

Figure 2-20: WAGASCI experiment setup.

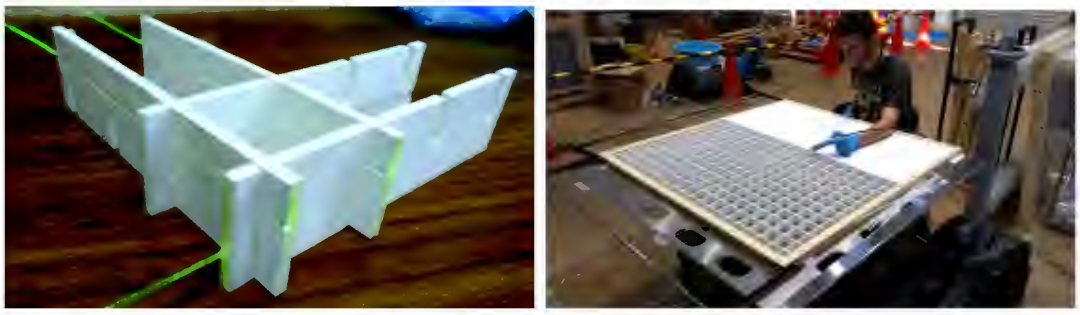

Figure 2-21: WAGASCI grid made of plastic scintillating bars.

structure made of scintillating bars. The WAGASCI module consists of 16 tracking layers in total, and each tracking layer consists of a scintillating plane made of 40 bars facing the neutrino beam and a scintillating grid made of 20 horizontal and 20

vertical bars which are glued to the scintillating plane, as is shown in figure 2-21. The

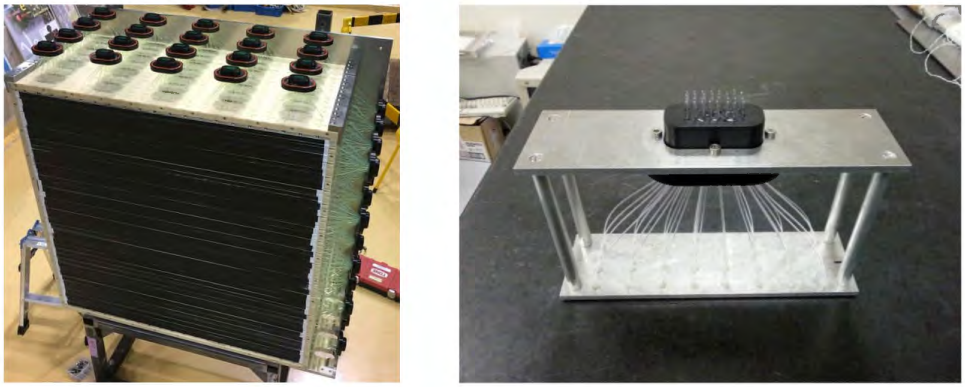

Figure 2-22: The WAGASCI module before installation in the water tank (left). Special connector for the wave length shifting fibers and the PCB mounted MPPCs (right).

readout electronics are based on SPIROC-2 chips, which is a 36-channel self-triggering front-end ASIC. As is shown in figure 2-22 each 32 WLS fibers are grouped together and fixed by a special connector to the PCB mounted MPPCs.
The assembled module is then inserted into the water tank. The total fraction of water target in the fiducial volume is about 80%, which is higher than the water content of the ND280 sub-detector, FGD2. The background due to the neutrino events in the scintillating bars can be subtracted using the empty WAGASCI module.

Figure 2-23: Wagasci module installation into the water tank (left). Electronic readout cards based on SPIROC chip.

2.5.2 Wall-MRDs

The two muon range detectors, located at both sides of the central WAGASCI modules are called Wall-MRDs. Their goal is to extend the detector acceptance to the high angle region by providing momentum measurements from range with 10% resolution for the muons created in neutrino interactions in target WAGASCI modules. The Wall-MRDs are made from 11 non magnetized steel plates, with a thickness of 3 cm, interleaved with 10 plastic scintillator layers composed of 8 vertical bars with dimension $1800 \times 200 \times 7$ mm^3. The scintillating bars have an S shape wavelength shifting fiber as shown in figure 2-24, which is readout from both ends by Hamamatsu MPPCs. Determination of the Y position of the hits is possible from the time difference between the two signals readout from both ends. The electronics used for the readout of 320 channels, is similar to the WAGASCI electronics with the exception of using a single MPPC interface card instead of the MPPC array interface used for the WAGASCI modules. The muon tracks can be selected by requiring a minimum number of iron planes to be penetrated in the Wall-MRDs.

2.5.3 Downstream magnetized MRD: Baby-MIND

The downstream MRD has a very important additional task apart from measuring muon's momentum, and that is to monitor the contamination of neutrino backgrounds in the anti-neutrino mode beam. The cross-section of neutrinos around 1 GeV is three times larger than that of anti-neutrinos, and this fact enhances the contamination of neutrino background events to 30%. To accomplish this task the downstream MRD needs to be magnetized. The charge sign of muons generated in the (anti-)neutrino interactions can be identified by curvature of their tracks in the magnetic field. The description of the Baby MIND detector, serving as the downstream magnetized MRD for the WAGASCI experiment, is presented in chapter 3.

2.5.4 Physics prospect

WAGASCI's principal purpose is to measure differential cross section for the (anti)neutrino charged-current (CC) interactions on water and hydrocarbon. As mentioned earlier, the WAGASCI water-out module can measure interactions on a pure hydrocarbon target with a very low momentum threshold for protons. This result can be subtracted from the WAGASCI water-in module measurement in order to cancel the hydrocarbon background and to provide a high purity measurement of neutrino cross section

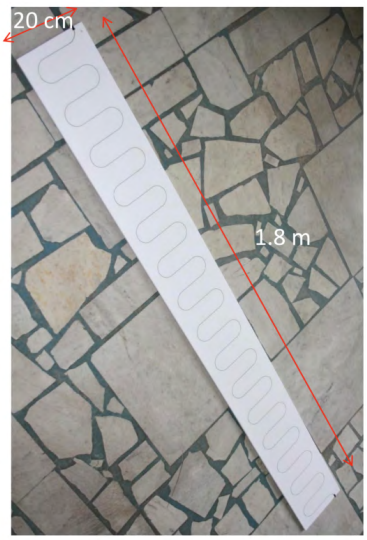

(a) Scintillating bar used in Wall-MRD.

(b) Wall-MRDs installed in B2 floor.

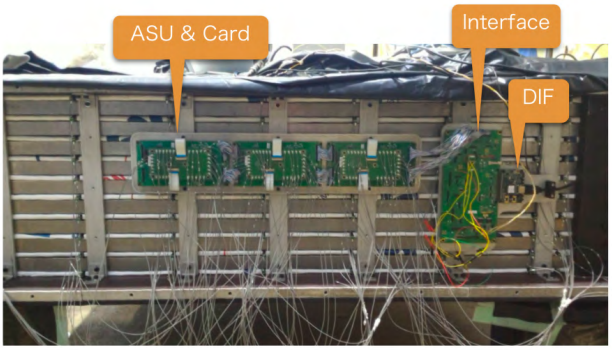

(c) Wall-MRD with electronics assembled.

Figure 2-24: Wall-MRD

on H_2O.

The WAGASCI setup allows the measurements of inclusive and also exclusive channels such as 1μ, $1\mu 1p$, $1\mu 1\pi \pm np$ samples, the first two of which are mainly caused by the quasi-elastic and 2p2h interaction and the latter is mainly caused by resonant or coherent pion production and deep inelastic scattering.

One of the features of accelerator produced neutrino beams is the existence of a high energy tail in the neutrino beam spectrum, even at off-axis angles. The high energy tail is due to rare final state processes, mainly kaon decays. A consequence of a non-monochromatic beam is that the neutrino energy reconstruction depends on different neutrino interaction models. One way to avoid this model dependence is to present a flux-integrated cross-section.

In addition, by combining WAGASCI measurements with those from ND280, a model-independent extraction of the cross section for a narrower energy spread becomes possible. The flux subtraction method is demonstrated in [75] and is also proposed by the NUPRISM experiment [98]. This method is illustrated in figure 2-25. The top two plots show the energy distribution of the neutrino flux (left) and the estimated neutrino interactions per 100 kg water target (right), at WAGASCI (1.5° off-axis) and ND280 (2.5° off-axis) locations. The bottom two plots feature two reconstructed flux samples obtained from the subtraction of fluxes at ND280 and WAGASCI with some coefficients. The flux subtraction method effectively provides measurement of the flux-integrated cross-section of these two artificially created samples.

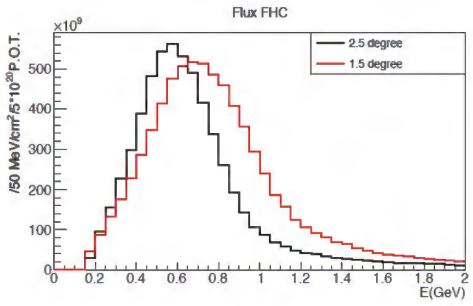

(a) Neutrino fluxes at WAGASCI (red) and ND280 (black).

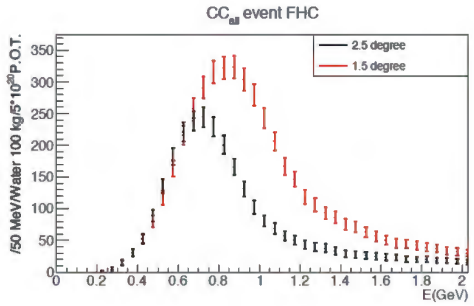

(b) Expected neutrino interaction events per 400 kg water for fluxes shown in a.

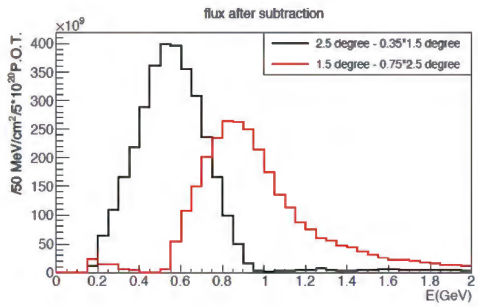

(c) Two reconstructed flux samples by subtraction method.

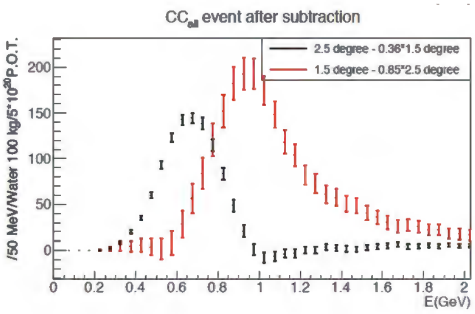

(d) Expected neutrino interaction events per 400 kg water for fluxes shown in c.

Figure 2-25: The flux subtraction method for WAGASCI and ND280.

Chapter 3

Baby MIND Detector

This chapter is dedicated to a description of the Baby MIND detector and its novel design features. We start the discussion from the origins of the detector concept and present the requirements and restrictions that led to its final design. The main detector systems, including the magnet modules, the scintillating modules, the connectivity system and the electronics are then described in more details. It is important to emphasize that for all detector systems a general methodology of prototyping, testing and validation has been rigorously pursued prior to final construction, in order to guarantee the functionality, quality and integration of the detector systems as well as to provide reliable assembly procedures and an accurate timeline estimation for the planning of the construction phases.

3.1 MIND Type Detectors

The acronym MIND, which signifies Magnetized Iron Neutrino Detector, was first proposed for near and far detectors of the *Neutrino Factory* (figure 3-1) at the NuFACT-99 conference [101, 100]. In Neutrino Factory environment, the $\nu_e \rightarrow \nu_\mu$ transitions, were referred as the *golden channel* because of the facility of the detection of the muon and its charge compare to that of the electron. The proposed MIND detector for the neutrino factory was thought to have a mass of 100 ktons to serve as a target for neutrino events with energies greater than 10 GeV, with a large solenoid coil around the whole detector to produce a 1 T magnetic field, needed for charge identification of muons in the neutrino oscillation analysis.

But detectors of this kind had already been in operation for decades. One such example is the CDHS detector [102], which had layers of magnetized iron interspersed with wire drift chambers, with a fiducial mass of 750 tons, to detect neutrinos in the

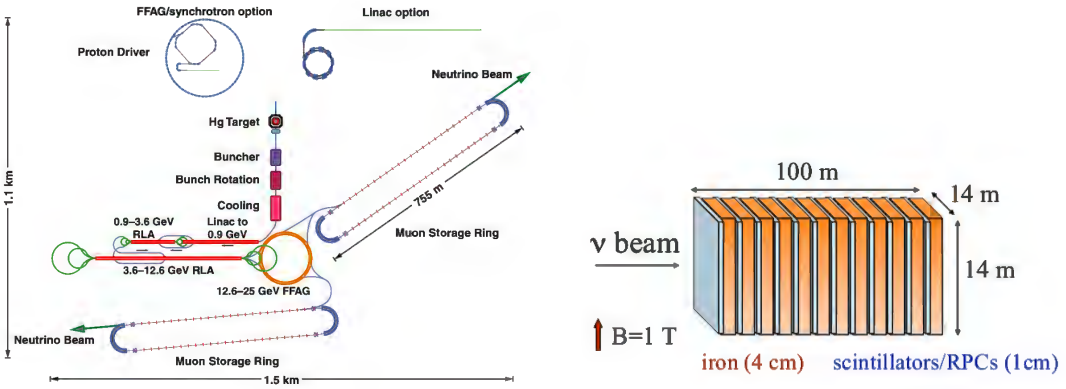

(a) Schematics of the neutrino factory.

(b) A 100 ktons MIND detector proposed for neutrino factory.

Figure 3-1: A MIND detector proposed for the neutrino factory.

range of 30-300 GeV. CDHS was operational at CERN in the late 70s (figure 3-2). Another more recent example is the MINOS experiment, launched in 2005 at Fermilab [103]. MINOS had a similar type of magnetized iron detectors for both its near and far detectors, shown in figure 3-3, and was able to provide momentum measurements from both range and curvature of the tracks, as well as charge sign for muons from neutrino interactions in the range of 4-15 GeV.

At present, MINDs are not foreseen to be used as a stand alone detector for any

Figure 3-2: The CDHS experiment at CERN (1976).

of the upcoming major experiments, however, they can offer the great advantage of charge identification (essential for CP-violation studies) and calorimetry for high energy muons, if positioned around any non-magnetized neutrino targets. This scenario has been realized for the WAGASCI experiment with Baby MIND as its downstream muon spectrometer.

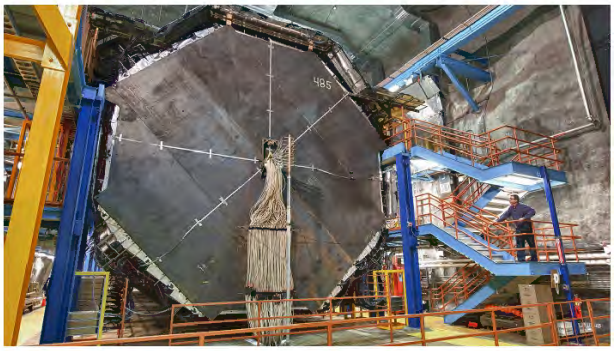

(a) MINOS far detector

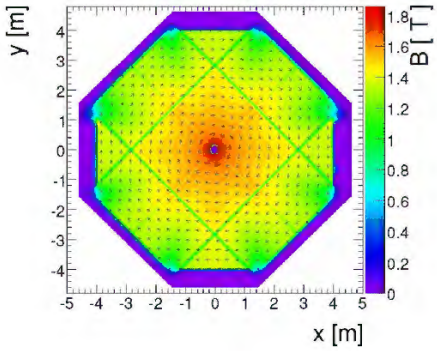

(b) Magnetic field map in a MINOS steel plate.

Figure 3-3: The MINOS experiment

3.2 Baby MIND modular design concept

Unlike previous magnetized iron detectors of this type, which are traditionally built as a single block with one or more coils threading through the whole arrangement, the Baby MIND design is based on individually magnetized steel modules. The evolution of the magnet module concept is described in section 3.3. The modular design concept was crucial for space constraints during handling and installation at J-PARC, since the only access to the B2 floor, where the WAGASCI and Baby MIND detectors are located, is through a narrow shaft shown in figure 3-4. Another important advantage of a modular design is the possibility to assemble and disassemble the detector in a relatively short time which was required for beam tests at CERN.

Baby MIND consists of a total of 33 magnet modules and 18 scintillating detector

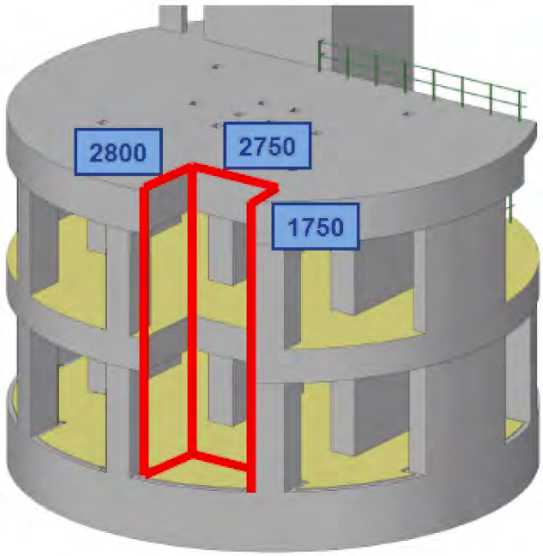

Figure 3-4: The the access shaft to the B2 floor in the near detector complex building at J-PARC.

modules. Fig 3-5 illustrates the final layout of distribution of scintillating modules amongst the magnet modules.

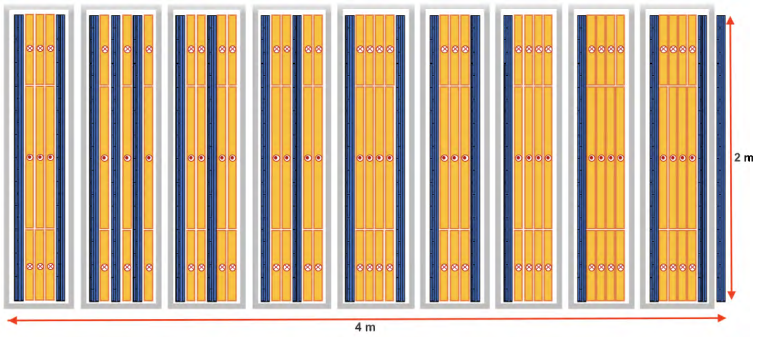

Figure 3-5: Layout of the distribution of 18 scintillating modules (blue) amongst 33 magnet modules (yellow) in their final configuration at J-PARC.

3.3 Magnet modules

A new and optimized magnetization scheme was developed for Baby MIND Iron plates, to address the physics requirements as well as the challenging timeline and space constraints for the installation in the ND280 pit. The main physics requirements related to the magnet design were:

- To determine momentum and charge sign for muons in the range of 0.5 to 2 GeV, by means of a predictable and homogeneous magnetic field with $B > 1.5$ T along the horizontal x axis.
- To maximize acceptance for muons originating from neutrino interaction in WAGASCI, by maximizing the useful tracking area with a homogeneous magnetic field.

The adopted magnetization scheme optimizes flux return for minimum stray field and operating current, while maximizing the useful tracking area with $B > 1.5$ T [106]. In this scheme the iron plates of the detector are individually magnetized by coils wound on their surface by sewing an aluminum conductor through two slits that are machined in the plates. To illustrate the reasons for the departure from traditional designs, we list hereafter the main constraints affecting the magnet design:

- Transportation from CERN to J-PARC by shipping containers, limiting the plate height to 2 m.

- Installation at J-PARC limited by the need to lower the magnet modules in their final orientation along the diagonal of a 3500 × 1630 mm^2 shaft with a 10 ton crane, limiting the width and the weight of the plate.

- Reduced power dissipation to prevent overheating of the scintillating modules as well as reduced operation costs (electricity) during the continuous operation of the detector.

- Fixed budget driving the choice of materials (iron plates and conductor for the coil) and the power supply.

3.3.1 Evolution of the magnetization scheme

Several conceptual designs for the magnetization scheme were studied in order to achieve the goals mentioned earlier. Some of the explored alternatives are presented briefly.

a) Traditional design:

The starting point for the conceptual design of the magnet was the traditional approach used in MINDs with one or more large coils threading through all iron plates. The first design proposed for the Baby-MIND magnet envisaged two large coils wound around the top and bottom halves of the stack of plates separated by a gap of 10 cm as illustrated in Figure 3-6 (right). Such design was simulated as is shown in fig-

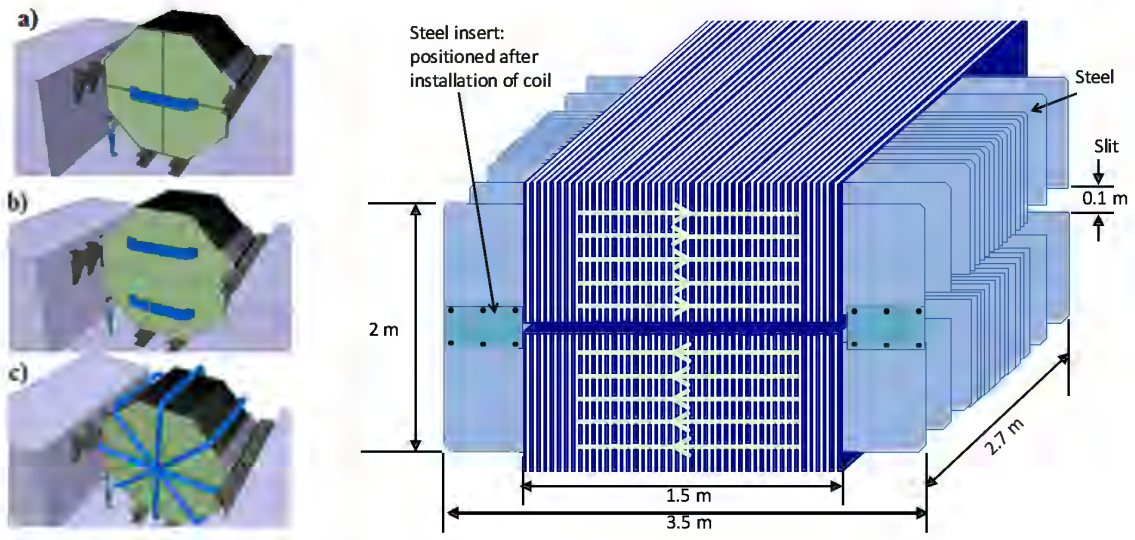

(a)

Figure 3-6: Traditional magnetization schemes with coils threading through the whole arrangement (left). Starting point of the magnetization scheme for Baby MIND (right).

ure 3-7. The estimated power consumption for this scheme is of the order of 1 kW

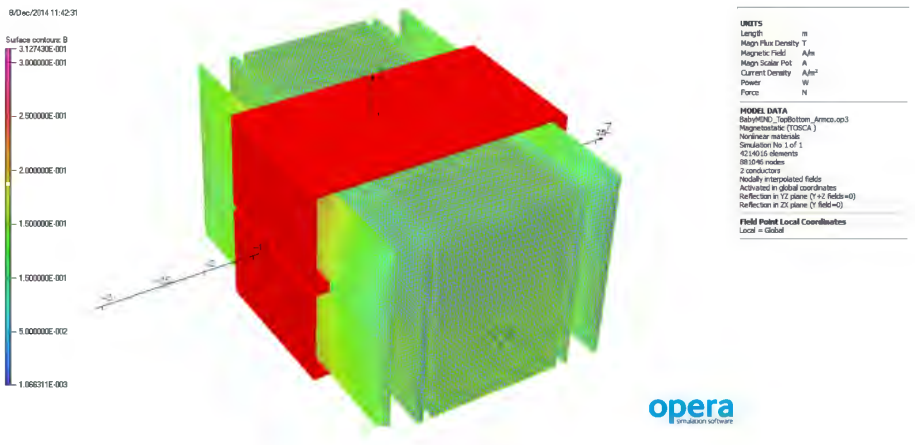

Figure 3-7: Simulation of the magnetic field for the first iteration of magnetization scheme with a traditional design.

which is favorable. However such design results in a bulky magnet not meeting the transportation and installation constraints. Moreover, the traditional coil winding approach requires the development of dedicate tools, increasing production time and cost.

b) Individual magnet module with no slit:

To satisfy the space and transportation constraints the new design for the Baby MIND magnet relies on the individual magnetization of the modules by normal conducting coils wound on the surface of the iron plates. The second studied scenario consisted of magnetization of one plate with no slit, as shown in Figure 3-8. In this scheme the

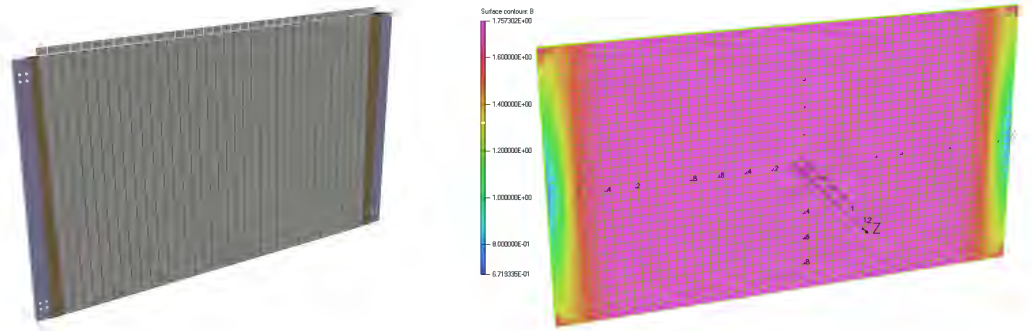

(a) Magnet module with no slit (b) Simulated magnetic field map with no slit

Figure 3-8: Magnetized steel plate with no slit has (too) high power dissipation ~ 6 kW/m

return path of the magnetic flux passes through the air, resulting in significant stray fields. The total current required for this scheme to compensate the loss due to the stray fields is estimated of approximately 50 kA, and a power dissipation of 6 kW/m,

which are both too high for our purpose.

c) Two half modules individually wrapped:

This scenario relies on the principle of flux return used in the current transformers, which minimizes power dissipation and stray fields. In its initial formulation two separate half module steels were wrapped individually by aluminum coils and then bolted together with additional joint plates as shown in figure 3-9. To test this concept a

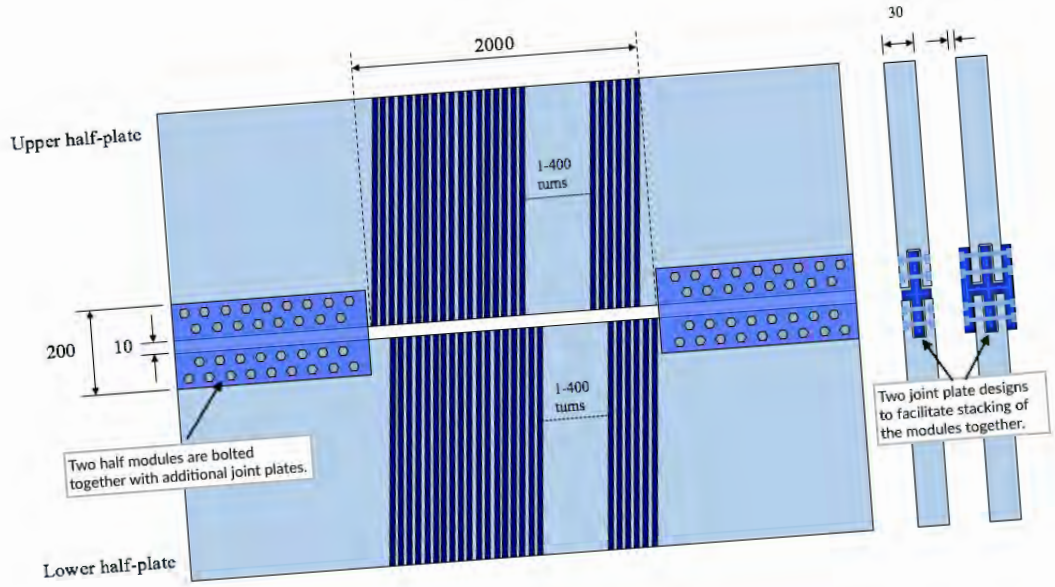

Figure 3-9: Two half plates wrapped individually by Aluminum coil and then bolted together with joint plates.

winding machine prototype was built to lift and turn a half module steel while the aluminum coil is being wrapped around it. The exercise found to be inefficient and motivated further investigation for easier and faster solutions. In addition, the simulations revealed that the bolted joint plates disrupt the magnetic return flux, resulting stray fields.

d) Single slit magnet module:

An alteration of this design was proposed to have one full steel module with a slit cut in the middle of the plate, rather than having two half modules. Similar to the previous scheme, the top and bottom sections of the steel plate were to have separate coils with current in opposite directions to magnetize the plate as shown in figure 3-10. In order to achieve complete magnetic return flux, for a steel plate of equal thickness throughout its entire area, the width of the side sections (H-H') needs to be at least equal to the width of each coil section (V-V') and therefore the width of the central tracking region with uniform magnetization is limited to 1.5 m.

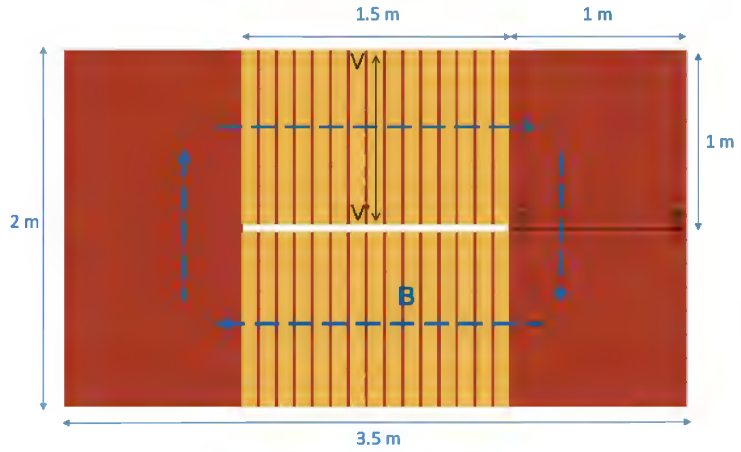

Figure 3-10: Magnetized steel plate with one slit

An alternative layout, realized by increasing the thickness of side sections by 5 cm could provide sufficient flux return, while increasing the tracking region to 2.6 m (see figure 3-11). But this extra thickness creates problems for stacking of the magnet modules and the scintillating modules.

e) Double slit magnet module:

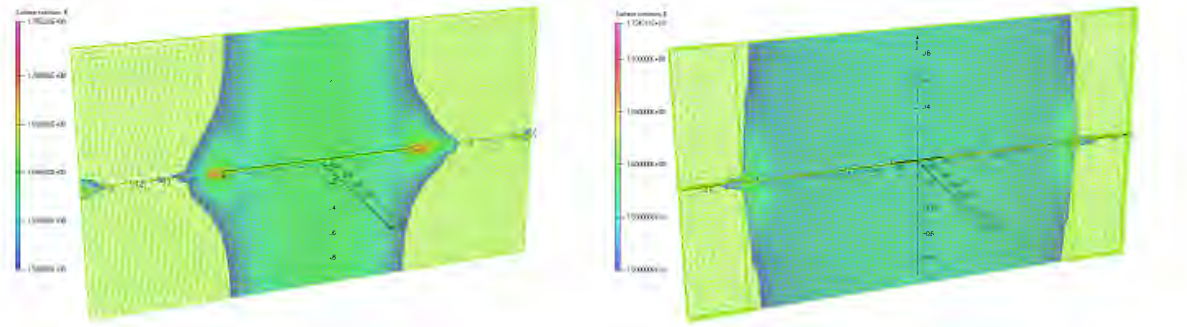

(a) Magnetized tracking region is limited to 1.5 m without extra iron.

(b) Magnetized tracking region can be increased to 2.6 m with 5 cm extra iron thickness on the sides.

Figure 3-11: Increasing magnetized surface by adding 5 cm extra iron thickness to the sides.

The final scenario addressed all these challenges. In this design the iron plate has two slits and three coils and hence the cross section area needed for the flux return is reduced. The top and bottom coils have currents flowing in the same direction, while the current flow in the central coil is reversed as shown in figure **??**. Additional 10 mm thick iron plates are added to both sides of the central plate, which corresponds to the maximum thickness reserved for the aluminum coil and its insulation. This allows the tracking region to extended up to 2.8 m. The Aluminum coil is wound in a sewing arrangement. This design optimizes the flux return for minimum stray field and operational current, and increases the tracking region to 2.8 m. The simulated

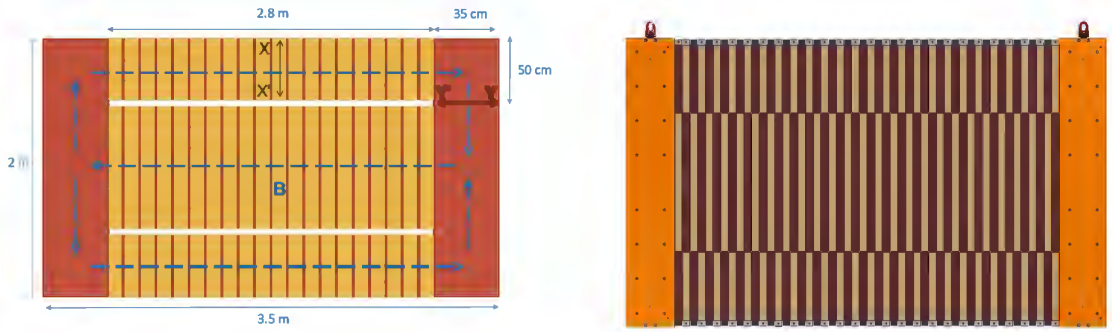

(a) Magnet module with two slits (b) Design of Aluminum coil (two slits)

Figure 3-12: Magnetized steel plate with two slits.

magnetic field for the double slit magnet module is shown in figure 3-13. Possible

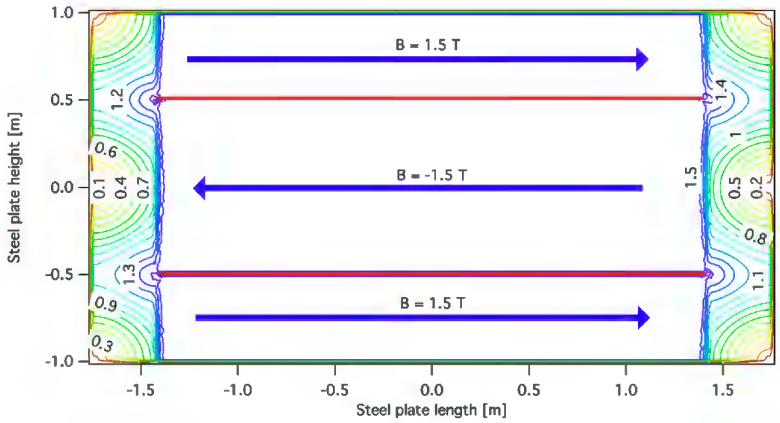

Figure 3-13: Simulated magnetic field for double slit magnet module.

disadvantages of this design are the presence of two 10 mm slits, although located away from the center of the plate, and the change of field direction, which could result in a more complex reconstruction of the trajectories of the particles. The proposed magnetization scheme is the optimal solution independent of the choice of material for the plates and of the coil winding technique.

3.3.2 ARMCO iron

The ARMCO pure iron (low carbon) [105], with an iron content of min 99.85%, was chosen after extensive study and comparison of the magnetic properties of the available options despite the factor ×3 higher cost compared to normal steel. Figure 3-14 shows the magnetization curves of various steels used as magnetic steel in different experiments and comparison of their power consumption for Baby MIND modules. It can be viewed that the extra cost of the ARMCO can be offset by its lower operation

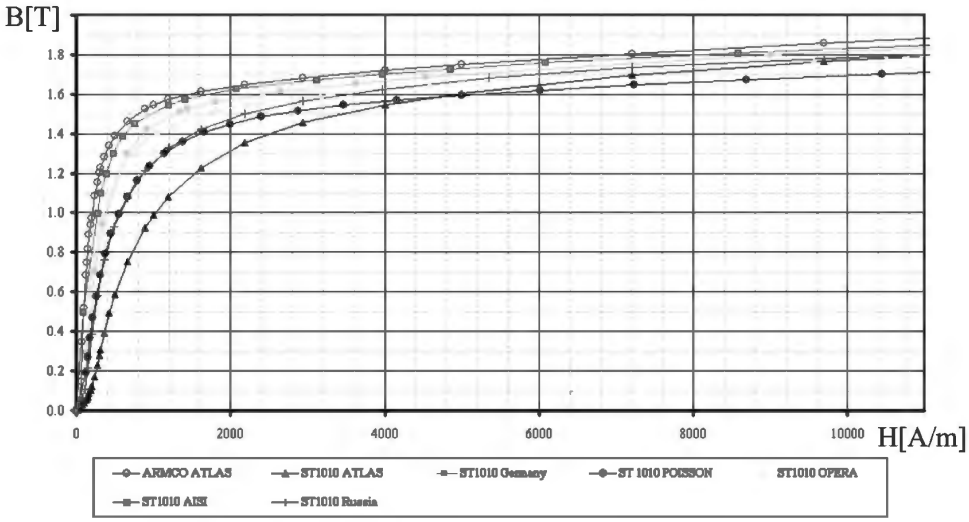

(a) Magnetization curves of different steels used as magnetic steel in different experiments (courtesy A. Vorozhtsov)

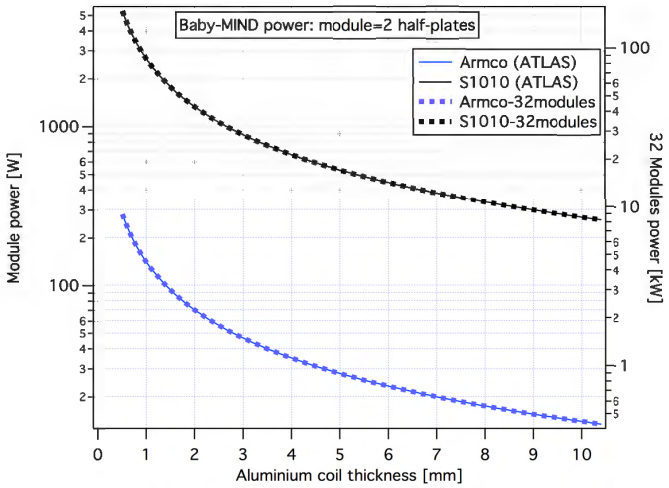

(b) Power consumption comparison between two steel types.

Figure 3-14: Comparison of steels with different carbon levels.

cost [electricity] over several years.

3.3.3 Assembly of magnet modules

After construction of a prototype magnet module from low carbon construction steel in the first quarter of 2016, the assembly procedure with several stations was validated, such that the work on various stages of magnet modules assembly could be performed in parallel in order to meet the tight schedule timeline. The 3 cm thick iron plates were cut to dimensions (3500 mm $\times$ 2000 mm) and the double slits of 2800 mm $\times$ 10 mm were machined, before delivery to CERN. The assembly of 33 magnet modules took place between July 2016 and February 2017 at building 180 at CERN. Various assembly

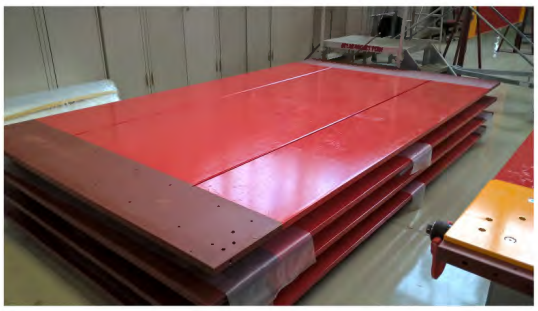

(a) Painting

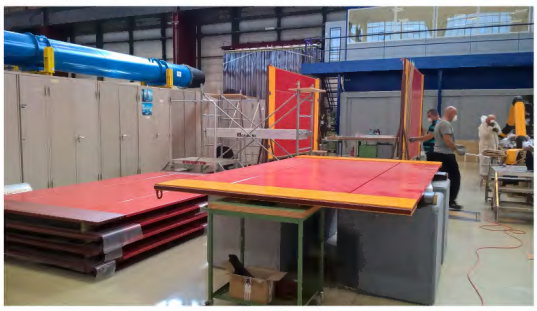

(b) Attachment of side plates

(c) Insertion of U shaped Aluminum conductor

(d) Folding Aluminuim coil in a sweing pattern

(e) Coil turn link detail

(f) Welding

Figure 3-15: Manufacturing of the magnet modules.

stages are shown in figure 3-15. The ribbon shaped aluminum alloy ($\rho = 2.8 \times 10^{-8}\ \Omega \cdot m$) is 50 mm wide and 4 mm thick, and completes 25 turns around each module. The resistance of the Aluminum conductor for one module is obtained to be 16.3 mΩ. The power consumption per module is given by equation 3.1 and is about 320 W.

$$P = R_{\text{coil}} I^2 = H^2 \times \frac{\rho_{\text{Al}}}{t_{\text{coil}}} \times (l_{\text{coil}} \times l_{\text{solenoid}}) \sim 320\text{W}. \tag{3.1}$$

In the final configuration the coils of consecutive magnet modules are connected together in series. There are two types of magnet modules, with two different coil directions to facilitate the inter-connection between consecutive modules.

3.3.4 Pick-up coil tests

In order to confirm the homogeneity of the magnetic field distribution, 10 pick-up coils were wound around the prototype magnet module. Each of the three coil sections was instrumented by a pick-up coil at center and two extremities (pick-ups 1 to 9) and one additional pick-up coil monitored the return flux in the side section (pick-up 10). Figure 3-16 (left) shows the location of the 10 pick-up coils by their number on the prototype magnet module. The induced voltage due to a fast current ramp was

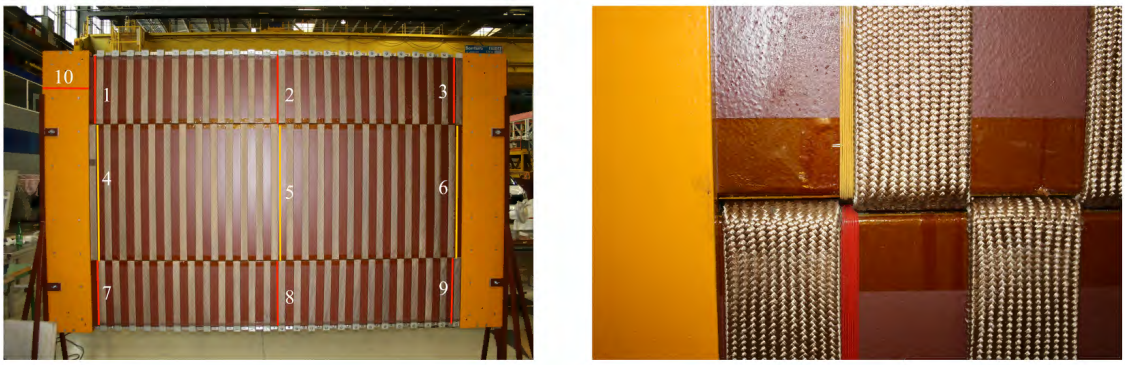

Figure 3-16: Pick-up coils wound around the prototype magnet module

measured. A current of 400 A was used for the test of prototype module in order to ensure that the plate is well into saturation. The plots in figure 3-17 show the measured current and voltage curves. The corresponding magnetic field change ΔB is obtained from equation 3.2.

$$\int_{t_{start}}^{t_{end}} V(t)dt = \int_{t_{start}}^{t_{end}} N_{pc} \cdot \frac{d\phi}{dt} dt = N_{pc} \cdot S \cdot \Delta B \tag{3.2}$$

As a ferromagnetic material, iron plates remain magnetic even when the current is removed. Figure 3-19 (a) shows a hysteresis loop of a ferromagnetic material with saturation B_s and residual B_r fields. The measured saturation field for the prototype module was 1.57 T, with a substantial residual field of 1.17 T. The comparison of pick-up coil data did not show any significant flux leakage, since the difference between field values at the edge (pick-up 10) and at the center of the plate (average of pick-ups 1-9) was below 3%. The result was further confirmed by Hall probe measurements on the surface of the plate, shown in figure 3-18.

The $B - I$ curve obtained from 10 pick-up coils measurements on the first ARMCO module is shown in figure 3-19 (b). In this plot the average of the measured values from pick-up coils 1-9 is plotted separately from the measured values from pick-up coil 10, to illustrate that there is no significant difference between the two. Based on this

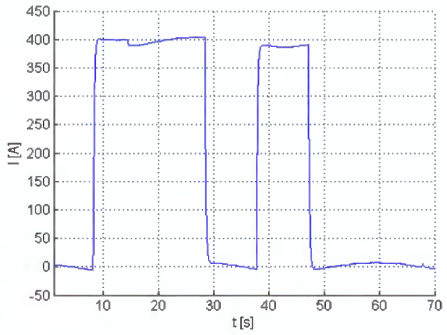

(a) Current curve with two ramps up and down.

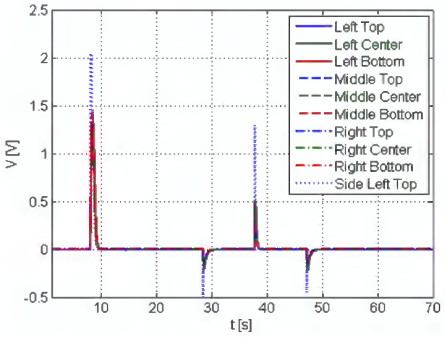

(b) Voltage curves on pick-up coils.

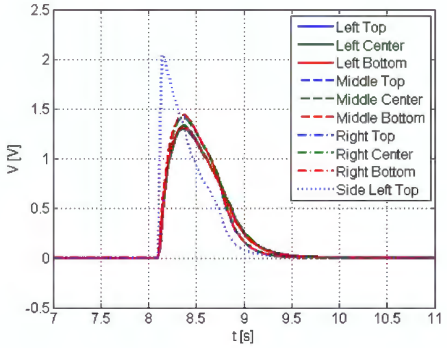

(c) First ramp up.

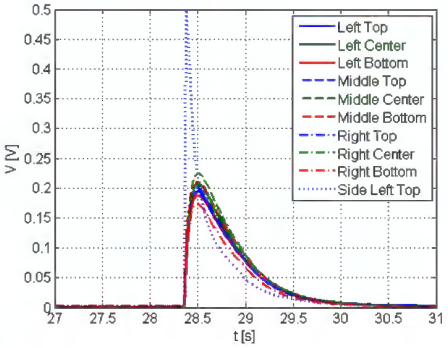

(d) First ramp down, inverted.

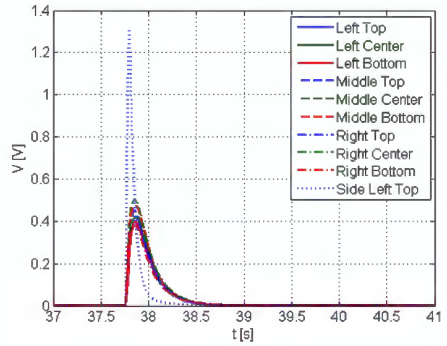

(e) Second ramp up.

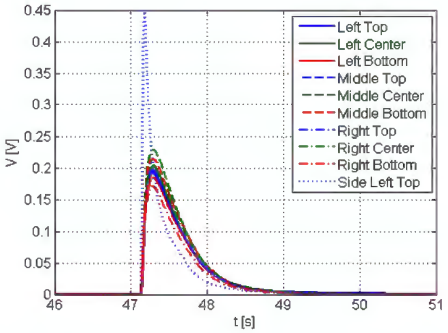

(f) Second ramp down,inverted.

Figure 3-17: The current and voltage curves for pick-up coil measurements of the prototype magnet module.

$B - I$ curve, the operational current of 140 A was chosen to achieve a magnetic field of 1.5 T with the desired homogeneity.

After completion of the assembly of all 33 magnet modules, the magnetic fields of each module were measured by pick-up coils for the operational current of 140 A. The results are shown in figure 3-20 and are reported in table 3.1.

Figure 3-18: Hall probe on the surface of magnet module measures 2.7 mT, confirming that there is not significant flux leakage.

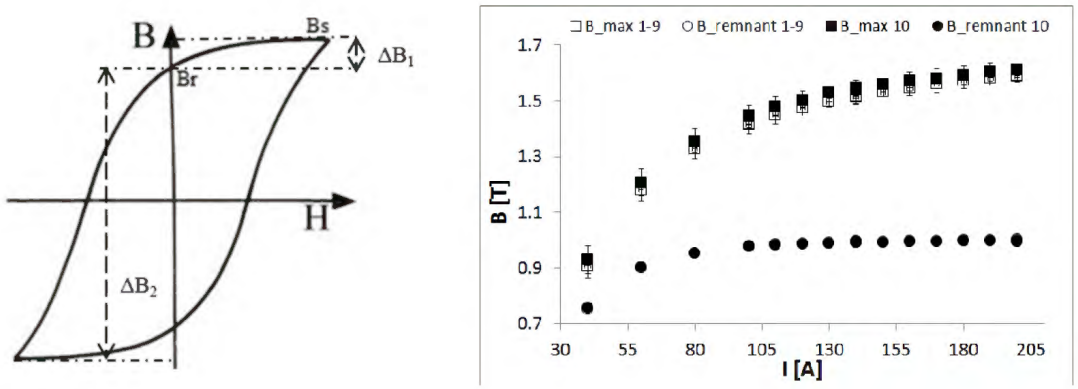

(a) Hysteresis loop of a ferromagnetic material.

(b) $B - I$ curve of ARMCO, measured on the first magnet module.

Figure 3-19: Saturated and residual magnetic fields in ARMCO.

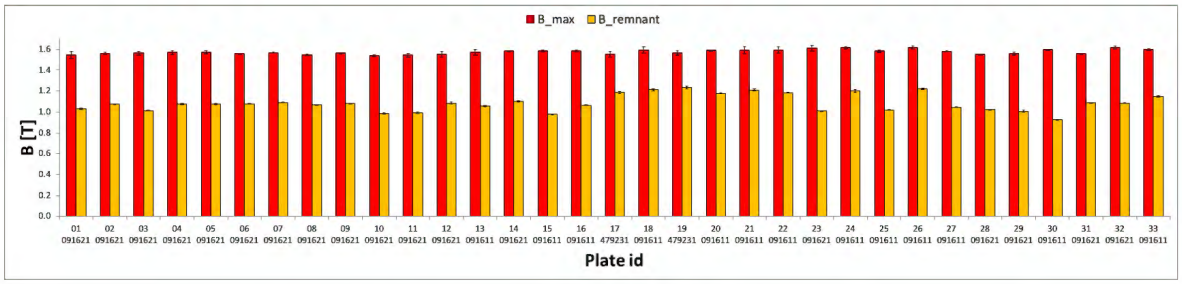

Figure 3-20: Magnetic field of 33 magnet modules measured for a current of 140 A. The average B_{max} is 1.58 T with a standard deviation of 0.02 T.

3.3.5 Power supply

In order to operate the entire setup at 140 A, a voltage difference of $\sim$ 80 V is required. The magneto-motive force to produce the B field was provided by two dc power supplies, Delta-Electronika SM 45140, compatible with a 400 VAC line, connected in series during CERN beam test and Japan commissioning in 2018 (figure 3-21). After encountering interference issues with ND280 power supply, the decision was made to

Table 3.1: Magnetic field measurements for all magnet modules.

Module plate #	Type	$B_{\max}$ [T]	$\sigma_{B_{\max}}$ [T]	B_{res} [T]	$\sigma_{B_{\text{res}}}$ [T]
01-091621	I	1.548	0.033	1.031	0.007
02-091621	II	1.562	0.012	1.074	0.004
03-091621	I	1.565	0.017	1.013	0.003
04-091621	II	1.571	0.018	1.078	0.004
05-091621	I	1.573	0.013	1.078	0.005
06-091621	II	1.559	0.002	1.080	0.002
07-091621	I	1.569	0.003	1.093	0.002
08-091621	II	1.547	0.007	1.068	0.003
09-091621	I	1.565	0.004	1.084	0.003
10-091621	II	1.541	0.008	0.986	0.005
11-091621	I	1.543	0.019	0.993	0.006
12-091621	II	1.554	0.025	1.085	0.009
13-091611	I	1.574	0.027	1.058	0.005
14-091621	II	1.583	0.006	1.104	0.007
15-091611	I	1.585	0.004	0.979	0.003
16-091611	II	1.586	0.006	1.065	0.004
17-479231	I	1.551	0.027	1.185	0.013
18-091611	II	1.593	0.030	1.214	0.010
19-479231	I	1.566	0.022	1.234	0.016
20-091611	II	1.594	0.001	1.176	0.003
21-091611	I	1.593	0.032	1.209	0.011
22-091611	II	1.595	0.032	1.184	0.004
23-091621	I	1.610	0.027	1.011	0.004
24-091611	II	1.616	0.010	1.202	0.011
25-091611	I	1.584	0.008	1.021	0.005
26-091611	II	1.618	0.012	1.221	0.007
27-091611	I	1.581	0.002	1.046	0.003
28-091621	II	1.552	0.002	1.024	0.001
29-091621	I	1.561	0.012	1.009	0.007
30-091611	II	1.596	0.003	0.927	0.002
31-091621	I	1.559	0.004	1.089	0.001
32-091621	II	1.619	0.012	1.151	0.006
33-091611	I	1.600	0.007	1.151	0.006

separate the main electrical lines of the two experiments and a new power supply, Keysight N8932A, compatible with a 200 VAC line was purchased for Baby MIND magnet modules. This device was qualified for long term operation at J-PARC.

3.4 Scintillating modules

The sensitive layers of the Baby MIND detector are made of scintillating plastic material. The scintillating material, when struck by a particle, absorbs its energy and scintillate in the form of light. The advantages of scintillating plastics are fairly high

(a) Delta-Electronika SM 45140 power supply. Two such devices were used during CERN beam test and J-PARC commissioning.

(b) Keysight N8932A power supply, for long term operation at J-PARC.

Figure 3-21: Rack mountable power supplies, meant to provide a current of 140 A for Baby MIND magnet modules. The voltage drop across the entire detector is about 80 V.

light output ($\sim$ 300 photons per particle), a relatively quick signal with a decay time of 2 to 4 ns, and their ability to be formed easily by the injection mold or extrusion, see figure 3-22. Given the short attenuation length of the scintillating plastics, the light produced by the particle interaction can be absorbed, and transmitted to the photo-sensors by wave length shifting (WLS) fibers. These fibers shift the light from blue to green wavelengths.

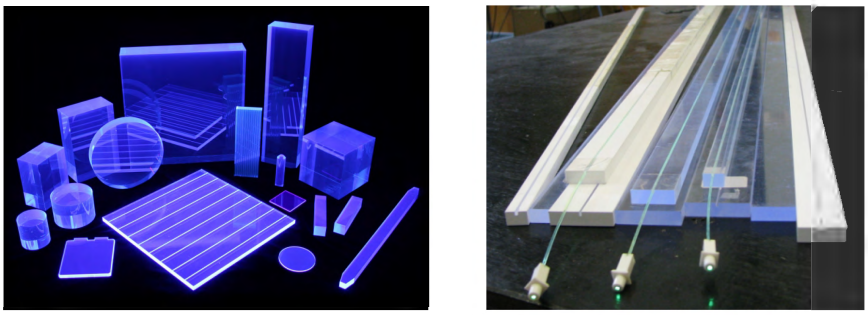

Figure 3-22: Scintillating plastic materials can be shaped easily into different forms (left), and can be coupled with wave length shifting fibers often used in particle detectors (right).

3.4.1 Design criteria

The main requirements and constraints affecting the design of scintillating modules are the following:

- Fixed cost, limiting the number of bars and affecting their dimensions.
- Coverage area, determined by the area of homogeneous magnetic field provided by the magnet modules (figure 3-23).
- Identification of minimum ionizing particles with high efficiency.
- High position resolution ($\sim$ 1 cm) along the Y axis, since the B field acts on the charged particles and bends the tracks in the Y direction. Position resolution along the x axis is less stringent.

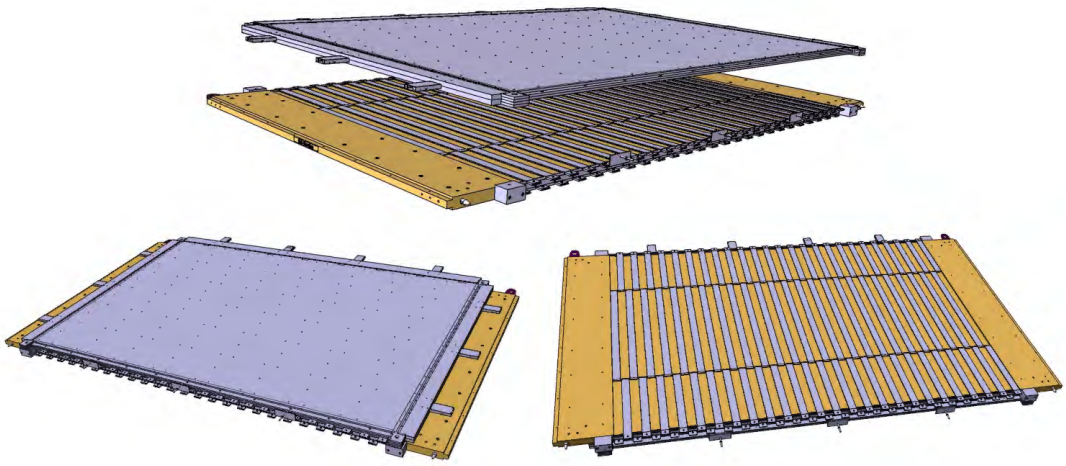

Figure 3-23: Scintillating modules were designed to cover the area with homogeneous magnetic field.

These requirements led to the design of scintillating modules with overall dimensions of $3000 \times 2130 \times 40$ mm^3. Each module is made of two staggered layers of horizontal bars, with dimensions $2900 \times 31 \times 7.4$ mm^3, and 2 staggered layers of vertical bars, with dimensions $1950 \times 210 \times 7.4$ mm^3.

Figure 3-24 shows the schematics of the scintillating bars of two half modules before they are folded together to form a full module. The 21 cm wide vertical bars, separated by plastic spacers of 14.5 cm, make up the outer layers of each half module. The 3 cm wide horizontal bars, separated by plastic spacers of 1 cm, compose the inner layers of each half module. When the half modules are folded together, the horizontal bars and vertical bars of the two half modules form overlaps to provide full coverage.

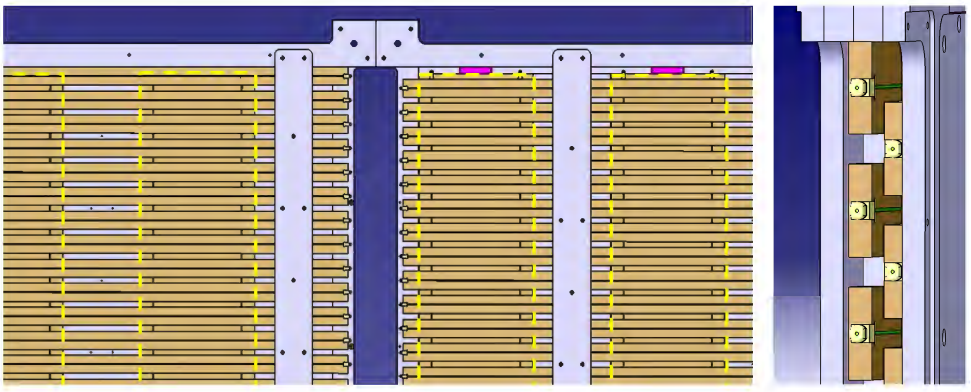

(a) Two half-modules viewed from inside.

(b) horizontal bars side view.

Figure 3-24: Schematics of the scintillating bars of two half modules. They form an overlapping pattern when folded together.

3.4.2 Scintillating bars

The Baby MIND plastic scintillating bars are manufactured by extrusion of polysterene-based scintillator, with 1.5% paraterpenyl (PTP) and 0.01% of POPOP by Uni-Plast, in Vladimir, Russia. After extrusion, the bars are covered by $30-100$ μm thick diffuse reflector by etching of the polystyrene surface with a chemical agent. Details about the extrusion technique and the method of etching a scintillator with a chemical agent can be found in [107] [108].

A groove with 1 mm width and 2 mm depth is machined along the length of the hor-

(a) Horizontal bars

(b) Vertical bars

Figure 3-25: Baby MIND scintillating bars at INR, russia.

izontal bars and in U-shape configuration for the case of vertical bars, where a 1 mm Kuraray Y11 multiclad WLS fiber is glued with optical cement to improve the optical contact between the scintillating plastic and the fiber. The WLS fiber absorbs the photons generated in the scintillating plastic by the passage of a particle, and deliver

the re-emitted shifted light to the photo-sensor connected to each end of the fiber. The absorption and emission spectra of kuraray Y11 WLS fiber is shown in figure 3-26.

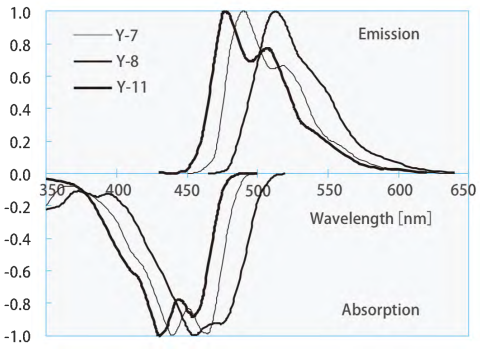

Figure 3-26: Kuraray WLS absorption and emission spectra [109].

Optical Connector

A special optical connector is embedded in the scintillating plastic at the end of WLS fibers. The optical connector is designed to align the fiber end with the sensitive area of the photo-sensor, and provide mechanical support for the MPPC in order to withstand vibrations and shocks during handling and transportation. components of the optical connector is shown in figures 3-27. The connector is composed of a

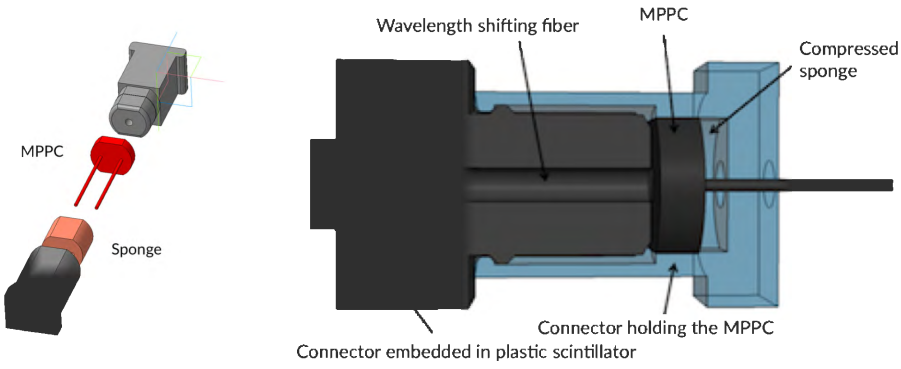

(a) Exploded view. (b) Section view, when put together.

Figure 3-27: Schematics of the optical connector, designed to align the MPPC with the fiber end.

male part, embedded in the scintillating bar and fixing the WLS fiber, and a female part which holds the MPPC. The optical connector is a crucial piece, since a slight misalignment of the fiber and photo-sensor can cause a significant reduction in the light yield.

For the signal readout, a mini PCB is glued to the connector which makes contact with the MPPC pins, and direct the signal to a micro-coaxial cable (figure 3-28).

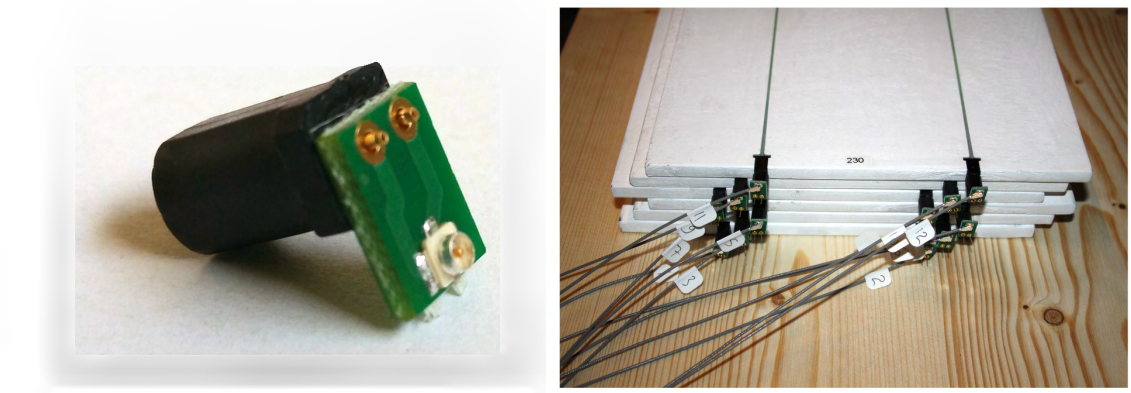

(a) PCB glued to the connector. (b) Optical connectors of vertical bars.

Figure 3-28: Optical connector with a mini PCB which transfers the signal to a micro-coaxial cable.

3.4.3 Test results for scintillating bars

To qualify the performance of scintillating bars separate tests for horizontal and vertical bars were conducted during beam tests at T9 area at CERN.

Horizontal bars test

Samples of 3 cm wide and 3 m long horizontal bars were tested in October 2015, during a scintillating bar test campaign for the SHiP experiment which compared bars of different dimensions from two different manufacturer [110].
The experimental setup for the test of 3 m long horizontal bars is shown is figure 3-29. The bars were instrumented by Hamamatsu MPPC, type S13081-050CS. The signal after amplification was sent to a waveform digitizer, CAEN DT5742 with a 5 GHz sampling frequency. The charge was derived by integrating the signal pulse within a 200 ns window and converting it to number of photoelectrons (p.e.) following a calibration procedure discussed in [110].
A sample of the waveform registered by the CAEN digitizer is shown in figure 3-30.

For the light yield measurements, a stack of three horizontal bars were irradiated simultaneously by a beam of 10 GeV muons. Two trigger counter scintillating slabs were positioned one in front, and the other behind the bars, to provide a coincidence signal from an active area of 1×5 cm^2. The position of the bars with respect to the beam was changed in steps of 10 cm, collecting 29 points altogether. The scan results

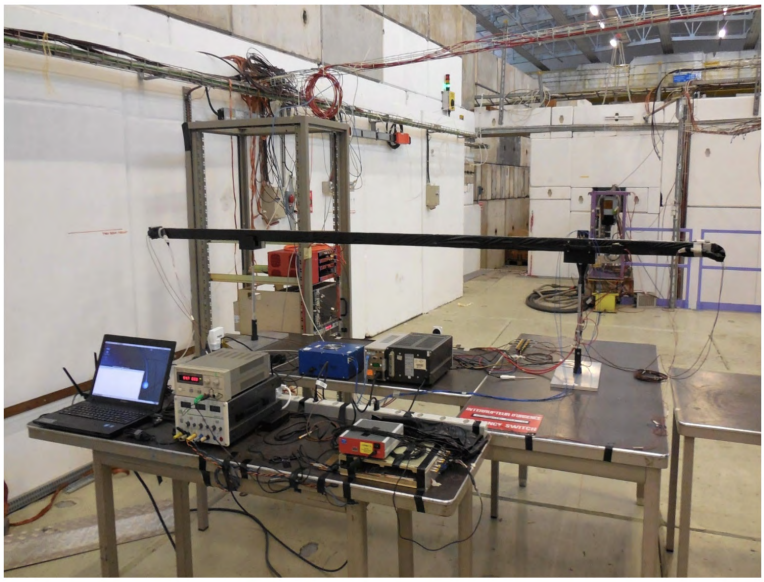

Figure 3-29: Experimental setup for the test of 3 m long horizontal bars.

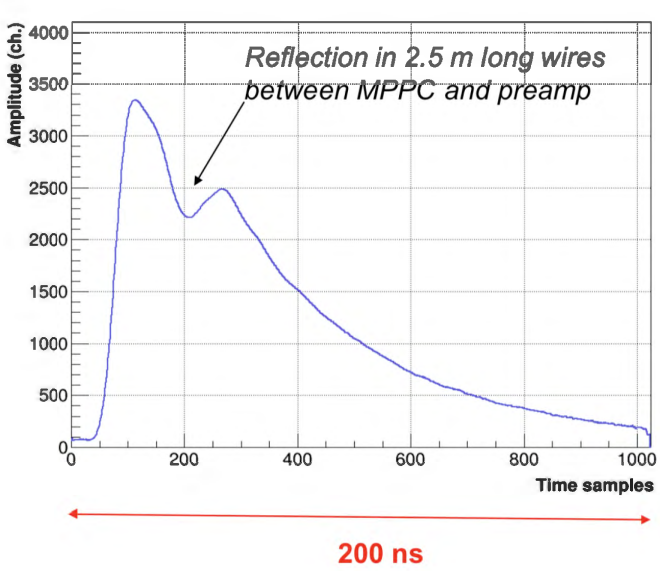

Figure 3-30: A typical waveform after pre-amplification

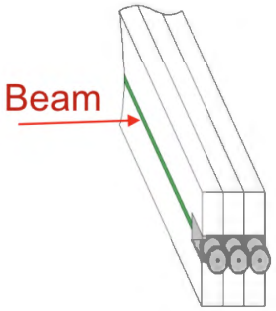

Figure 3-31: For light yield measurements a stack of 3 bars were irradiated by the beam simultaneously.

are shown in figure 3-32. The sum of the light yields from both ends was measured to be about 60 p.e. per minimum ionizing particles when the beam impinges at the center of the bars, and about 20 % higher when the beam impinges near the ends. The hit detection efficiency for the horizontal bar is above 99 % for thresholds up to 10 p.e. (figure 3-32).

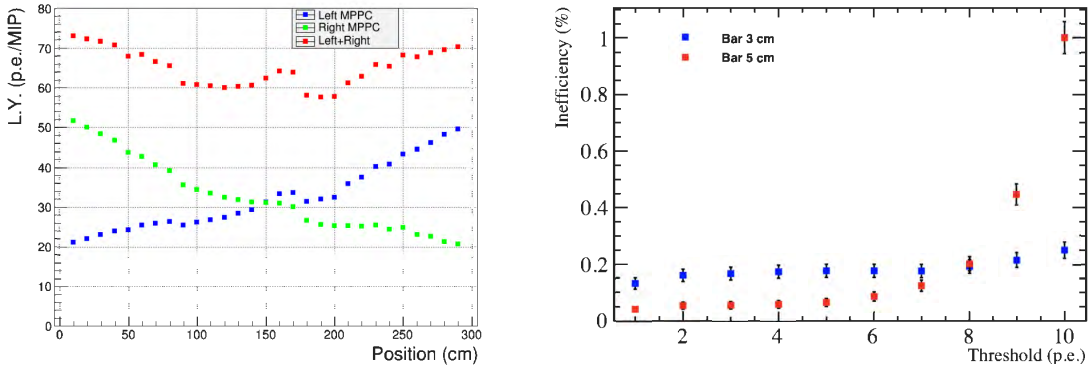

Figure 3-32: Light yield measurements along the length of the horizontal bar (left). The horizontal bars inefficiency with respect to threshold.

Vertical bars test

The vertical bars were tested in July 2016. The experimental setup is shown in figure 3-33. The 21 cm wide, vertical bars, have a U-shape WLS fiber, which indicates that

Figure 3-33: Experimental setup for test of the vertical bars.

both MPPCs are placed at the same end, on top of the bar. The consequence of such arrangement is a non symmetric response to particle hits along the bar. To illustrate the performance of vertical bars, detailed light yeild measurements across the width of the bar at different distances from the MPPCs were carried out to map the light yield as a function of hit position.

Similar to the horizontal bars test setup, a stack of three vertical bars were irradiated simultaneously by the beam of 10 GeV muons. The trigger consisted of small scintillating slabs in cross configuration with an effective area of 1×1 cm^2, placed in front and behind the vertical bars [111]. Figure 3-34 shows a schematics of the vertical bars and the light yield measurement map. For each indicated line at a fixed distance from the MPPC, multiple light yield measurements across the width of the bar was performed. The results are presented in figure 3-35. The two peaks in the light yield

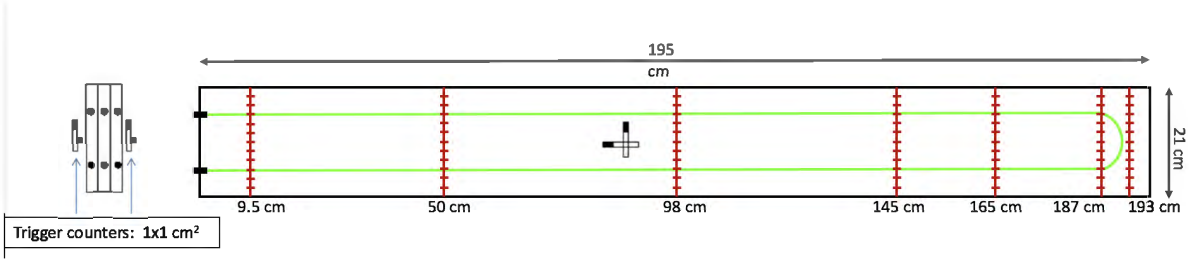

Figure 3-34: Schematics of the vertical bars light yield measurement. For each indicated line at a fixed distance from the MPPC, multiple light yield measurements across the width of the bar was performed.

distribution correspond to the position of WLS fibers. The shape of the distribution as we move away from the WLS fiber, contains information about attenuation length of light in the scintillating plastic. The result of an exponential fit to the distribution suggests an effective attenuation length of 86 mm in the scintillating plastic.

The hit detection efficiency of the vertical bars for a threshold of 4 p.e. is evaluated and presented in figure 3-36. The results show that requiring a coincidence signal from both ends of the fiber (AND logic) leads to a hit detection efficiency of above 90 % in most regions of the bar (apart from bottom corners) and the exact value depends on the distance of the hit from the WLS fiber. In comparison by requiring either fiber end signals above the threshold (OR logic), hit detection efficiency is 100% in most regions of the bar, dropping to 98% in the corners furthest from the MPPCs.

This represents a large body of work to ensure the bar design is validated and their performance match with the requirements of the detector.

After manufacturing, all the 1744 horizontal bars and 315 vertical bars were tested by cosmic rays at INR, Russia, prior of shipment to CERN. The average light yield distribution of the horizontal and vertical bars is shown in figure 3-37. A first batch of scintillating bars was delivered to CERN in March 2016. It contained all the vertical bars and a subset of horizontal bars. The second batch of scintillating bars was delivered end of November 2016. Each individual bar was tested again with an LED

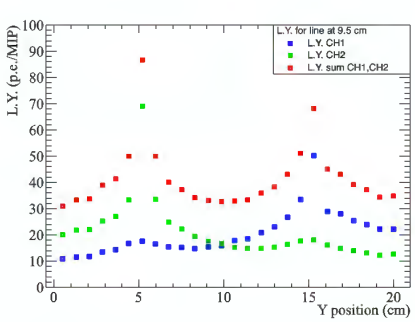

(a) 9.5 cm

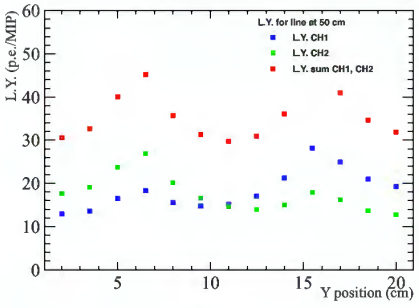

(b) 50 cm

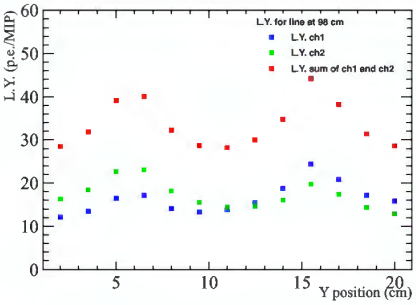

(c) 98 cm

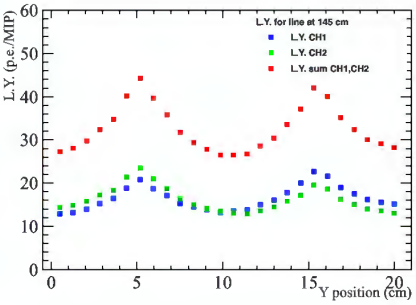

(d) 145 cm

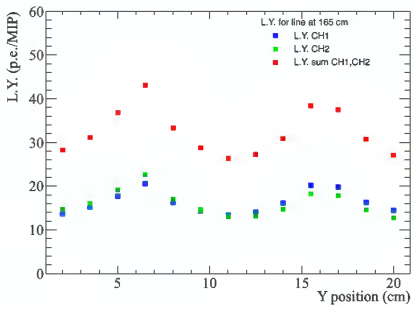

(e) 165 cm

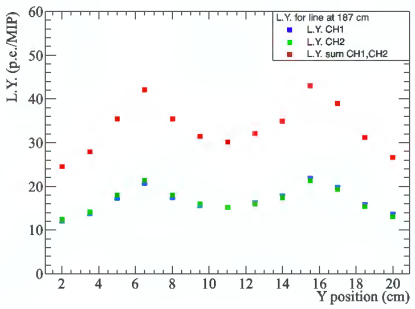

(f) 187 cm

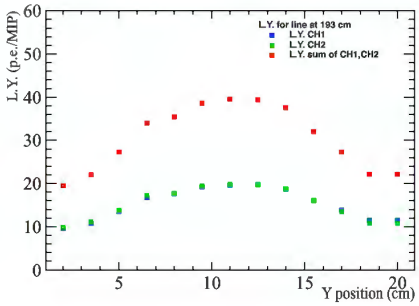

(g) 193 cm

Figure 3-35: Results of the Light Yield measurement across the width of the vertical bar for lines of different distances to the MPPC.

setup at CERN to ensure that they are not damaged before mounting them on the scintillating module.

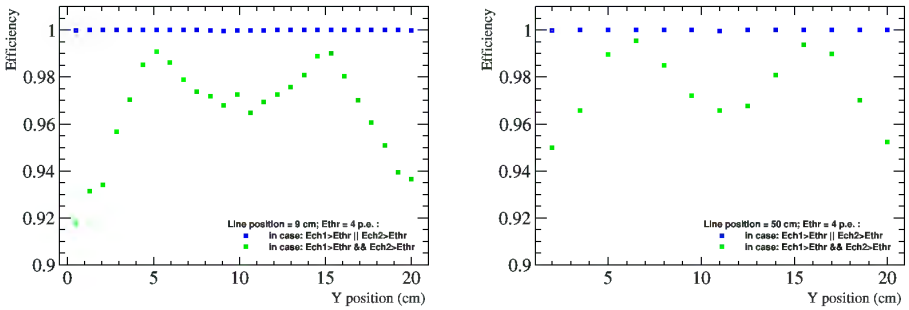

(a) 9.5 cm

(b) 50 cm

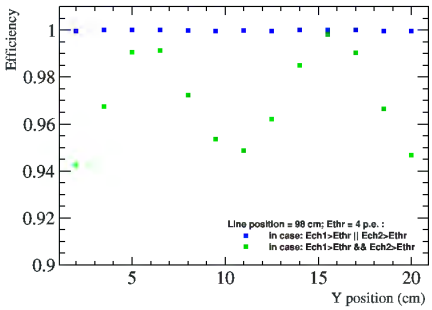

(c) 98 cm

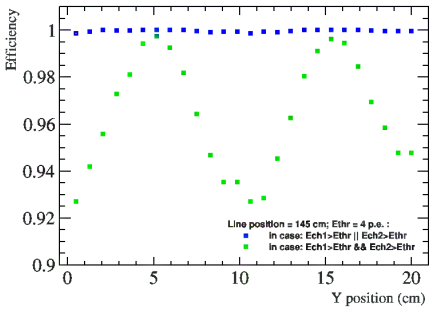

(d) 145 cm

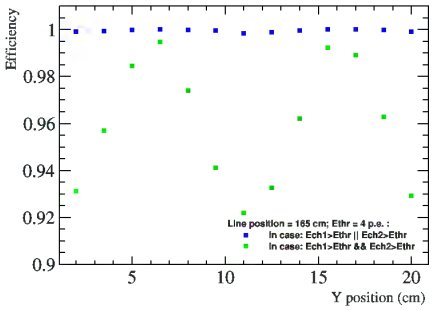

(e) 165 cm

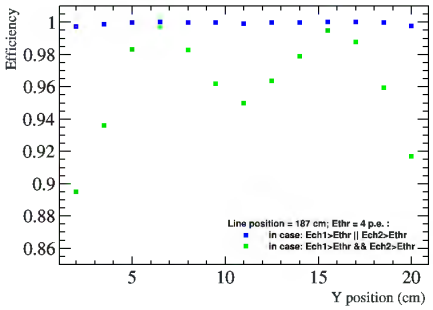

(f) 187 cm

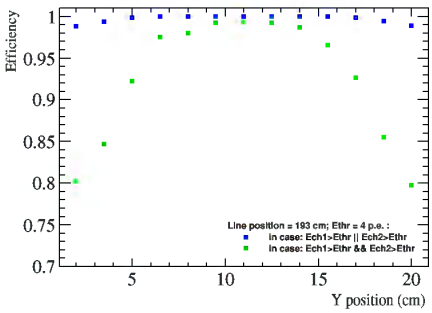

(g) 193 cm

Figure 3-36: Hit detection efficiency across the vertical bar with a threshold of 4 p.e.. The green points require a coincidence at both ends of the fiber(AND logic), whereas the blue points represent the case where either fiber ends has a signal above threshold (OR logic).

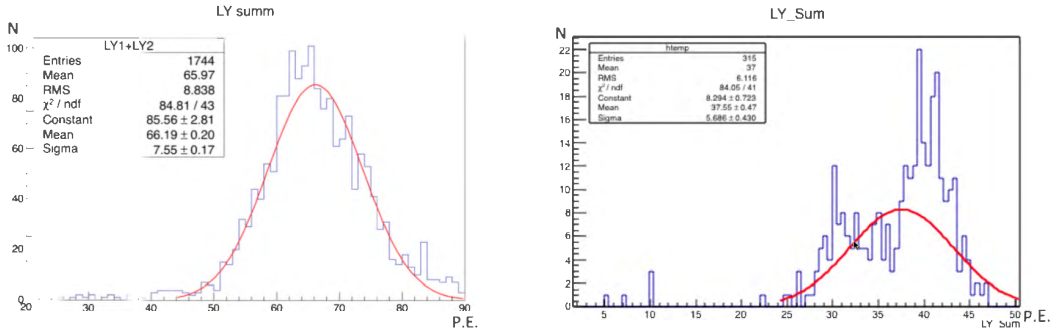

(a) Horizontal bars

(b) Vertical bars

Figure 3-37: Average light yield of all manufactured bars with cosmic ray test at INR.

3.4.4 Scintillating modules assembly

The design of support mechanics and assembly solution for the scintillating modules were the responsibility of University of Geneva. The assembly of 18 scintillating modules took place in building 180, at CERN. The first prototype module was assembled in October 2016, in order to validate the design of support mechanics, the assembly procedure and the integration with magnet module. The assembly of the remaining 17 modules took place from February to June 2017. Each module consists of four layers of scintillating bars, making up a total of 95 horizontal bars and 16 vertical bars, and are covered with Aluminum plates on the front and the back to provide light tightness and some degree of mechanical stability. The pieces fit together perfectly without any glue and the cover plates are screwed to the spacers and the frame. The steps of assembly are shown in figure 3-38.

Three rotating stands were fabricated to facilitate the assembly procedure and support the heavy and fragile scintillating module prior to its integration to the magnet module. The scintillating bars are first assembled into independent half-modules consisting of an outer vertical layer and an inner horizontal layer. The bars in any given orientation in each half-module are separated from each other using ladder like plastic spacers, which align and maintain them in place. The spacer material was chosen to have a density close to the scintillating plastic density, in order to keep variations in material densities to a minimum within the tracking volume. When both half-modules are assembled, they are brought together and bolted at four corners to make a full detector module in such a way that the horizontal bars of two half modules form an overlap of 1 cm with each other and the vertical bars an overlap of 3.5 cm. In the final step the module is sealed and the slits and screw holes are covered by thick aluminum tape to prevent light leakage into the module. Once the assembly is complete, the

(a) Three rotating stands.

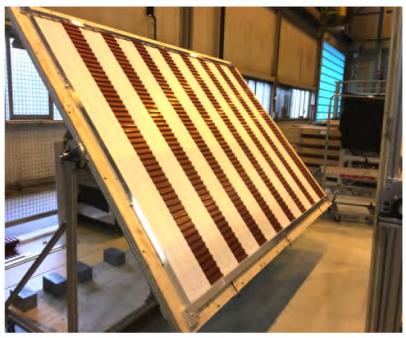

(b) Loading of the vertical bars and plastic spacers.

(c) Loading of the horizontal bars.

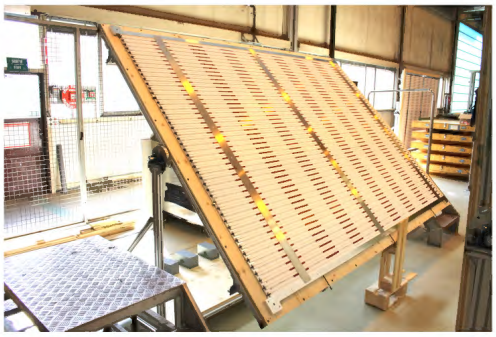

(d) Attachment of the reinforcing aluminum bars.

(e) Bringing two half modules together.

(f) Bolting the four corners.

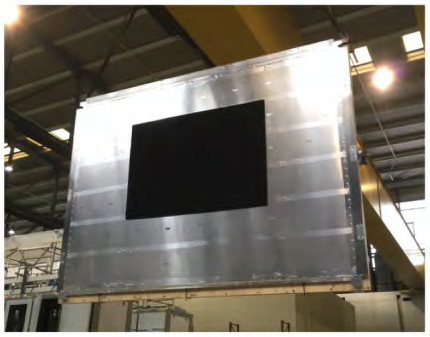

(g) A full scintillating module.

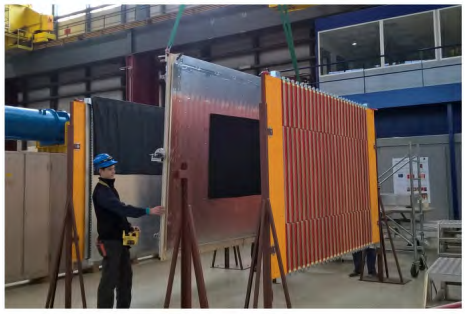

(h) Integration of scintillating module to a magnet module.

Figure 3-38: Scintillating module assembly steps, part1.

scintillating module has to be removed from the assembly jig, and integrated onto a magnet module on an integration stand, since the scintillating module mechanics do not confer enough structural rigidity for the module to be self-supporting.

3.4.5 MPPC assembly and inner cabling

The pre-assembly of the MPPCs and the optical connector, including gluing the mini PCBs to the optical connectors were done in advance and the pre-assembled MPPC were stored safely until the assembly on to the scintillating modules, which took place on the integration stands. The assembly of MPPCs onto the scintillating modules and

Figure 3-39: Pre-assembly of the MPPCs and optical connectors.

the connection of the micro-coaxial cables inside the cable tray is shown in figures 3-40 and 3-41.

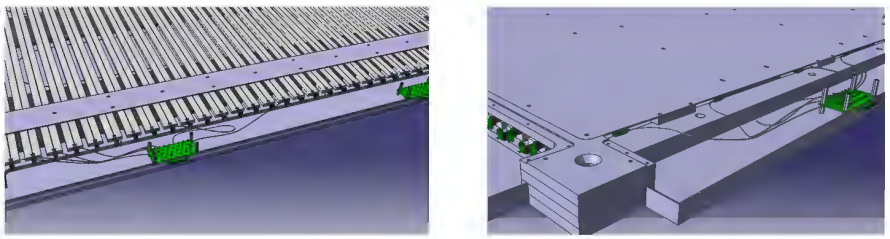

Figure 3-40: Cable tray design and micro-coaxial cables connectivity.

Figure 3-41: Assembly of MPPCs onto the scintillating modules.

3.4.6 Scintillating module qualification tests

The scintillating module qualification tests took place on the integration stands after MPPC instrumentation and inner cabling of the modules was completed. Since at this stage the final version of Front-End boards was not manufactured yet, the qualification tests were carried out using the first generation of the Baby MIND electronics Front End Board (FEB-v1). The first phase of testing aimed to check channel connectivity and was performed by acquiring dark count data with low thresholds and checking the quality of fingerplots (see section 3.6.2) for every individual channel. The second phase

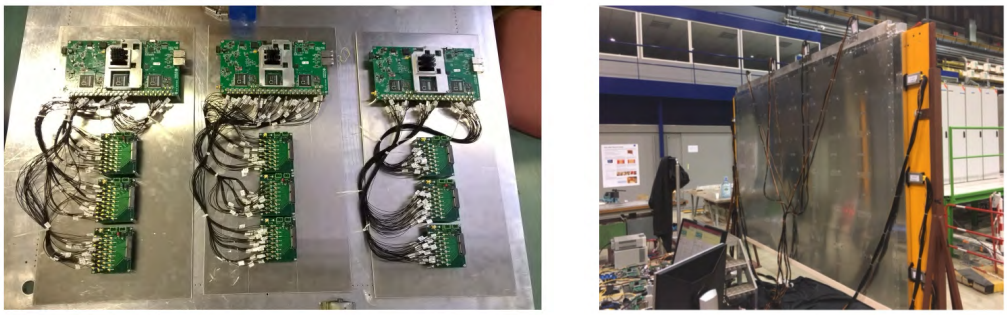

Figure 3-42: Scintillating module qualification tests with FEB-v1.

of testing aimed to verify signals from scintillating bars and check proper connection between the MPPCs and the fiber end as well as the light tightness of the module. For this stage cosmic ray data was acquired with a synchronized setup, consisting of three FEB-v1, which were each connected to the right, left and top of the scintillating module. Figure 3-42 shows the test setup and figure 3-43 shows an example of the 2D hit map generated from cosmic ray tests using hit time coincidence. The 5 missing channels on this plot are due to broken channels on FEB-v1, the channels on the module were all healthy and this was confirmed later with FEB-v2 data.

3.5 Connectivity scheme and cable bundles

3.5.1 Choice of cabling scheme and mechanical integration of electronics

Design choices for the cabling and mechanical integration of electronics on the scintillating modules are discussed in this section. Since the cabling layout affected the design of the FEB, it was critical to adopt a cabling scheme as early as possible, but one which would still integrate feedback from ongoing prototyping and qualification

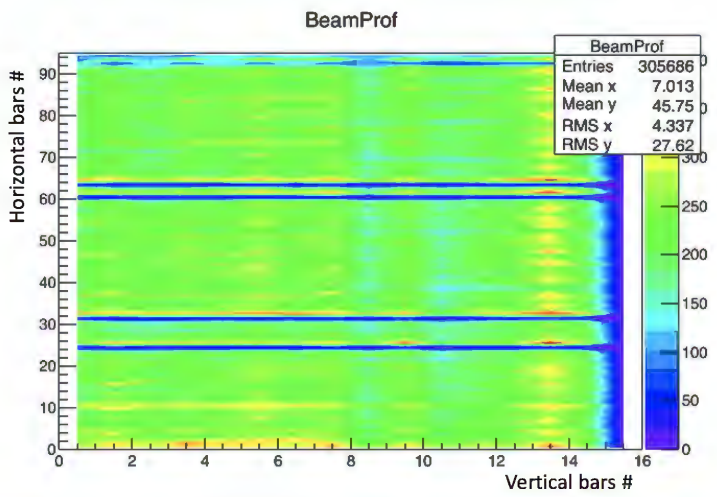

Figure 3-43: Example of cosmic ray test for module qualification test.

tests. A comparative study of several options was carried out initially, based on where to locate the FEBs, given the location of the scintillating modules is fixed.

- All FEBs mounted in two large racks or crates.
- FEBs fixed on scintillating module: left, right and top
- FEBs fixed on scintillating module: left and right
- FEBs fixed on scintillating module: left only

The starting point in the study was the first version of Baby MIND Front-End board (FEB-v1), embedding 3 CITIROC readout ASICs with 96 channels in total and one ARIA5 FPGA optimized for 3 ASICs in terms of pin numbers, cell numbers and speed grade. Given that the scintillating modules each have 95 horizontal channels on either side left/right, and 32 vertical channels on top, a direct consequence of the architectures listed above was different FEB layouts:

- 4×32: One FEB design with 4 CITIROCs. Each FEB can connect the horizontal channels of one side of the scintillating module (95 ch) and half of its vertical channels (16 ch).
- $3 \times 32 + 1 \times 32$: Two different FEB designs, one with 3 CITIROCs for horizontal channels of each side of a module (95 ch), and another FEB design with 1 CITIROC for vertical channels of the module (32 ch).

- $3 \times 32 + 3 \times 32$ (1 CITI): Two variants of the same FEB design, one with 3 CITIROCs for horizontal channels of each side of a module (95 ch), the other with a single CITIROC mounted for vertical channels of the module (32 ch).

- $3 \times 32 + 3 \times 32$ (3 Vmod): One FEB design with 3 CITIROCs, Each FEB can connect the horizontal channels of one side of the scintillating module (95 ch) or the vertical channels of three consecutive modules (3×32 ch).

Connectivity scheme evaluation table	Total	Cost			Electronics design effort			Mechanics design effort			Installation effort			Noise			Cabling			Cooling			Accessibility and Maintenanc			Failure impact			Robustness		
Grades range from -2 to 2, and Coefficients from 1 to 5		grade	coef.	value	grade	coef.	value	grade	coef.	value	grade	coef.	value	grade	coef.	value	grade	coef.	value	grade	coef.	value	grade	coef.	value	grade	coef.	value	grade	coef.	value
4x32 FEB Rack	0	No advantage																												
4x32 left, right and top	0	No advantage																												
4x32 left and right	9	1	5	5	-2	4	-8	1	3	3	2	3	6	1	5	5	1	2	2	0	1	0	0	3	0	-2	2	-4	0	5	0
4x32 left only	-13	-1	5	-5	-2	4	-8	1	3	3	2	3	6	-1	5	-5	-1	2	-2	-1	1	-1	1	3	3	-2	2	-4	0	5	0
3x32 + 1x32 FEB Rack	0	No advantage																												
3x32 + 1x32 left, right and top	-11	0	5	0	-1	4	-4	-1	3	-3	-1	3	-3	2	5	10	2	2	4	1	1	1	-2	3	-6	0	2	0	-2	5	-10
3x32 + 1x32 left and right	-1	-1	5	-5	-1	4	-4	1	3	3	1	3	3	0	5	0	1	2	2	0	1	0	0	3	0	0	2	0	0	5	0
3x32 + 1x32 left only	-19	-2	5	-10	-1	4	-4	-1	3	-3	1	3	3	-1	5	-5	-1	2	-2	-1	1	-1	1	3	3	0	2	0	0	5	0
3x32+ 3x32(1 CITI) FEB Rack	0	No advantage																												
3x32+ 3x32(1 CITI) left, right and top	-3	0	5	0	1	4	4	-1	3	-3	-1	3	-3	2	5	10	2	2	4	1	1	1	-2	3	-6	0	2	0	-2	5	-10
3x32+ 3x32(1 CITI) left and right	12	0	5	0	1	4	4	1	3	3	1	3	3	0	5	0	1	2	2	0	1	0	0	3	0	0	2	0	0	5	0
3x32+ 3x32(1 CITI) left only	-11	-2	5	-10	1	4	4	-1	3	-3	1	3	3	-1	5	-5	-1	2	-2	-1	1	-1	1	3	3	0	2	0	0	5	0
3x32+ 3x32(3 Vmod) FEB Rack	**14**	**-1**	**5**	**-5**	**0**	**4**	**0**	**2**	**3**	**6**	**-1**	**3**	**-3**	**-2**	**5**	**-10**	**2**	**2**	**4**	**2**	**1**	**2**	**2**	**3**	**6**	**2**	**2**	**4**	**2**	**5**	**10**
3x32+ 3x32(3 Vmod) left, right and top	1	2	5	10	2	4	8	-2	3	-6	-2	3	-6	2	5	10	1	2	2	1	1	1	-2	3	-6	-1	2	-2	-2	5	-10
3x32+ 3x32(3 Vmod) left and right	-2	1	5	5	2	4	8	-2	3	-6	-2	3	-6	-1	5	-5	-1	2	-2	0	1	0	2	3	6	-1	2	-2	0	5	0
3x32+ 3x32(3 Vmod) left only	-20	-1	5	-5	2	4	8	-2	3	-6	-2	3	-6	-2	5	-10	-2	2	-4	-1	1	-1	2	3	6	-1	2	-2	0	5	0

Figure 3-44: Evaluation of different connectivity schemes.

The selection criteria for comparison of different options were cost, electronics design effort, mechanics design effort, installation effort, noise, cabling, cooling, accessibility and maintenance, failure impact and robustness.

An exercise was carried out, with a table for each selection criterion comparing the different options and a grading from -2 to 2 for each option. Furthermore a coefficient from 1 to 5 was assigned to each selection criterion, which would reflect the importance of each criterion in overall decision. The results of the comparison are summarized in figure 3-44.

The main factor that played significant role in comparison of options was accessibility and maintenance of the FEBs. Since the width (along x axis) of the scintillating modules is smaller than the width of the magnet modules, the options of fitting each electronics readout FEB right next to its corresponding scintillating module, effectively led to the FEBs being sandwiched between magnet modules with little access for

maintenance tasks such as firmware upgrade and repair works.
The final solution that the collaboration adopted in October 2016 was a hybrid of combinations cited above, taking the positive features of several of these earlier options, with FEBs grouped in sets of 6 within mini crates at several locations around the detector, but several meters away from the scintillating modules. Regarding the FEB design the consensus was reached to proceed with a single FEB design embedding 3 CITIROCs and modifying the SiPM connector side, where the mini-coaxials were replaced by three 66 pins female connectors to host three cable bundles. In this configuration each FEB can be connected to either the horizontal bars of one side of a module (95 channels) or the vertical bars of three consecutive modules (3×32 channels).
An extensive design and qualification program for both cable bundles and the FEB was launched to determine signal attenuation, noise, crosstalk between channels as a function of cable length.

3.5.2 Validation of EMOS coaxial cables

After adaption of a design where the electronics units are located over five meters away from the photosensors and scintillating bars, efforts were made to find a supplier who can deliver several km of RG174 co-axial cables in a short time scale to instrument $\sim$ 4000 channels over 5 m each at an affordable cost. The seemingly large disparity in cost and lead times of RG174 co-axial cables motivated a study to validate the signal quality of a candidate cable from EMOS in comparison with different cables and different lengths. These tests were performed in December 2016.
The measurements centered on the resolution of single photoelectron peaks from dark count data of silicon photo-multipliers (Hamamatsu S12571-025C MPPC) readout with the first version of Baby MIND Front-End board (FEB-v1). The signal quality in this case reflects pick-up noise and attenuation over several meters. Four independent channels were used, each with their own MPPC, interconnects etc. All four channels were connected to one of the CITIROC ASICs on the FEB. A cautionary note must be made here that the tests were not carried out on the final signal chain components between MPPC and FEB-v2. Adapter boards were required to patch signals from MPPCs with U.FL connectors to RG174 cables with SMA connectors, and from RG174 to the FEB-v1.
Two sets of data runs were taken. One set of reference data with four similar length (157 cm) cables from the same commercial supplier labeled as Unige cables, to monitor

potential differences due to MPPCs and electronics induced variations like different channel offsets. And the other set of data with co-axial cables from different suppliers, all of different lengths, including the candidate cable sample from EMOS. The finger-plots obtained from these measurements are shown in figure 3-45. The data for each

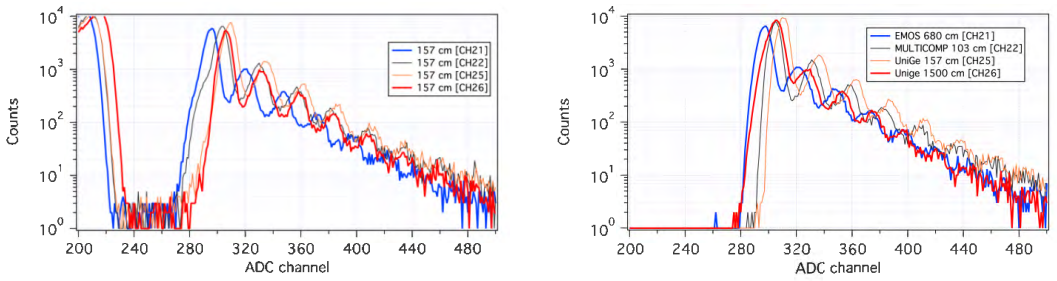

(a) Reference data, Unige cables.

(b) Test data

Figure 3-45: Fingerplots form Unige reference cables (left) and test cables (right).

cable was analyzed using a multi-peak Gaussian fit. An example of the fitting fuction is shown in figure 3-46 for the candidate cable from EMOS. Parameters extracted from the fits were compared for different cables. The full width half maximum (FWHM) for each peak and the sigma on FWHM were extracted from the gaussian fits. The sigma on FWHM represents the error associated to the fit parameter. It reflects the quality of the fitted data peak. A fit of a high quality data peak returns a small error on the fit parameter FWHM. The plots in figure 3-47 present the FWHM (left) and FWHM sigma (right) for the cables under test. The results do not show significant difference between different cables.

Another parameter under study was the MPPC gain. The gain is derived by taking the average of the distance between 4 consecutive photo-electron peaks, excluding the first peak. The reduction in gain as a function of co-axial cable length due to signal attenuation is presented in figure 3-48. The 15 m cable shows about 10 % gain reduction.

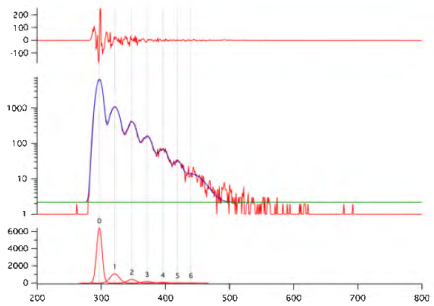

Figure 3-46: Example of a multi-peak gussian fit with IGOR pro.

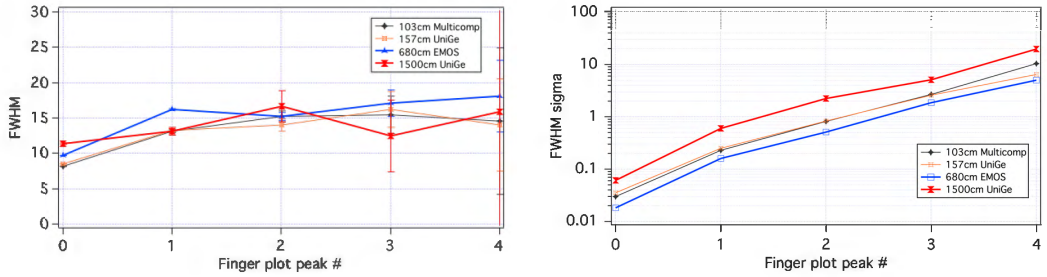

Figure 3-47: The multi gaussian fit parameters for test cables: FWHM (left) and FWHM sigma (right)

In summary the dark count data from the photosensors showed very little qualitative

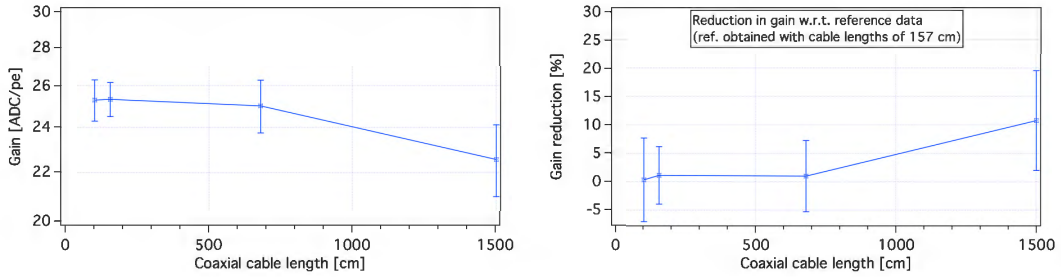

Figure 3-48: Gain coefficient value for different cables (left). Gain reduction as a function of cable length (right).

difference between the EMOS cable and much shorter (1 m or 1.57 m) reference cables and the analysis of the distance between photo-electron peaks revealed no significant difference in calculated gain expressed in ADC/pe, which is an indicator of very little attenuation of the signal down 6.8 m. These results were considered sufficient to validate the choice of RG174 co-axial cable.

3.5.3 Cable bundle design

The connectivity between the SiPM and the FEB is defined based on a single connector per 32 channels and a dedicated cable bundle. The design limits the U.FL micro coaxial cable length to 50 cm which connect the MPPC mini PCBs to a 32-channel adaptor board (module I/F PCB) with an HSEC-8 male connector. These components along with the MPPC are all protected by metallic enclosure of cable trays, at the sides and top of the scintillating module (figure 3-49)-a. The module I/F PCB can either be directly connected to the FEB (maintenance, short connections, lab) or through a male-female extender made of a single bundle of 33 RG174 coaxial cables (ϕ 2.8 mm). The length of this cable bundle is limited to 5 m for better noise immunity. At the other end of the cable bundle the FEBs are located in mini crates. Each mini crate

can host up to 6 FEBs and provides mechanical support for the boards as well as the cable bundles which are screwed to its frame (figure 3-49)-b. The schematics

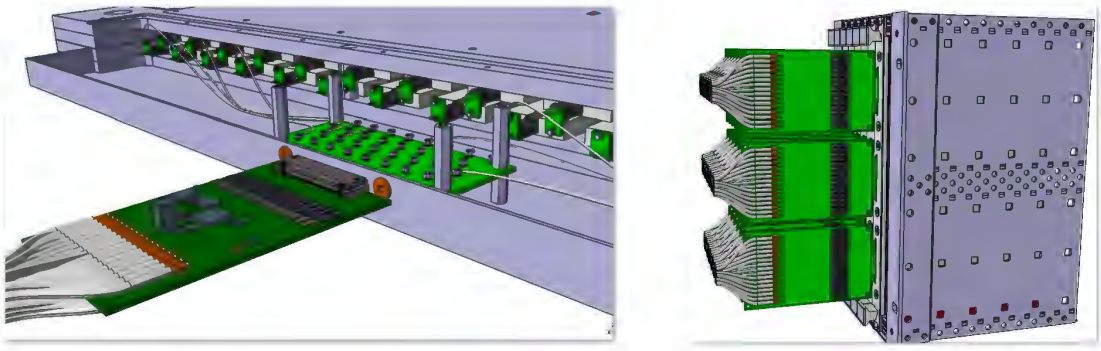

(a) View of the cable tray and connectivity to a cable bundle.

(b) Schematics of cable bundles connected to a Mini-crate

Figure 3-49: Connectivity details on scintillating module side and mini crate.

of a 32-channel cable bundle for horizontal bars is shown in figure 3-50. The high

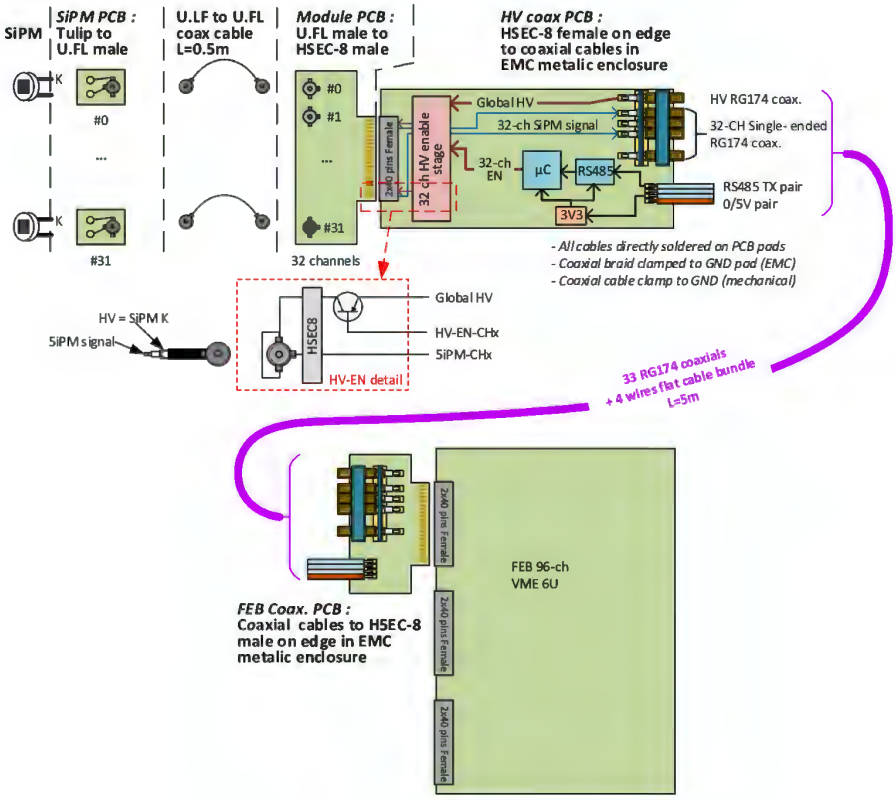

Figure 3-50: Schematics of the MPPC to FEB connectivity for horizontal bars (1 to 1).

voltage (HV) line per 32 channels is drawn separately along the cable bundle from the FEB to the HV-coax PCB, and is applied to each channel via an individual micro-controller ON/OFF enabling stage, and is then transmitted via a 0.5 m micro coaxial

cable through its shielded copper braid to the MPPC cathode. The 5 m coax cable copper braid is connected to ground for noise immunity of the MPPC signal carried in the inner conductor wire. An amplifier on the FEB side rather than the MPPC side ensures a current-mode signal transmission, with good noise immunity (preferable to a single-ended voltage mode signal transmission with amplification close to the MPPC). The cable bundles for vertical bars are modified to have four 8-channel bundles on the module side instead of a single 32-channel. This was necessary since the 32 vertical bar MPPCs are spread in the span of 3 m, and the micro-coaxial cables connecting them to the module I/F PCBs are only 50 cm long, therefore each 8 channels are grouped together and are connected to one of the four module I/F PCBs located in the top cable tray. And four HV-coax PCBs are used with only 8 channels mounted on each and all of them are connected to one single FEB-coax PCB. This leads to 4 bundles going to 1, regrouping 32 channels. On all the HV-coax PCBs, always the same channels 0 to 7 are connected and their slot address is programmed by the micro-controller. Figure 3-51 shows the schematics for vertical cable bundle.

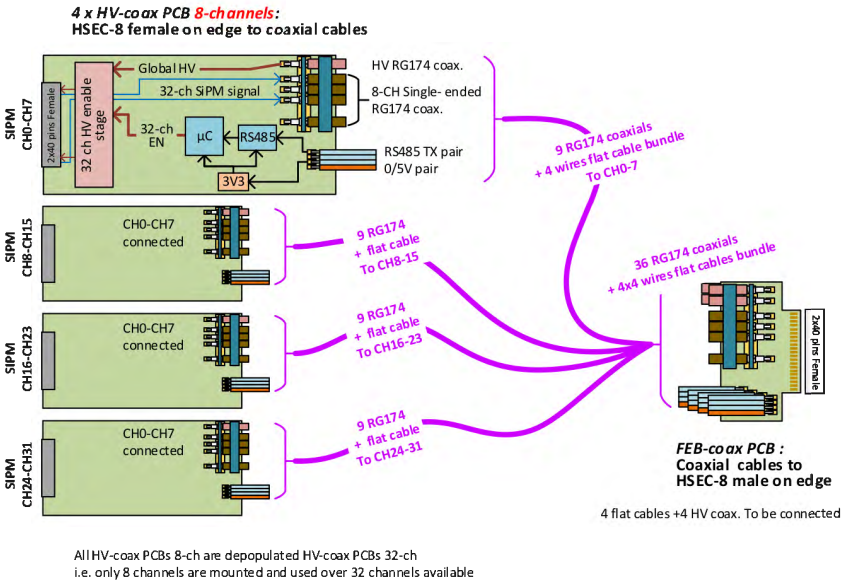

Figure 3-51: Schematics for the vertical bars cable bundle (4 to 1).

Mechanical box

The mechanical design of the aluminum boxes protecting the HV-coax PCB and the FEB-coax PCB at two ends of a cable bundle is shown in figure 3-52. The boxes are screwed to the scintillating module or to the mini crate in order to support the considerable weight of the cable bundle (figure 3-53).

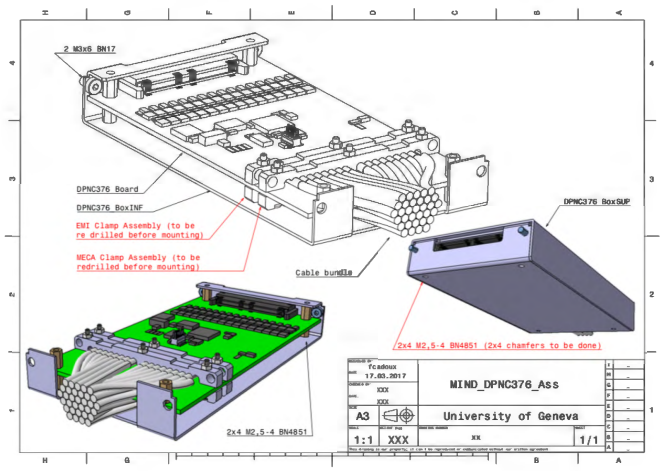

(a) Box design for HV-coax PCB, connected to a module.

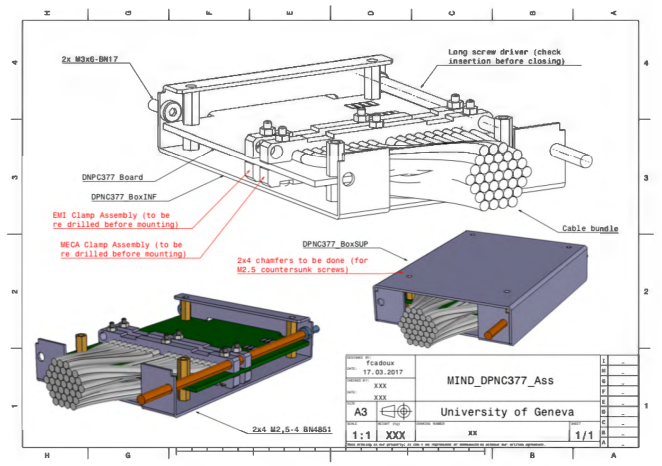

(b) Box design for FEB-coax PCB, connected to a mini crate.

Figure 3-52: Mechanical design of the aluminum protection boxes.

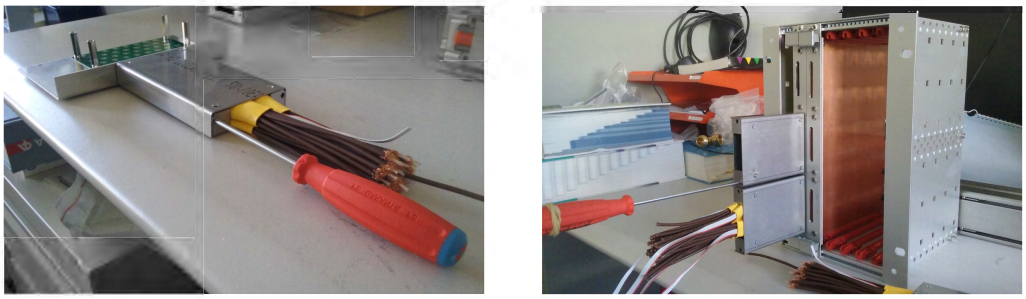

Figure 3-53: Prototype of aluminum boxes screwed to a module cable tray mock up (left) and a mini crate (right) with long screw driver.

3.5.4 Cable bundle prototype tests

In order to validate the design and various PCB components, two cable bundle prototypes, one with 5 m cables and only four active channels and the other with 1 m long

cables and 32 channels were fabricated. The tests were carried out in the dark room at CERN, bldg 595, acquiring dark count data and LED data with FEB-v1.

Crosstalk tests with a 5 m prototype cable bundle:

The general purpose of these measurements were to measure crosstalk due to the components of the cable bundle. Four channels (65, 69, 73, 77) on FEB-v1 have been modified to be compatible with the new cabling scheme with additional PCBs and 5 m coaxial cable. Modifications to FEB1 v1 was necessary because FEB-v1 carries the SiPM high voltage on the external multithreaded shield of the coaxial cable, whereas FEB v2 carries ground on the same external multithreaded shield. The high voltage was supplied from a separate line. In this setup one of the channels was connected to an SiPM receiving the LED signal whose intensity could be controlled remotely. The figure 3-54 shows the test setup. The results are presented for the configuration where

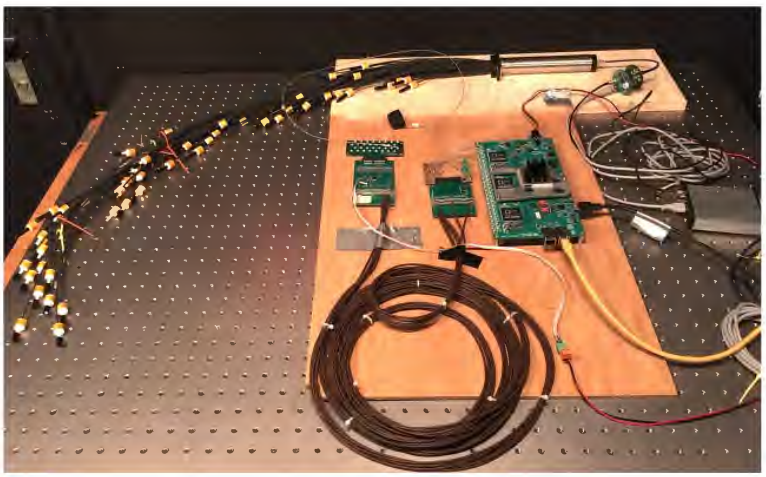

Figure 3-54: A 5 m Prototype cable bundle test setup.

the LED signal is sent to one channel [73 in this case] and three other channels are monitored. In the plots bellow the LED amplitude was increased in stages with hexadecimal setting values of 0x0b, 0x0c, 0x0d, 0x0e and 0x0f, until complete saturation of the high gain signal path on the CITIROC was reached (see section 3.7.3). The CITIROC was enabled to trigger on any of the four channels so long as the signal is above the discriminator DAC threshold, set to 200. As we can see from the plots in figure 3-55, by increasing the LED intensity we start to see some crosstalk signals on the monitor channels. The crosstalk signal amplitude remains below 3 photoelectrons even with the high intensity of the LED device.

In order to determine whether the signal leakage to monitor channels is due to cable

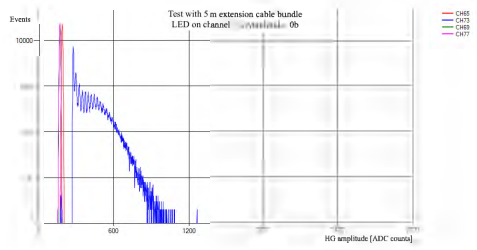

(a) LED amplitude: 0x0b. No crosstalk signal is observed on the monitor channels.

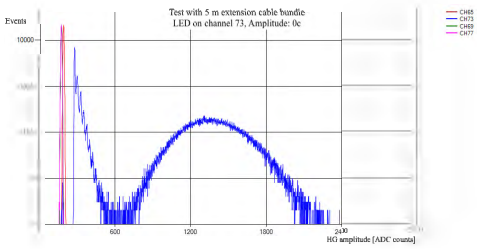

(b) LED amplitude: 0x0c. No crosstalk signal is observed on the monitor channels.

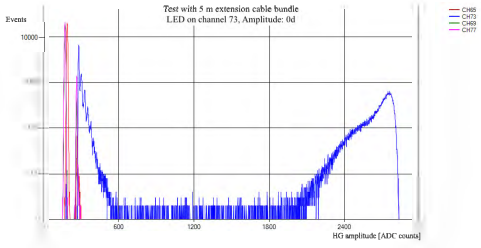

(c) LED amplitude: 0x0d. Crosstalk signal is observed on the monitor channels.

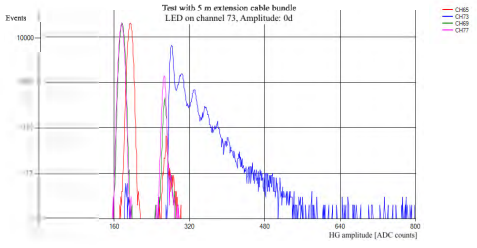

(d) LED amplitude: 0x0d, zoom in the crosstalk region.

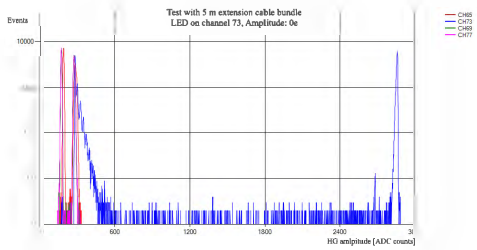

(e) LED amplitude: 0x0e. Crosstalk signal is observed on the monitor channels

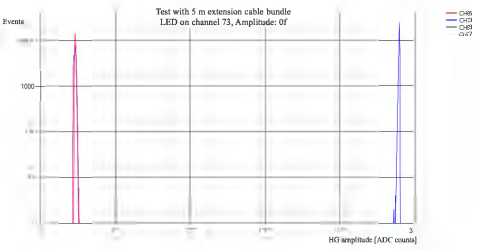

(f) LED amplitude: 0x0f, Complete saturation of channel 73, and crosstalk signals on the monitor channels.

Figure 3-55: Crosstalk test for 5 m prototype cable bundle. LED light is injected on channel 73 on ASIC-2.

bundle components or is an effect of the electronics and CITIROC chip itself, the same measurements was obtained on the identical channels of ASIC-1, i.e channels 33, 37, 41, 45 with the SiPM directly connected to the FEB without the 5 m cable bundle. And similar crosstalk behaviour has been observed. The results are displayed in figure 3-56.

For an additional check, the measurements were repeated with the discriminator mask switched ON on the three monitor channels not receiving the LED, i.e the CITIROC triggers only on the channel receiving the LED, and the crosstalk completely disappeared. Confirming the fact that the crosstalk signal is indeed triggering the CITIROC in these cases. It could be due to some delayed signal i.e reflection, baseline level fluctuations, common HV line fluctuations , etc.

It is important to note that the Front-End board has a multilayer PCB design and

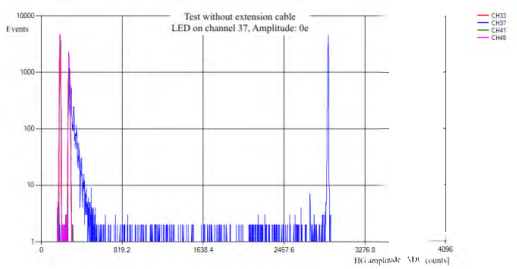

(a) LED amplitude: 0x0e, No cable bundle, crosstalk observed on monitor channels.

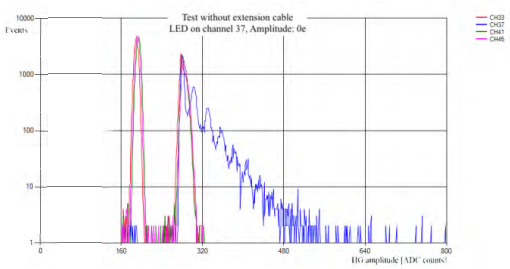

(b) LED amplitude: 0x0e, zoom in the crosstalk region.

Figure 3-56: Crosstalk test without the 5 m prototype cable bundle shows similar crosstalk behaviour. LED light is injected on channel 37 on ASIC-1.

the adjacent channels of a CITIROC were routed in different layers to maximize their distance and lower the chance of crosstalk between them. The channels that were used in this study correspond to nearest neighbors on the same layer of the FEB.
The measurements were then continued with higher LED intensity up to saturation of the low gain (LG) signal path, and it was observed that the levels of the crosstalk signal always remains below a few p.e. It was verified that by setting a higher discriminator DAC threshold value of 250, the crosstalk signal can be safely eliminated.
The investigation was continued with a 32-channel cable bundle prototype.

Validation tests with a 1 m prototype cable bundle:

The test setup for the 1 m long prototype cable bundle with 32 channles is shown in figure 3-57. In the first stage of the test, the transmission of signal through all

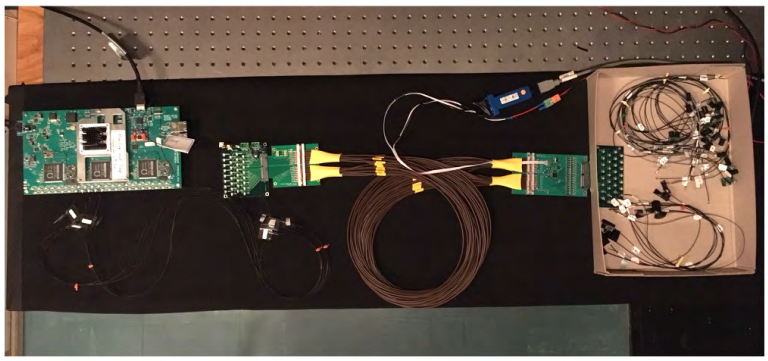

Figure 3-57: Test setup of the 1 m prototype cable bundle with 32 channels.

32 channels were verified by acquiring dark count data one channel at a time and consequently on all channels simultaneously. The fingerplots were analyzed and the gain and the first peak location for each channel were extracted (figure 3-58). The

functionality of the HV-coax PCB in switching ON and OFF the HV for individual channels were tested as well.

In the second stage of the test, the electric crosstalk due to high intensity LED signal

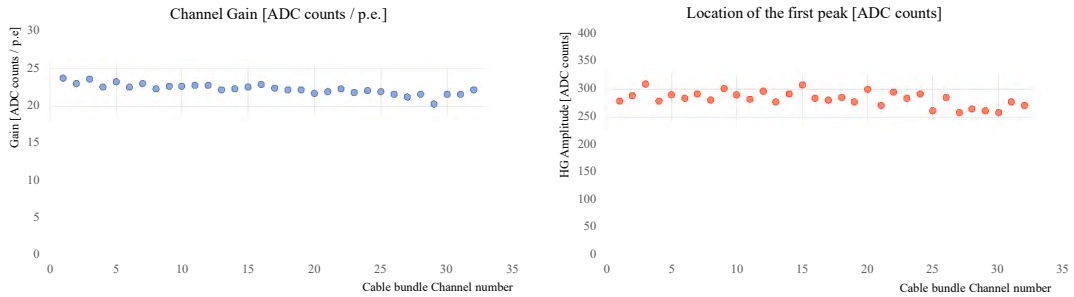

(a) Gain coefficient (b) First peak location

Figure 3-58: Data acquired by 1 m prototype cable bundle indicate healthy signal on 32 channles.

were revisited, with 32 channels, and presence of the aluminum cable tray. The cable trays has a 2 mm tick slit through which the module I/F PCB and the module end of the cable bundle (HV-coax PCB) connect to each other. Concerns about possible additional crosstalk via the Aluminum motivated this measurement. For this purpose,

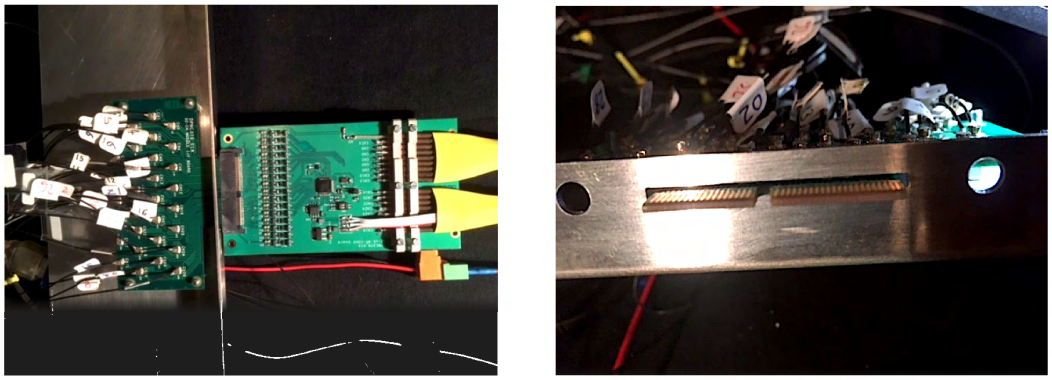

Figure 3-59: Mechanical insertion of the module I/F PCB into the 2 mm wide slit of the cable tray.

32 AIDA scintillating bars were used. All bars were connected to an LED fiber on one end and an MPPC connected to a channels of the extension cable on the other end. 24 channels of the cable bundle were connected to ASIC-1 and 8 remaining channels were connected to ASIC-2 on FEB-v1. The LED light was injected in one channel at a time with activated HV, while for all other channels the HV was set to OFF. The amplitude for LED system has been chosen such that the high gain output signal is above saturation, but the low gain is not saturated. The plot in figure 3-60 shows the electrical crosstalk super-imposed for all the channels except the one which received

the LED signal [ch32 in this case]. This plot has been used in order to locate the maximum level of electrical crosstalk in terms of ADC counts. The exercise has been

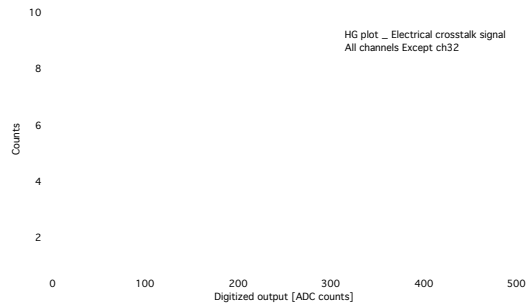

(a) Electric crosstalk for all readout channels (except the LED channel) are super imposed.

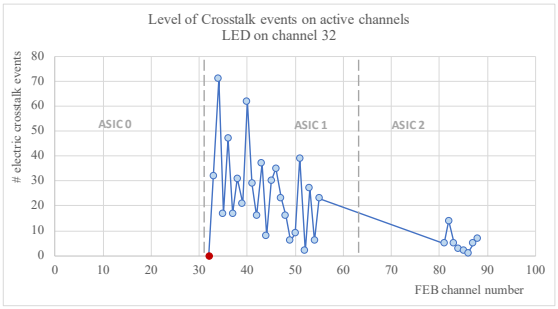

(b) Number of recorded crosstalk events as a function of FEB-v1 channel number.

Figure 3-60: Electric crosstalk induced on all readout channels by the LED light injected on channel 32.

repeated for all 32 channels. The highest amplitude crosstalk signal was detected at 420 ADC counts. Considering the average baseline location at 280 [ADC counts] and the average gain to be 23 [ADC/p.e], we can estimate that the maximum level of the electrical crosstalk is about 6 photo-electrons. The plot in figure 3-60 shows the number of crosstalk events for each global channel on FEB-v1, when the LED light was injected on channel 32. This plot was motivated to investigate whether the electric crosstalk is limited to one ASIC or it can leak to channels on the other ASICs, which could be an indication of the signal leakage in the routing on the PCB.
The conclusion of the validation tests of the cable bundle was that no additional noise associated to the extension cable bundle, or the aluminum cable tray was identified. The signal transmission of all channels were verified and the functionality of the micro-controller on the HV-coax PCB was successfully tested. The overall design and functionality of the new cabling system was validated. In addition, the tests revealed the existence of an electrical crosstalk which is induced on all readout channels when a high intensity signal is fired on any channel of the FEB. Identification of the exact source of this leakage signal, is beyond the scope of the validation tests.

3.5.5 Production of extension cable bundles

Production of a total of 134 horizontal 1 to 1 and 23 vertical 4 to 1 extension cable bundles took place between March and June 2017. The 25000 m of coaxial cable of type RG174/U, supplied by EMOS, were delivered in reels of 200 m (figure 3-61). The cable was chosen following validation tests reported in section 3.5.2. An assembly jig,

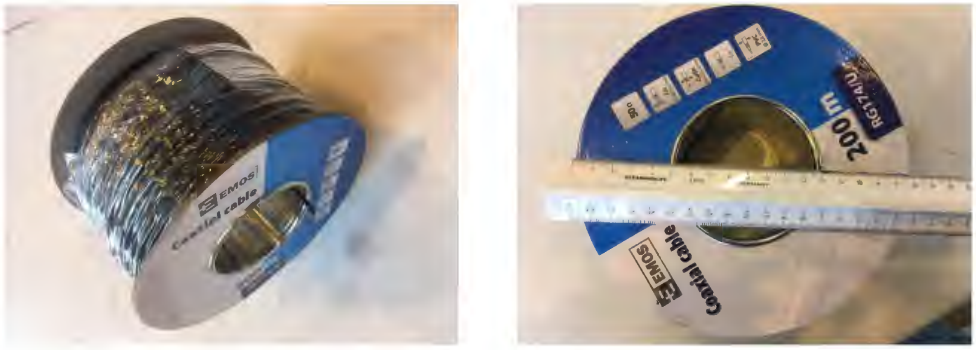

Figure 3-61: 25 km of EMOS coaxial cables is used in cable bundles.

shown in figure 3-62, was prepared to assist the production task with four coaxial cable reels, a 5 m long measuring platform, three cable holders with 4 slots and an end clip to fix and cut the cables to 5 m long. After 32 coaxial cables are cut, both ends are

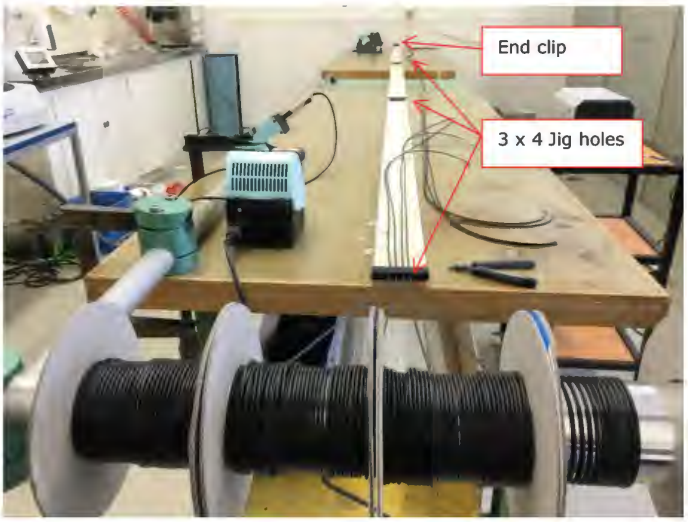

Figure 3-62: Assembly jig for extension cable bundle production.

stripped with three cuts using ST730 cable stripper machine (figure 3-63). In the next

Figure 3-63: Cable stripper ST730.

step the soldering of coaxial cables for each individual channel (0-31) to the HV-coax

PCB and the FEB-coax PCB is performed. Once all cables are soldered, two sets of clamps tighten the coaxial braids on the copper area of the boards for grounding connection and mechanical tightness (figure 3-64). The 4 wires flat cable and HV

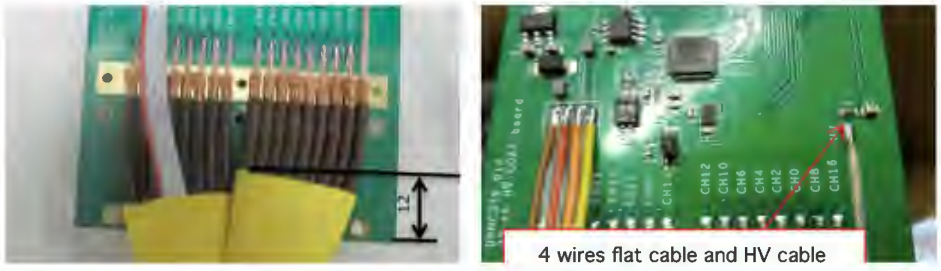

(a) Soldering of coaxial braid on the common ground copper area.

(b) Soldering of 4 wires flat cable and HV-coax cable.

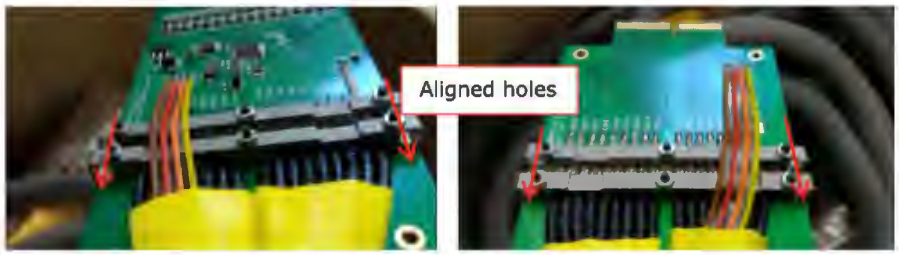

(c) Clamps tighten the coaxial braids on the copper area of the boards.

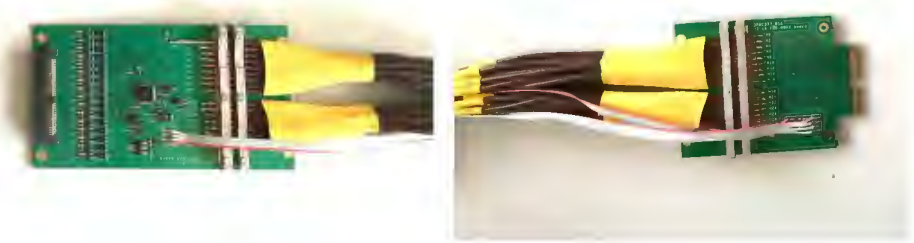

(d) HV-coax PCB.

(e) FEB-coax PCB.

Figure 3-64: Soldering stages of the cable bundle end PCBs.

carrier cable are then soldered separately to their designated areas. Heat shrinks are used to arrange the cables within the mechanical box and a grey braided cable sleeve wraps the 5m long coaxial cables for protection.

Once the soldering and fixation of the coaxial cables to the end PCBs are finished, the mechanical boxes are assembled around the PCBs to protect the sensitive components. It should be noted that the mechanical boxes on the module side had to be retrofitted because of alignment problems between the holes on the mechanical box and the clamp holes on the PCBs, which made it impossible to access the tiny screws with a long screw driver. This issue was revealed during cabling process of the detector for CERN beam test. The retrofitting is reported in section 4.2.2.

Each cable bundle is then required to be programmed for a dedicated slot number. For

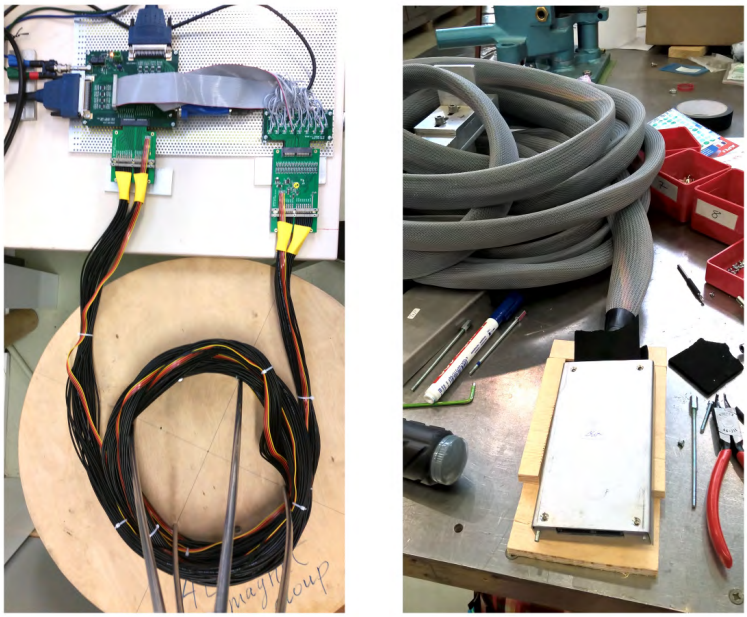

Figure 3-65: A completed cable bundle.

the 1 to 1 horizontal cables there are three configurations labeled as bottom, middle and top which reveals their relative connection position on a scintillating module as well as the FEB slots. For the 4 to 1 vertical cables in addition to the bottom, middle, top labels, which in this case reveals the FEB connection slot, there are four programmable address configurations labeled as a, b, c and d which reveals the positioning of the cable on the scintillating module.

3.5.6 Qualification test of cable bundles

A dedicated test system was developed in March 2017 for the qualification test of cable bundles. A tester board was designed and manufactured at Unige to operate together with a National Instrument DAQ unit (NI USB6363). Figure 3-66 shows the setup with two ends of a cable bundle attached to the tested board which is connected to the NI DAQ unit. A LabView program (figure 3-67) was developed to perform the qualification test which consisted of two stages, a digital test and an analogue test. In the digital test one channel at a time was enabled and then the digital output of all channels were readout to verify that only the selected channel is enabled.

In the analogue test the cable bundle micro-controller was configured to activate HV on just one channel at a time, and then the analogue output of all channels was readout. For the channel with HV, the nominal expected voltage is $\sim 2.9 \pm 0.2$ V while for other channels nominal voltage of $\sim 0 \pm 0.1$ V is expected.

All the 133 horizontal cables and the 23 vertical cables were tested. The fluctuations in

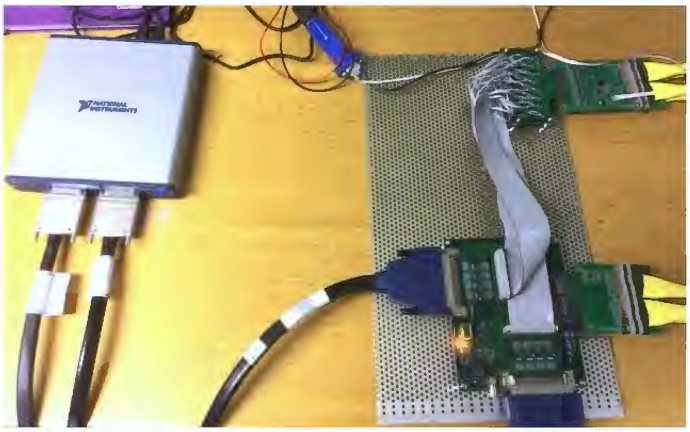

Figure 3-66: Qualification test system for cable bundles.

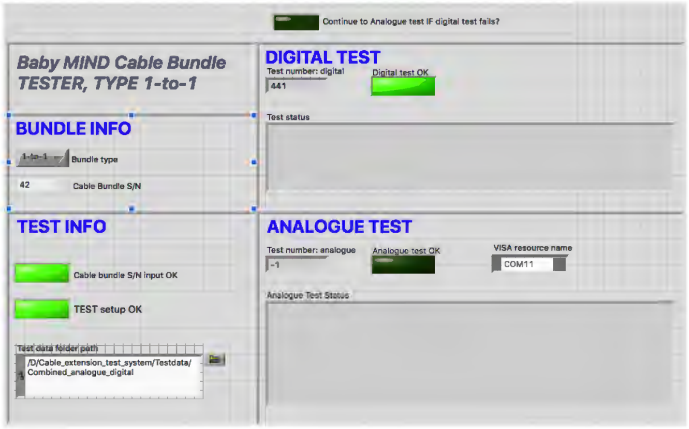

(a) Front panel of the virtual instrument (VI) program for testing of horizontal cables 1 to 1. This program calls several sub-VIs to perform specific tasks.

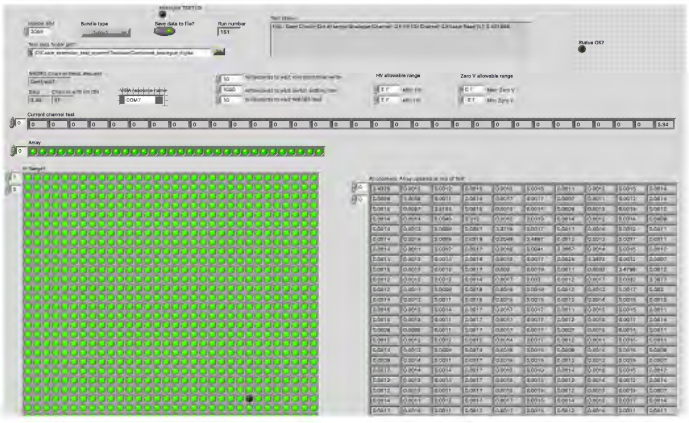

(b) Front panel of the analogue test sub-VI. In this instance channel 24 has failed due to out of range voltage value of 3.5 V.

Figure 3-67: LabView cable bundle tester program.

the analogue output values and the narrow range allowed in the program, led to high failure rate. Those cases had to be re-examined several times, and in case of hardware failure, they were sent back to the cable production station for fixing possible soldering

disconnects or short circuits. The qualified cable bundles were labeled and sent for detector cabling.

3.6 Photosensors

Hamamatsu Multi-Pixel Photon Counters (MPPC) of type S12571-025C were chosen for the readout of 3996 channels of Baby MIND detector (figure 3-68). MPPC is a type of silicon photo-multiplier (SiPM), a photon counting device using Avalanche Photo-Diodes (APD) pixels operating in Geiger mode. It has excellent photon counting capability and can detect extremely weak light at the single photon counting level.

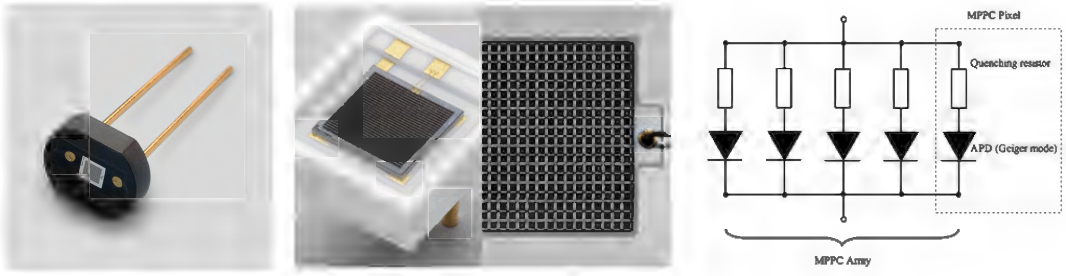

(a) SiPM (b) Close view of the sensitive area

Figure 3-68: Hamamatsu MPPC type S12571-025C

3.6.1 Operation principle

The APD has a p-n junction under a reverse bias voltage that is above its breakdown voltage, which functions as a diode. When a photon hits the silicon layer on the APD, an electron-hole pair is created via the photoelectric effect. These electrons are then accelerated by the high electric field in the depletion region of the p-n junction, causing them to collide with the atomic electrons and create new electron-hole pairs. This process would trigger an avalanche in the junction which produces a high exponential gain that can reach 10^5 to 10^6 electrons for one photon. The output current caused by Geiger discharge is a pulse waveform with a sharp rise time. The Geiger discharge is then halted by the quenching resistor which introduces a voltage drop and bring back the APD to the bias voltage, making it ready to accept new photons. This mechanism gives the pulse waveform a characteristic with a relatively slow fall time. A pulse waveform is shown in figure 3-69.

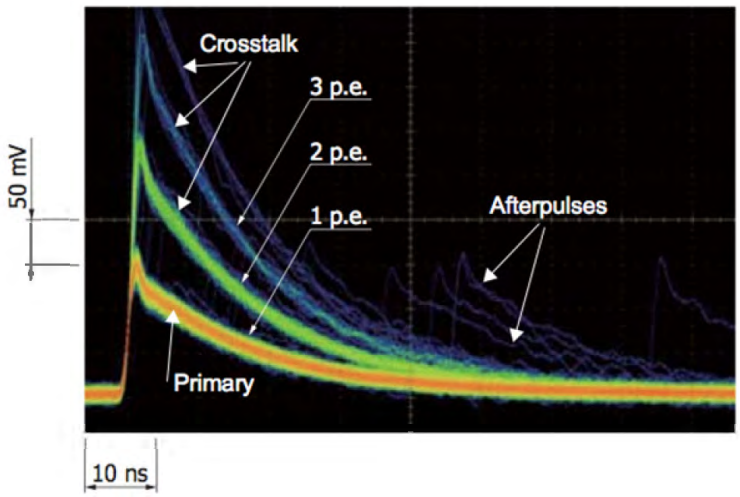

Figure 3-69: Pulse waveform (S12571-050C), using a linear amplifier (120 times) [112]

3.6.2 Device characteristics

The device that has been chosen has an active area of 1×1 mm^2 with 1600 pixels, a geometrical fill factor of 65 %, average gain of 5.15×10^5, quoted Photo Detection Efficiency (PDE) of 35 % and a peak sensitivity wavelength of 450 nm. The typical intrinsic noise level, known as dark count rate is 100 kHz. This intrinsic noise reflects the individual pixels firing randomly due to the thermal fluctuations. Compared to the previously marketed products, this device has drastically reduced afterpulses to below 10%, which is shown in figure 3-70. Another important feature of MPPCs is the level of

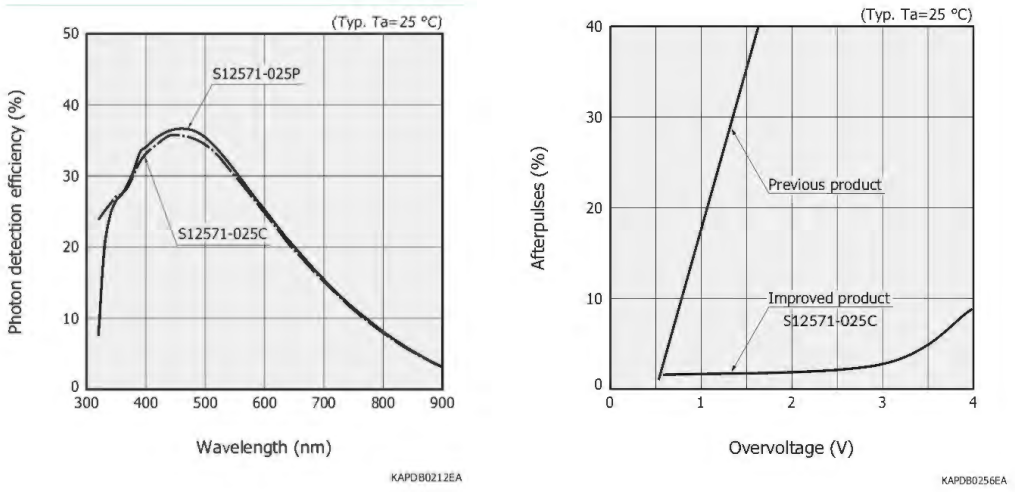

Figure 3-70: S12571-025C has a peak sensitivity wavelength at 450 nm (left) and a low level of afterpulses (right) [112].

pixel crosstalks, which reflects the probability of a pixel firing as a result of a neighbor pixel going through Geiger discharge. This device has about 22 % pixel crosstalk,

which is relatively high. A consequence of having high crosstalk probability is the characteristic fingerplot shape for the dark count noise data acquisition, where each peak represents the number of pixels discharged simultaneously. While this feature

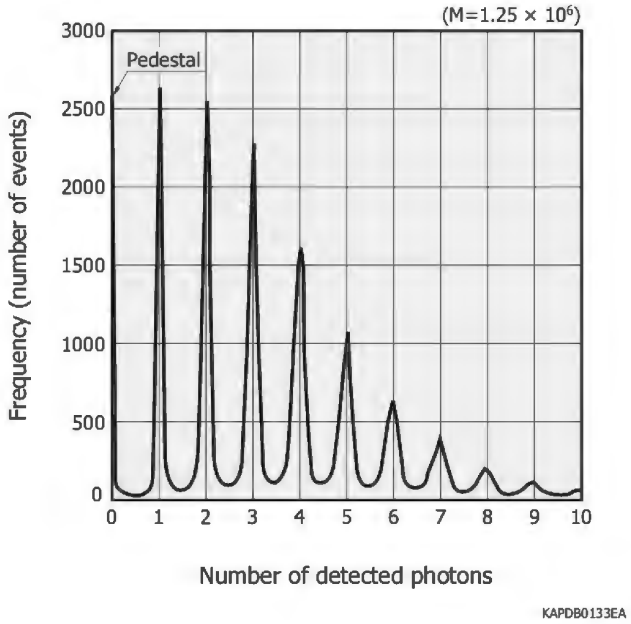

Figure 3-71: MPPC dark count distribution, referred to as fingerplot.

might be unfavorable for applications with low light yield signals, it can provide an easy method for amplitude calibration of the incoming signal in terms of the number of photoelectrons.

Some MPPC characteristics vary with the operating voltage. In general, increasing

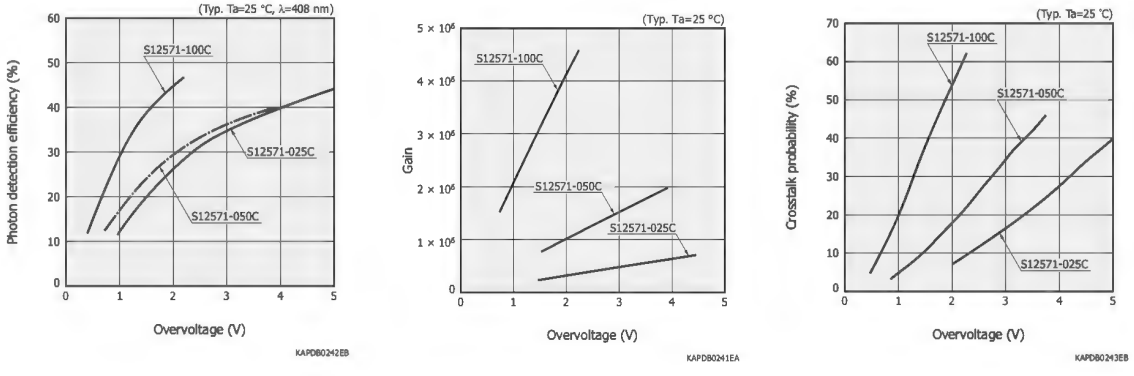

Figure 3-72: The PDE, gain and crosstalk dependence on overvoltage [112].

the operating voltage improves the photon detection efficiency and the time resolution, at the same time it increases the dark count rate and the crosstalk probability, so an optimum operating voltage must be selected to match the application. Table 3.2

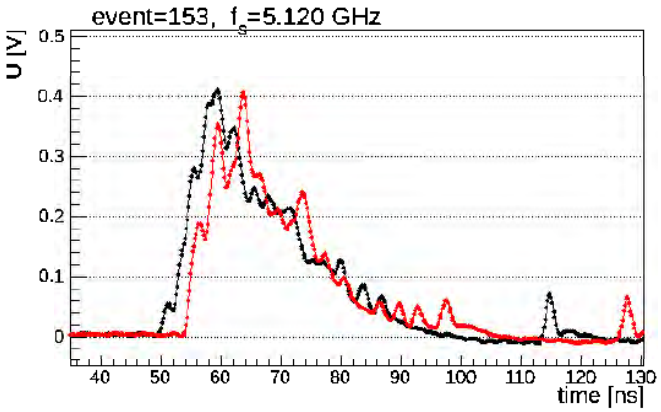

Figure 3-73: Waveforms registered by two MPPCs from a comics ray event in a plastic scintillating bar with a WLS fiber, sampled by a DRS4 waveform digitizer.

summarizes the parameters of MPPC type S12571-025C, measured at the operating voltage and at 25 °C.

Table 3.2: MPPC S12571-025C characteristics [112].

Parameter	**Symbol**	**S12571-025C**	**Unit**
Effective photosensitive area	-	1×1	mm^2
Pixel pitch	-	25	μm
Number of pixels	-	1600	-
Spectral response range	λ	320 to 900	nm
Peak sensitivity	λ_p	450	nm
Photon detection efficiency	PDE	35	%
Breakdown voltage	V_{Br}	65 ± 10	V
Operating voltage	V_{op}	$V_{\mathrm{Br}} + 3.5$	V
Dark count	-	80	kcps
Temperature coefficient of operating voltage	-	60	mV/°C
Gain	M	5×10^5	-
Temperature coefficient of gain	-	8.2×10^3	/°C

The response of an MPPC to a physical signal, which is generated by the passage of a particle in plastic scintillator, and traveled through a WLS fiber before arriving at the MPPC, can be very diverse. Various delay factors smear the time distribution of the arrival of photons to the MPPC, resulting a waveform that is a superposition of multiple pixel waveforms with displaced lead times. An example is shown in figure 3-73.

3.6.3 HV for MPPCs

The MPPCs needed for instrumentation of the Baby MIND 3996 channels were procured by Hamamatsu in two batches of 3000 in 2016 and 1400 in 2017. From which a subset of 384 MPPCs were used for instrumenting of AIDA modules for the 2016

beam test, discussed in section 3.7.2. Following the requests and arrangements made, the MPPCs were delivered, in pre-sorted groups according to their operating voltages. As is shown in figure 3-74, the spread in operating voltages is well contained, with an RMS of 0.14 V for a mean of 67.49 V.

The HV for the MPPCs of each individual channel is delivered through the FEB and cable bundles. Each FEB provides a common high voltage of 69.7 V, applied to all cathodes. Each channel MPPC operating voltage is adjustable independently, from 69.7 V down to 65.2 V, with the CITIROC embedded 8-bit (4.5 V) input DAC connected to the anode. Homogeneity of operating voltages for the 32 MPPCs connected to a given CITIROC was ensured by sorting MPPCs in batches of 32 with operating voltages within ± 100 mV from the batch average.

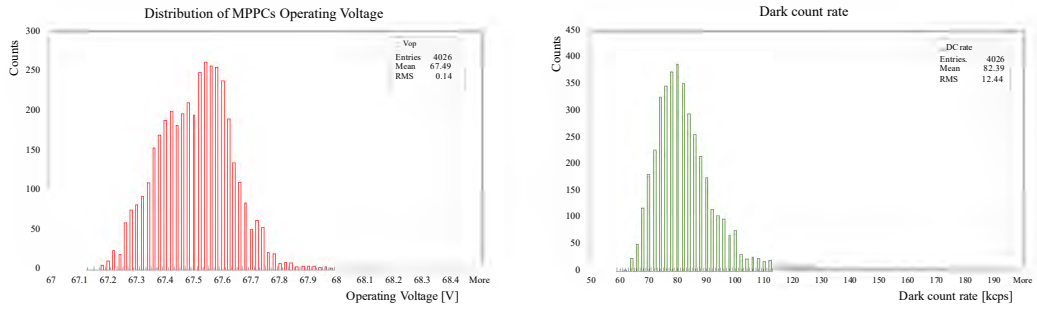

Figure 3-74: The distribution of operational voltage (left) and dark count rate (right) of Baby MIND MPPCs.

3.7 Electronics

A new readout scheme has been developed for the readout of scintillating bars of the Baby MIND detector modules, with the criteria to record hits with high efficiency in neutrino experiment environment where the particle rates are orders of magnitude lower than the LHC environment [113] [114]. Given rapid progress in the development of MPPCs with high efficiency and low cost, it was decided to select a commercially available photosensor and focus on the development of customized readout electronics. As was introduced in section, 3.6, Hamamatsu MPPCs were chosen for the readout of the Baby MIND detector.

3.7.1 Readout architecture

The Baby MIND electronics readout scheme includes several boards. At the heart of the system is the Front-End board (FEB) developed at Unige. Daisy chaining and

synchronization functions are carried out by two ancillary boards, the Backplane and the master clock board (MCB), developed by Unige and INRNE. A diagram of the overall readout architecture is shown in figure 3-75.

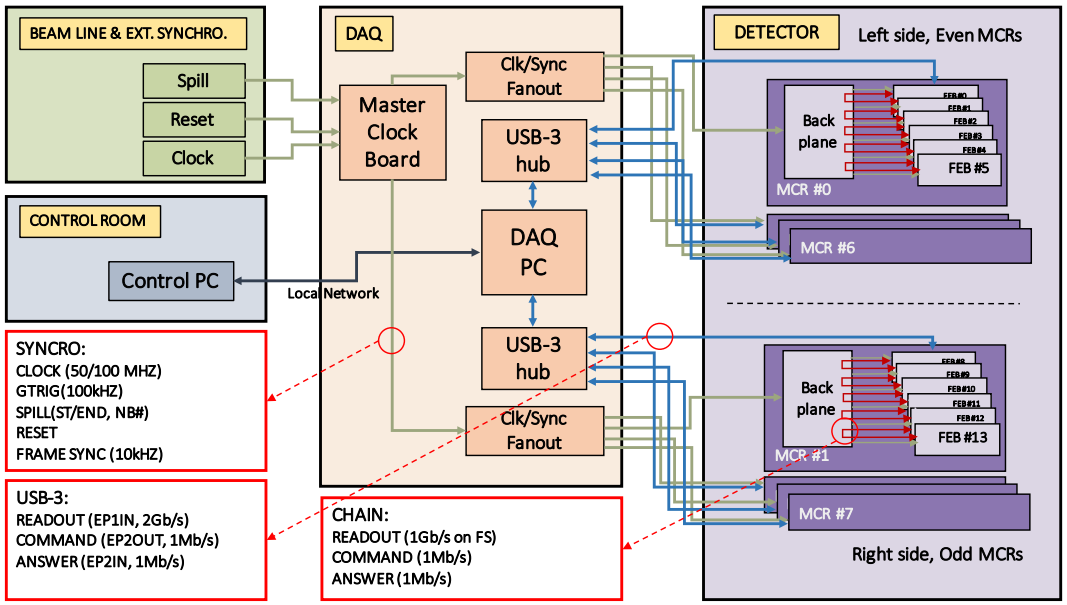

Figure 3-75: Overall readout architecture.

3.7.2 Front-End board

The preliminary studies about the choice of the ASIC (Application Specified Integrated Circuit) to be used in the electronics started in 2014, much earlier than the design of the first version of the FEB. After comparative studies between EASIROC and CITIROC ASICs, the later was selected as the baseline of the new electronics and a series of characterization studies were performed with a CITIROC evaluation board. It was

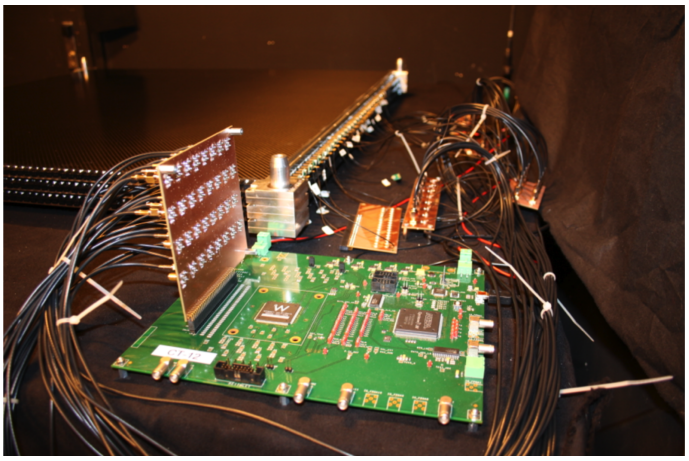

Figure 3-76: CITIROC characterization studies with the CITIROC evaluation board.

demonstrated that CITIROC could offer all the functionalities of the EASIROC chip plus some additional features, that were particularly interesting for the readout of MPPCs in the T2K environment:

- Peak detection function over a tunable hold period, for the analogue amplitude output.
- Additional time triggering digital outputs, essentially making the readout dead time free.
- Lower starting values for the slow shaper time constant (12.5 ns).
- Tunable pre-amplifier gains (4-bits), which provides higher gain values.

FEB-v1

The first version of the Baby MIND Front-End board, FEB-v1 was developed in 2016 based on a set of requirements, and feedback from EASIROC and CITIROC characterization studies. FEB-v1 was tested thoroughly in the summer 2016 beam test at

Figure 3-77: First version of Baby MIND Front-End board, FEB-v1.

CERN. It was also used for the tests of scintillating bars and the extension cable bundle validation during the detector construction phase, described in previous sections.

Electronics beam test at CERN 2016

The 2016 beam test at the T9 beamline at CERN, was dedicated to electronics performance. A detailed description of the T9 beamline is presented in section 4.1. The test setup consisted of 4 FEB-v1 connected to 384 channels of the prototype AIDA

scintillating modules [115]. The AIDA modules have a dimension of 90×90 cm^2, consisting of two layers of horizontal and vertical plastic scintillating bars. Each layer has 84 bars with a width of 1 cm and thickness of 0.7 cm. Only 16 bars in the middle of each side of 6 modules were instrumented, in order to cover the beam center at T9. Figure 3-78 shows the setup of the beam test.

Two different triggering schemes were tested during the 2016 beam test. One utilizes

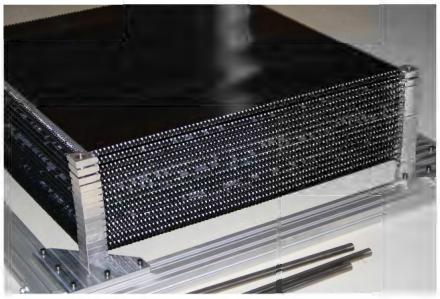

(a) AIDA scintillating modules.

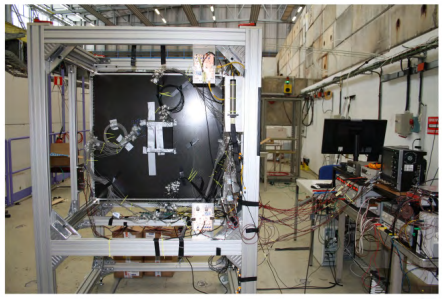

(b) Test setup at the T9 beamline.

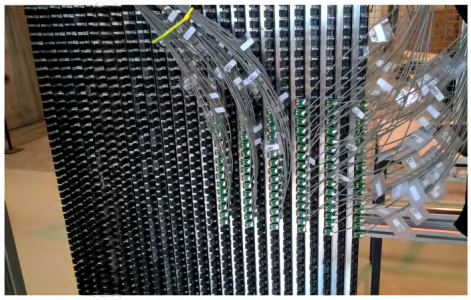

(c) 16 bars from 6 modules were instrumented.

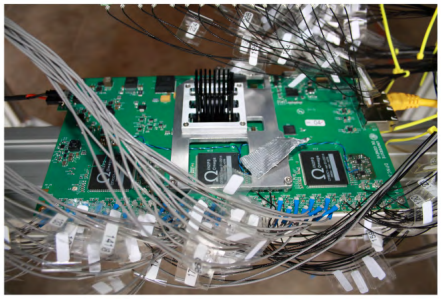

(d) FEB-v1 with 96 channels, connected with micro-coaxial cables.

Figure 3-78: Electronics beam test at CERN, 2016

the beamline spill arrival signal and a pulse generator to send an external trigger signal to FEBs in order to mark the start of acquisition and also to synchronize the 4 FEBs. The other scheme uses two additional scintillating slabs, in front and back of the detector modules, to generate a coincidence signal for the passage of particles by a trigger board shown in figure 3-79. There were 4 input channels connected by logic gates and 4 RJ45 outputs to send the trigger signal to the 4 FEBs for a synchronized start of the acquisition.

During the beamtest, data with different beam settings was acquired and basic response such as the signal amplitude for minimum ionizing particles (MIP) were demonstrated (figure 3-80). Different electronics parameters were scanned in order to understand their impact on data quality. All channels of the 4 FEBs were calibrated by acquiring dark count data, and extracting MPPC gain and pedestal values shown in figure 3-81. At this stage some basic tools were developed to extract hit informa-

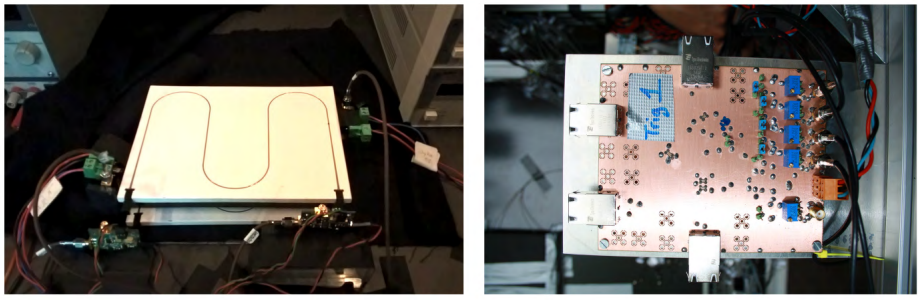

(a) Scintillating slab (b) Trigger board

Figure 3-79: Triggering scheme with additional scintillating slabs.

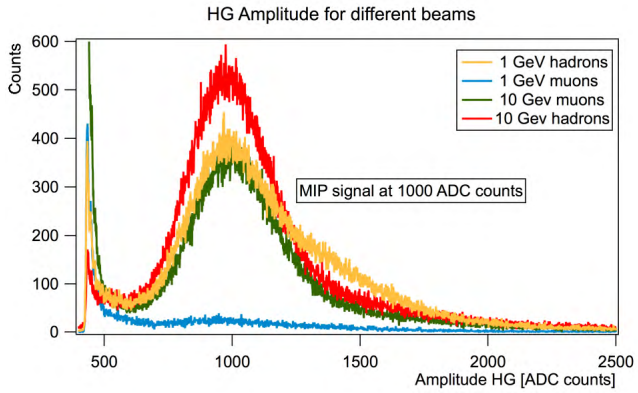

Figure 3-80: HG amplitude distribution for runs with different beam settings.

tion from the binary data and verify the synchronization of FEBs by producing 2D beam profiles from combining data of different FEBs and requiring coincidence signals. Figure 3-82 shows the beam profiles recorded by the first, third and sixth modules. The beam profile becomes wider as it penetrates through the detector due to multiple scattering.

FEB-v2

Based on the experience gained during the 2016 tests and identification of the design shortcomings, a new version of the Front-End board, FEB-v2 was developed. The FEB-v2 integrates the layout changes dictated by the new connectivity scheme and has additional features for daisy chaining and synchronization of multiple boards. It is designed to fit into a slot in a mini crate as shown in figure 3-84, where it is connected to a back plane from the rear side and is chained to the next FEB. The first series of FEB-v2 were produced in March 2017, and after series of functionality tests, they were made available just in time for the Baby MIND beam test at CERN in May 2017.

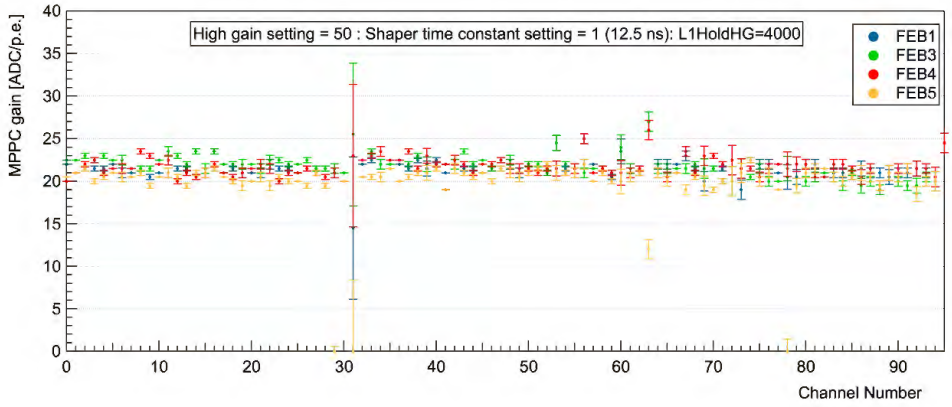

(a) MPPC gain (ADC/p.e.)

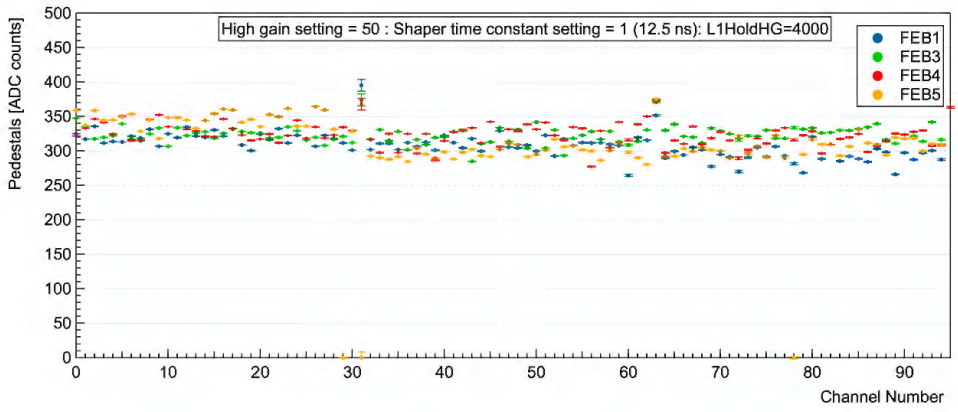

(b) Pedestal location

Figure 3-81: Calibration results of all channels.

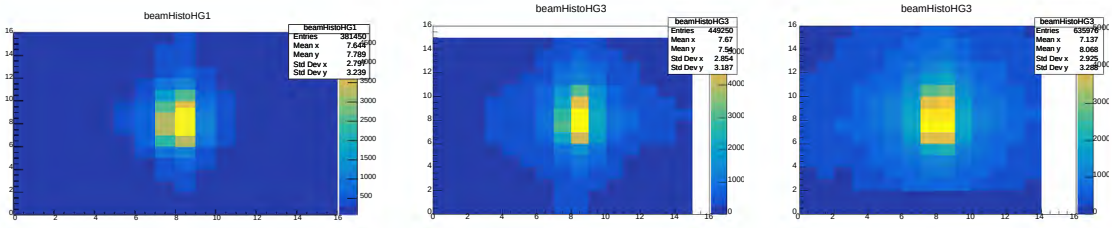

(a) Module 1. (b) Module 3. (c) Module 6.

Figure 3-82: Beam profile in the first, third and sixth AIDA modules.

The FEB-v2 electronics architecture is shown in figure 3-85. The main elements include:

- 3 CITIROC ASICs, each reading out 32 channels of a cable bundle connected to the FEB.
- A 12 bit, 8-channels ADC (analogue-digital converter) for sampling the high gain (HG) and low gain (LG) analogue outputs of the 3 ASICs.

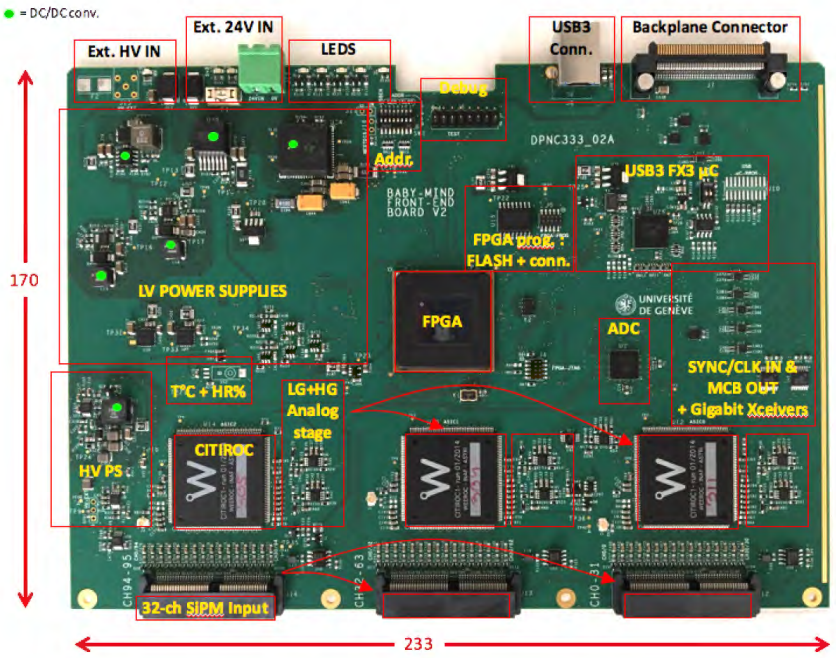

Figure 3-83: Second version of the Baby MIND Front-End board, FEB-v2.

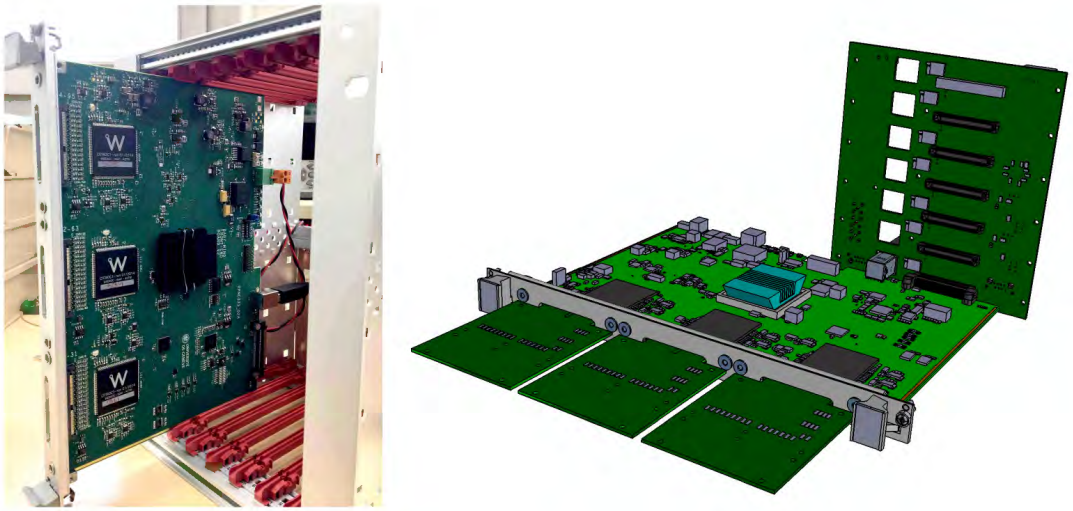

(a) (b)

Figure 3-84: FEB-v2 is designed to fit into a mini crate (left) and connect to a back plane and cable bundles (right).

- An FPGA Altera Aria V to control and manage the timing and data flow from the CITIROCs and the ADC.
- A USB micro-controller for transmission of data to a DAQ system.
- The clock and SYNC receivers and the gigabit transceiver and the rear connector for the FEB chaining through the back plane.

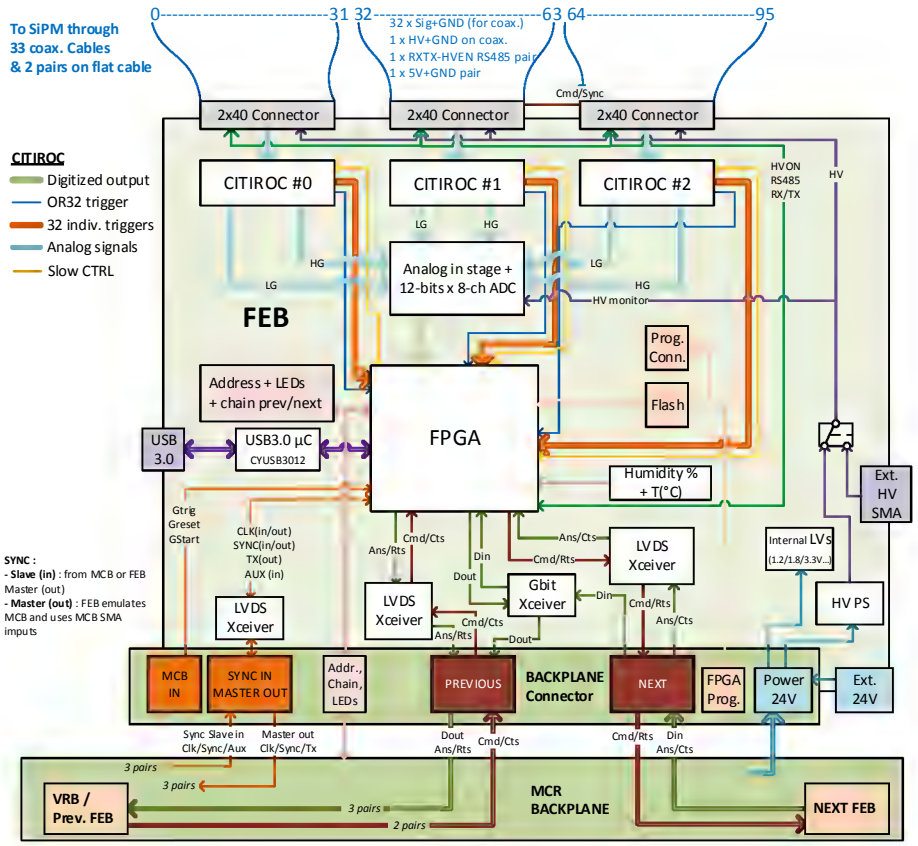

Figure 12: FEB bloc diagram with VME backplane connectivity

Figure 3-85: Front-End board hardware architecture.

- Some housekeeping sensors (temperature, humidity) directly connected to the FPGA.
- DC/DC converters for internal low voltage usage and high voltage for MPPCs.
- LEDs with ON/OFF/blinking stages, showing the state of data taking.

3.7.3 CITIROC ASIC

EDMS xxxxxx v.2.5

The CITIROC chip is a 32-channel, self-triggering, fully analogue ASIC, suitable for read-out of MPPC devices [116]. Figure 3-86 shows a block diagram of the CITIROC chip.

For each channel, there are two analogue signal paths, high gain (HG) and low (LG), each composed of a variable gain pre-amplifier followed by a slow shaper with a tunable time constant for noise reduction. Upon arrival of a trigger signal from the trigger line, a hold time window is initiated on the analogue signal paths of all channels of the ASIC, during which a peak detector function samples and the highest amplitude for a given channel. In the scenario when several hits occur on the same channel, during a hold

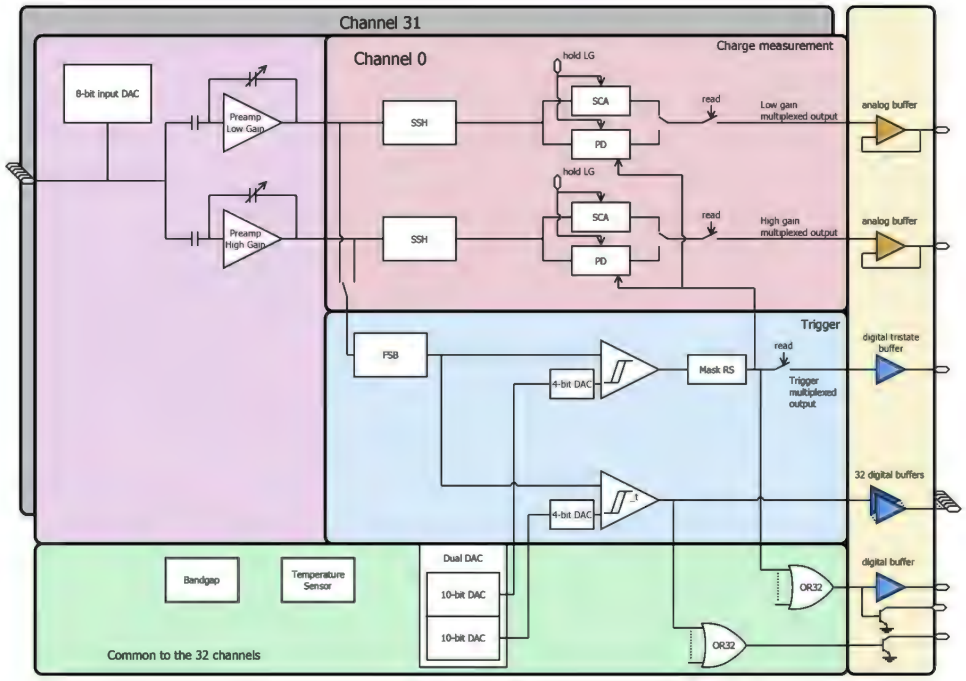

Figure 3-86: CITIROC chip block diagram

time window, the output of the analogue amplitude sampling will corresponds to the hit with the highest amplitude, regardless of the order of occurrence. At the end of the hold time window, the signals of all 32 channels are multiplexed on the CITIROC and pushed out on one single output line (one HG and one LG) towards an external ADC (Analogue-digital converter) unit.

For the timing measurements, a trigger line is extracted from either the HG or the LG pre-amplifiers outputs. It is composed of a fast shaper with a 15 ns time constant, followed by two discriminators, one provides the trigger for charge readout, with a programmable mask to block unwanted channels, and the other output is sampled at 400 MHz by the FPGA timing block. The discriminators thresholds can be set by two internal 10-bit DACs, common to the 32 channels, with fine tuning of individual channel threshold via independent 4-bit DACs.

The main configurable variables of the CITIROC ASIC are shown in table 3.3.

3.7.4 FPGA architecture

The main FPGA firmware functional blocks are organized according to three distinct clock domains running at 400 MHz, 100 MHz and 50 MHz (Levels L0, L1, L2). An overview of the FPGA architecture is shown in figure 3-87. The main FPGA blocks are summarized below:

Table 3.3: Main tunable parameters of the CITIROC ASIC

Parameter	domain	bits
HG and LG slow shaper time constants	Global	3 bits
Trigger and time readout discriminator values	Global	10 bits
HG and LG pre-amplifier gain settings	Individual channel	6 bits
HV input DAC value	Individual channel	8 bits
HV enable	Individual channel	1 bit
Trigger pre-amplifier enable	Individual channel	1 bit
Trigger line and time readout discriminator fine tuning	Individual channel	4 bits
Discriminator mask enable	Individual channel	1 bit

7.3.4 FPGA firmware overview

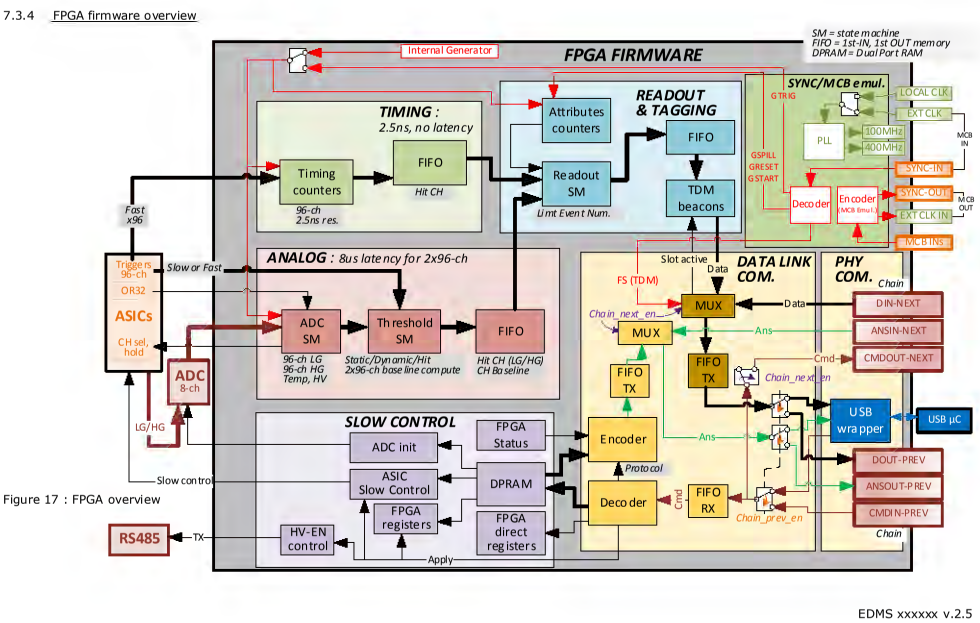

Figure 17 : FPGA overview

Figure 3-87: FPGA firmware overview.

- Timing block: Each of the individual ASICs channels fast shaper trigger output for time measurement are sampled directly on both rising and falling edges by the FPGA with a 2.5 ns counter resolution within a 10 μs Global Trigger (GTRIG) window. The Time over Threshold (ToT), calculated from the rising and falling edges of the signals, provides an additional dead-time free measurement of amplitude. The GTRIG, which is an internal clock signal produced to manage various tasks performed by the FPGA, can be generated upon arrival of an external global trigger decoded from the SYNC signal used for synchronization of multiple boards or by a continuous internal time frame generator. The hit time information is then pushed into the level zero (L0) FIFO (first-in first-out). In order to associate a hit time information to the GTRIG time stamp in which it occurred, the two least significant bits of the GTRIG counter are added to the hit time information as the hit-tag.

- Analogue Block: An ADC state machine manages the analogue output from the HG and LG signal paths of the 3 ASICs. The digitization of the multiplexed analogue outputs require 6 independent ADC channels. Due to channel to channel multiplexer commutation time, the sampling duration will introduce a 9.12 μs dead-time for the analogue amplitude readout, illustrated in figure 3-88. The ADC output is directed to a threshold state machine, in order to process the individual channel analogue hit amplitude and compare it to the FPGA L1-threshold before pushing the amplitude information to the L1-FIFO, together with a 2-bit hit-tag as explained before.

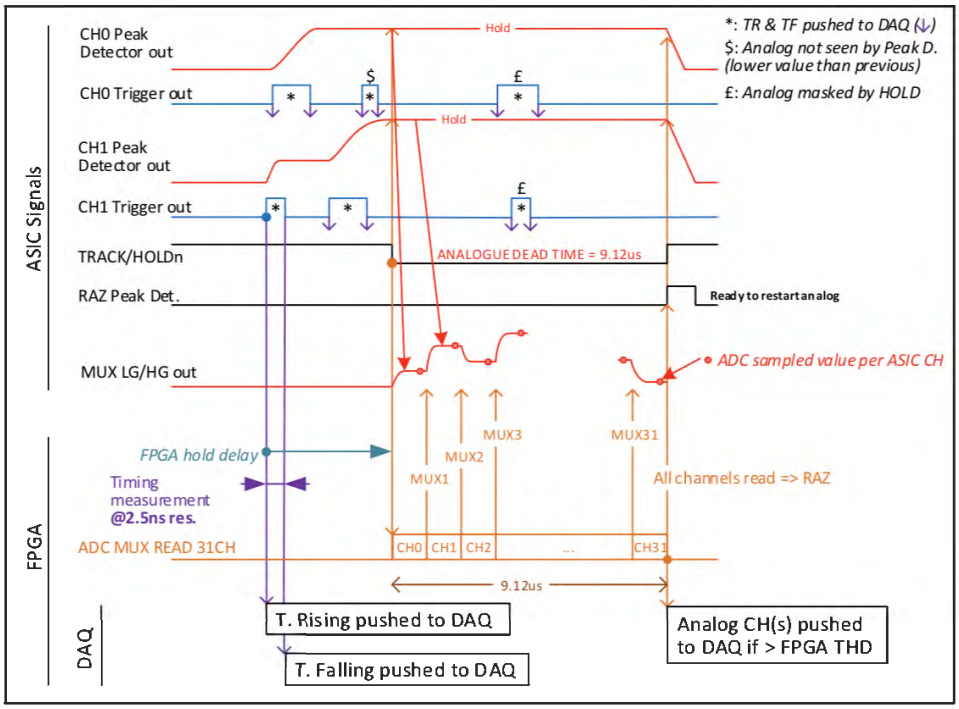

Figure 3-88: Illustration of FPGA signal sampling of CITIROC individual trigger outputs and the analogue signal hold scheme and peak detector output processing.

- Readout and Tagging block: A readout state machine, located within the 100 MHz clock domain, has the duty of building the readout frame by pulling out data from L0-FIFO and L1-FIFO, and receiving the attribute counters (spill tag, GTRIG tag and time counters), and pushing the formatted data into L2-FIFO. Since the L0-FiFO is located within the 400 MHz clock domain, the hit time info can be pushed in, 4 times faster than it can be pulled out. This creates a potential bottleneck in environments with high data rates. After observation of data loss due to L0-FIFO full, during CERN beam test, the depth of L0-FIFO was increased from 8 to 64 for groups of 8 channels in the end of 2018.

- Data Link block: Several functions related to reading the commands and sending data through the RJ45 link or the USB interface are carried out by this block, which is located within the 50 MHz clock domain. The transfer mechanism can operate in two modes, either USB mode or Gigabit mode, depending on the location of the FEB in the chain. A multiplexer is used to check correct behavior of data sent or received on a TDM time slot referenced to the frame synchronization (F-SYNC) signal. Each FEB board is accessed by the protocol through its single board ID built with the mini crate address (3 most significant bits) and the FEB slot (3 least significant bits). The commands are decoded and actions are taken accordingly. Examples are data readout commands, reading and writing of configuration settings for ASICs and FPGA, reading status registers and board global commands.

3.7.5 Signal sampling with a hold mask scheme

The T2K beam spill is composed of 8 bunches of roughly 80 ns each in width separated by 580 ns. A spill duration is therefore $\sim$5 μs, repeated every 2.48 s. One obvious requirement for the electronics is to be capable of recording all neutrino-related events within a T2K spill. Given the low event rate, the probability that the same channel records multiple neutrino-related hits within the same spill is estimated to be $< 0.1\%$, based on event rates in INGRID. For the operation in T2K beamline, the default acquisition window is set to 60 μs, during which the analogue output stage can undergo more than one readout cycle (hold window for peak detection + dead-time due to ADC read). In order to ensure that the neutrino related hit amplitude information gets recorded, a hold time window of 10 μs is chosen to cover the T2K spill and a hold mask scheme is implemented, which disables the analogue data sampling for a period as long as one full analogue readout cycle, see figure 3-89. At the end of the hold mask, all FEBs are ready for a new analogue readout cycle, and operate in self-triggering mode thereafter.

3.7.6 Daisy chaining

The architecture of Baby MIND electronics readout is based on 8 chains, each with up to 6 FEBs. In general the maximum number of FEBs that can be chained together is determined by the application data rate and the USB capability for data transfer.
The central hardware piece that provides the links for daisy chaining is the back plane

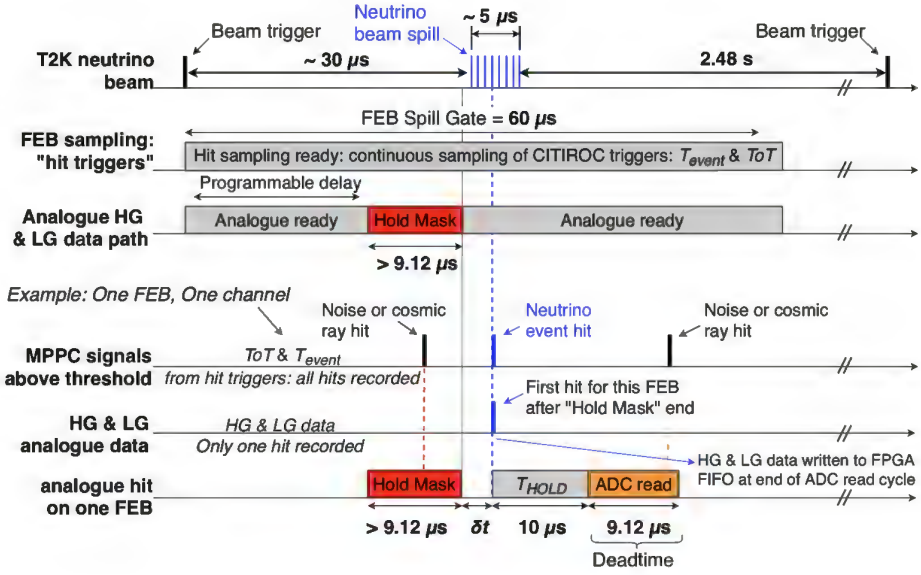

Figure 3-89: Signal sampling at T2K beamline with a 60 μs acquisition window and a hold mask scheme.

PCB, which is mounted at the rear side of the mini crate (see figure 3-90). When an FEB is inserted into a slot in the mini crate, it connects to the back plane via a single connector. The back plane receives signals, such as the 100 MHz experiment clock,

Figure 3-90: The 6 FEBs in a mini crate are daisy chained together via the back plane.

16-bit beam spill number, beam trigger signal and TDM 10 kHz frame synchronization (F-SYNC), from the master clock board via an RJ45 cable of type SFTP CAT6, and transmits these to each FEB in the chain.

The chain is able to carry the protocol commands from the PC to all the FEBs. The FPGA decodes the command according to its address and processes it if an answer is required. Command answers are sent back to the DAQ PC through the entire chain

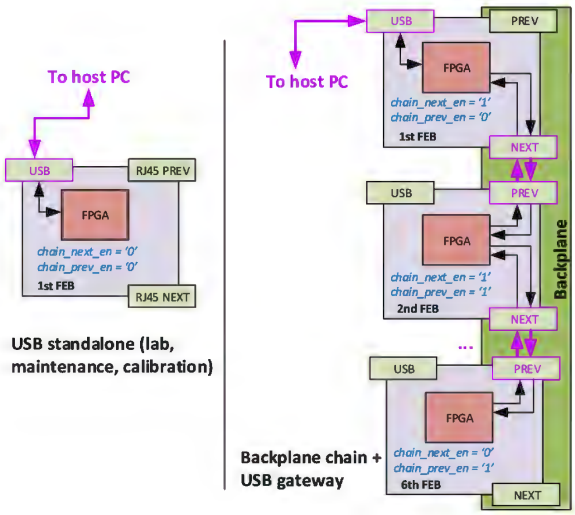

Figure 3-91: FEBs chain via the back plane and the USB gateway.

from the 1st FEB via USB to the PC. Each intermediate FEB acts just as a repeater with a concurrent access protection mechanism. For the readout data from all the FEBs in the chain, the Time Division Multiplexing (TDM) mechanism is used. In this

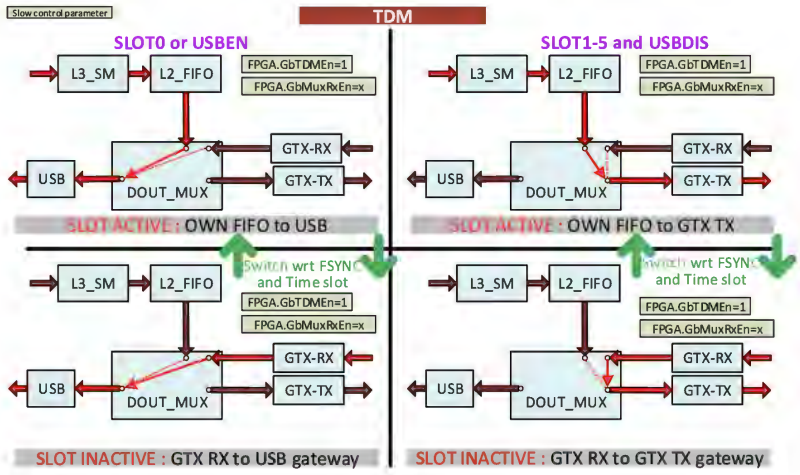

Figure 3-92: Data flow overview in the TDM mode for cases where the USB gateway is enabled or disabled and the slot is active or inactive according to the F-SYNC time slot.

mode, each FEB in the chain is allocated a dedicated time slot for data throughput, which is identified by a decoded F-SYNC signal received by each FEB. Figure 3-92 shows the state of the TDM mode multiplexer in different scenarios.

3.7.7 Synchronization

The master clock board (MCB) is used to drive all the FEBs of the Baby MIND detector (figure 3-93). The MCB provides the common detector clock signal (CLK)

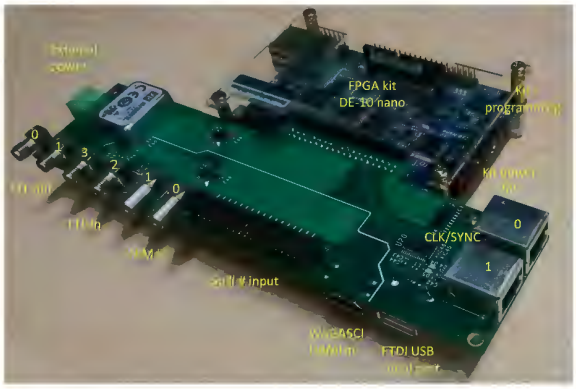

Figure 3-93: Master clock board (MCB) components explained.

and combines user signals (reset, start readout), synchronization signals (GTRIG, F-SYNC for inter boards communication) and input signals from the accelerator beam line including a spill number and a beam trigger issued 30 μs before the arrival of the T2K spill, into a single digital synchronization signal (SYNC). The schematics of the synchronization scheme is shown in figure 3-94. In the absence of input signals

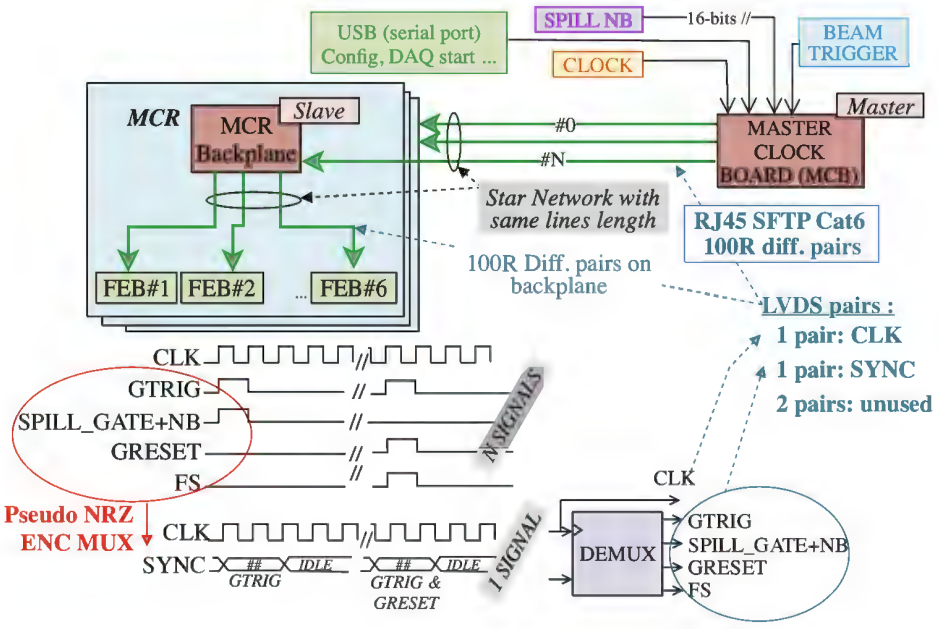

Figure 3-94: The synchronization scheme.

from the beam line, the spill number is incremented within the FEB with an internal counter.

Both SYNC and CLK signals are transmitted from the MCB to the mini crates and distributed locally to the FEBs within one mini crate via the back plane. Two fanout boards are introduced to distribute the signals to 8 mini crates. The FEB to FEB CLK (SYNC) delay difference is measured to to be 50 ps (70 ps) [117]. The internal 400 MHz clock on each FEB is synchronized to the common detector clock (CLK). The GTRIG, which is a local to FEB reference clock, issues a time stamp every 10 μs, and is used for the post-processing assembly of all the data.
The MCB is programmed to provides several acquisition modes with different spill gates, listed in table 3.4.

Table 3.4: Different acquisition modes available by the MCB.

Mode name	**width**	**Input signal**	**Description**
Beam-DAQ	60 μs acq.	NIM-0	Beam mode synchronized with beam trigger.
Cosmic-DAQ	20 ms gap + 1.966 s acq.	NIM-0	Cosmic mode synchronized with beam trigger.
Beam-Cosmic-DAQ	60 μs acq. + 20 ms gap + 1.966 s acq.	NIM-0	Combined beam mode and cosmic mode synchronized with beam trigger.
WAGASCI-DAQ	60 μs acq. + 6 x 5 ms acq.	HDMI	WAGASCI acquisition mode, delivered to MCB via an HDMI input.
Ext-IN-NIM1	Tunable width	NIM-1	External acquisition window, generated by a pulse generator.

3.7.8 Readout data

Readout is asynchronous and based on a data push mode. Two data transfer mechanisms operate for the DAQ Data flow:

- FEB to DAQ PC transfer via USB-3.0 at 3.2 Gbit/s max., but often limited to the DAQ hard disk capability ($\sim$ 2 Gbit/s on BabyMind).
- FEB to FEB transfer via MCR backplane at 1 Gbit/s max..

Several readout modes are possible. The standalone mode allocates the full USB bandwidth to the USB-connected FEB. For a chain of mini crate FEBs (6 FEBs maximum per back plane), the Time-division Multiplexing (TDM) mode is used whereby every FEB automatically sends its data through the back plane to the first FEB of the chain which is connected to USB. The USB bandwidth is shared by six FEBs and every FEB in the chain communicates on a dedicated time slot synchronized by the MCB Frame Synchronisation (FS) signal operating at 10 kHz.

The DAQ protocol is based on a modulo 32-bit words due to the USB micro-controller 32-bit interface connected to the FPGA. Every 32-bit word is built with the 4 most

Figure 3-95: Data readout protocol.

significant bits reserved for the word ID which defines the content for the remaining 28 bits as shown in figure 3-95.

Raw binary data transfer rates average 500 MB per day of running at T2K for the full Baby MIND detector (all 8 MCRs).

Chapter 4

BabyMIND Beam Test at CERN

In order to fully characterize the Baby MIND detector, a beam request for 2017 on the T9 beam line in the East Area was submitted to the PS/SPS run coordinators at CERN. The schedule of the beam line changed multiple times between January and May 2017, as did the construction schedule of Baby MIND. Finally, we were allocated one week in the beginning of May and 5 weeks in June and July 2017, which was extended for one week in parasitic mode with another group. This chapter covers the activities associated to the beam test and the demonstration of detector functionality. The construction schedule of the detector systems was extremely tight. Most of the Baby MIND hardware systems went through the phases of design, prototyping and construction in less than one year time span, leading to a compressed construction phase over the course of the last few months before the beginning of the beam test. Table 4.1 presents a comparison of the status of Baby MIND systems between July

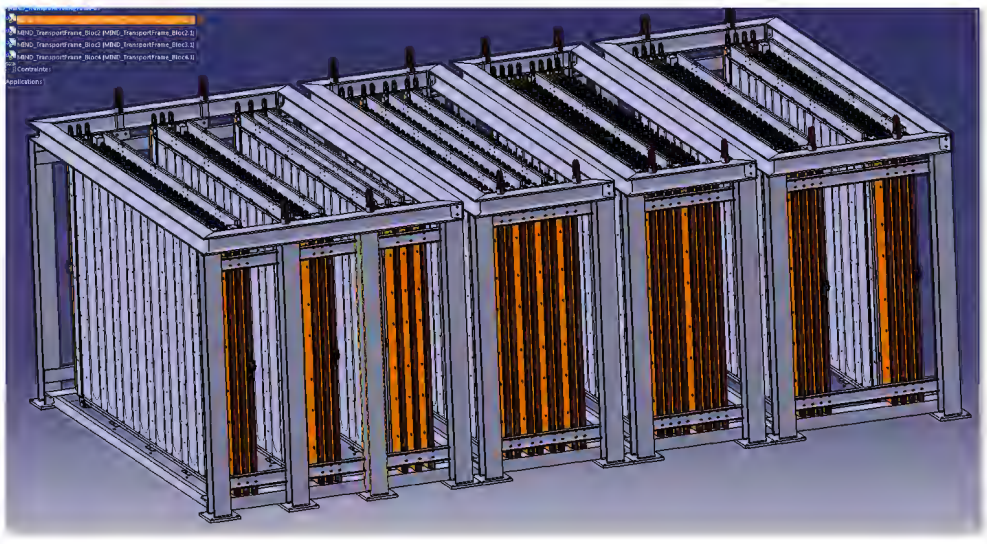

Figure 4-1: Schematics of the Baby MIND detector layout for the beam test at CERN.

2016 and July 2017.

Table 4.1: Baby MIND systems construction status in July 2016 and in July 2017.

	Design		**Prototyping**		**Production**	
	07/2016	07/2017	07/2016	07/2017	07/2016	07/2017
Magnet modules						
Standard steel plates	✓	N/A	✓	N/A	N/A	N/A
ARMCO plate machining	×	✓	×	✓	×	✓
Coil engineering	✓	✓	✓	✓	×	✓
Magnet module assembly	✓	✓	✓	✓	×	✓
Scintillating modules						
Scintillating bars	✓	✓	✓	✓	✓	✓
Scintillating module mechanics	×	✓	×	✓	×	✓
Scintillating module assembly	×	✓	×	✓	×	✓
Cable bundles						
Cable selection	×	✓	×	✓	×	✓
HV Coax PCB	×	✓	×	✓	×	✓
FEB Coax PCB	×	✓	×	✓	×	✓
Cable bundle assembly	×	✓	×	✓	×	✓
Electronics modules						
FEB-v1	✓	✓	✓	✓	×	✓
FEB-v2	×	✓	×	✓	×	✓
Back plane	×	✓	×	✓	×	✓
Master Clock Board	×	✓	×	×	×	×
Mini crate mechanics	×	✓	×	✓	×	✓
Mechanics						
Support frame #1	×	✓	×	✓	×	✓
Support frame #2	×	✓	×	✓	×	✓
Support frame #3	×	✓	×	✓	×	✓
Support frame #4	×	✓	×	✓	×	✓

4.1 T9 beam line

The T9 beam line is one of the four beam lines available for beam tests in the East area at CERN, an experimental hall receiving 24 GeV/c protons from the Proton Synchrotron (PS). A plan of the experimental hall is shown in figure 4-2.

4.1.1 Target and beam optics

The primary beam, coming from the PS accelerator impinges on a target before it enters the secondary T9 beam line area. There are different target heads available. The core of the target is in all cases a light material (aluminum or beryllium). In some targets a tungsten plate enhances the electron content of the beam. The target

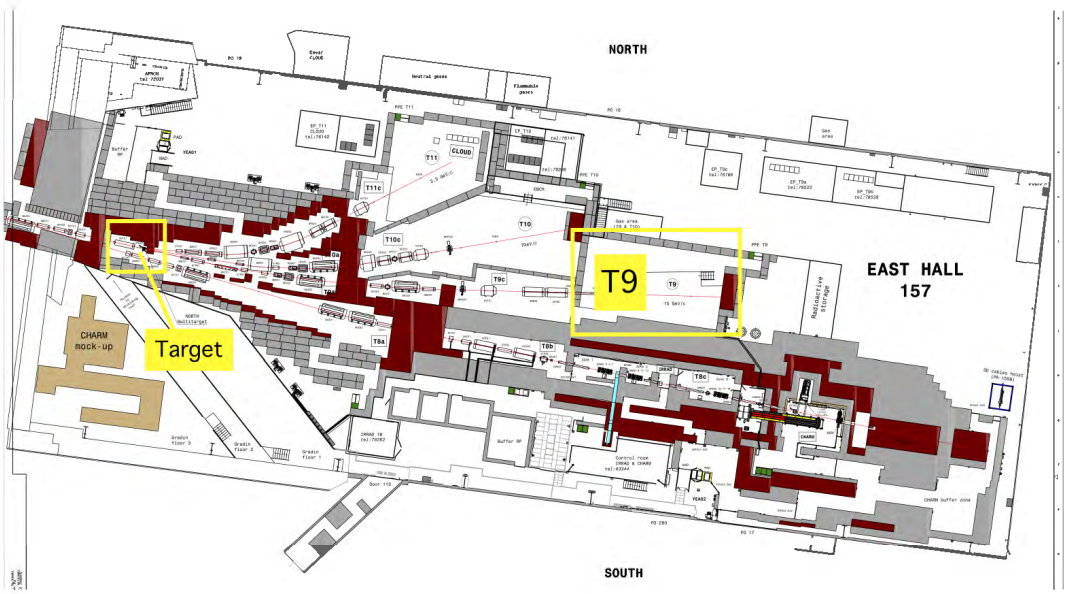

Figure 4-2: East area experimental hall and T9 beam line at CERN.

used for the Baby MIND beam test was a 200 mm long aluminum rod with 10 mm diameter. An overview of the T9 beam line optics is shown in figure 4-3. The beam

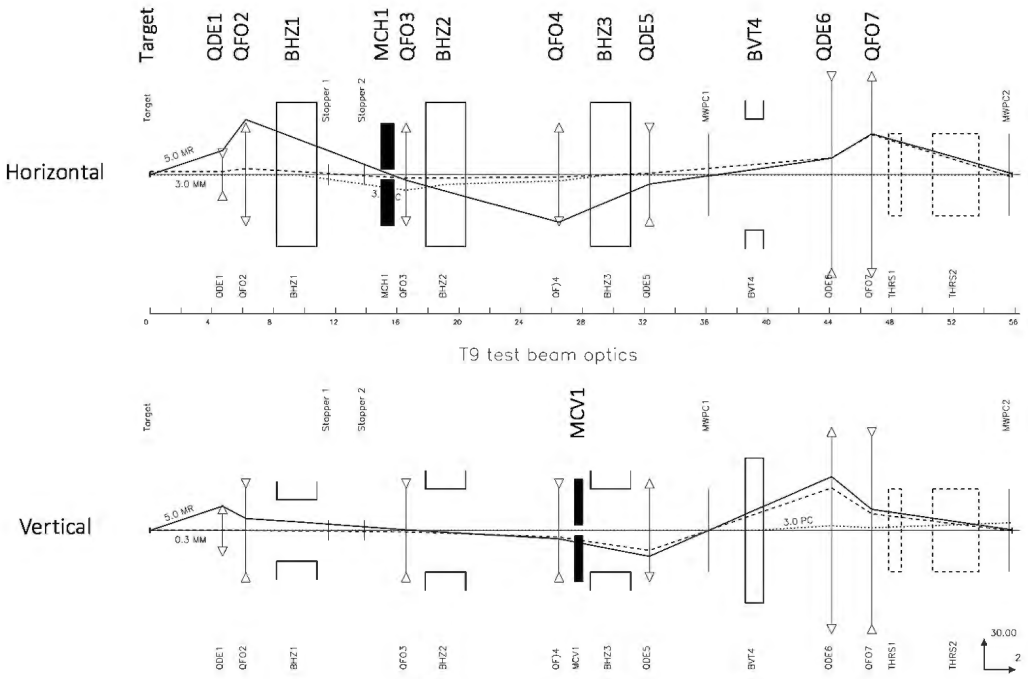

Figure 4-3: T9 beam line optics.

line performs three functions over three sequential stages [118]:

- **Momentum selection:** The first stage, including quadrupoles QDE1, QFO2 and bending magnet BHZ1, performs the momentum selection at a variable-aperture horizontal collimator MCH1 (momentum slit).

- **Momentum recombination:** The second stage, including bending magnets BHZ2, BHZ3 and quadrupoles QFO3, QFO4 and QDE5, performs the momentum recombination and sets an intermediate focus. A vertical collimator MCV1 (acceptance slit) is placed between quadrupoles QFO4 and QDE5 to improve the selection efficiency.

- **Final focus:** The third stage, with QDE6 and QFO7 quadrupoles, refocuses the beam in the experimental area. The final focus may be moved along the area by changing the currents in the last quadrupole doublet.

The line is expected to be under crude vacuum (< 10 pa) from the upstream face of QDE1 up to the downstream face of BVT4. This will ensure minimal multiple scattering in air and vacuum windows.
By adjusting the currents for the different optics components, the beam momentum can be selected.

4.1.2 Beam composition

The collision of protons with the target generates a variety of particles, such as electrons, positrons, muons, pions, kaons and protons. The T9 beam line therefore delivers a mix of hadrons and leptons in the beam, and can transport either positive or negative particles with momenta between 0.5 GeV/c and 15 GeV/c, by tuning the magnets current polarity and intensity. To obtain a muon beam mode two additional beam stoppers can be inserted in the path of the beam, which absorb most of the particles, except for the muons.
The extrapolated beam flux in the positive and negative modes for T9 beam line energies (from a simulation study originally performed for the SPS extracted beam line energies) is shown in figure 4-4.

4.1.3 Beam time structure

The PS machine accelerates proton bunches with an RF harmonic of 84 and a bunch spacing of 25 ns. The proton beam is guided towards the east area utilizing slow extraction technique over approximately 200000 machine revolutions, in order to suppress the RF component and achieve a flat top spill of $\sim$ 400 ms. In practice, the residual undulation on the power supplies can induce ripples in the extracted beam intensity.

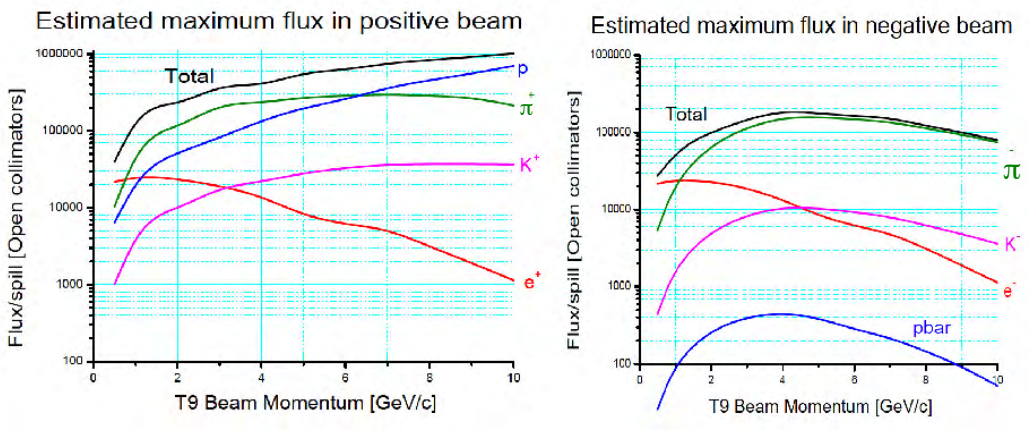

Figure 4-4: Extrapolated beam flux in the positive and negative modes for T9 beam line energies. For wide open collimators, i.e. $\Delta p/p \approx \pm 17.5\%$

Lau Gatignon, 10 March 2014 The T9 beam line 1

The shape of a T9 spill recorded by Baby MIND electronics is shown in figure 4-5. Clear ripples are visible on the rising edge of the spill. Depending on scheduling, such

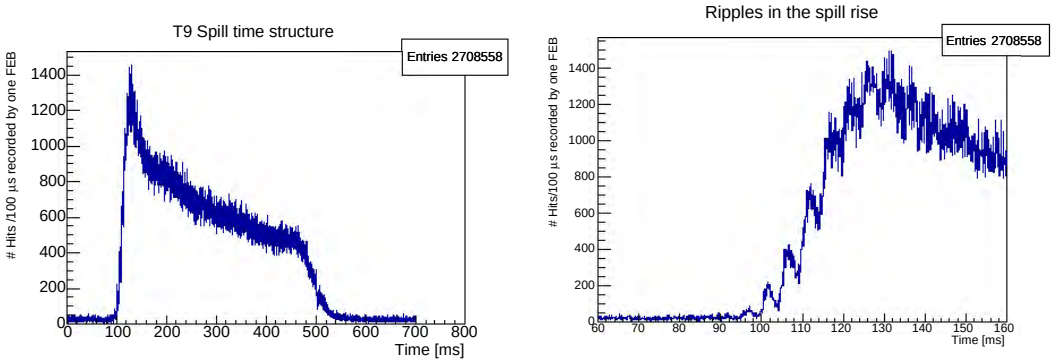

Figure 4-5: T9 spill shape recorded by Baby MIND electronics (left). Clear ripples are visible on the rising edge of the spill in the zoom plot on the right hand side.

a spill is provided once or twice per super-cycle, which is a multiple of the PS cycle which has a period of 1.25 s. The super-cycle last typically 40 seconds.

4.2 Commissioning at T9

A summary of the CERN beam test timeline, mentioning the main milestones, is shown in figure 4-6.

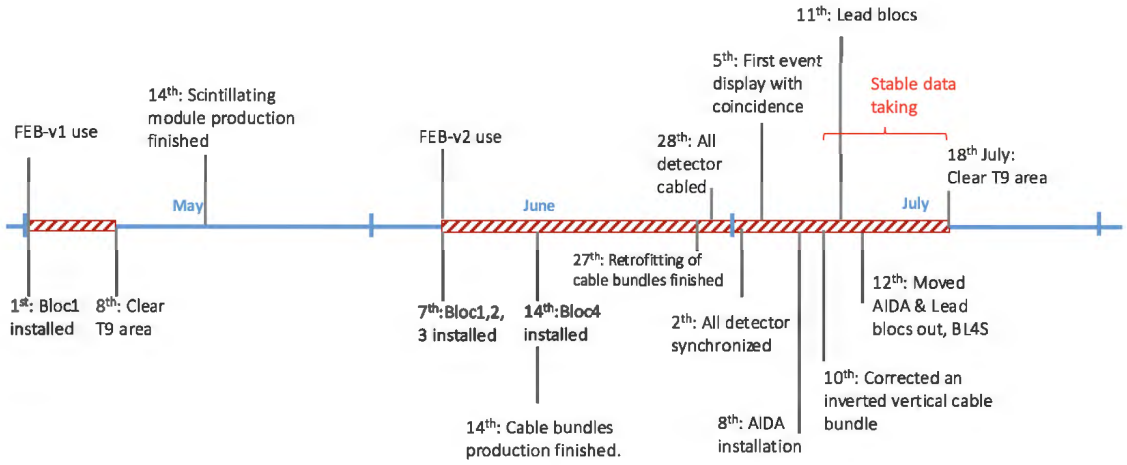

Figure 4-6: CERN beam test timeline from May to July 2017.

4.2.1 Transportation and installation

The initial plan for transportation and installation of Baby MIND at the T9 area was based on 33 magnet modules each transported and installed at T9 individually. Given the fact that long periods for assembly and removal of detector modules at T9 was not acceptable, the solution was adopted to design four mechanical support frames that could each hold a number of modules. These support frames or chassis were designed to serve the dual purpose of hosting the detector modules for the CERN beam test, and later acting as transport frames for the shipment to Japan. Therefore considerations such as admissible load per meter, dimensions of the container and loading methods were taken into account. The four chassis were fabricated at UniGe, delivered to CERN and passed a loading test, before finally hosting the detector modules. Each chassis was transported separately by a lorry within CERN, from building 180 to the East Area, building 157, and were lifted into the T9 area by crane (figure 4-7).

In practice, the available integration stands in building 180 were limited to eight,

Figure 4-7: Transport of the first chassis to T9.

therefore in order to proceed with the integration of the next group of scintillating and

magnet modules, the previous ones had to be placed into their corresponding chassis. The first chassis was loaded with detector modules and transported to T9 area on April 24th, making room for the next series of integration to start.
Upon the arrival of the first beam slot in the first week of May, only one chassis with 9 magnet modules and 7 scintillating modules was positioned at T9. The data taking of individual modules, one at a time, with the available set of three FEB-v1, and different beam momentum settings was launched, to observe beam profiles with magnet OFF and ON, reported in section 4.3.1.

In parallel, the integration of the remaining scintillating modules and magnet mod-

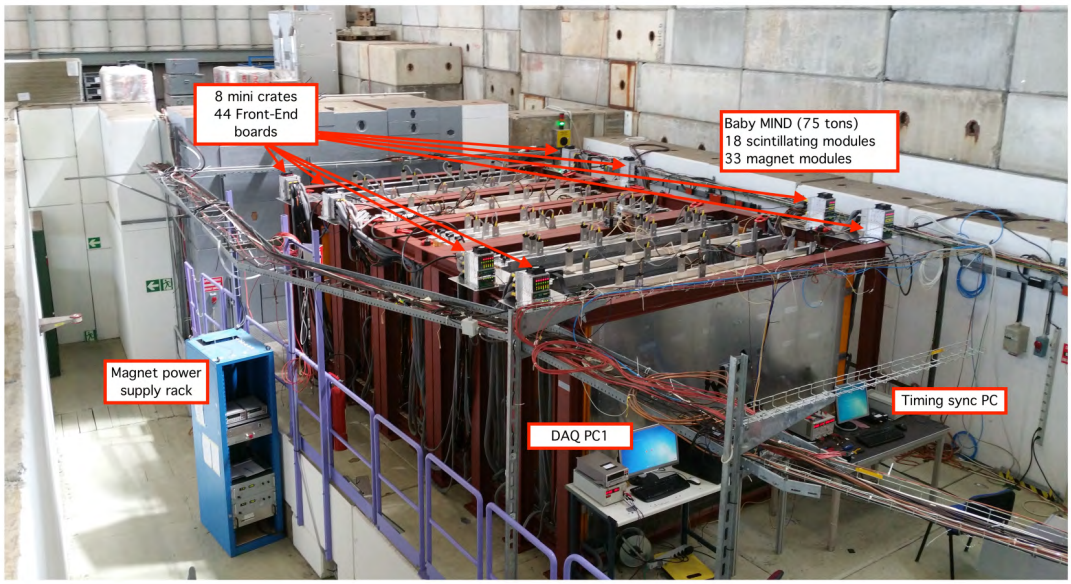

Figure 4-8: Baby MIND detector at T9 after full installation in June 2017.

ules, and their loading into three other chassis was ongoing in building 180, so were the cable bundle production and the FEB-v2 and the back plane qualification tests.
The second allocated beam slot and access to T9 started on June 7th, when the second and third chassis were transported to T9. This was followed by the installation of 8 mini crates with 44 FEB-v2 on top of the detector chassis. The fourth and last Baby MIND chassis was transported to T9 on June 14th.

AIDA setup as an additional beam trigger

Towards the end of the beam test period, on July 8th 2017, the AIDA setup which was used in the electronics beam test in 2016, was brought to the T9 area, to act as an additional beam trigger and tracker with a better position resolution, see figure 4-9. Only two AIDA modules, 37 cm apart, were instrumented to monitor the beam center with an effective area of 16×16 cm^2 for the upstream AIDA module and an effective

area of 64×64 cm^2 for the downstream AIDA module.

Figure 4-10 shows the detector modules layout and the cabling scheme between the

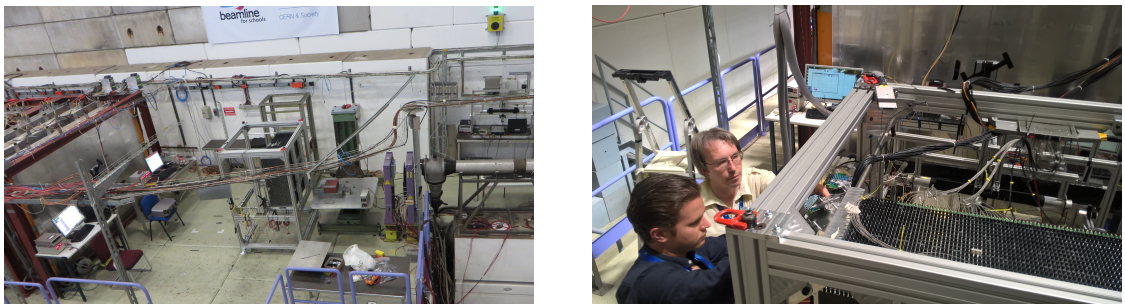

Figure 4-9: Installation of AIDA setup as an additional beam trigger.

scintillating modules and the mini crates.

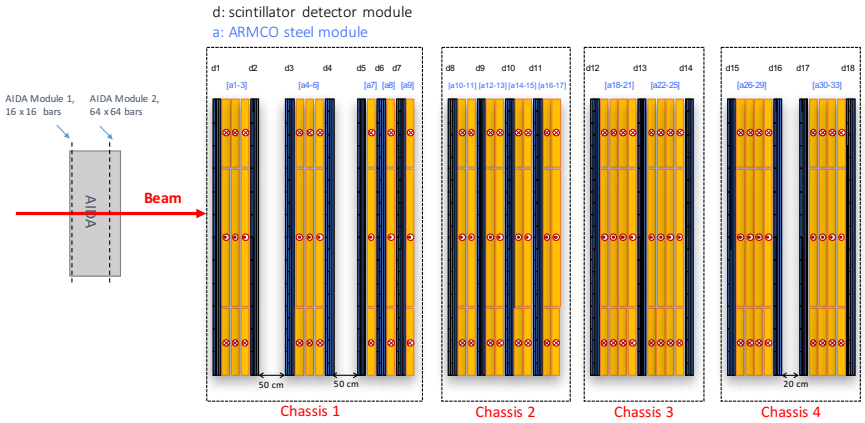

(a) Side view.

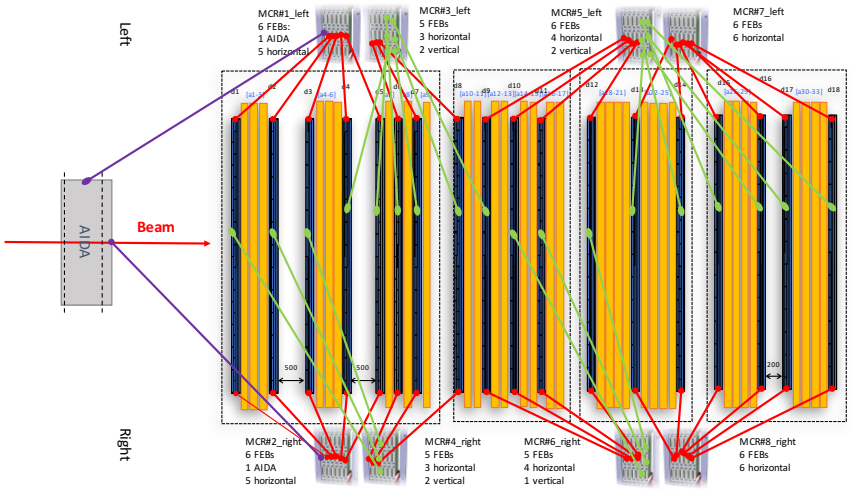

(b) Cabling layout, top view

Figure 4-10: Baby MIND detector layout during the 2017 beam test at CERN.

4.2.2 Retrofitting cable bundles

The detector cabling proved to be very challenging, as we encountered an alignment issue inside the aluminum shielding boxes. This mechanical detail caused problems for accessing the short screws, which were critical for the attachment of the cable bundles to the scintillating modules or the FEBs, and were initially planned to be reached with a long screw driver. The miss-alignment issue is shown in figure 4-11. Moreover, it

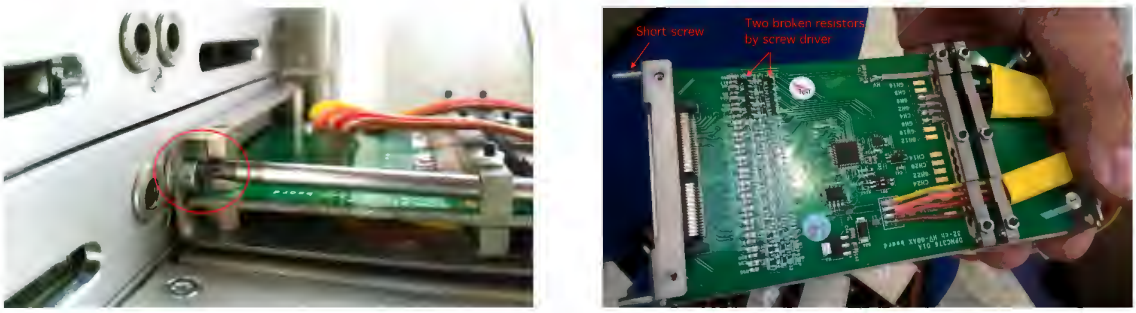

(a) Critical Miss-alignment issue. (b) Broken resistors by screw driver.

Figure 4-11: Critical Miss-alignment issue and accidentally broken resistors by long screw driver, motivated retrofitting of the aluminum shielding boxes.

was revealed that the use of the long screw drivers would accidentally knock off some resistors on the HV-coax PCBs inside the shielding boxes.

The effective quick fix solution consisted in retrofitting the mechanical boxes. The

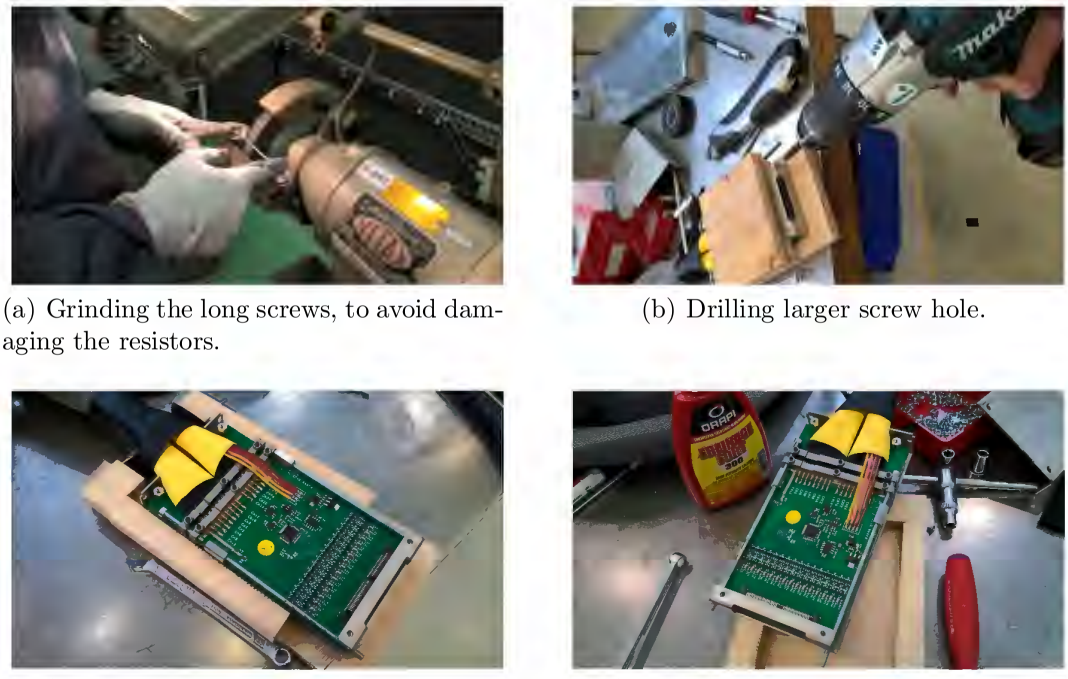

(a) Grinding the long screws, to avoid damaging the resistors.

(b) Drilling larger screw hole.

(c) Before gluing a new screw head.

(d) After gluing a new screw head.

Figure 4-12: Retrofitting connectivity in the cable bundle module side aluminum boxes.

original short screws were replaced with long non-standard screws made by cutting and gluing together two standard screws. Figure 4-12 shows the stages of retrofitting process.

The FEB side of the cable bundles was less affected by the misalignment, since the length of the mechanical box in that case is shorter. It was decided to not proceed with retrofitting of the FEB side in order to start data taking earlier. In all cases it was possible to secure the cable bundles to the FEBs. The retrofitting work of the cable bundles finished on June 27th, and the detector cabling and fingerplot testing of all the 18 scintillating modules succeeded on June 28th.

4.2.3 Magnet commissioning

The 33 magnet modules were serially connected to the power supplies, with special inter-connects to attach the coils of the adjacent modules either from top or bottom corners (figure 4-13) and two longer power cables from the first and last magnet module to the power supplies.

The two power supplies were mounted in a rack and configured in series as master and

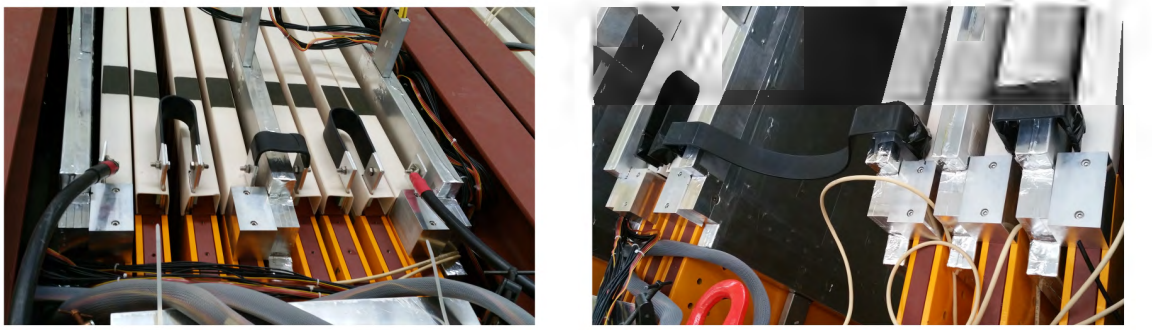

Figure 4-13: Aluminum coil inter-connect between modules.

slave units and were equipped with an emergency stop button. In order to facilitate the changing of the magnet current polarity, a switch panel shown in figure 4-14, was prepared and installed on the rear side of the magnet power supply rack. Changing the orientation of the two copper slabs from vertical to horizontal switches between forward-current and reversed-current modes.

The voltage drop across the whole detector operating at the nominal current of 140 A was about 82 V, resulting in a total power dissipation of 11.5 kW.

A hot air extractor fan system consisting an array of fans to be mounted on top of the magnet was studied and designed but never implemented. Without it, the heat produced by the magnet could be dissipated by the large area of the magnet modules,

Figure 4-14: Panel for switching magnet current in forward (left) and reversed (right) mode.

maintaining operational temperatures in a room-temperature environment. However, commissioning of the Baby MIND coincided with a heat wave in July 2017, during which the detector modules were heated up considerably during the nearly one month of magnet operation.

A temperature sensor was used to probe the temperature around the scintillating modules. Especially 6 scintillating modules that were sandwiched in between magnet modules with little room for air convection. The highest temperature was reported in the gap between a magnet module and a scintillating module at 41° C. The temperature near the vertical bar MPPCs, on top of one of the sandwiched scintillating modules, was monitored for several days, and is presented in figure 4-15. The average day-night temperature was measured to be 38.9° C. Given the recommended temperature

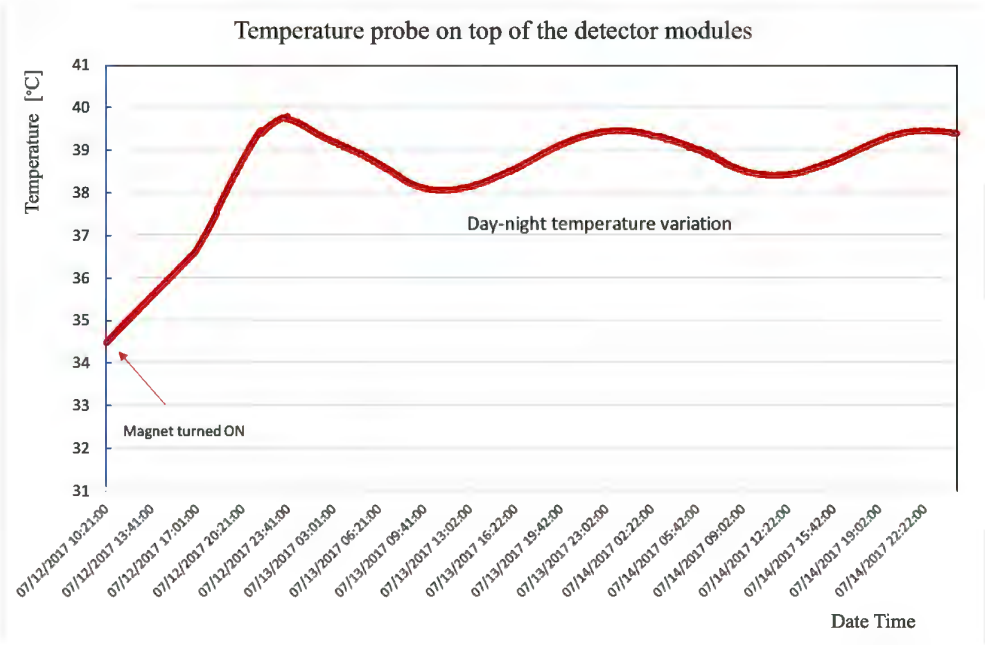

Figure 4-15: Temperature recording on top of the detector modules during the beam test, from 12 to 14 July 2017.

for operation of MPPC devices is between -20 and 40° C, the vertical MPPCs were operating in extreme temperature conditions. There was much less concern about the horizontal MPPCs, near which 31° C was recorded.

The MPPC gain value is inversely related to the temperature. The gain variation due to temperature was observed by comparing the distribution of MPPC gain from a calibration data collected in the beginning of the beam test in June and another one collected in July at the peak of the heat wave shown in figure 4-16.

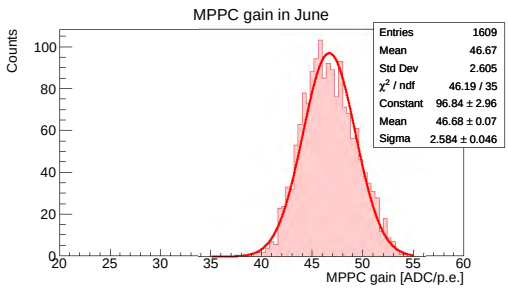

(a) MPPC gain in June, with a mean value of 46.7.

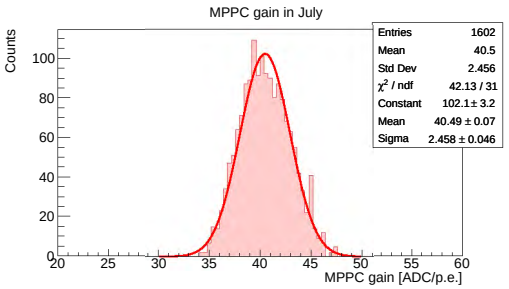

(b) MPPC gain in July, with a mean value of 40.5

Figure 4-16: The MPPC gain [ADC/p.e.] variation due to temperature difference between June and July 2017.

4.2.4 Trigger system and synchronization

The only piece of Baby MIND hardware that was not yet produced at the time of the CERN beam tests, was the Master Clock Board (MCB), described in section 3.7.7. In the absence of the MCB, the emulation of the clock signal was done by an extra FEB. This functionality was foreseen in the FPGA firmware, and was used for small test setups, to synchronize a few FEBs. We refer to the FEB emulating the clock as the *Master Clock FEB*.

The trigger signal for the start of data acquisition was taken from the beam line spill warning signal. There were two such signals available. The PS spill warning which arrives 1 s before the spill, and an adjustable delayed signal, for which the delay can be set on the C-Train counter at the T9 control room (figure 4-17). We took the latter signal and used a pulse generator to prepare a 700 ms acquisition window, before sending the signal to the Master Clock FEB which was placed in a separate mini crate. A sketch of the trigger signals is shown in figure 4-18. The emulated clock signal was then distributed via 3 Fanout boards to 8 mini crates with high quality RJ45 cables (category 6, S/FTP), of same length (figure 4-19).

Figure 4-17: C-train counter unit at T9 control room.

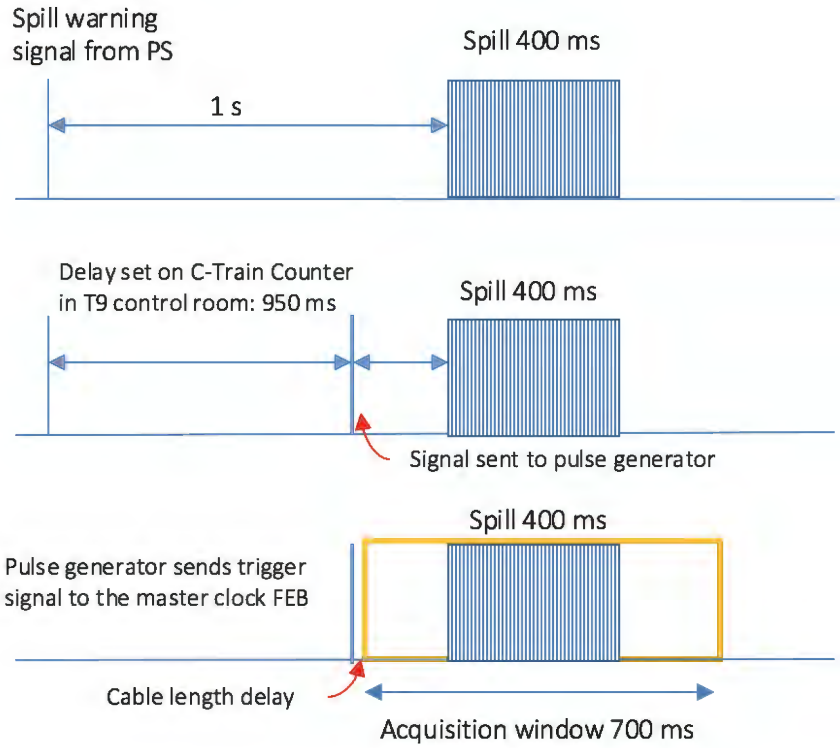

Figure 4-18: Trigger signal generated from PS spill warning.

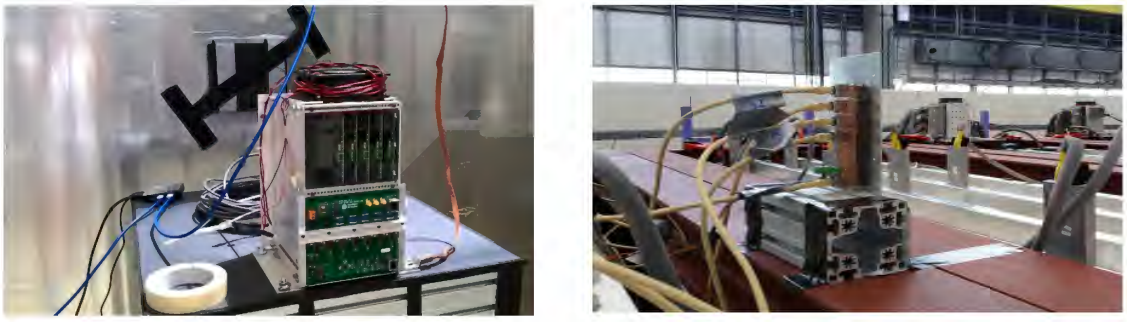

Figure 4-19: An FEB in slot-0 of a separate mini crate emulates the CLK and SYNC signals (left). A fanout board with one input and 4 outputs distributes the CLK and SYNC signals to other mini crates (right).

4.2.5 Beam test DAQ

An interface application for communication with the Front-End boards (AFE) was used for data taking during the CERN beam tests. This application was initially developed for development and testing purposes of individual FEBs, and was adapted for the operation with a large chain of electronics. Many of its features were implemented in stages as the beam test proceeded. The Front-End interface application allowed access to various ASIC and FPGA parameters, HV settings and the USB parameters shown in figure 4-20, as well as the handling of the data readout and some basic visualizations and data processing functions like conversion of the binary data to a comma separated value (CSV) format [119].

For the data taking at the CERN beam test, additional scripting functionality, with

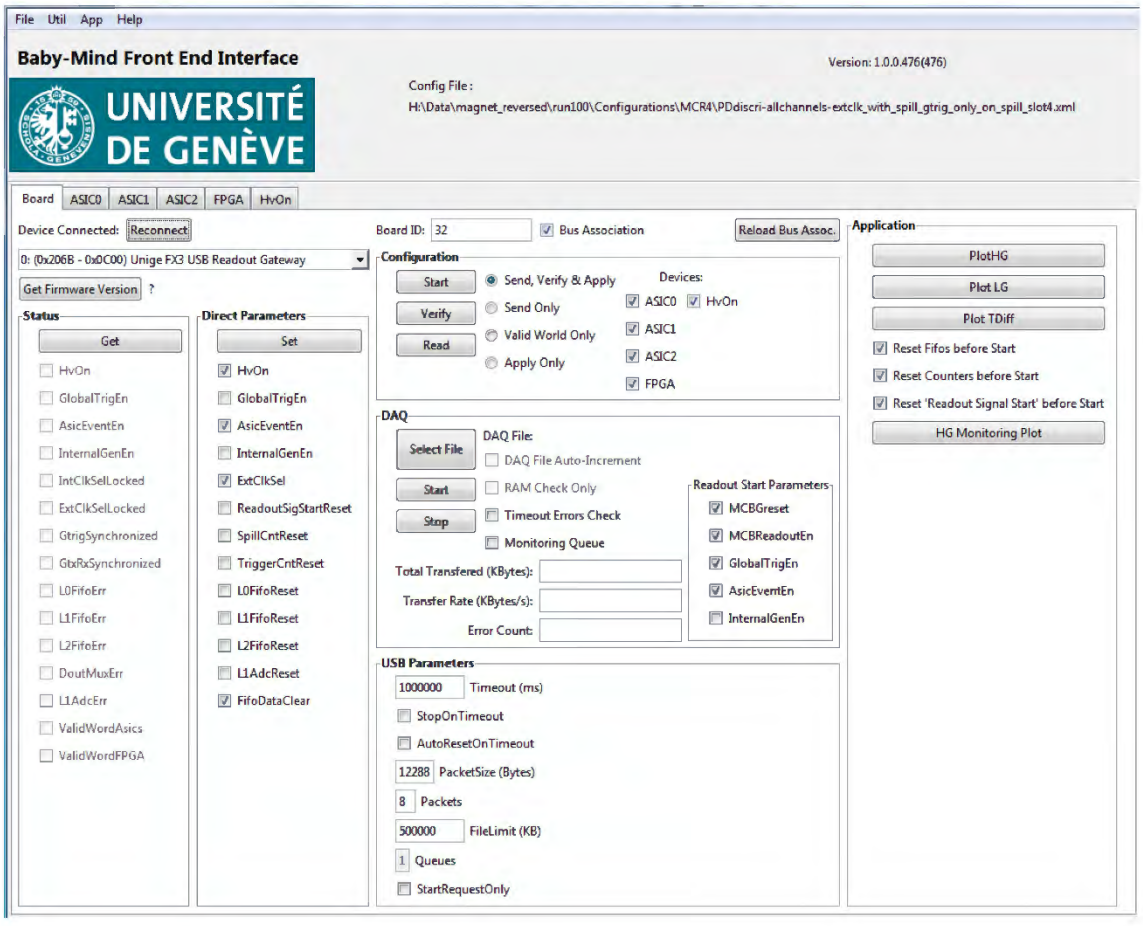

Figure 4-20: AFE host application was used for data taking during CERN beam tests.

C# syntax [120], was added to the AFE application, to perform data taking from a chain of FEBs which are hosted by the same mini crate. The scripting tool allowed to launch a sequence of commands that would take care of the configuration files for individual FEBs and the preparation for different acquisition modes as well as the

handling of the output data file. The limitation was that each instance of the AFE application could communicate with only one mini crate at a time. In order to operate the Baby MIND detector with 8 mini crates, 8 instances of the AFE application had to be launched in parallel.

The overall configuration of the data acquisition system (DAQ), as it was used for the CERN beam test is shown in figure 4-21. Two PCs were dedicated to the data readout, each hosting 4 instances of the AFE application and communicating with 4 mini crates through USB-3 links. One data file was created per mini crate. A separate PC was responsible for enabling the trigger. For this purpose one Instance of the AFE application was linked to the Master Clock FEB in a separate mini crate and a dedicated script was sent to enable the CLK and SYNC signals.

During the beam test two modes of data acquisition were used:

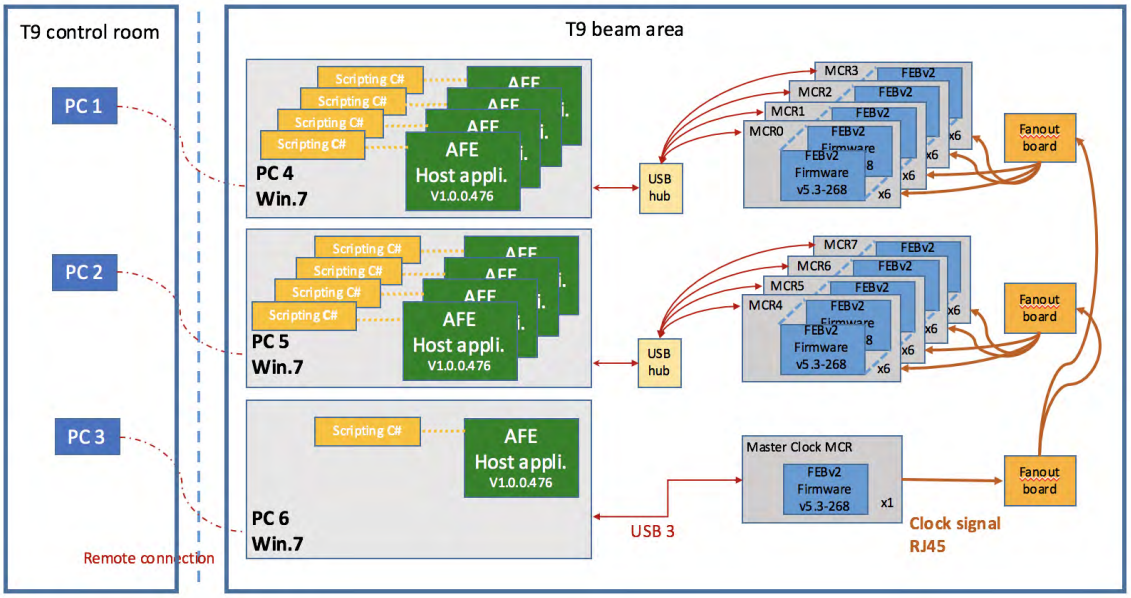

Figure 4-21: Schematics of the data acquisition system for the CERN beam test. The remote connection is established via Ethernet.

- **Full Bandwidth mode:** In this mode all the USB-3 bandwidth is dedicated to one FEB regardless of its relative position in the mini crate. This mode was typically used for the dark count calibration acquisition where no synchronization is required.

- **Time Division Multiplexing (TDM) mode:** The TDM mode was used for beam data taking with a synchronized detector. In this mode each FEB in a chain, hosted by the same mini crate, has a dedicated time slot for asynchronous

data readouts. The stream of data is pushed to the PC through one USB-3 link per mini crate, and one data file per mini crate is created.

4.2.6 Electronics parameter setting

MPPC HV adjustment

The high voltage (HV) applied on each channel's MPPC is adjustable by an 8-bit input DAC parameter. Figure 4-22 shows the measurement of HV on the MPPC pins by a multimeter for different input DAC values. The measurements were repeated for 10 channels on different FEBs, to ensure the stability of the mapped values. Based on these results the input DAC parameter corresponding to the average operating voltage of the MPPCs read by each ASIC was set. The homogeneity of the operating voltages for the 32 MPPCs connected to a given ASIC was ensured by sorting MPPCs in batches of 32 with operating voltages within ± 100 mV from the batch average, as was discussed in section 3.6.3.

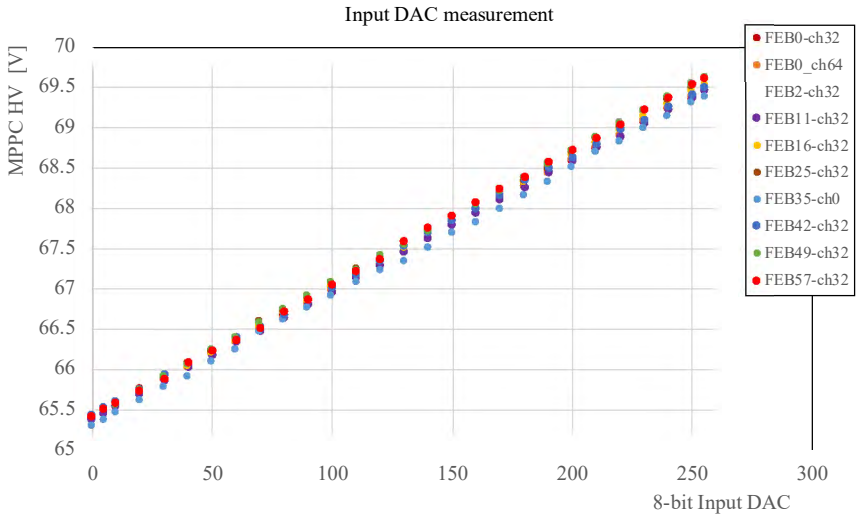

Figure 4-22: MPPC high voltage measurement for different input DAC values. The measurements were repeated for 10 channels on different FEBs.

Pre-amplifier settings

Both HG and LG pre-amplifiers are adjustable by a 6-bit setting in the CITIROC. The HG pre-amplifier gain setting, allows adjustment of the MPPC gain in terms of ADC/p.e.. While a higher gain would facilitate the HG calibration, by providing a better peak separation for a multi-gaussian fit, it would translate into lower dynamic

range. The strategy is to choose the HG setting which results in a high quality fingerplot (see section 3.6.2) and can cover the equivalent of two MIPs and rely on the LG signal path for a greater dynamic range. Figure 4-23-a shows the fingerplot on the same channel with different HG pre-amplifier settings. By extracting the p.e. peak locations and fitting a regression line to the points for each pre-amplifier setting, we get the plot in figure 4-23-b. The intersection of the regression lines determines the pedestal value, which is different for every channel.

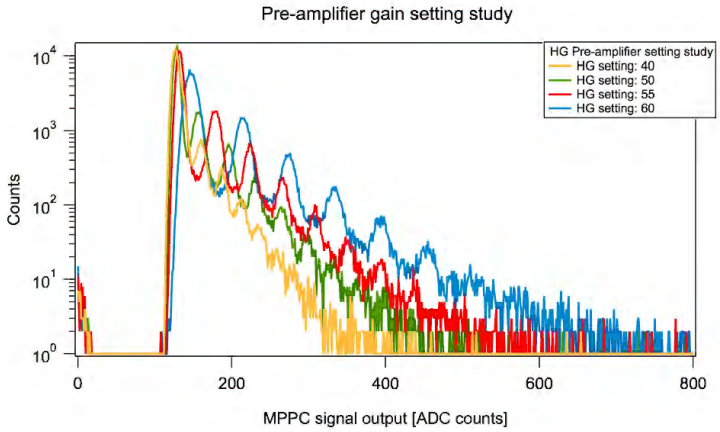

(a) Fingerplots.

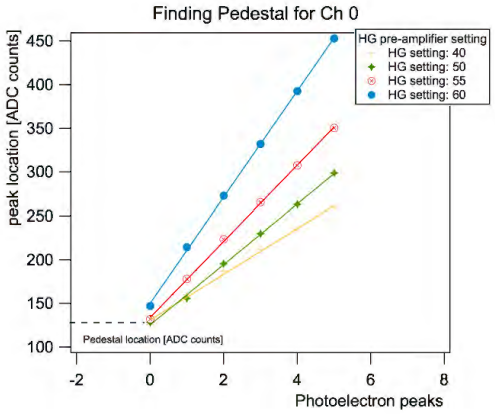

(b) Peak locations.

Figure 4-23: HG pre-amplifier gain setting study.

Slow shaper time constant settings

The slow shapers on both LG and HG signal paths are used for adapting the waveform of the amplified signal for the amplitude sampling. The shaper has an adjustable peaking time depending of the value of the time constant (τ_{Shaper}: 12.5 to 87.5 ns), which allows the user to optimize the transmitted signal for the final application. The

shaped pulse peaking time corresponds to $T_{\text{Peak}} = 2.08 \times \tau_{\text{Shaper}}$, and the overall pulse is contained (from baseline to max to 5% of the max) within a time corresponding to $T_{\text{Signal}} = 7.52 \times \tau_{\text{Shaper}}$. Example: $\tau_{\text{Shaper}} = 12.5$ ns $\Rightarrow$ $\text{T}_{\text{Peak}} = 26$ ns, $T_{\text{Signal}} = 94$ ns. The effect of different slow shaper time constant values on the spectrum of MPPC dark counts noise (fingerplots) with a fixed value of hold window was investigated. It was observed that higher values of shaper time constant brings a reduction in resolution and the individual photo-electron peaks can not be resolved. This is shown in figure 4-24. The best quality fingerplot is obtained with the lowest shaper time constant setting.

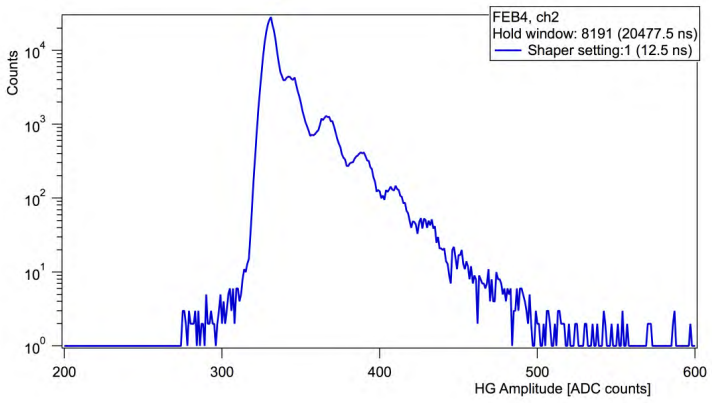

(a) Slow shaper setting: 1 (12.5 ns)

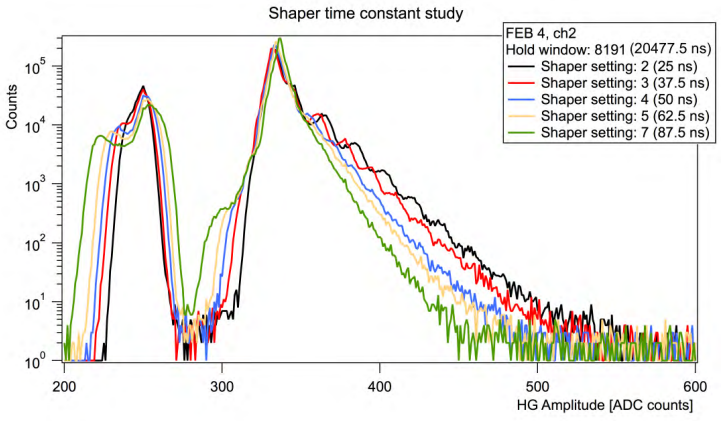

(b) Slow shaper setting from 2 to 7

Figure 4-24: Scan of slow shaper time constant settings with a fixed hold window set to maximum value of 8191 ticks (20.2 μs). The best photo-electron peak separation is achieved with the lowest slow shaper time constant of 12.5 ns (top plot).

Hold window settings

As was explained in section 3.7.3, the signal sampling happens during a hold window with an adjustable width. The first consideration for choosing a hold window is to cover fully the shaped signal, and is therefore dependent on the choice of the shaper time constant. A study was carried out to understand the impact of different combinations of the hold value and the shaper time constant, based on the quality of fingerplots. An example is shown in figure 4-25, where the shaper time constant is fixed at 25 ns, and a scan of different hold values is performed. We observe that for low hold values, the

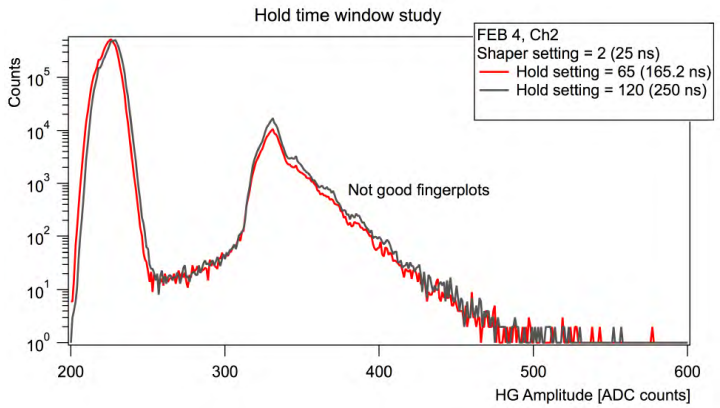

(a) Lower hold values result in poor fingerplots.

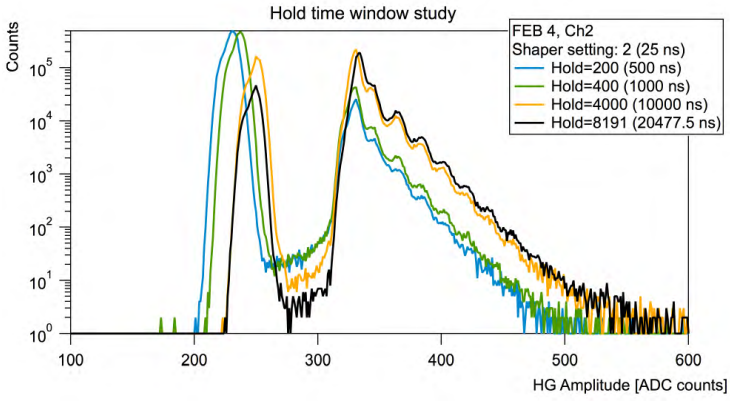

(b) Higher hold values result in higher fingerplot quality.

Figure 4-25: Scan of hold values with a fixed shaper time constant setting: 2 (25 ns).

photo electron peaks are smeared and the calibration coefficients can not be extracted. A summary of the results is presented in table 4.2.

The other consideration for the choice of the hold value is related to the existence of a dead time in the analogue data sampling cycle. Depending on the final application specifics, namely the beam time structure and data rates, we can optimize a hold

Table 4.2: Combinations of the shaper time constant and hold value with calibrateable fingerplots.

Shaper setting	τ_{shaper} [ns]	CITIROC sampling hold time window [2.5 ns]					
		65	120	500	1000	4000	8191
1	12.5	ok	ok	ok	ok	ok	ok
2	25	×	×	ok	ok	ok	ok
3	37.5	×	×	ok	ok	ok	ok
4	50	×	×	×	×	×	×
5	62.5	×	×	×	×	×	×
6	75	×	×	×	×	×	×
7	87.5	×	×	×	×	×	×

duration to balance the active time window with respect to the dead-time.

Discriminator threshold and baseline variation

The discriminator threshold, acting on the trigger line (fast shaper), is the main threshold for the detector. If a signal is above the threshold level, the hit time information will be recorded and if not in the dead time, a new analogue readout cycle, for all channels of the same ASIC, will be initiated. The discriminator threshold can be adjusted by a

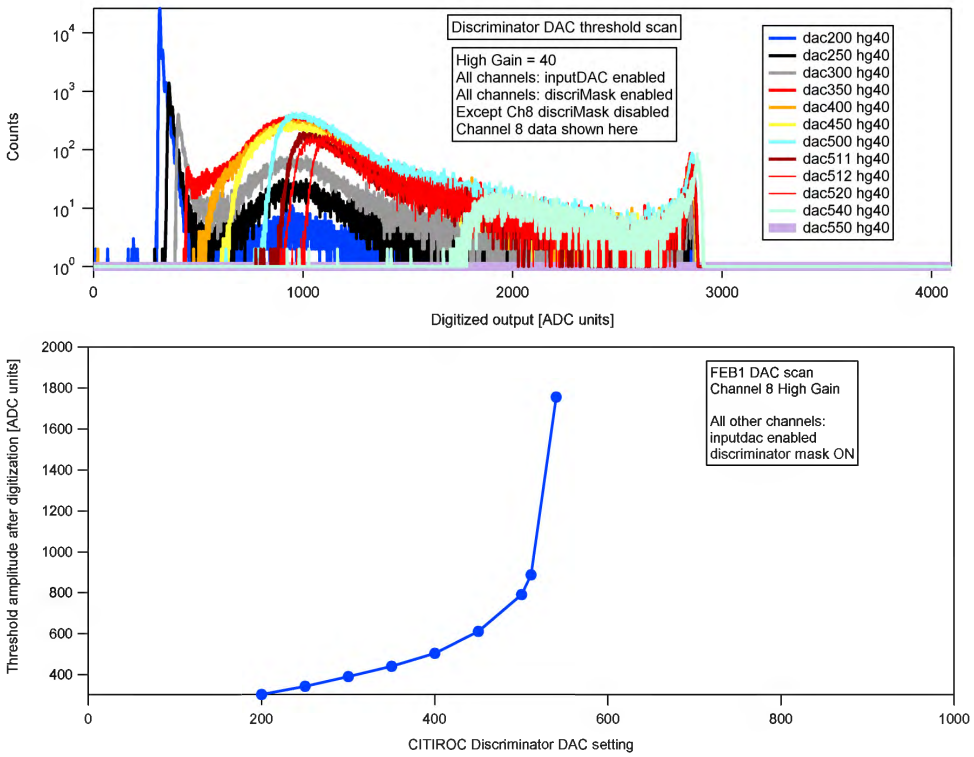

Figure 4-26: Discriminator threshold setting impact on the HG amplitude.

10-bit DAC parameter for each ASIC. Figure 4-26, shows the HG amplitude behavior for one channel with different values of discriminator threshold. Although this plot

is illustrative of the general behavior of the threshold, the ADC values corresponding to each setting of the discriminator threshold varies slightly between channels on the same ASIC, and to a greater extent between different ASICs. This baseline variation is shown in figure 4-27, where the discriminator threshold setting of 350 is applied on all channels, but the cut off value in terms of ADC counts is different for each ASIC.

The baseline shift is largely due to the matching of the voltage levels between the

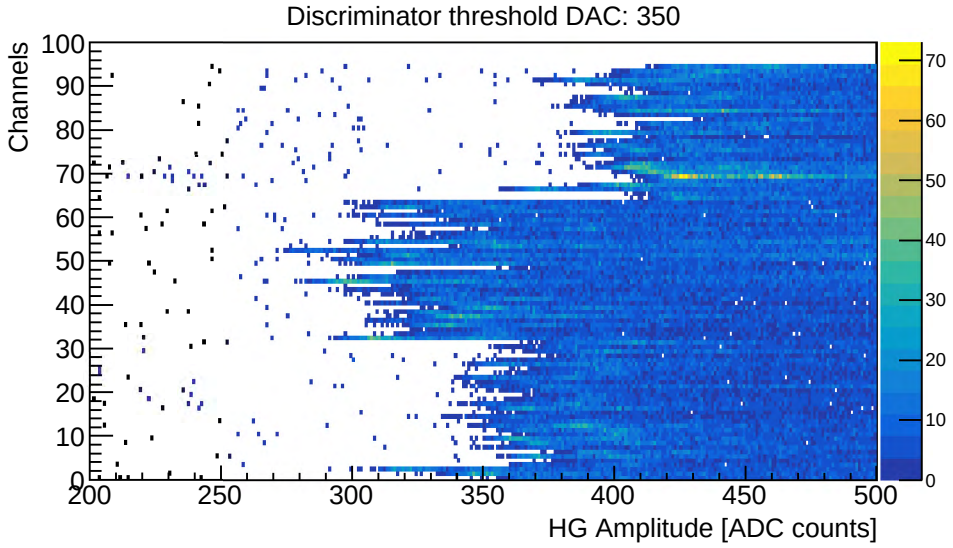

Figure 4-27: Plot of the HG amplitude for 96 channels of one FEB, with discriminator threshold setting of 350. The variation in cut-off values is visible between 3 ASICs.

ASIC output and ADC input. This variation is taken into account in the calibration stage where the pedestal value for each channel is subtracted before the amplitude conversion from ADC to p.e..

4.3 Summary of the collected data

4.3.1 Beam profiles

The first exercise that was carried out during the May 2017 beam slot, was to map the beam profile per module, utilizing a set of three FEB-v1, each reading data from one side of the detector module (left, right and top), and were synchronized with an external pulse generator. Figure 4-28 shows examples of the beam profile recorded by one of the Baby MIND scintillating modules with different beam momentum settings. In these plots the horizontal and vertical axis correspond to the horizontal and vertical bar numbers in the module. The plots were created by requiring coincidence between hits recorded by three FEB-v1. The beam profile is very similar with different beam

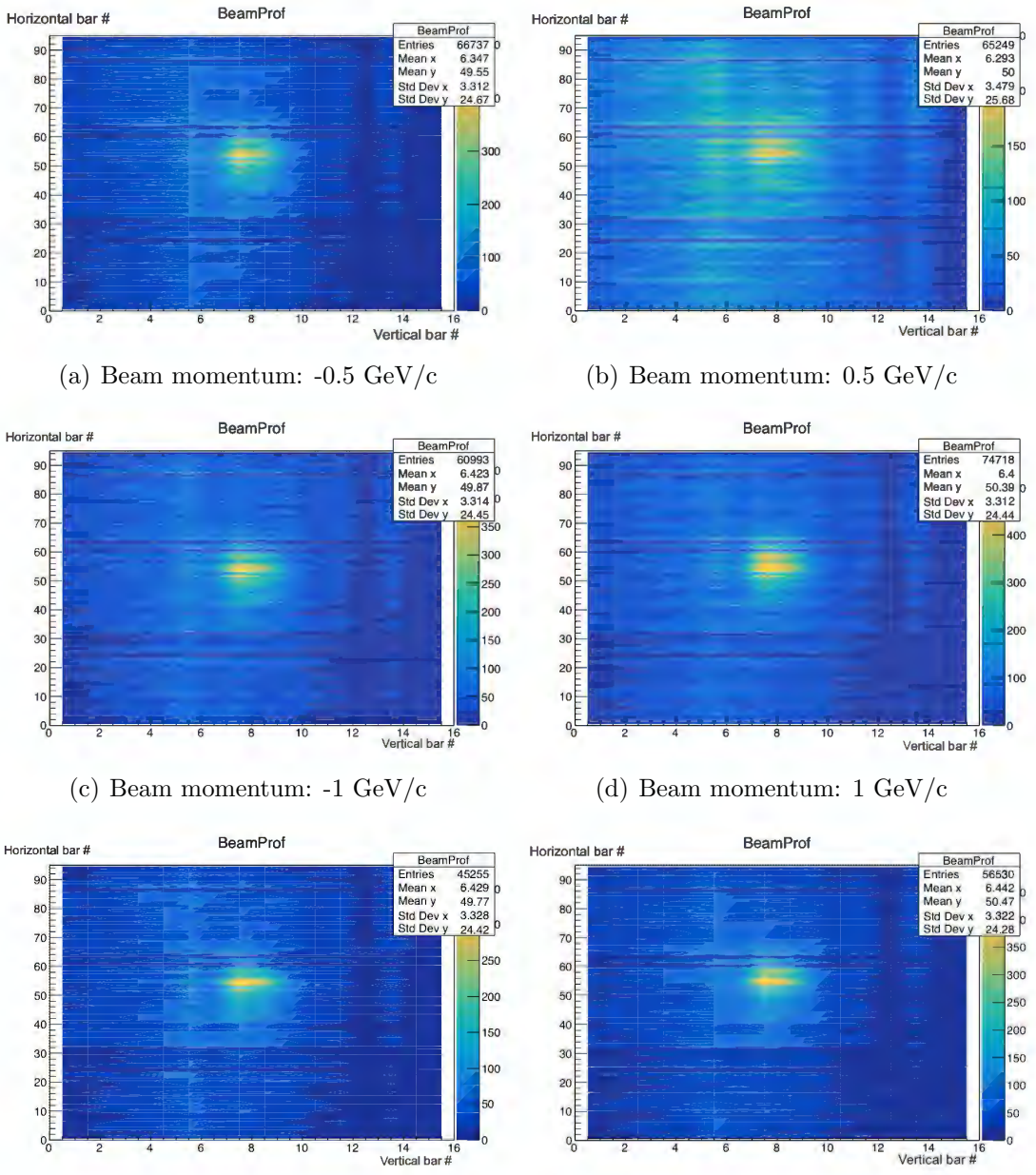

(a) Beam momentum: -0.5 GeV/c

(b) Beam momentum: 0.5 GeV/c

(c) Beam momentum: -1 GeV/c

(d) Beam momentum: 1 GeV/c

(e) Beam momentum: -1.5 GeV/c

(f) Beam momentum: 1.5 GeV/c

Figure 4-28: Beam profiles recorded by scintillating module 3 with different beam momentum.

momentum settings, indicating that the beam is well focused in all cases.

The location of the beam center in the Y axis is of particular interest, since it can reveal the deflection of the particle tracks due to the magnetic field. Figure 4-29 shows the hits Y distribution for scintillating modules 2, 4 and 6 for a muon beam with momentum setting of -1 GeV/c, showing the beam center moving upwards in Y direction. A broad beam related background is observed around the focused beam center, which motivated the usage of AIDA modules as additional beam trigger.

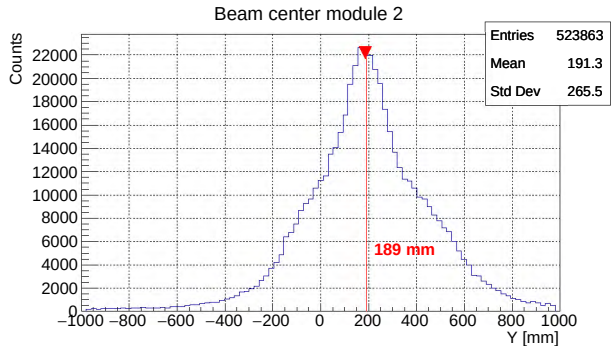

(a) Module 2

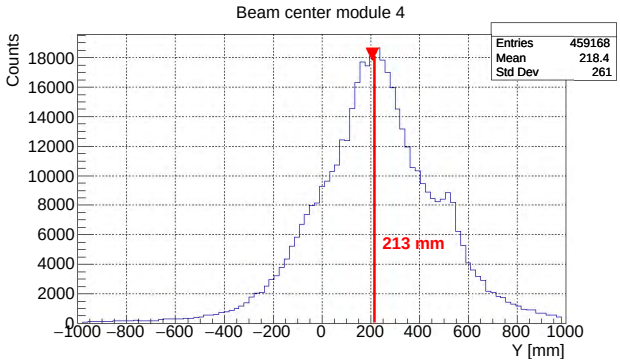

(b) Module 4

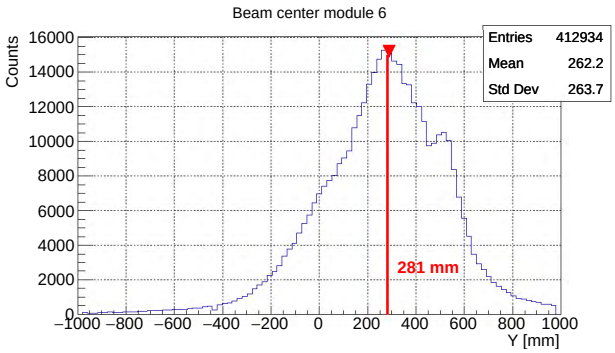

(c) Module 6

Figure 4-29: Location of the beam center in different scintillating modules for a beam of -1 GeV/c muons.

4.3.2 Event displays

The first event displays showing a particle track through the entire detector modules was produced on 5th of July, three days after the whole detector was synchronized. This was a major milestone for a detector that was put together for the first time on the beam line at T9. The event displays were produced by imposing a time window for each trigger hit in the AIDA module and requiring coincidence between right, left and top hits for each scintillating modules. Given the data recorded for different sides of the 18 scintillating modules is readout by 44 different FEBs. It is a manifestation

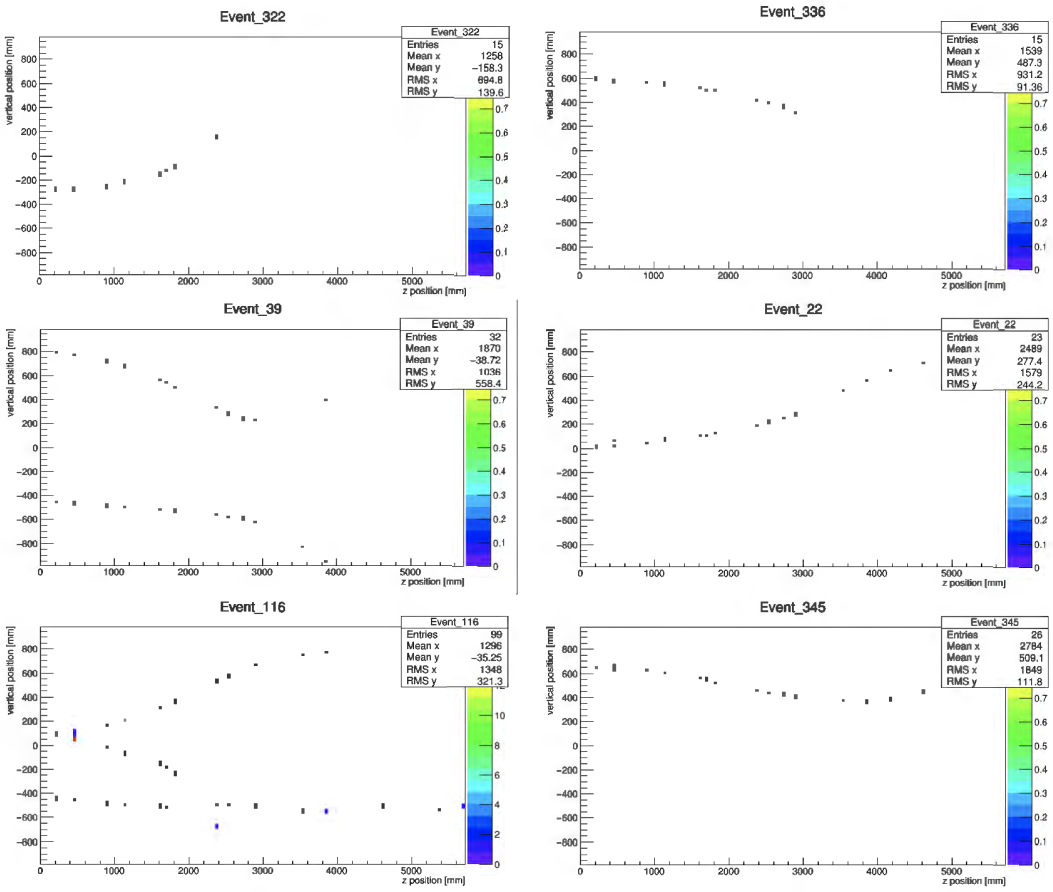

Figure 4-30: Examples of event displays with particle trajectories bending by the magnetic field.

that the detector is fully synchronized and all the modules are functioning as expected. The events displays in figure 4-30, show the side view (Y-Z) of the particle trajectories which are bent by the 1.5 T magnetic field in the magnet modules. The direction of the magnetic field changes sign at $Y = 500$ mm and $Y = -500$ mm, so does the direction of the curvature of the tracks.

4.3.3 Hits amplitude distribution

One of the challenges of operating at the T9 beam line was the very high data rate over a 400 ms spill window. A high discriminator threshold of 350 was therefore chosen to reduce the rate of the recorded hits. This threshold value corresponds to 6 or 7 p.e. Figure 4-31 shows the distribution of the calibrated amplitude for all channels of the detector, expressed as global channel which is defined as FEB ID $\times$ 96 + channel number.

The distribution of the calibrated hit amplitude for the hits generated by minimum

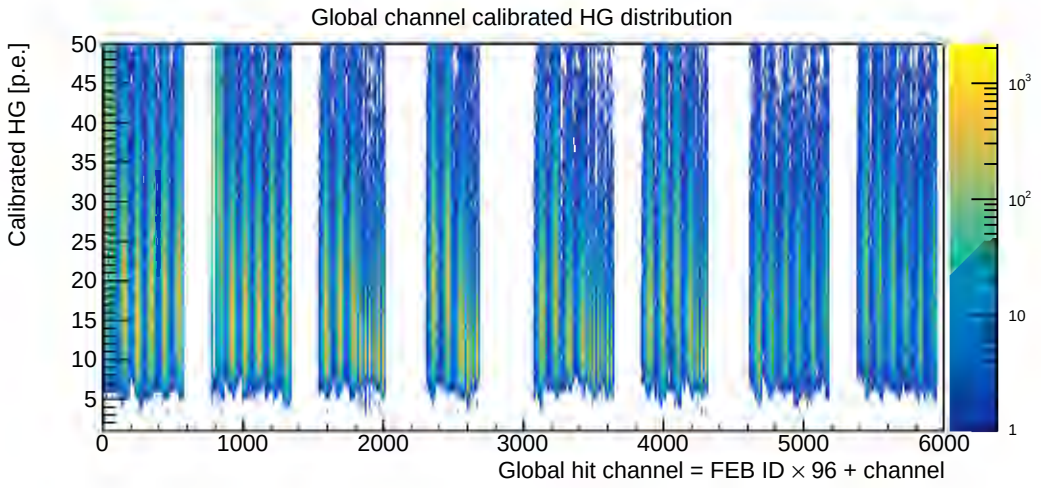

Figure 4-31: Distribution of calibrated amplitude for all channels of the detector, expressed as global channel.

ionizing particles in the horizontal bars and the vertical bars are shown in figure 4-32, and fitted with a landau distribution which describes the energy loss probability distribution in thin detector layers. The most probable value (MPV) of the calibrated amplitude was measured to be 15.4 p.e. with a sigma of 4.0 p.e. for the hits in the horizontal bars and 8.9 p.e. with a sigma of 1.6 p.e for the hits in the vertical bars.

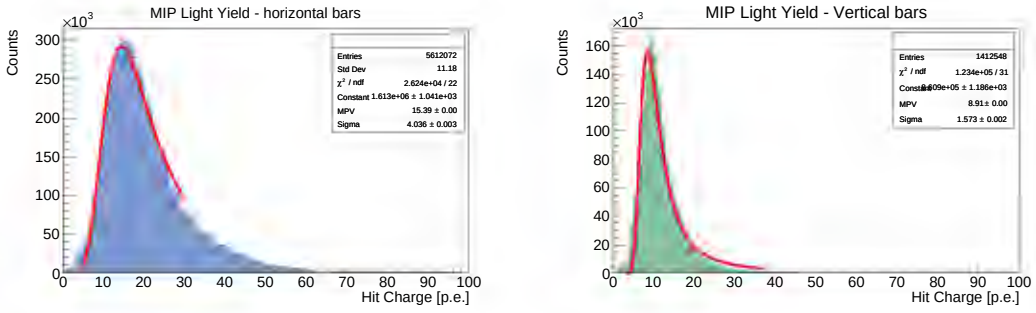

(a) Horizontal bars

(b) Vertical bars

Figure 4-32: Distribution of the calibrated hit amplitude for the hits in the horizontal bars and the vertical bars fitted with a landau distribution.

4.3.4 Momentum Scan

Towards the end of the beam test period, having resolved many challenges and scanned detector settings, we had a week of stable data taking with our choice of an optimized configuration, collecting reference data with positive and negative beams with momentum from 0.5 to 5 GeV, and both magnet polarities. The list of reference data files are summarized in table 4.3.

An effective illustration of the run summaries is achievable through the hit maps,

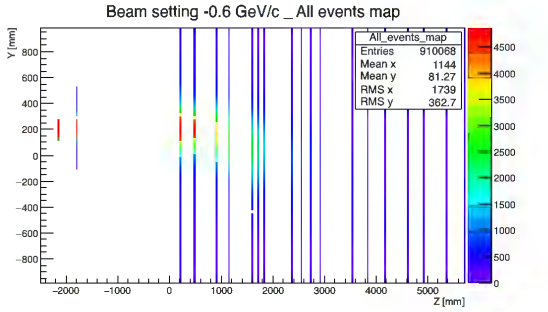

(a) -0.6 GeV/c

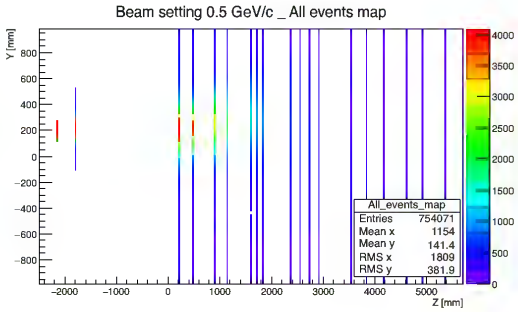

(b) 0.5 GeV/c

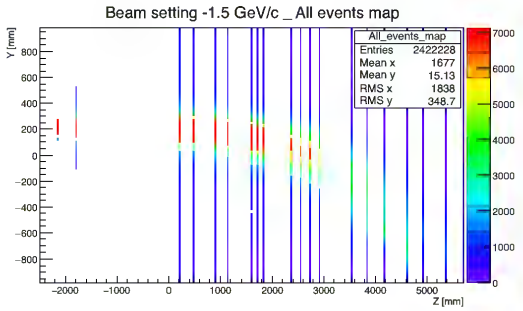

(c) -1.5 GeV/c

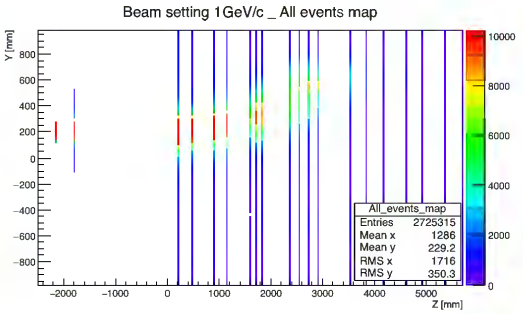

(d) 1 GeV/c

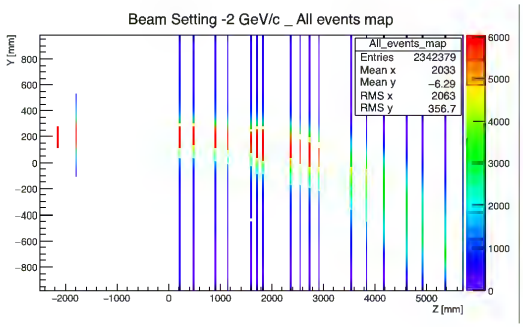

(e) -2 GeV/c

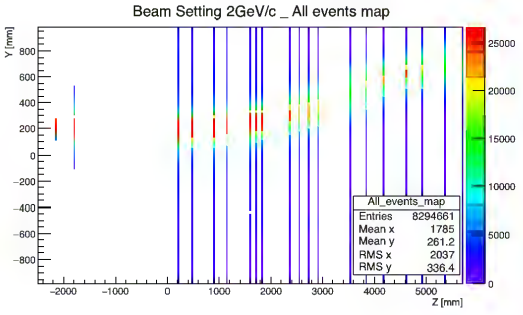

(f) 2 GeV/c

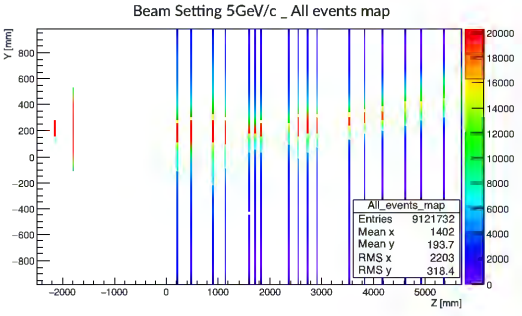

(g) 5 GeV/c

Figure 4-33: Hit map of data runs with different beam momenta.

shown in figure 4-33. The plots are produced from the muon runs with magnet current in the forward mode. A selection using the AIDA trigger hits is used to remove the

Table 4.3: Reference data files collected at CERN beam test 2017.

Beam type	Magnet current	Beam Momentum [GeV]						
Muons	Forward	-0.5	-0.6	-0.8	-1	-1.5	-2	-5
		0.5	0.6	0.8	1	1.5	2	5
	Reversed	-0.5	-0.6	-0.8	-1	-1.5	-2	-5
		0.5	0.6	0.8	1	1.5	2	5
Hadrons	Forward	-0.5	×	×	-1	-1.5	-2	-5
		0.5	×	×	1	1.5	2	5
	Reversed	-0.5	×	×	-1	-1.5	-2	-5
		0.5	×	×	1	1.5	2	5

unwanted hits and clean up the track profiles, by imposing a time window of 50 ns around the trigger hit time. The side view profile of the particle trajectories and their curvature due to the magnetic field is visible through the hit intensity color palette.

4.3.5 Understanding data corruptions

As was mentioned earlier, the FEB-v2 were delivered in the beginning of the beam test campaign and many new functionalities of the system for a large setup were commissioned for the first time during the beam test. Understanding of the data features and data inconsistencies took place gradually during several months that followed the beam test.

The data rates at T9 beamline, with 10 kHz particle rate within 400 ms spills, are orders of magnitude higher than the expected data rates at T2K beamline, with 1 to 10 Hz particle rate within 5 μs spills, for which the Baby MIND electronics was designed for. Despite the fact that a relatively high discriminator DAC thresholds of 350 was chosen, in order to reduce the data throughput, in the post processing of the collected data, it was noticed that the high data rates have affected the data integrity in different ways. In this section some cases of the data corruption identified in the beam test data is discussed briefly.

Incoherent data and skipped spill

The new unpacking software compatible with FEB-v2, was developed simultaneously with the data taking during the beam test 2017 at CERN. The unpacking software is responsible to convert the binary data to root based data files. One of the new features implemented in the FEB-v2 data protocol was a dedicated 32-bit word for data quality warnings. In the newly developed unpacking software upon identification of incoherent data such as FIFO full error, TDM error or the GTRIG header and trailer mismatch

the whole spill was skipped. The skipped spill was particularly observed in data runs with beam settings that had higher particle rates. An example is shown in figure 4-34, from a data run with momentum setting of +5 GeV muons, and a particle rate of 7500 per spill. The figures show the run summary of two FEBs (FEB 1 and FEB 12), with the spill number on the Y axis and the GTRIG time stamps within a spill on the x axis. The missing horizontal lines indicate the skipped spills by the unpacking software due to incoherent data.

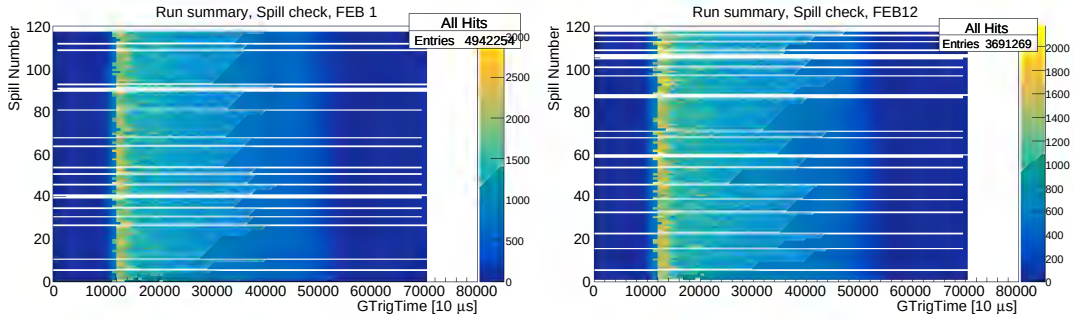

Figure 4-34: Skipped spills of FEB 1 and FEB 12 in a data run with 5 GeV muons and average particle rate of 7500 per spill.

Missing hit time information due to high data rates

In the post processing of the beam test data, instances were identified whereby a hit which had a recorded rising edge time was missing the corresponding falling edge time. The occurrence rate of such cases in the beam test data was about 0.1%. The missing of hit falling edge time information, is an indicator of data loss at an intermediate FIFO stage of the timing path in the FPGA (figure 4-35). Originally, this intermediate

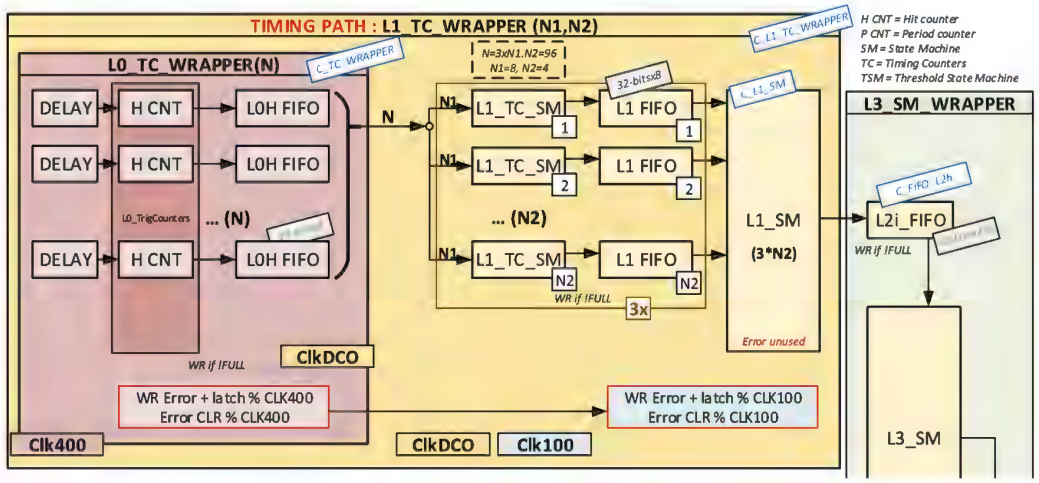

Figure 4-35: The detailed schematics of the hit timing path

FIFO (L1-FIFO) had a depth of 8 words per group of 8 channels. Indicating that for each FEB with 96 channels, there are 12 such FIFOs storing the hit time information temporarily. The bottle neck occurs as the state machine which is responsible for the concentration of 12 FIFOs into 1 output FIFO, can only pull out one word per 10 ns clock cycle and the order is defined by a round cycle from 8-channel group 0 to 11. If every group has a data word in its FIFO, it will take 120 ns to pull out the next element in group 0.

A complementary study with an LED injection system was performed to reproduce this behavior systematically. The problem was resolved with a new FPGA firmware which increased the FIFO depth from 8 to 64. The plots in figure 4-36 show the recording order of the hits induced by the LED pulse with different FIFO depths.

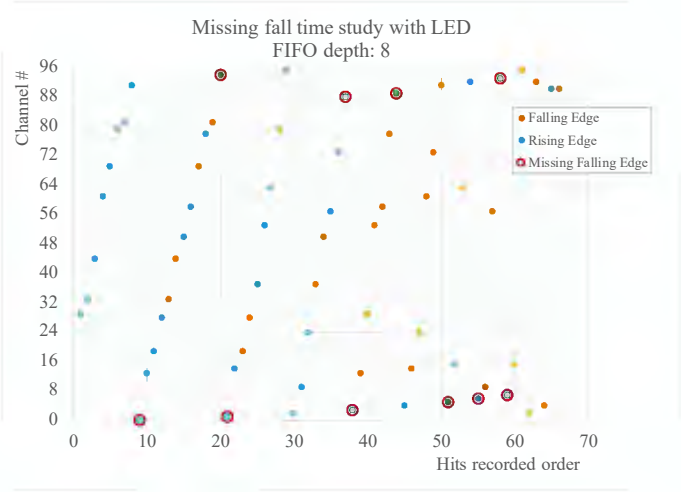

(a) FIFO depth: 8. Out of 38 hits, 10 were missing the fall time.

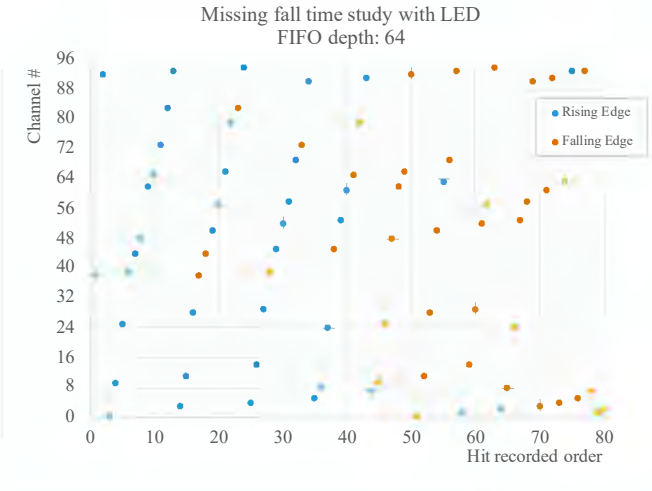

(b) FIFO depth: 64. No hit fall time missing.

Figure 4-36: Study of missing hit fall time with LED. The problem was resolved by increasing the FIFO depth from 8 to 64.

Clock signal lost

Another issue observed in the beam test data was that some FEBs stopped recording data in the middle of a data run. An example is shown in figure 4-37, where the data acquisition run has lasted for 95 spills but FEB 12 and FEB 19 have stopped acquiring data after spills 53 and 65 respectively. This behavior is likely due to a clock signal not reaching the corresponding FEB.

We had previously encountered many synchronization issues due to the RJ45 cables.

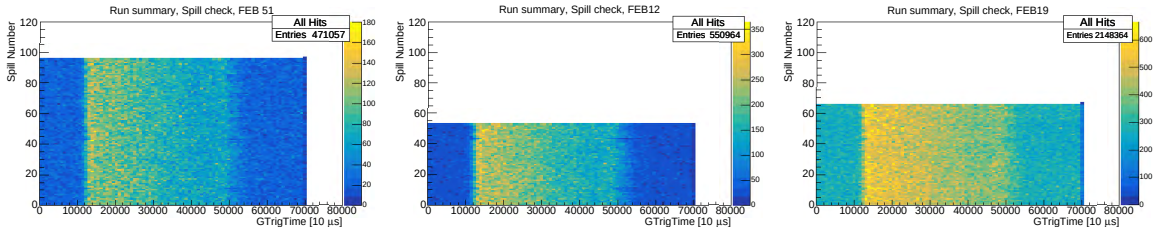

Figure 4-37: Clock signal lost during a data acquisition run which lasted for 95 spills. FEB 12 and FEB 19 stopped acquiring data after spill 53 and 65.

We opted for Cat 6 S/FTP cables, and even those did not always perform as expected. We tried several different manufacturers, trial and error led to our choice of S/FTP cables, but we still had this type of issue online occasionally, a sign that the clk and trig signals were very sensitive to the environment and connectivity.

Hit time and hit amplitude mismatch

As was discussed in section 3.7.3, the hit time is recorded continuously for hits above the trigger threshold on the fast shaper signal path. Whereas for the hit amplitudes the sampling takes place during a hold period which can be initiated by the trigger line, if not already in the middle of a hold or in the dead time. At the end of a hold period, the maximum amplitude for each channel, if above the FPGA threshold, is pushed to the readout data. The problem rises when there are more than one hit occurring on the same channel during a hold period. In this case, the largest analogue amplitude (ADC) is assigned to the last hit time occurred on that channel by the FPGA readout state machine, which causes the hit time and hit amplitude mismatch. The assignment is done via a 3-bit hit ID counter per channel, which is written in the 32-bit words containing the hit time or the hit amplitude information. An example of such a case from data is shown in figure 4-38, where three consecutive hits have occurred on channel 20. The first hit has a large Time over Threshold (ToT) of 38 ticks followed by two after pulse ripples hits with ToT of 7 and 2 ticks respectively.

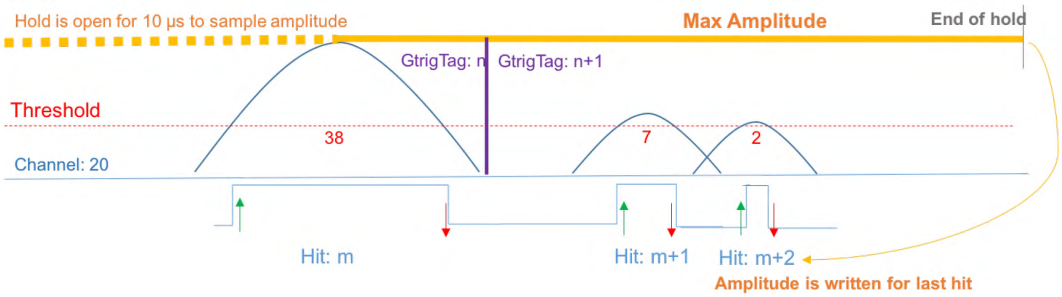

Row #	GTrigTag	channel	HitTimefromSpill	Amplitude	TimeoverThreshold	RiseTime	FallTime
429263 *	5000911 *	20 *	203769828 *	1959 *	19 *	220 *	239 *
429532 *	5003291 *	20 *	213292681 *	3680 *	26 *	3073 *	3099 *
429577 *	5003658 *	20 *	214761315 *	237 *	9 *	3707 *	3716 *
429628 *	5004079 *	20 *	216442496 *	916 *	15 *	888 *	903 *
429674 *	5004511 *	20 *	218171241 *	83 *	5 *	1633 *	1638 *
429721 *	5004673 *	20 *	218821564 *	0 *	38 *	3956 *	3994 *
429724 *	5004674 *	20 *	218821772 *	0 *	7 *	164 *	171 *
429725 *	5004674 *	20 *	218821835 *	3789 *	2 *	227 *	229 *
429813 *	5006672 *	20 *	226814383 *	3756 *	29 *	775 *	804 *
429863 *	5012840 *	20 *	251486852 *	231 *	9 *	1244 *	1253 *
432256 *	5200391 *	20 *	101700156 *	0 *	-1 *	1820 *	-1 *
432275 *	5200398 *	20 *	101728627 *	0 *	-1 *	2291 *	-1 *

Figure 4-38: An example from data in which more than one hit occurs on the same channel during a hold period and the hit time and amplitude are mismatched.

The recorded high gain amplitude for this channel, which is 3789 ADC counts, has then been misassigned to the last hit.

One way to observe the hit time and amplitude mismatch, is via comparison of the

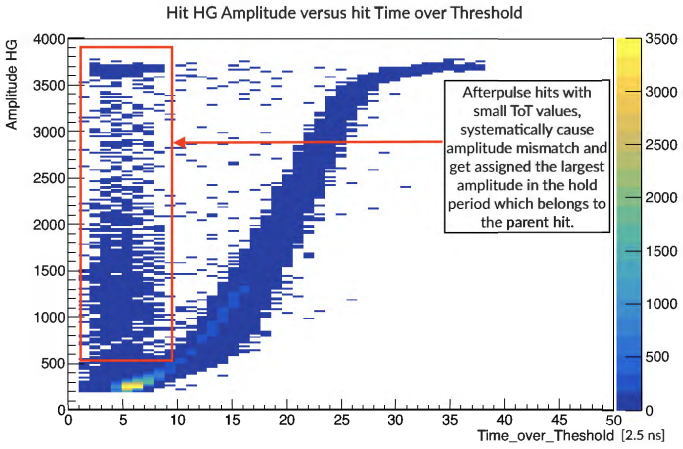

Figure 4-39: Misassignement of hit amplitude is visible in the plot of HG amplitude with respect to ToT.

hit high gain amplitude with the hit ToT in the data sets, as shown in figure 4-39. The unexpected population of hits with small values of ToT and large high gain amplitudes correspond to the afterpulse hits which systematically cause amplitude mismatch. The problem was resolved in a later version of the FPGA firmware in which new data words were foreseen for recording of the time of beginning and end of a hold period. With

this information available the unpacking software was modified to search in the hold period and assign the recorded amplitude correctly to the hit with the largest ToT value (see figure 6-4).

Chapter 5

Detector Performance at J-PARC

5.1 Detector transport from CERN to Japan

The transport of the four Baby MIND detector chassis from CERN to J-PARC was assigned to DB Schenker transport company. The transport route is shown in figure 5-1, which consisted of four stages.

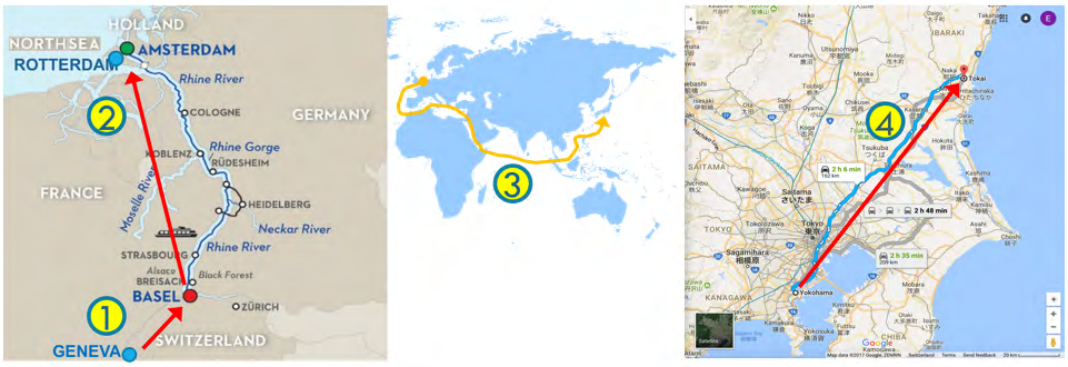

Figure 5-1: Baby MIND detector shipping trajectory from CERN to J-PARC.

- Stage 1: Road transport by truck, from: Geneva (CH) to: Basel (CH)
- Stage 2: Rhine river transport via barge, from: Basel (CH) to: Rotterdam (NL)
- Stage 3: Ship via Suez, from: Rotterdam (NL) to: Yokohama (JP)
- Stage 4: Road transport by truck, from: Yokohama (JP) to: Tokai (JP)

The four detector chassis listed in table 5.1, together with boxes of cable bundles and tools, were transported via four separate open top containers, with admissible load per area of 19.2 kg/cm^2 (case for Baby MIND 5.54 kg/cm^2).

The packaging of the chassis was foreseen to ensure the fragile connectors at the top of the scintillating modules are well protected (figure 5-2). Temperature, humidity

Table 5.1: Baby MIND detector transport chassis specifications.

	Mag. mod.	Scint. mod.	Length [mm]	Width [mm]	Height [mm]	Weight [kg]
Chassis-1	9	7	3925	2150	2260	21205
Chassis-2	8	4	3835	1160	2260	18355
Chassis-3	8	3	3835	1080	2260	17955
Chassis-4	8	4	3835	1520	2260	18955

and shock sensors were placed inside each container to monitor the detector state throughout the journey. These monitors did not provide dynamic feedback during the journey, but they recorded the state of the containers so that it could be studied if any degradation of the detector had taken place. The chassis were fixed against

Figure 5-2: The packaging of detector chassis for transportation.

the container walls using wooden beams shown in figure 5-3. The four containers were

Figure 5-3: Loading detector chassis into the transport containers.

loaded onto separate lorries, the first two left CERN on 17th October 2017 (figure 5-4), the last two left the following day. The detector arrived at J-PARC on 13th December 2017. The report of temperature and humidity of one of the containers during the trip is shown in figure 5-5.

The mechanical parts for 9 permanent B2 chassis were manufactured, painted and prepared for shipment mid January 2018 and were sent to Japan by air transport.

Figure 5-4: Loading the container on the lorry.

Logging Results

Highest Temperature:	28.1 °C; 2017-10-17 09:38:23	Transit Start at:	2017-10-17 09:38:23
Lowest Temperature:	11.6 °C; 2017-10-31 06:38:23	Arrived at:	not available
Average Temperature:	14.7 °C	Alarm at:	none
MKT	15.1 °C	File created:	2017-12-14 01:54:04
Highest rel. Humidity:	67.6 %rH; 2017-10-19 22:13:23		
Lowest rel. Humidity:	34.0 %rH; 2017-10-17 09:43:23		
Average rel. Humidity:	60.5 %rH		

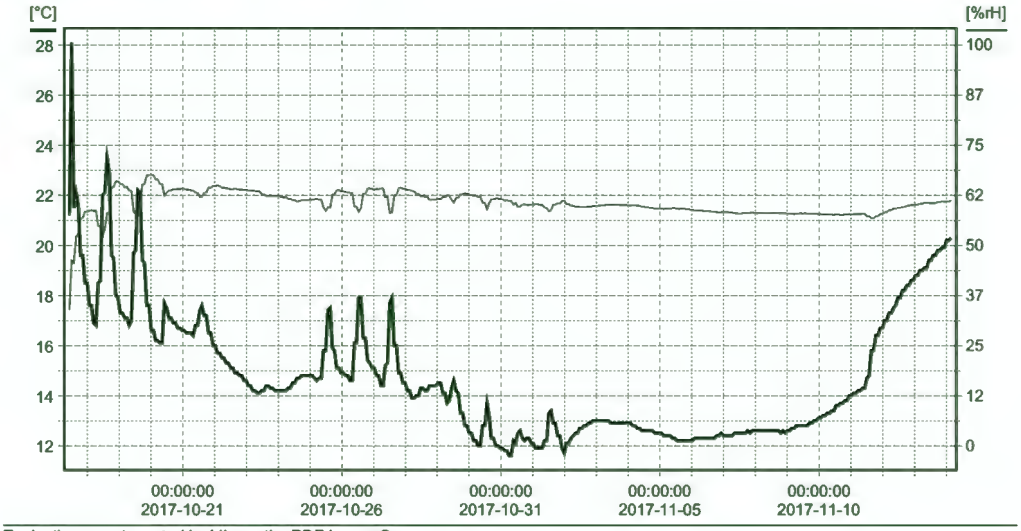

Evaluation report created by Libero, the PDF Logger®

Figure 5-5: Report of temperature and humidity sensor attached to chassis-1.

Figure 5-6: Manufactured parts of the B2 chassis prepared for shipment to Japan.

The electronics were shipped separately also by air transport, at the beginning of February 2018.

5.2 Detector installation and commissioning

5.2.1 Installation of detector modules

The installation of Baby MIND detector modules at the B2 floor of the near detector complex building, was carried out by a team consisting of external contractors *Daiichi-Tekko*, engineers from CERN and Unige, from 5th to 16th February 2018. The project was overseen by Prof. Ichikawa-san, and Dr. E. Noah. The layout of Baby MIND in its J-PARC configuration comprises of 9 B2 chassis with 3 or 4 detector magnet modules inside each, some accompanied with a scintillating module.

The preparatory phase consisted of assembly, alignment and drilling of anchor holes for the 9 B2 chassis, shown in figure 5-7. During the design stage of the B2 chassis,

Figure 5-7: Assembly of B2 chassis.

a simulation study based on the finite element method (FEM), using ABAQUS 6.14. [121] package, was carried out by the mechanical engineering team to identify and address the risk factors in case of earth quake during the assembly and installation of the detector modules into the B2 chassis. The worst case scenario is a single B2 chassis

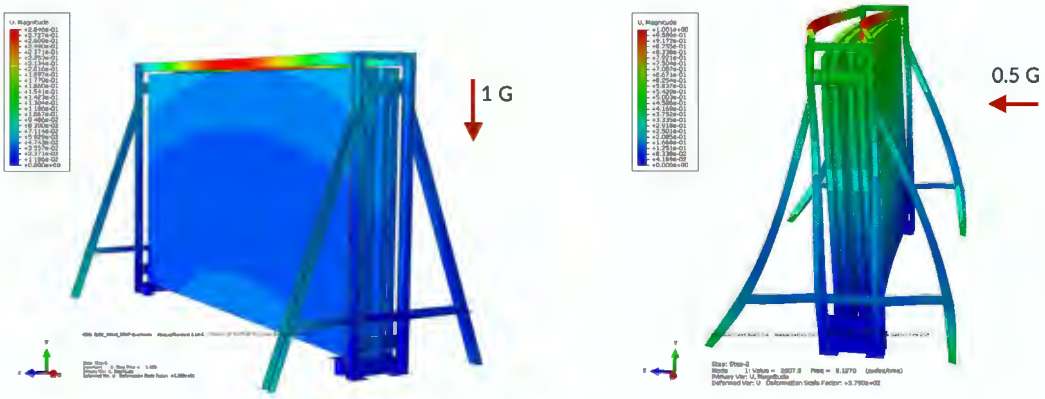

(a) Deformations in a stationary case.

(b) Exaggerated deformations due to a horizontal force in a hypothetical earthquake case.

Figure 5-8: Stabilizer oblique beams for the isolated B2 chassis during the installation phase.

loaded with magnet modules and isolated from the rest of the detector. Additional

stabilizer oblique beams were foreseen to reinforce the B2 chassis for the loading and rolling phase (figure 5-8).

The stages of heavy installation consisted of detaching the detector modules one by one from the transport chassis, lowering them by crane down the narrow shaft to the B2 level, and inserting them into the permanent B2 chassis. The order of installation of the detector modules is shown in figure 5-9. After 19 crane operations, all the

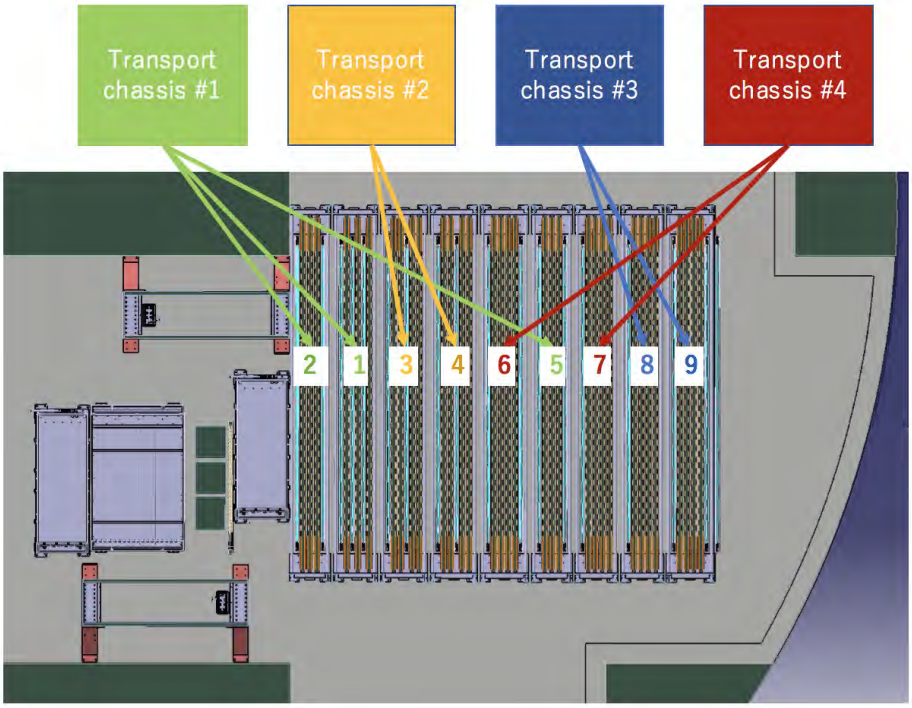

Figure 5-9: Order of installation of detector modules from the transport chassis to the B2 chassis.

modules of Baby MIND detector were installed in their final location at the B2 floor downstream of WAGASCI modules. Once all B2 chassis were bolted to the ground, special interlinks between neighbor chassis were installed on both sides of the full assembly to secure the whole parts and prevent any individual swinging in case of lateral accelerations (earthquake cases). Figure 5-10 captures glimpses of this work.

5.2.2 Installation of the electronics and cable bundles

After the installation of Baby MIND detector modules, 8 Mini crates (MCR) hosting the electronic cards, were installed on top of Baby MIND detector chassis. 126 cable bundles were connected to the FEBs and the scintillating modules (figure 5-11) and tested in the dark counts mode to verify good connection for all channels. The connection layout of the scintillating modules and the FEBs in the mini crate is shown in

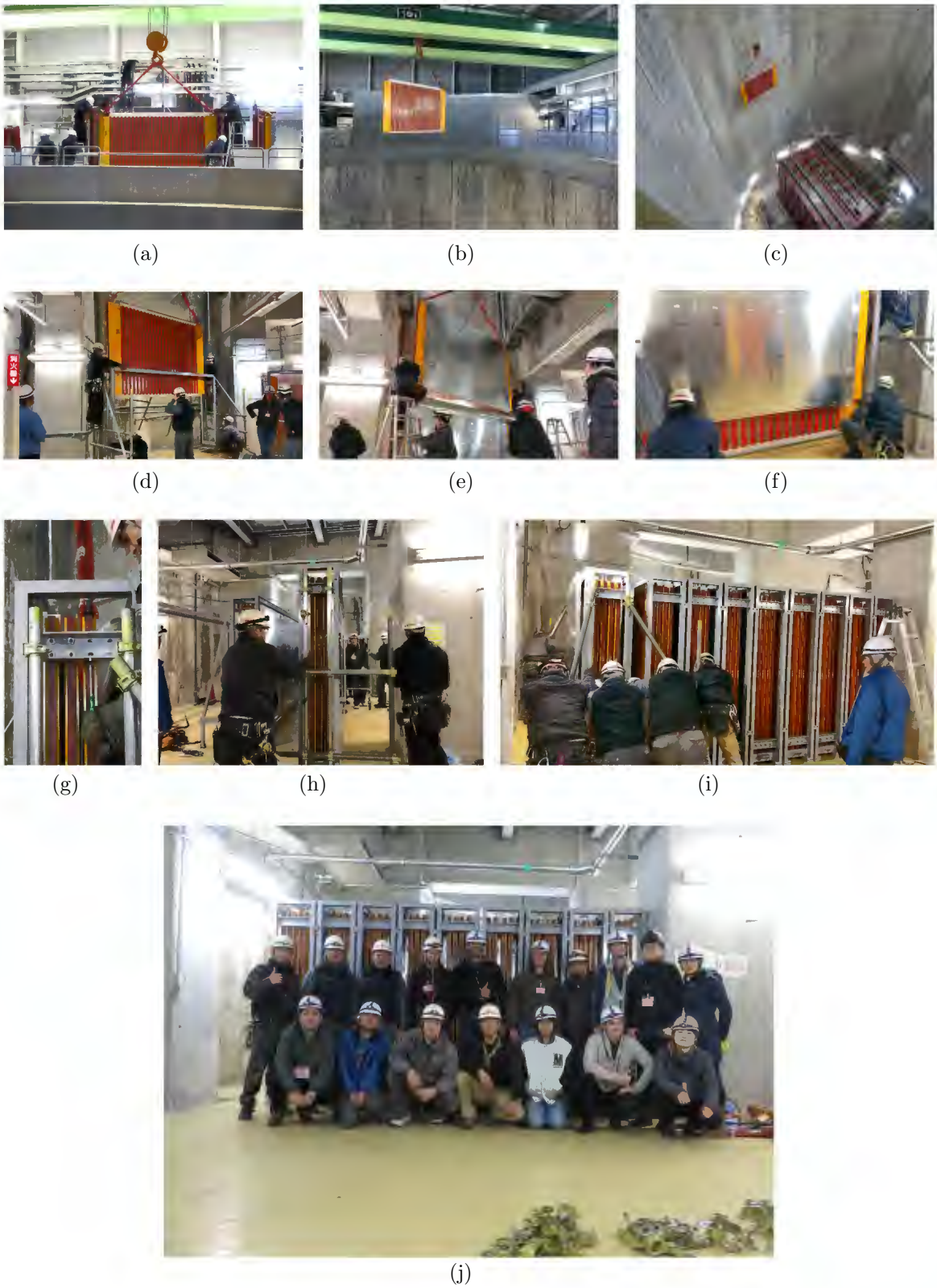

Figure 5-10: Installation of detector modules

figure 5-12. A detailed list of the scintillating modules and the cable bundle connectivity information is summarized in figures 5-13 and 5-14.

A stock of spare cable bundles including 3 vertical cables and 12 horizontal cables

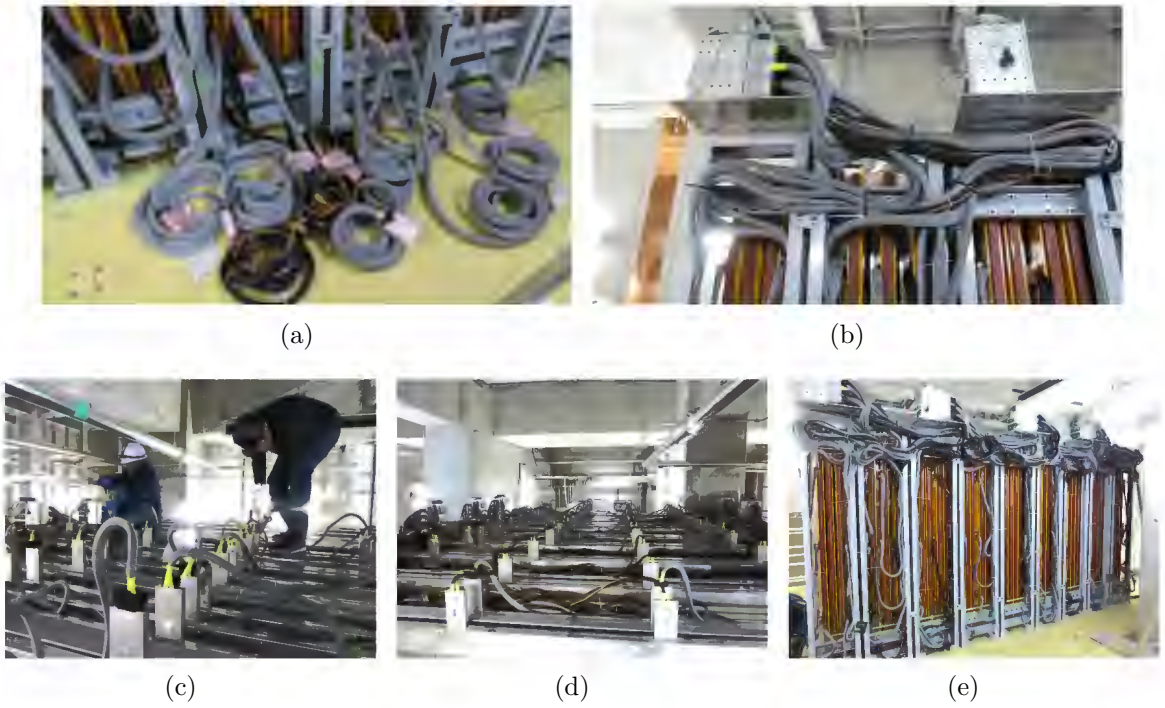

(a) (b)

(c) (d) (e)

Figure 5-11: Installation of cable bundles.

were prepared and stored at J-PARC for future need.

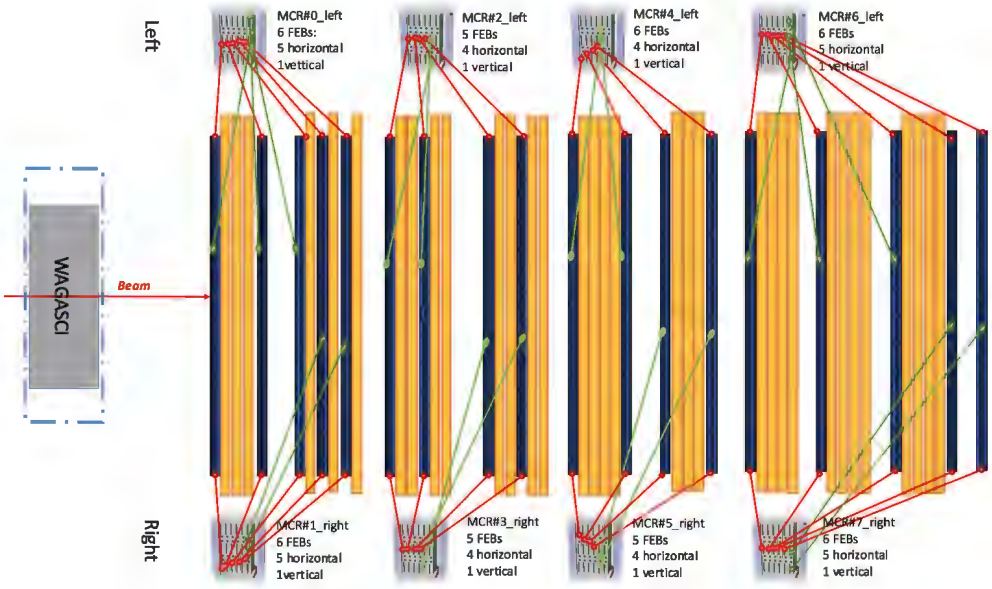

Figure 5-12: Connection layout of the cabling of the scintillating modules to the electronics.

Scintillator module		Cable bundle connectivity						
B2 Order	Orientation	Module side position	Cable Bundle ID	MCR ID	FEB Hardware label	FEB Slot #	FEB Board ID	FEB position
1	Normal	BOTTOM-LEFT	67	0	23	0	0	Bottom
		MIDDLE-LEFT	68	0	23	0	0	Middle
		TOP-LEFT	79	0	23	0	0	Top
		BOTTOM-RIGHT	53	1	30	0	8	Bottom
		MIDDLE-RIGHT	48	1	30	0	8	Middle
		TOP-RIGHT	54	1	30	0	8	Top
		VERTICAL	149	0	38	5	5	Bottom
2	Back-to-front	BOTTOM-LEFT	90	0	24	1	1	Bottom
		MIDDLE-LEFT	94	0	24	1	1	Middle
		TOP-LEFT	92	0	24	1	1	Top
		BOTTOM-RIGHT	93	1	31	1	9	Bottom
		MIDDLE-RIGHT	91	1	31	1	9	Middle
		TOP-RIGHT	95	1	31	1	9	Top
		VERTICAL*	144	0	38	5	5	middle
3	Normal	BOTTOM-LEFT	49	0	35	2	2	Bottom
		MIDDLE-LEFT	43	0	35	2	2	Middle
		TOP-LEFT	50	0	35	2	2	Top
		BOTTOM-RIGHT	15	1	33	2	10	Bottom
		MIDDLE-RIGHT	77	1	33	2	10	Middle
		TOP-RIGHT	78	1	33	2	10	Top
		VERTICAL	142	0	38	5	5	Top
4	Normal	BOTTOM-LEFT	70	0	36	3	3	Bottom
		MIDDLE-LEFT	71	0	36	3	3	Middle
		TOP-LEFT	72	0	36	3	3	Top
		BOTTOM-RIGHT	58	1	39	3	11	Bottom
		MIDDLE-RIGHT	59	1	39	3	11	Middle
		TOP-RIGHT	113	1	39	3	11	Top
		VERTICAL	147	1	48	5	13	Bottom
5	Normal	BOTTOM-LEFT	8	0	37	4	4	Bottom
		MIDDLE-LEFT	27	0	37	4	4	Middle
		TOP-LEFT	10	0	37	4	4	Top
		BOTTOM-RIGHT	9	1	40	4	12	Bottom
		MIDDLE-RIGHT	29	1	40	4	12	Middle
		TOP-RIGHT	28	1	40	4	12	Top
		VERTICAL	145	1	48	5	13	Middle
6	Normal	BOTTOM-LEFT	84	2	26	0	16	Bottom
		MIDDLE-LEFT	88	2	26	0	16	Middle
		TOP-LEFT	121	2	26	0	16	Top
		BOTTOM-RIGHT	64	3	52	0	24	Bottom
		MIDDLE-RIGHT	65	3	52	0	24	Middle
		TOP-RIGHT	66	3	52	0	24	Top
		VERTICAL	148	2	53	4	20	Bottom
7	Normal	BOTTOM-LEFT	19	2	41	1	17	Bottom
		MIDDLE-LEFT	24	2	41	1	17	Middle
		TOP-LEFT	31	2	41	1	17	Top
		BOTTOM-RIGHT	25	3	43	1	25	Bottom
		MIDDLE-RIGHT	23	3	43	1	25	Middle
		TOP-RIGHT	32	3	43	1	25	Top
		VERTICAL	136	2	53	4	20	Middle
8	Normal	BOTTOM-LEFT	96	2	45	2	18	Bottom
		MIDDLE-LEFT	97	2	45	2	18	Middle
		TOP-LEFT	44	2	45	2	18	Top
		BOTTOM-RIGHT	55	3	42	2	26	Bottom
		MIDDLE-RIGHT	123	3	42	2	26	Middle
		TOP-RIGHT	57	3	42	2	26	Top
		VERTICAL	141	3	50	4	28	Bottom
9	Normal	BOTTOM-LEFT	105	2	46	3	19	Bottom
		MIDDLE-LEFT	109	2	46	3	19	Middle
		TOP-LEFT	110	2	46	3	19	Top
		BOTTOM-RIGHT	108	3	54	3	27	Bottom
		MIDDLE-RIGHT	106	3	54	3	27	Middle
		TOP-RIGHT	107	3	54	3	27	Top
		VERTICAL	151	3	50	4	28	Middle

Figure 5-13: Connectivity detail of scintillating modules 1 to 9.

Scintillator module		Cable bundle connectivity						
B2 Order	Orientation	Module side position	Cable Bundle ID	MCR ID	FEB Hardware label	FEB Slot #	FEB Board ID	FEB position
10	Normal	BOTTOM-LEFT	0	4	13	0	32	Bottom
		MIDDLE-LEFT	38	4	13	0	32	Middle
		TOP-LEFT	2	4	13	0	32	Top
		BOTTOM-RIGHT	3	5	16	0	40	Bottom
		MIDDLE-RIGHT	30	5	16	0	40	Middle
		TOP-RIGHT	5	5	16	0	40	Top
		VERTICAL	150	4	49	4	36	Bottom
11	Back-to-front	BOTTOM-LEFT	112	4	18	1	33	Bottom
		MIDDLE-LEFT	126	4	18	1	33	Middle
		TOP-LEFT	69	4	18	1	33	Top
		BOTTOM-RIGHT	41	5	17	1	41	Bottom
		MIDDLE-RIGHT	125	5	17	1	41	Middle
		TOP-RIGHT	47	5	17	1	41	Top
		VERTICAL*	143	4	49	4	36	Middle
12	Normal	BOTTOM-LEFT	82	4	21	2	34	Bottom
		MIDDLE-LEFT	124	4	21	2	34	Middle
		TOP-LEFT	83	4	21	2	34	Top
		BOTTOM-RIGHT	51	5	20	2	42	Bottom
		MIDDLE-RIGHT	46	5	20	2	42	Middle
		TOP-RIGHT	52	5	20	2	42	Top
		VERTICAL	200	5	28	4	44	Bottom
13	Back-to-front	BOTTOM-LEFT	127	4	32	3	35	Bottom
		MIDDLE-LEFT	62	4	32	3	35	Middle
		TOP-LEFT	117	4	32	3	35	Top
		BOTTOM-RIGHT	73	5	27	3	43	Bottom
		MIDDLE-RIGHT	74	5	27	3	43	Middle
		TOP-RIGHT	75	5	27	3	43	Top
		VERTICAL*	146	5	28	4	44	Middle
14	Normal	BOTTOM-LEFT	98	6	34	0	48	Bottom
		MIDDLE-LEFT	56	6	34	0	48	Middle
		TOP-LEFT	6	6	34	0	48	Top
		BOTTOM-RIGHT	11	7	3	0	56	Bottom
		MIDDLE-RIGHT	14	7	3	0	56	Middle
		TOP-RIGHT	20	7	3	0	56	Top
		VERTICAL	138	6	25	5	53	Bottom
15	Normal	BOTTOM-LEFT	99	6	9	1	49	Bottom
		MIDDLE-LEFT	100	6	9	1	49	Middle
		TOP-LEFT	116	6	9	1	49	Top
		BOTTOM-RIGHT	102	7	4	1	57	Bottom
		MIDDLE-RIGHT	103	7	4	1	57	Middle
		TOP-RIGHT	104	7	4	1	57	Top
		VERTICAL	140	6	25	5	53	Middle
16	Normal	BOTTOM-LEFT	80	6	10	2	50	Bottom
		MIDDLE-LEFT	89	6	10	2	50	Middle
		TOP-LEFT	101	6	10	2	50	Top
		BOTTOM-RIGHT	87	7	5	2	58	Bottom
		MIDDLE-RIGHT	86	7	5	2	58	Middle
		TOP-RIGHT	85	7	5	2	58	Top
		VERTICAL	135	6	26	5	53	Top
17	Back-to-front	BOTTOM-LEFT	37	6	12	3	51	Bottom
		MIDDLE-LEFT	35	6	12	3	51	Middle
		TOP-LEFT	40	6	12	3	51	Top
		BOTTOM-RIGHT	36	7	56	3	59	Bottom
		MIDDLE-RIGHT	34	7	56	3	59	Middle
		TOP-RIGHT	39	7	56	3	59	Top
		VERTICAL*	154	7	44	5	61	Bottom
18	Back-to-front	BOTTOM-LEFT	16	6	14	4	52	Bottom
		MIDDLE-LEFT	22	6	14	4	52	Middle
		TOP-LEFT	21	6	14	4	52	Top
		BOTTOM-RIGHT	26	7	15	4	60	Bottom
		MIDDLE-RIGHT	7	7	15	4	60	Middle
		TOP-RIGHT	18	7	15	4	60	Top
		VERTICAL*	137	7	44	5	61	Middle

* vertical cables connected to scintillating modules with orientation Back-to-front have to be connected inversly to the module side positions (a,b,c,d ->d,c,b,a)

Figure 5-14: Connectivity detail of scintillating modules 10 to 18.

5.2.3 Connection of magnet power supplies

The Baby MIND magnet system, described in section 3.3, consists of 33 magnet modules, each with their own aluminum coil. The modules are connected together in series via aluminum interconnect pieces shown in figure 5-15. Two rack mountable power supplies, serially connected, provide the 140 A current for generation of 1.5 T magnetic field in the steel plates. The power supplies require a 400 V three phase AC input power source. For this purpose a new power line was extracted from the ND280 mag-

(a) Aluminum interconnects between B2 chassis

(b) Power supplies rack

(c) Serial connection of power supplies

(d) Magnet switch panel

Figure 5-15: Magnet connection details.

net power line, and installed on the B2 floor for the Baby MIND magnet on February 20th 2018. The copper cables between the detector magnet coil, the magnet switch panel and the power supplies were installed on February 27th 2018 . The first stand alone operation of the Baby MIND magnet took place on March 14th 2018, after the J-PARC facility inspection was carried out.

5.2.4 Safety requirements

Following the request of J-PARC facility, two warning lights and an emergency shutdown button (interlock) were installed on the Baby MIND magnet rack at B2 floor. The red warning lights are to be ON as soon as the power supplies are energized (figure 5-16).

Furthermore, approval of 24h operation of the Baby MIND magnet was conditional

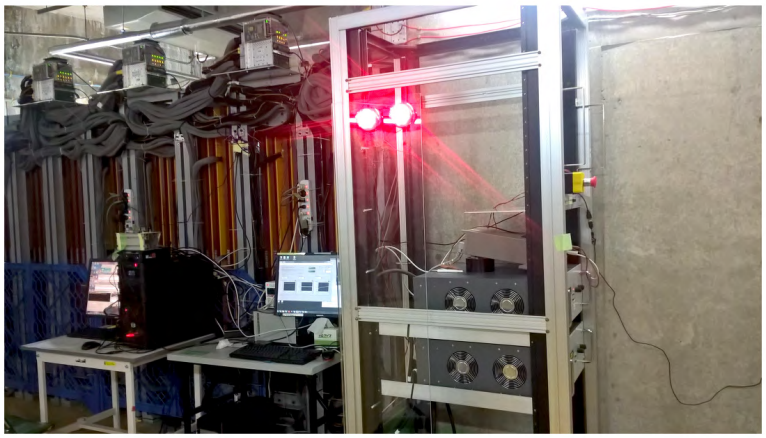

Figure 5-16: Warning lights and emergency stop button for the Baby MIND magnet power supplies.

on the development of a live monitoring and an alarm system for the magnet power supplies current and voltage and remote control capabilities from the control room. For this purpose, a magnet monitoring application was developed as a LabVIEW program which would allow the user to set and monitor magnet current and voltage, and to activate a remote shutdown. The monitoring system was programmed to generate an alarm signal and automatically activate a remote shutdown if the current or voltage went out of a predefined range. Figure 5-17 shows the front panel of the magnet monitoring application. The software was installed on a PC located on the B2 floor and connected to the master power supply via an RJ45 link. The plots in figure 5-18 show the voltage and current of the master power supply, recorded by the magnet monitoring application.

5.2.5 Synchronization with the T2K beam

In order to synchronize the Baby MIND data readout with the J-PARC neutrino beam, a beam trigger signal, arriving 30 μs prior to the beam was used. The beam trigger signal which is provided on the yellow crates shown in figure 5-19 has a 100 ns width and signal level of -760 mV. This signal was measured with an oscilloscope in order to

Figure 5-17: LabView program for live monitoring of the magnet power supplies.

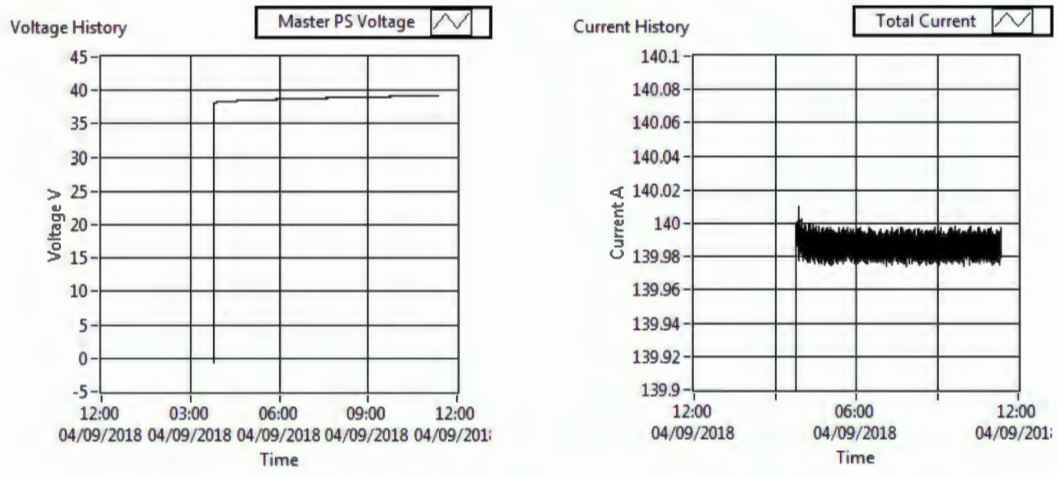

(a) Voltage monitoring

(b) Current monitoring

Figure 5-18: Voltage and current monitoring of the master power supply.

finalize the MCB input signal compatibility, before it was sent to Japan.

The spill number is available on a unit located on the WAGASCI rack (figure 5-20).

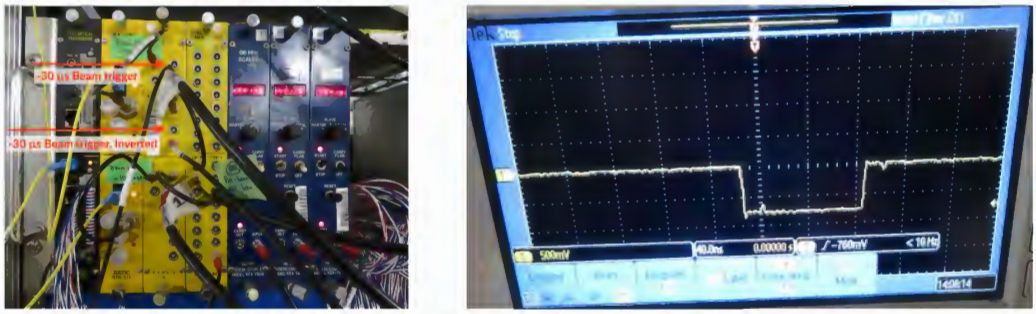

Figure 5-19: Beam trigger signal available on the beamline rack at B2 floor.

The spill number is transmitted by a 2×17 pins connector from which the last row is not connected. The voltage difference between the pins of each row can take two

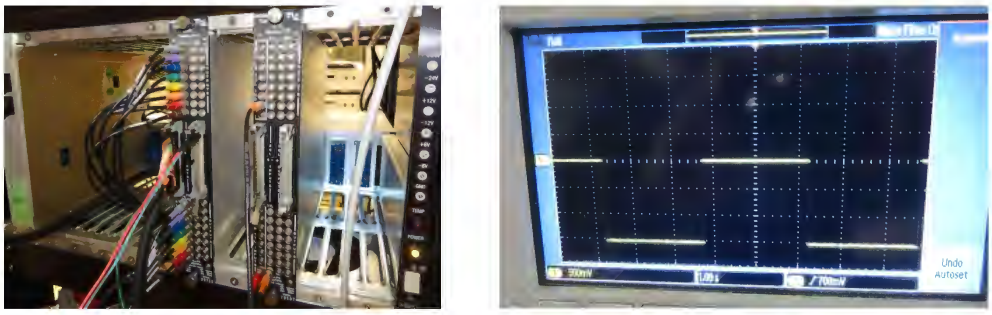

Figure 5-20: Spill number unit and an example of the signal level of a positive pin of a bit counter.

values of -0.9 V or +0.9 V, indicating the bit to be 0 or 1 respectively. From the 16 bit counter which holds the spill number, the most significant bit is always stuck to value 1, as a consequence the spill number runs from the smallest value 32768 to the largest value 65535. With the current accelerator spill period of 2.479 s, the overflow of the spill number occurs after about 22 hours and 33 minutes.
Figure 5-21 shows the master clock board installed on the rack, with the input beam trigger signal and the spill number flat cable connected to the board. The overall

Figure 5-21: Master clock board installed at J-PARC with cables connected.

schematics of the synchronization utilizing the beam trigger signal and the spill number, is shown in figure 5-22. More details on the functionality of the master clock board is covered in section 3.7.7.

5.2.6 Interference with the ND280 magnet

The commissioning of the Baby MIND magnet at J-PARC in March 2018, coincided with major technical problems occurring for the ND280 UA1 magnet. These events delayed the scheduled plans for testing the simultaneous operation of the Baby MIND

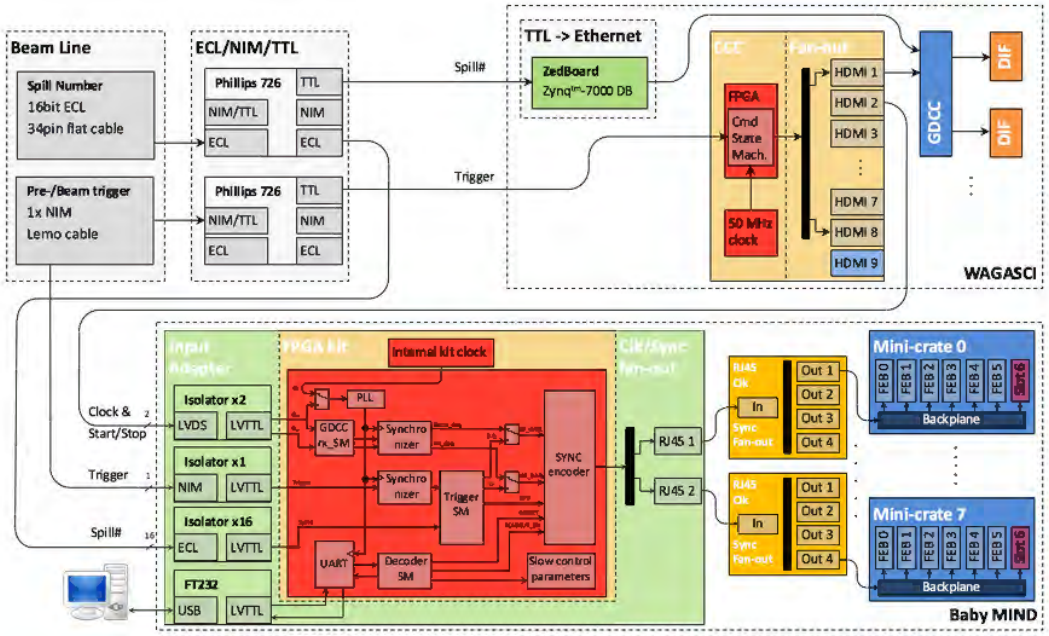

Figure 5-22: Synchronization scheme at J-PARC.

magnet and the ND280 magnet. The test was finally carried out on 2nd of May 2018, where the Baby MIND power supply was ON with nominal current 140 A and the current for the ND280 magnet was increased slowly in several steps. It was observed that upon setting the ND280 magnet current higher than 1500 A, the Baby MIND power supply experienced an AC failure and automatically executed a shutdown. A summary of the measurements is reported in table 5.2. The AC failure was associated

Table 5.2: ND280 and Baby MIND magnet operation test 2nd of May 2018.

ND280 magnet current [A]	Baby MIND magnet ON, 140 A	wait time
500	OK	3 min
1000	OK	3 min
1500	OK	3 min
2000	**AC Failed**	immediately
1000	OK	3 min
1500	OK	3 min
1510	**AC Failed**	immediately

with the noise spikes produced by the ND280 magnet power converter. These spikes are rather normal in this kind of switching power devices, and it was known to the J-PARC experts since 2009. Upon consultation with the Baby MIND magnet power supplies manufacturer, a solution was put forward to modify the *AC Fail* circuitry and make it less sensitive to the noise spike on the mains. The modification of the power supplies consisted of replacement of a 5.6 kΩ with a 15 kΩ resistor and the addition of a 470 nF capacitor to the AC Fail circuitry, which was carried out on 10th of May 2018.

On the same day new series of tests were conducted with both magnets successfully

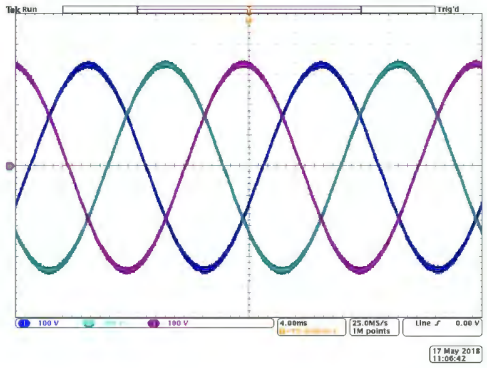

(a) ND280 magnet current: 0 A,
Baby MIND magnet current: 0 A

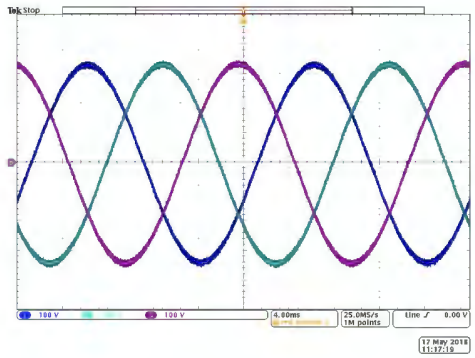

(b) ND280 magnet current: 0 A,
Baby MIND magnet current: 140 A

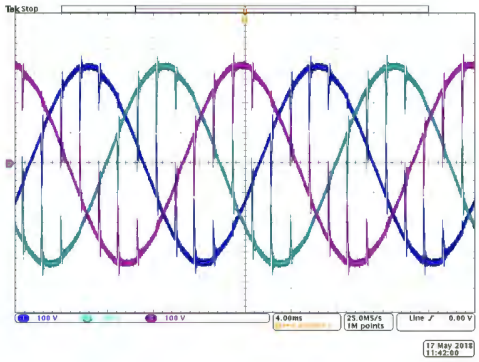

(c) ND280 magnet current: 2900 A,
Baby MIND magnet current: 0 A

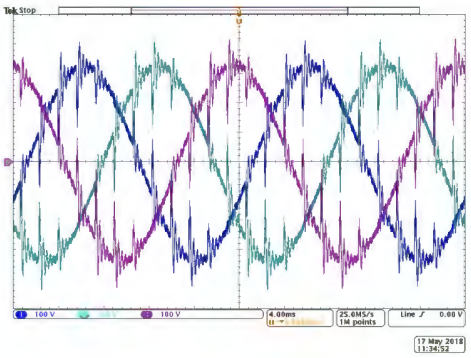

(d) ND280 magnet current: 2900 A,
Baby MIND magnet current: 140 A

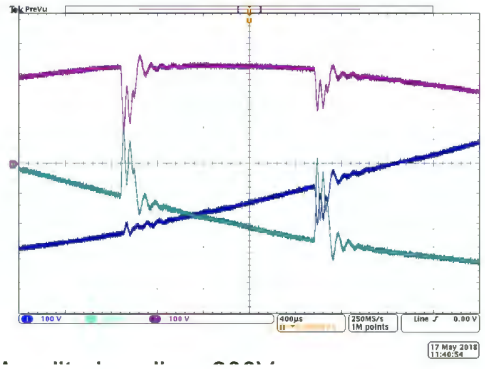

(e) ND280 magnet current: 2900 A,
Baby MIND magnet current: 0 A, zoom

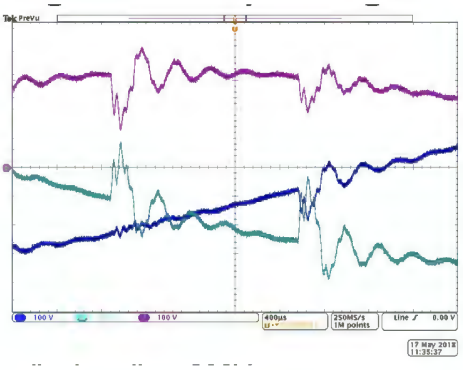

(f) ND280 magnet current: 2900 A,
Baby MIND magnet current: 140 A, zoom

Figure 5-23: Noise measurement on the 400 V power line, induced by the ND280 magnet power converter and modified by Baby MIND power supplies.

energized to their nominal currents. It was observed that the noise spectrum of the ND280 magnet power converter gets modified by the presence of the Baby MIND power supplies which act as a resistive load and induce a ringing effect shown in figure 5-23. It was also confirmed by measurement that the Baby MIND power supplies do not generate any noise on the 400 V line, if operated in the absence of the ND280

magnet. There were further complications as the reports suggested that the INGRID modules had tripped during the ND280 and Baby MIND magnet tests. This problem was resolved after improvements of the grounding connections of the INGRID module at the B2 floor on the 24th of May 2018.

Finally, in the last week of the run period, the 24h operation of the Baby MIND magnet in parallel to the ND280 magnet was approved by the near detector run coordinators, allowing one week of data taking with the magnet ON from 24th to 31st of May 2018. A summary of the Baby MIND commissioning run is presented in table 5.3 and in figure 5-24.

The beam configuration during the commissioning run was anti-neutrino beam mode,

Table 5.3: Summary of the commissioning run from March to May 2018.

Date	**Firmware**	**Baby MIND magnet**	**ND280 magnet**	**Comments**
9 March to 28 March	6.2 v. 306	OFF	OFF	Waiting for approval of Baby MIND magnet operation.
29 March to 10 April	6.2 v. 306	ON	OFF	Day time only operation of Baby MIND magnet.
11 April to 24 April	6.2 v. 349	ON	OFF	
24 April to 2 May	6.2 v. 349	OFF	ON	ND280 magnet repair works.
4 May to 7 May	6.3 v. 351	ON	OFF	24h operation of Baby MIND in absence of ND280 magnet.
7 May to 23 May	6.3 v. 351	OFF	ON	ND280 magnet fixed, priority to ND280 data taking.
24 May to 31 May	6.3 v. 351	ON	ON	Green light given for both magnets ON simultaneously.

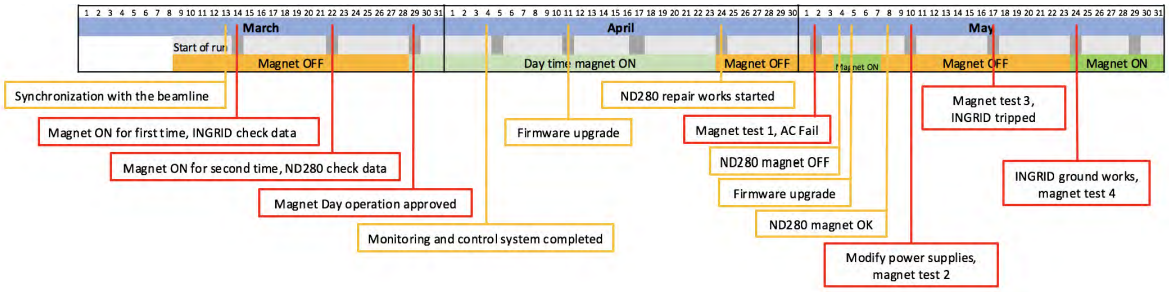

Figure 5-24: Time line of the commissioning run from March to May 2018.

with an average beam power of 470 kW. A total of 5×10^{20} POT were delivered during the 2018 run. Approximately 1.1×10^{20} POT data with magnet ON was collected by Baby MIND.

Regarding the magnet interference issue, the decision was made at the end of the commissioning run to separate the power lines of the ND280 magnet and the Baby MIND magnet, and use an existing 200 V power line for the Baby MIND magnet. A new power supply compatible with the new power line was therefore procured and installed for the 2019 run.

5.3 Development of a DAQ system

After the commissioning run in 2018 which utilized the same DAQ setup as the CERN beam test with eight instances of the AFE host application, a general plan was adopted to develop a DAQ system in two stages. The first stage, aimed to be a stand alone Baby MIND DAQ, operational for the first physics run of Baby MIND in 2019. The second stage, which foresees an integrated DAQ within the T2K MIDAS environment together with other WAGASCI sub-detectors, is yet to be developed.

The standalone Baby MIND DAQ software for the first physics run, was based on the already existing Unige library, consisting of the VHDL application firmware library for the FPGA, USB-3 Cypress FX3 micro-controller and the C# host application (AFE) monodev library. Figure 5-25 shows the VHDL library within the FPGA firmware which handles the bi-directional slow control channel and the fast one directional data readout channel.

The objectives for the DAQ software were to:

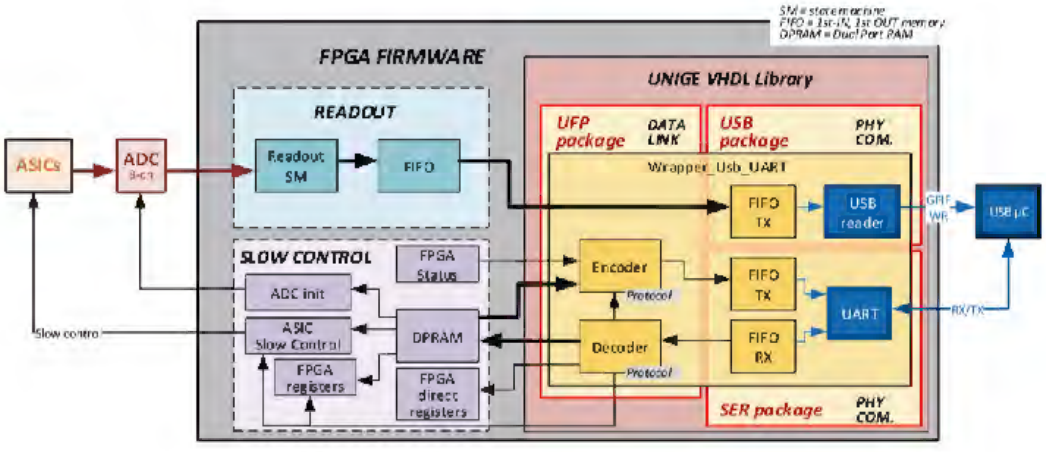

Figure 5-25: Unige VHDL library

- Operate multiple MCRs simultaneously.
- Control the MCB and the trigger signals.
- Handle data output to file (or UDP socket).

- Handle error messages.
- Monitor data taking status.

The old AFE application was designed to communicate with one mini crate at a time as illustrated in figure 5-26. Whereas the core concept of the new DAQ software,

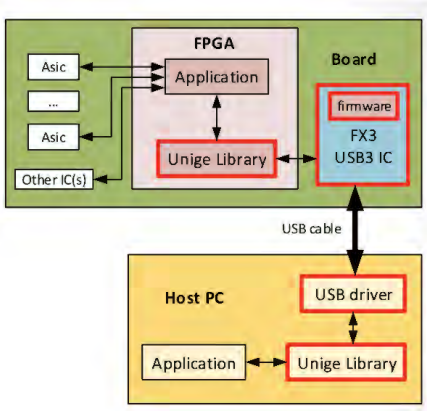

Figure 5-26: AFE host application communicates with one mini crate at a time.

shown in the diagram in figure 5-27, is centered around the ability to drive multiple mini crates simultaneously. This task was accomplished by adopting a multi-threading

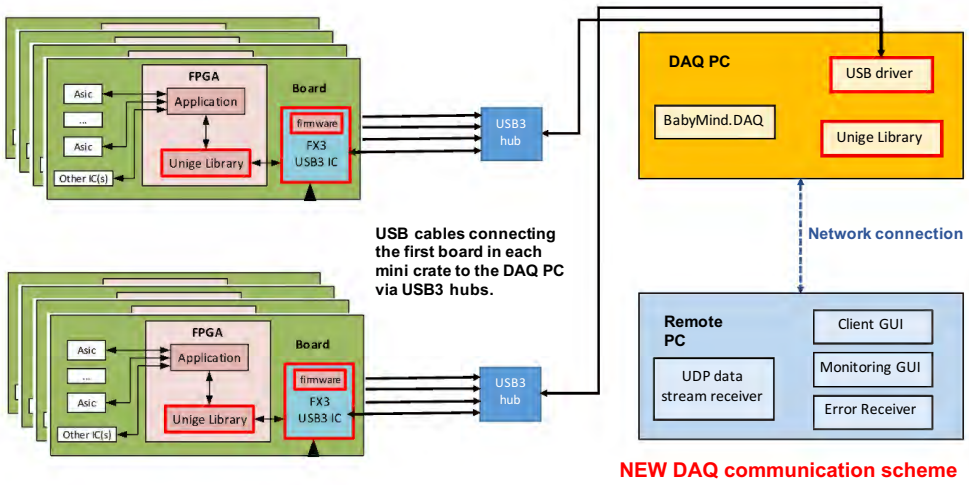

Figure 5-27: New DAQ software handles communication with multiple mini crates.

strategy. The main drive to go for a multi-threading concept was the complexity of handling multiple USB communications, which cannot be properly handled by one thread. The overall architecture of the DAQ software for the Baby MIND first physics run is shown in figure 5-28. It consists of the DAQ main program running on a local PC at the B2 floor which is physically connected to the detector hardware and some client units running on a remote PC located in the control room which are connected to the

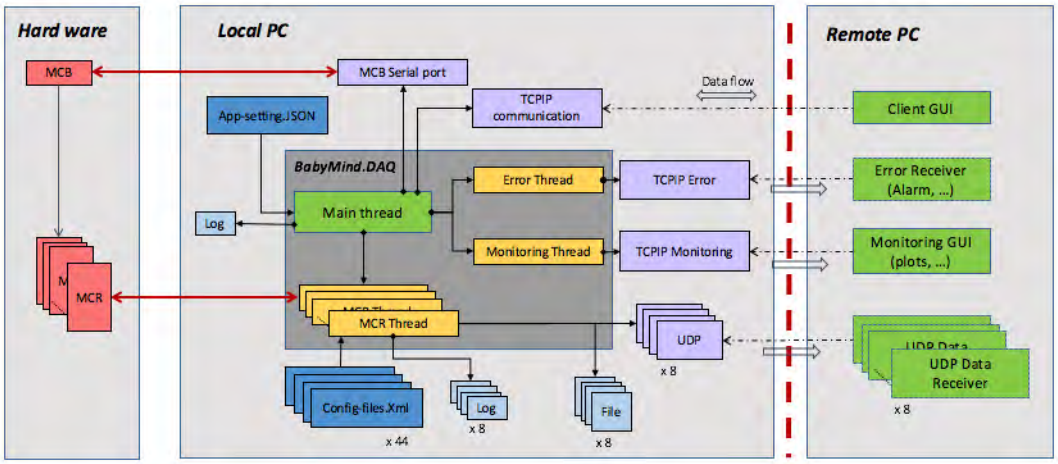

Figure 5-28: DAQ software overall architecture and communication links.

main DAQ through the J-PARC local network. In this architecture, the initialization tasks are performed autonomously by the main DAQ program, and simplified control commands are delivered to the main program by a client unit through a TCP/IP communication channel. This scheme is designed to minimize the shifter interaction for a 24h operation of the detector. At the same time it allows for immediate intervention and problem solving by providing continuous monitoring of the system parameters and generating error messages to alert the shifter if an action is required.

Upon the launch of the DAQ software, several actions are performed (see figure 5-29) in order to build the environment according to the hardware description which contains number of active MCRs, number and ID of FEBs, etc. In this process a dedicated thread is created per MCR, which is tasked to establish a link with the chain of FEBs in the MCR for control and data readout. During an acquisition run, a binary data file is created and stored to disk per MCR. After the creation of the MCR threads, the error thread and the monitoring thread, and the establishment of the communication socket, the program enters an idle state, waiting for a client to connect, and to request execution of different commands. This communication scheme is at the core of the DAQ architecture which foresees the operation of detector from distance.

The tasks performed by different threads in the DAQ software are described below:

- DAQ program main thread:
  - Building the environment based on an app-settings input file in JSON format [122], describing the hardware.
  - Creating individual mini crate (MCR) threads and linking them to the corresponding USB port.
  - Creating the monitoring thread and the error threads and their corresponding

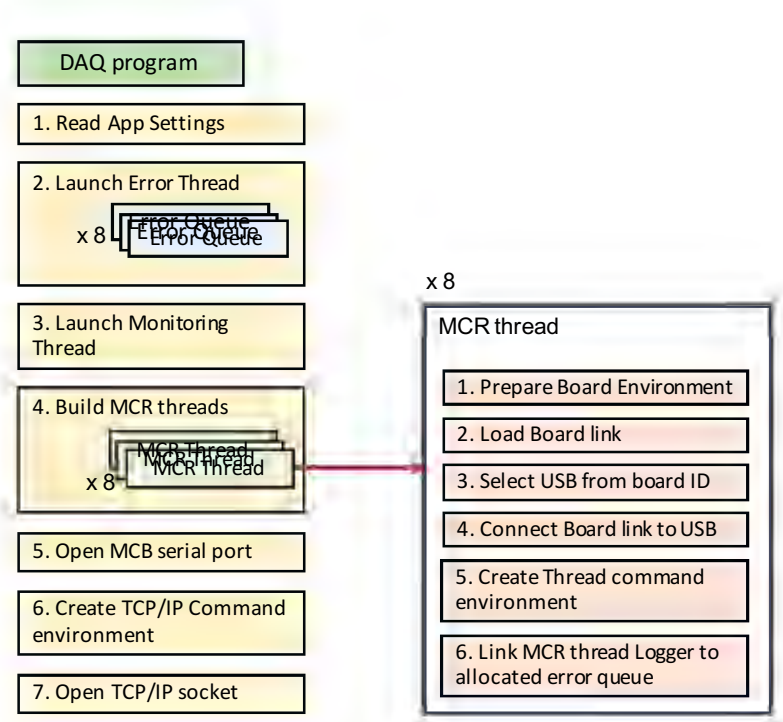

Figure 5-29: Building of the environment upon launch of the DAQ software.

sockets.

- Creating TCP/IP command environments in order to execute client commands.
- Handling MCB communications
- Creating an application logger to record action messages and send exceptions to the error sockets.
- Handling client communication through a TCP/IP socket.

- MCR thread
  - Creating an instance of the Board link and Baby MIND lib, to have access to the hardware functions (figure 5-30).
  - Creating thread command environment and executing commands which are called in the main thread.
  - Creating a dedicated thread logger to record action messages and send exceptions to the error sockets.

- Monitoring thread
  - The monitoring thread can be activated or dis-activated upon client request.
  - After activation, it periodically updates a monitoring data object with JSON format, and sends it to the monitoring socket.
  - The monitoring thread has no interference with the main thread or the MCR threads command execution.

- Error thread

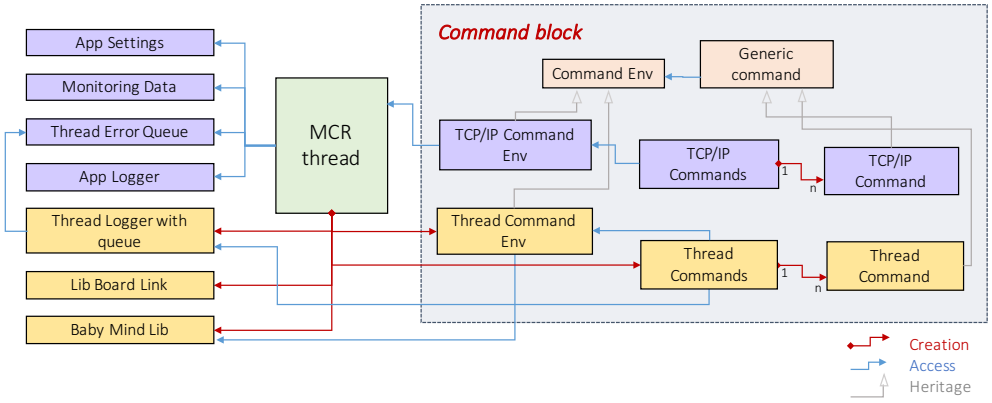

Figure 5-30: Diagram of the classes associated to the MCR thread.

– The error thread is activated by the main thread.
– If any of the several loggers belonging to different threads, record a message with severity level of *Critical* or *Failure*, the message automatically gets pushed to the error socket (figure 5-31).
– A client can join the error socket, and listen to the error messages.

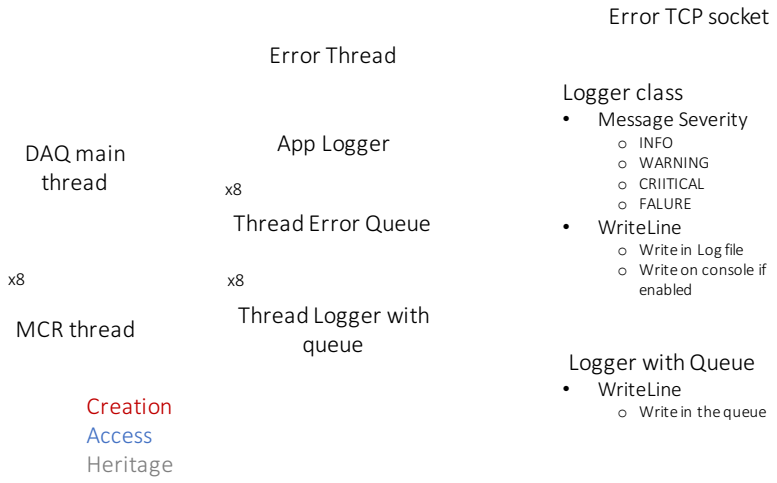

Figure 5-31: Diagram of the logger class and the error thread.

5.3.1 Client GUI

In addition to the main DAQ software, a Client GUI with a simple interface was developed, for the testing and debugging of the different functionalities of the DAQ software, and was later adapted as a temporary solution for the remote control of the DAQ software. A proper MIDAS implementation is planned to replace the Client GUI in the future. The role of the Client GUI is to establish a connection with the TCPIP server socket opened by the DAQ main thread and to send pre-defined command

strings to the DAQ server, by means of clickable buttons on the GUI, and receive and display corresponding answer strings. The run number and run type can be manually set by the shifter, which will appear in the output data file names. The Client GUI can be operated from the same PC which runs the main DAQ program or from a remote PC connected via network to the DAQ PC. Figure 5-32

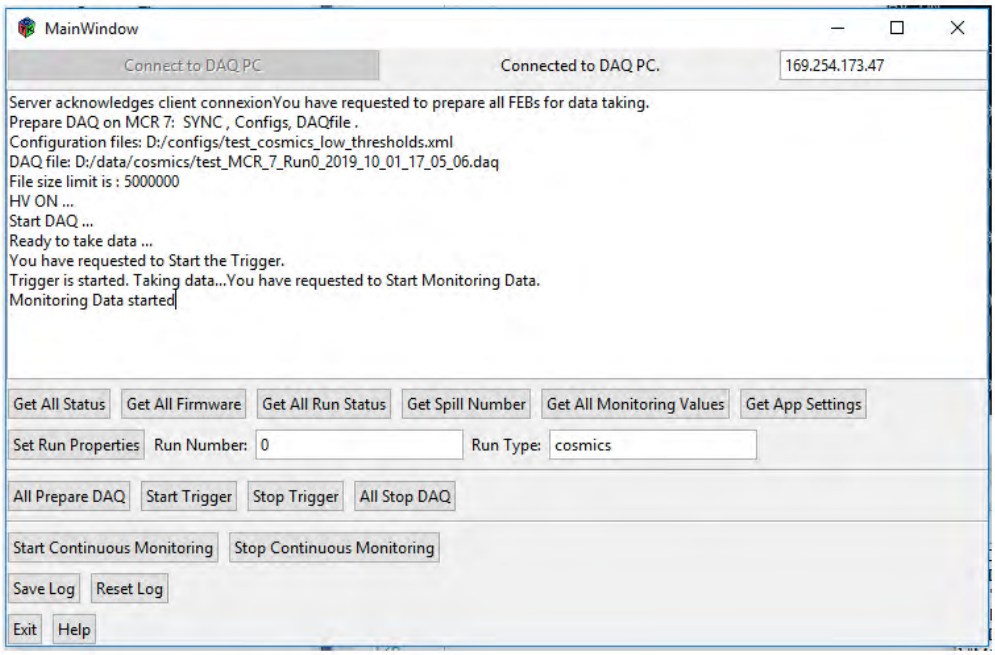

Figure 5-32: The Client GUI is developed for sending pre-defined command strings to the DAQ software.

5.3.2 Monitoring data

For continuous monitoring of the parameters related to the detector status during data taking, a monitoring data class with JSON data format was created. The class consists of 15 FEB board parameters, 9 MCR parameters and 2 MCB related parameters, shown in figure 5-33. An instance of the monitoring data class is created during the initialization of the monitoring thread, based on the detector hardware description. Upon activation of the monitoring thread and connection of a monitoring client, the monitoring data is periodically updated with the latest parameters values and sent to the monitoring client in string format. A demo Monitoring GUI was developed to demonstrate the concept of receiving, decoding and displaying the monitoring data (figure 5-34). In absence of a dedicated monitoring client a TeraTerm application [123] can be used to receive the monitoring data in string format.

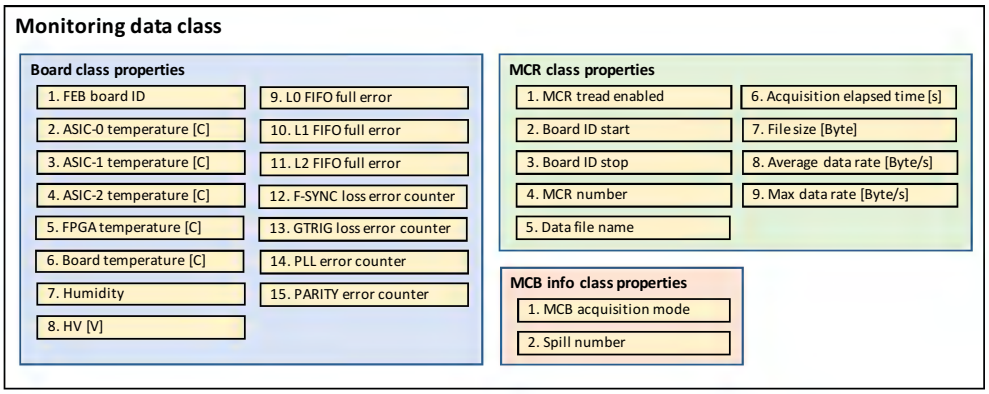

Figure 5-33: Monitoring data class properties.

Figure 5-34: A Monitoring GUI receiving, decoding and displaying the monitoring data.

5.3.3 Receiving errors with Tera Term

For receiving and monitoring the error messages, the Tera Term was used. Figure 5-35 shows examples of critical error messages from the MCR threads 0, 2, 4 and 6, all of which experienced the loss of CLK signal.

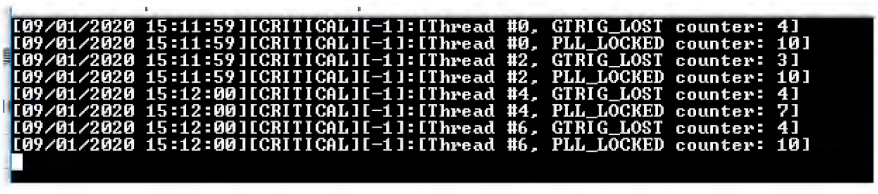

Figure 5-35: Error monitoring with Tera Term.

5.3.4 Output data files

For each data run a binary data file is created per MCR (8 in total). Each file contains the asynchronous data readout of all the FEBs in a daisy chain within a MCR, pushed out in TDM mode (see section 3.7.8). In the post processing phase, the data is first separated based on the TDM time slots into individual files per FEB by a process called TDM unpacking and then each FEB binary file is unpacked based on the data protocol which was presented in figure 3-95 to create data root files. The data processing and the root file structures are explained in section 6.1.

5.3.5 UDP data stream

In addition to the default mechanism of writing the binary data to local files per MCR on the DAQ PC, the option of writing the data stream to a UDP socket was fully implemented in the core functions of the DAQ. This functionality was tested with the Packet Sender application [124], where the data from two mini crates were sent to two separate UDP sockets and received successfully by two instances of the Packet Sender application. A dedicated data receiver program needs to be developed if the UDP data stream option is to be used. The diagram in figure 5-36 shows a general plan for data handling and event builder which can be implemented.

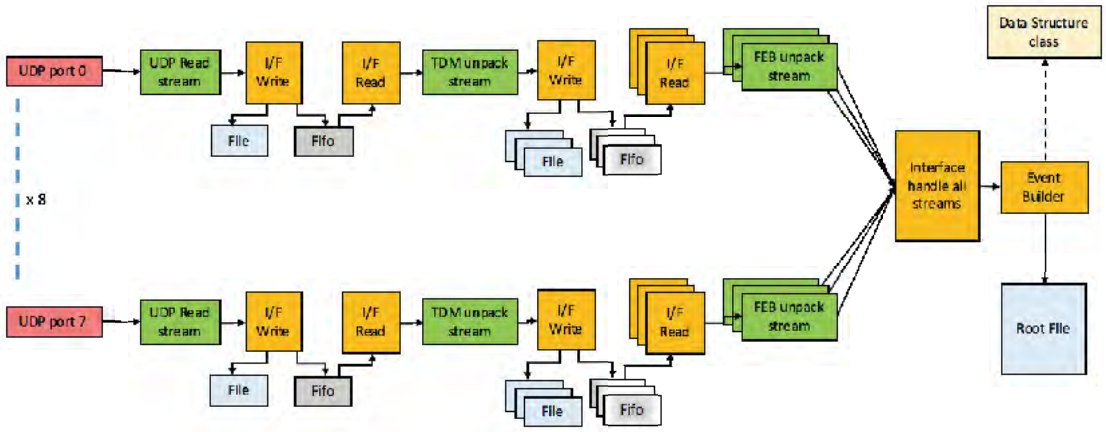

Figure 5-36: Plan for the UDP data stream receiver and event builder.

5.4 First physics run

The first physics run for WAGASCI-Baby MIND in the neutrino beam mode took place between November 2019 and February 2020, coinciding with efforts to increase

the T2K beam power, which eventually reached a record maximum power of 522.6 kW. During this period (T2K run 10) a total of 4.8×10^{20} POT was delivered. Baby MIND succeeded in collecting the data with 97 % data collection efficiency (figure 5-37). All detector systems including the magnet system, the electronics, the synchronization unit and the newly developed DAQ system were stable throughout the data taking campaign.

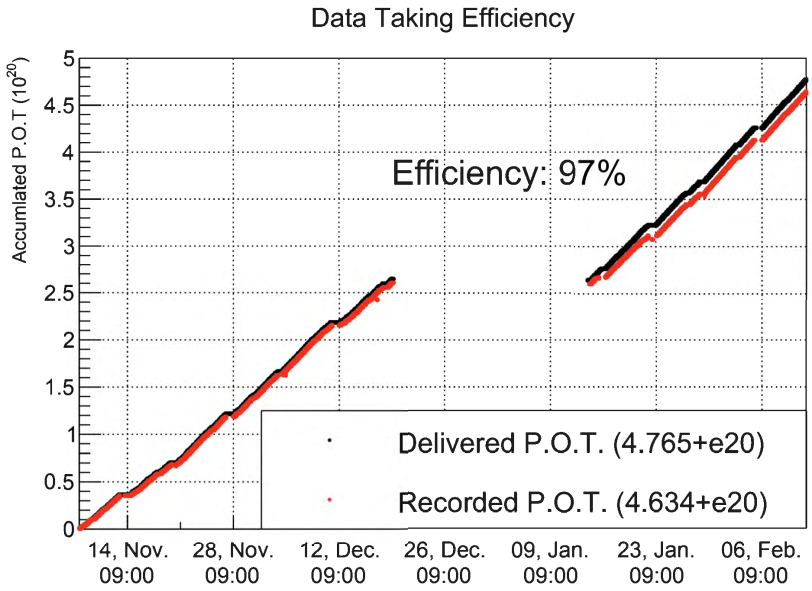

Figure 5-37: Data taking efficiency during the first physics run. The gain in the plot corresponds to the end of year shutdown of the facility.

5.5 Detector response

The detector performance studies were carried out by selecting sand muons, which are generated from neutrino interactions in the cavern walls or other sub-detectors upstream of the Baby MIND modules. The requirement for having at least ten active modules in Baby MIND with a low hit multiplicity were enforced to select clean high energy muons as highly penetrating minimum ionizing particles.

5.5.1 T2K bunch structure

The T2K neutrino beam spill has a time structure with 8 distinct bunches of 80 ns width (3 σ), separated from each other by 581 ns. The cycle period is currently generating a spill every 2.479 s. The bunch structure recorded by the Baby MIND modules is shown in figure 5-38. The horizontal axis shows the hit time calculated from the beam

trigger signal. Clear separation of the eight bunches is shown, demonstrating that the Baby MIND electronics is well synchronized with the beam. Table 5.4 summarizes

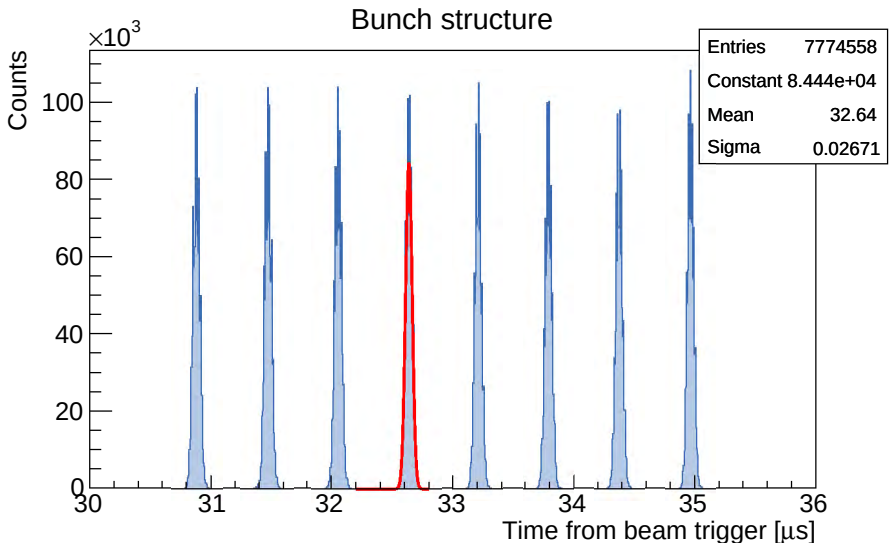

Figure 5-38: T2K neutrino beam bunch structure.

the timing information for each bunch obtained from fitting a Gaussian distribution to the bunch histograms. The average bunch width and the average bunch separation is found to be 26.6 ns and 583.8 ns respectively, which agrees with the expected beam parameters.

Table 5.4: T2K neutrino beam bunch timing information, obtained from a Gaussian fit to each bunch.

Bunch #	Bunch center [μs]	Bunch width [μs]	Bunch separation [μs]
1	30.881	0.0265	-
2	31.474	0.0264	0.593
3	32.058	0.0270	0.584
4	32.635	0.0267	0.577
5	33.210	0.0267	0.575
6	33.791	0.0270	0.581
7	34.377	0.0267	0.585
8	34.968	0.0255	0.591

5.5.2 Calibration results for HG, LG and ToT

The signal sampling and different signal paths of High Gain (HG), Low Gain (LG) and Time over Threshold (ToT), were described thoroughly in section 3.7.5. The HG

amplitude is calibrated by extracting the MPPC gain [ADC/p.e] from the dark count fingerplots. The distribution of the MPPC gain coefficient for all detector channels is shown in figure 5-39-d. Using the gain coefficient and the pedestal value for each channel the HG amplitude is converted to the hit light yield in terms of number of photo electrons (p.e.). The HG amplitude is the most sensitive charge readout and has

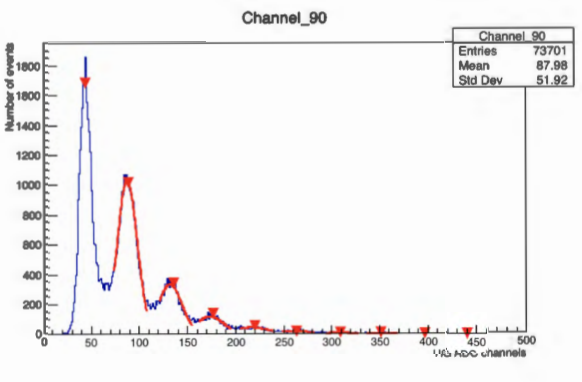

(a) Extraction of MPPC gain from a fingerplot.

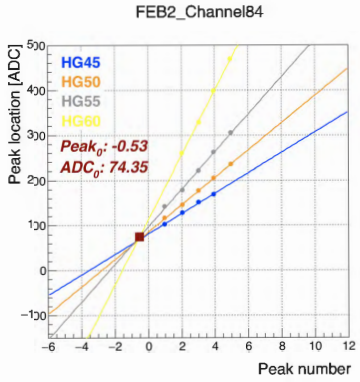

(b) Extraction of pedestal value.

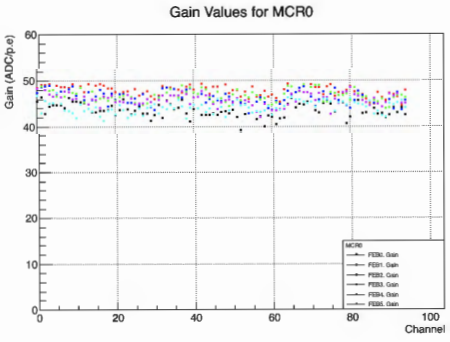

(c) MPPC gain values for one mini crate.

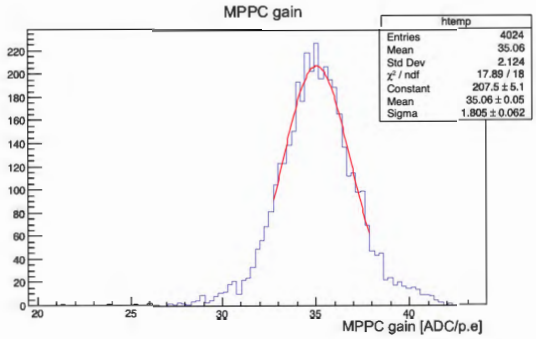

(d) Distribution of MPPC gain values for all channels.

Figure 5-39: Calibration of HG signal path.

a range up to 100 p.e. with our choice of HG pre-amplifier setting. The LG analogue amplitude is linearly proportional to the HG amplitude before the HG saturation and has a larger range of up to 1000 p.e. with our choice of LG pre-amplifier setting. The digital signal path of ToT has the advantage of experiencing no dead time but has a lower resolution in determination of the hit charge. The calibration of ToT is achieved by fitting a polynomial to its curve with respect to HG and LG separately as shown in figure 5-40. All three calibrated amplitudes (HG-pe, LG-pe and ToT-pe) are stored for analysis use. In addition an overall hit charge is reconstructed by selecting the most reliable calibrated amplitude in each case.

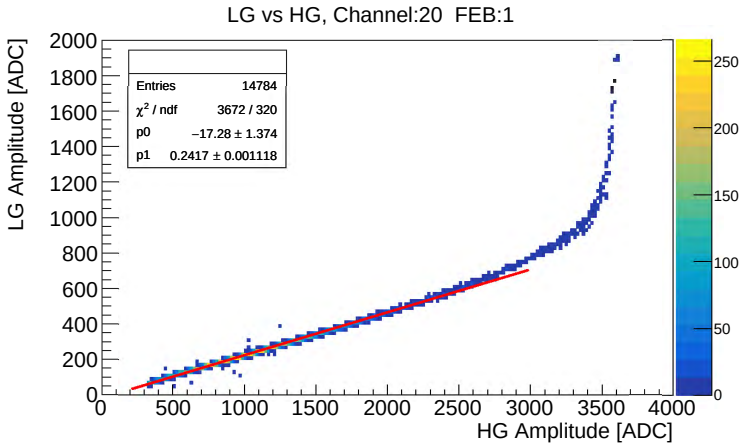

(a) LG amplitude versus HG amplitude.

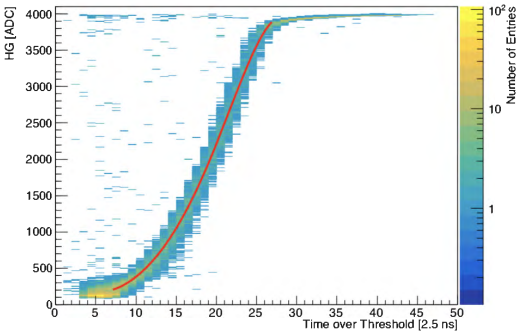

(b) HG amplitude versus ToT.

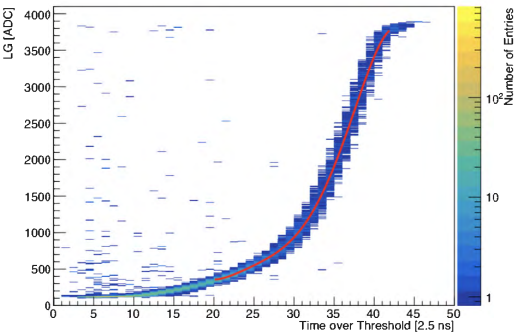

(c) LG amplitude versus ToT.

Figure 5-40: Extracting calibration coefficients for the LG amplitude and the ToT signal paths.

5.5.3 Light Yield of the scintillating bars

Using a sample of through going sand muons, a study was conducted to extract the light yield of the scintillating bars from the neutrino run data. The sum of the signal readout from both ends of the fiber is shown in figure 5-41. The average light yield of horizontal bars and vertical bars were measured to be 48.2 p.e. and 15.6 p.e. respectively. The

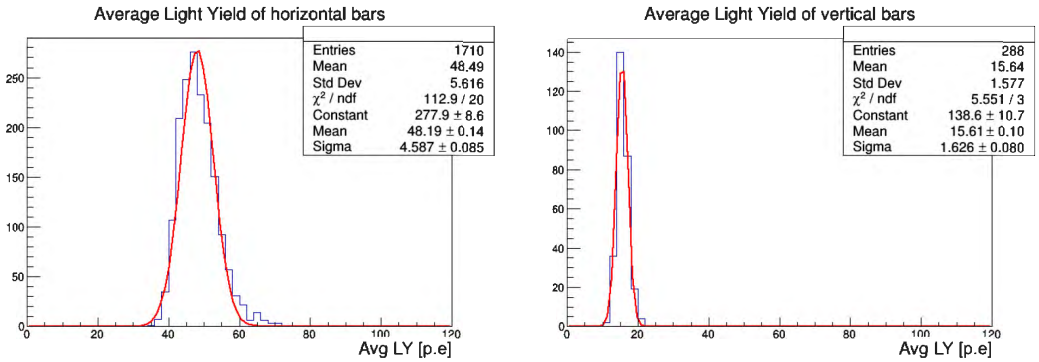

Figure 5-41: Light yield of both fiber ends for horizontal and vertical bars.

discrepancy between these results and the scintillating bars light yield measurement reported in section 3.4.3, and summarized in table 5.5, is likely due to different readout electronics and different calibration methods. The light yield measurements with the waveform digitizer CAEN DT5742 electronics is calibrated by integrating the amplified signal and converting the measured area to the number of p.e., whereas the calibration method used with the Baby MIND electronics, converts the signal amplitude to the number of p.e.. Given that the photons produced in the scintillating bars have a spread in the arrival time as they reach the MPPC, the calibration method by the signal amplitude might underestimate the light yield. Further studies are required to determine with certainty the cause of the light yield discrepancy between the two measurements.

Table 5.5: Comparison of the light yield measurements with different readout electronics and calibration methods.

Light Yield measurement	CAEN electronics	Baby MIND electronics
Horizontal bars	66.2 p.e.	48.2 p.e.
Vertical bars	37.5 p.e.	15.6 p.e.

5.5.4 Timing studies

The internal 400 MHz clock of the Baby MIND electronics provides hit times in units of 2.5 ns. The hit time information is principally used to group hits belonging to the same event within a bunch. In order to extract high accuracy timing information such as track directionality from the time of flight, some corrections need to be applied, namely the delays induced by the WLS fiber and the electronics time walk. Both studies have been performed using the sand muons sample. The effective velocity of the light propagation in the WLS fiber of horizontal bars was measured to be 154.72 ± 2.12 mm/ns (figure 5-42). The effective time walk was parametrized by a double exponential function as shown in figure 5-43.

After these time corrections, the time of flight for through-going sand muons was investigated. In figure 5-44, each point represents the module z position versus the mean value of the hit time distribution in the module relative to the hit time of the last module. Note that the angle and curvature of the tracks have not been corrected for. Based on this result, the direction of particles which have a track length of 1 m

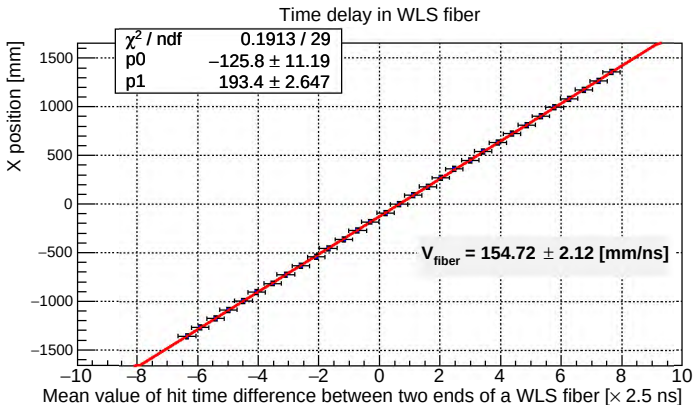

Figure 5-42: Extraction of the light propagation velocity in the WLS fiber from the time difference of two fiber end readouts.

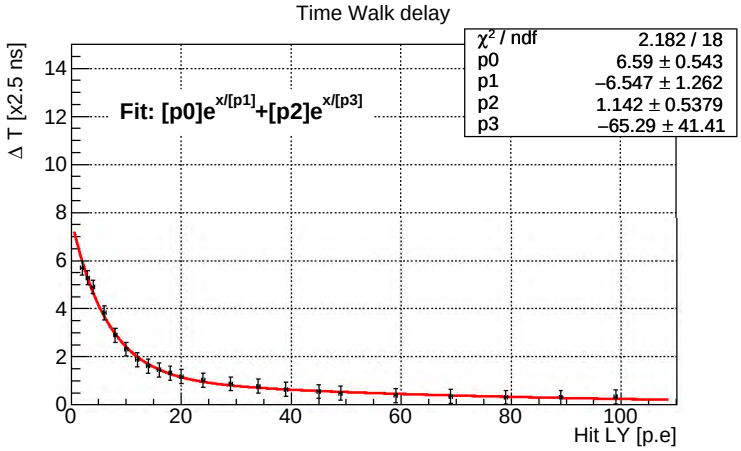

Figure 5-43: Time walk of signals with low signal amplitude

or longer can be determined with the timing capabilities of Baby MIND.

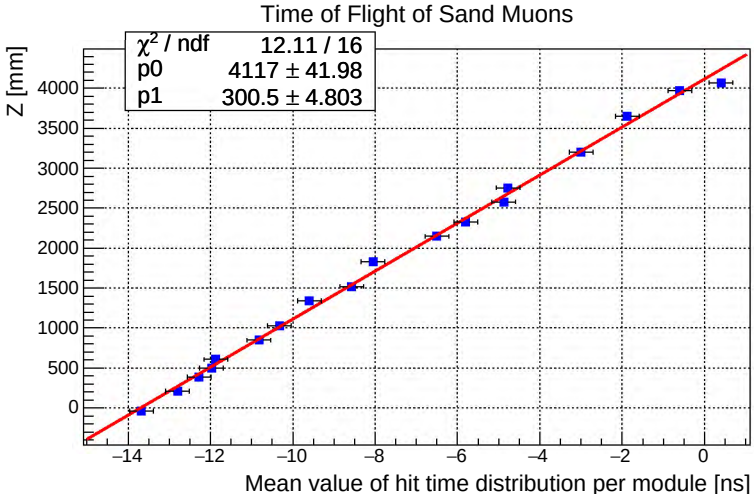

Figure 5-44: Time of flight of through going sand muons.

5.5.5 Electronics afterpulse

After having identified several cases of low amplitude secondary signals on a channel recording a particle hit, and the observation of a systematic hit amplitude and hit time mismatch which was discussed in section 4.3.5, a detailed study was carried out to understand this behavior and characterize the secondary pulses, based on the amplitude of primary signal and delay time distributions of the secondary signal. Thoughout this section these secondary pulses are referred to as afterpulses.

In order to select the candidate afterpulse signals, a search window of 100 ticks (250 ns), starting from the rising edge of the primary signal was established and any secondary hits with a low amplitude (ToT¡ 10 ticks) were selected. The plot in figure 5-45 shows the ToT values for the primary and secondary signals identified in the search window. Two distinct populations are visible in the plot which correspond to the afterpulses following a dark count hit as the primary signal and afterpulses following a particle hit as the primary signal.

By selecting and varying the ToT value of the primary hit, the probability of the

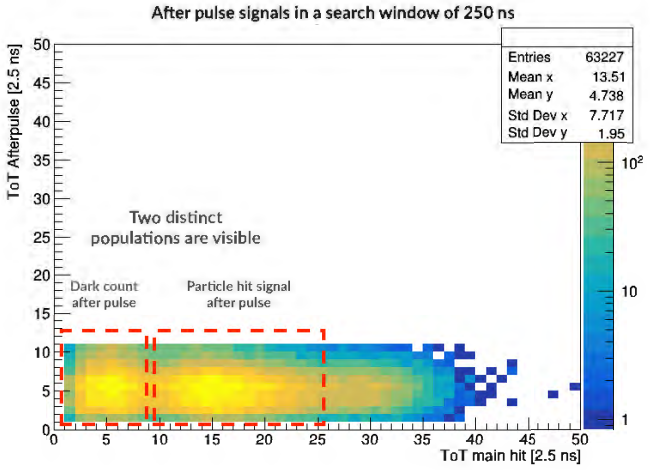

Figure 5-45: Distribution of the time over threshold of the afterpulse hit and the main primary hit, identified in the search window of 250 ns. The primary hits

occurrence, and the time distribution of the secondary signals are investigated. The plots in figure 5-46 show the distribution of the elapsed time from the primary signal for different values of the ToT for the primary signal.

For the low ToT values of the primary signal (below 8 ticks), corresponding to the dark count level, the elapsed time distribution of the afterpulses look similar to the expected distribution dominated by the MPPC pixel afterpulses shown in figure 5-47. The plot is taken from a study published in [125], which is focused on the MPPC

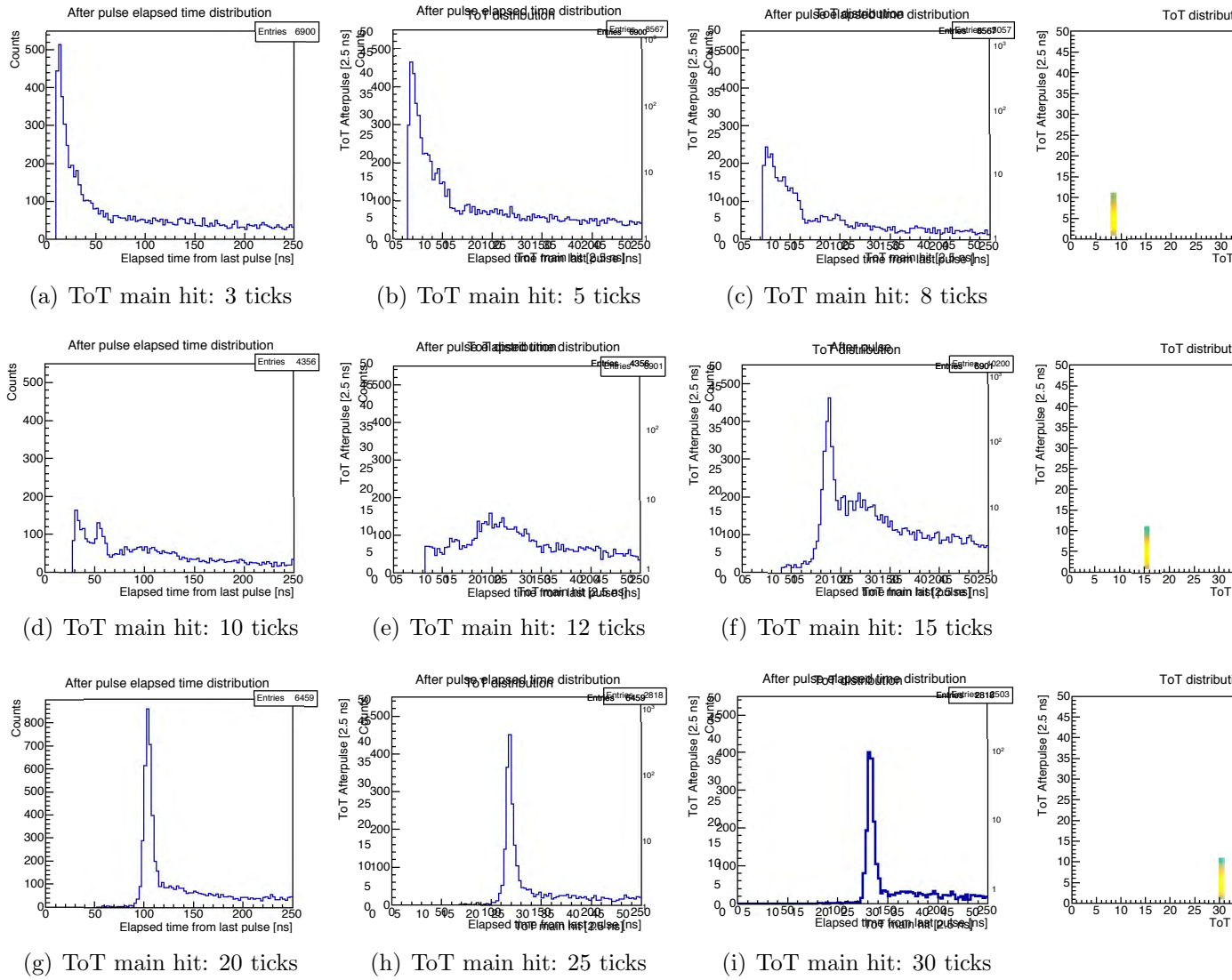

(a) ToT main hit: 3 ticks (b) ToT main hit: 5 ticks (c) ToT main hit: 8 ticks

(d) ToT main hit: 10 ticks (e) ToT main hit: 12 ticks (f) ToT main hit: 15 ticks

(g) ToT main hit: 20 ticks (h) ToT main hit: 25 ticks (i) ToT main hit: 30 ticks

Figure 5-46: Afterpulse elapsed time distribution for different ToT values of the primary signal.

dark count afterpulsing and clearly distinguishes contributions from the delayed pixel crosstalk pulses and the uncorrelated darkcounts from the MPPC pixel afterpulses which are the dominant components of the distribution.

As the ToT value of the primary signal increases to values above 15 ticks (37.5 ns), the secondary pulses once again show a well behaved signature. In this region the after pulse elapsed time distribution features a high and narrow peak whose location is linearly dependent on the ToT of the primary signal (figure 5-48-a). This secondary signal is the result of the electronics shaped signal undershoot and overshoot which can cross the discriminator threshold as shown in figure 5-49. The afterpulse occurrence probability is shown in figure 5-48-b. Here also the difference between the two regions is clearly visible. The darkcount afterpulses have an occurrence probability below 5

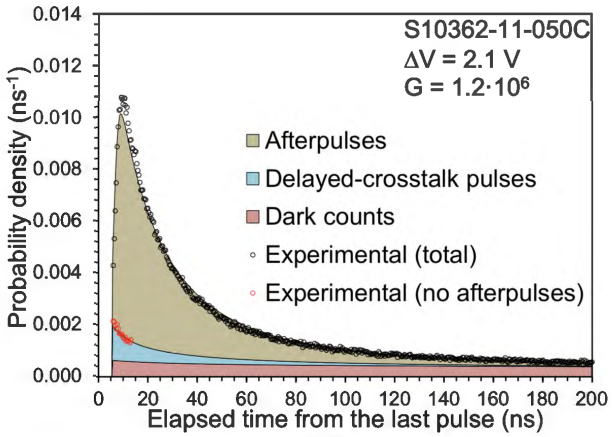

Figure 5-47: A hamamatsu MPPC afterpulse distribution. Plot taken from [125]

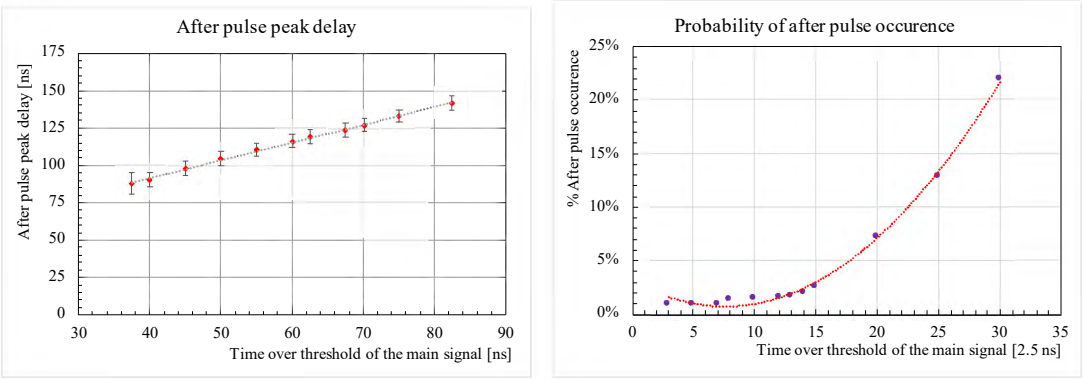

(a) Afterpulse peak delay time. (b) Afterpulse occurrence probability.

Figure 5-48: Afterpulse signal characterization.

% which is compatible with the MPPC characterization whereas the probability of the afterpulses associated to the electronics signal overshoot increases rapidly with the amplitude of the primary signal.

In summary, the afterpulse candidates that were selected in this study were quali-

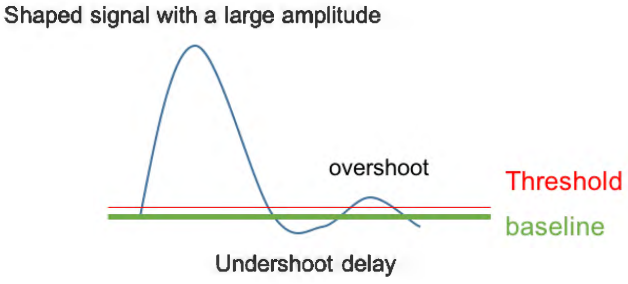

Figure 5-49: Sketch of a shaped signal undershoot and overshoot.

tatively described as two dominant populations including the MPPC pixel afterpulse and the electronics signal overshoot with different behavior.

5.5.6 Common baseline noise and electronics crosstalk

Another noise component that was identified in the data consist of low amplitude signals occurring on many channels of the electronics FEB in a synchronous behavior when a very high amplitude particle hit is registered by one of the channels of the FEB. An example event is shown in figure 5-50, where multiples channels on the same ASIC were fired after a few channels registered very high amplitude signals. Similar

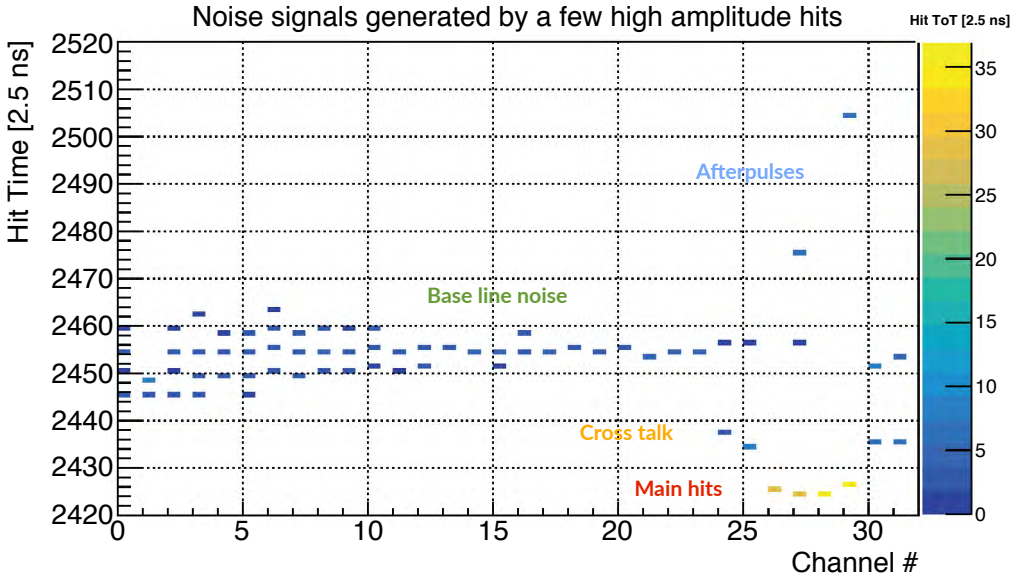

Figure 5-50: Example event with multiples channels of the same ASIC firing after a few channels registered high amplitude signals. The categorization of the noise signals is explained in the text.

behavior was observed during the cable bundle prototype validation tests with high intensity LED system, reported in section 3.5.4.

The existence of a population of low amplitude hits was also observed in the distribution of hit amplitudes vs hit times of the pre-selected particle track candidates. The plot in figure 5-51 shows a population of low amplitude hits as a shadow of the main track hits.

In order to study this effect more systematically a sample of very high amplitude monitor hits with a deposited charge of $>$ 300 p.e. was considered, and all the other hits occurring on the same electronics ASIC within 100 ticks (250 ns) from the monitor hit were tracked. The plot in figure 5-52 shows the distribution of the delay time and the channel proximity of these signals with respect to the monitor hit. Different populations in this plot are labeled as crosstalk, baseline noise and afterpulse.

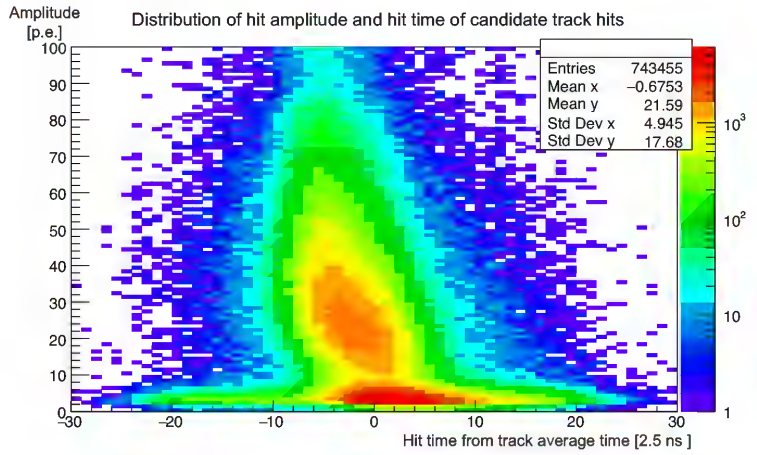

Figure 5-51: Distribution of hit charges and hit times in a sample of pre-selected tracks.

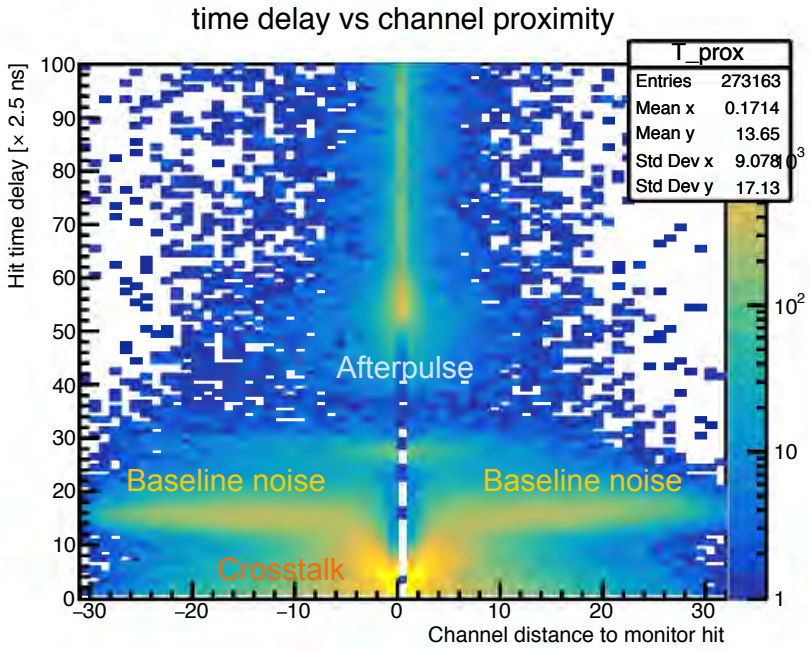

Figure 5-52: Distribution of the noise hit time delay and channel proximity to the high amplitude monitor hit.

The crosstalk noise is identified as a signal occurring on a channel with close proximity to the monitor hit and a delay time of less than 12 ticks (30 ns). The occurrence rate of these noise signals drops sharply as the distance to the monitor hit grows. Figure 5-53 shows the channel correlation map, relating the channel of a crosstalk noise signal and the monitor hit.

The baseline noise is characterized as a noise spread with equal probability on all channels of the same ASIC, occurring within a narrow band of delay time between 12

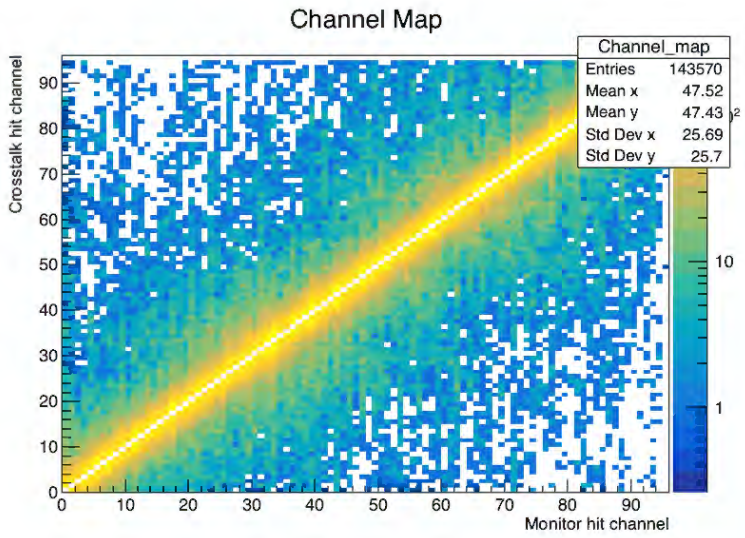

Figure 5-53: Channel correlation map, relating the channel of a crosstalk signal, with a delay time <12 ticks, and the monitor hit.

and 20 ticks.

The Afterpulses are very loosely categorized as any remaining noise signal in the study window with a delay time larger than 20 ticks.

A follow up investigation showed that the baseline noise is limited to one ASIC and the channels of the other ASICs on the same FEB are not affected by the baseline noise (figure 5-54). These results were presented to Omega experts, the designer of

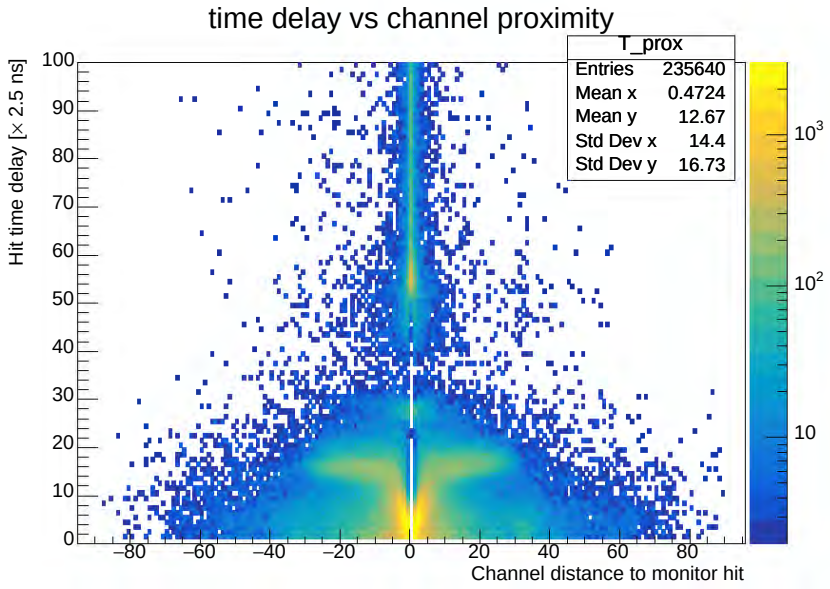

Figure 5-54: The baseline noise is limited to one ASIC and does not leak to the channels of other ASICs on the same FEB.

the CITIROC chip. The Omega experts, confirmed having seen similar behavior, and that in their new data sheet they recommended using a higher decoupling capacitors in the electronics design. The design of Baby MIND FEBs was done prior to these recommendations.

In conclusion, the result of the electronics noise study has shed light on the understanding of the raw data recorded by Baby MIND. This information is used in the data processing to categorize hits and remove the noise elements from the particle tracks in the analysis stages.

Chapter 6

Analysis of clean single track neutrino events in Baby MIND

This chapter is dedicated to the analysis of neutrino data collected during Baby MIND first physics run (see section 5.4). We start from the data processing scheme and present the event pre-selection based on topology criteria before diving in the analysis of clean single track neutrino events in Baby MIND.

6.1 Data processing and root file structure

Raw data: The raw binary data is stored by the DAQ PC as one file per mini crate (8 in total). An extract of the asynchronous binary data (see section 3.7.8) converted to CSV format with its original word ordering is shown in figure 6-1. In this extract two channels (ch 31 and ch 32) were fired within GTRIG tag 51266 on the FEB with board ID 2, the hits time information (rising edge and falling edge) is pushed to the data stream immediately whereas their analogue amplitude information is pushed with a delay accounting for the analogue readout cycle (hold + dead time) and can appear in the next few GTRIG tags. After the end of the TDM slot for board ID 2 and the start of the TDM slot for board ID 3, the hit information of two other channels (ch 33 and ch 35) is recorded within GTRIG tags 51260 and 51261 on the FEB with board ID 3, the latter hit is missing analogue amplitude information because it has occurred after the end of the hold time window (see section 3.7.5).
The CSV data conversion tool was used regularly throughout the project as a primary debugging tool to monitor the changes in the data protocol brought to the FPGA firmware and coherency of the readout data.

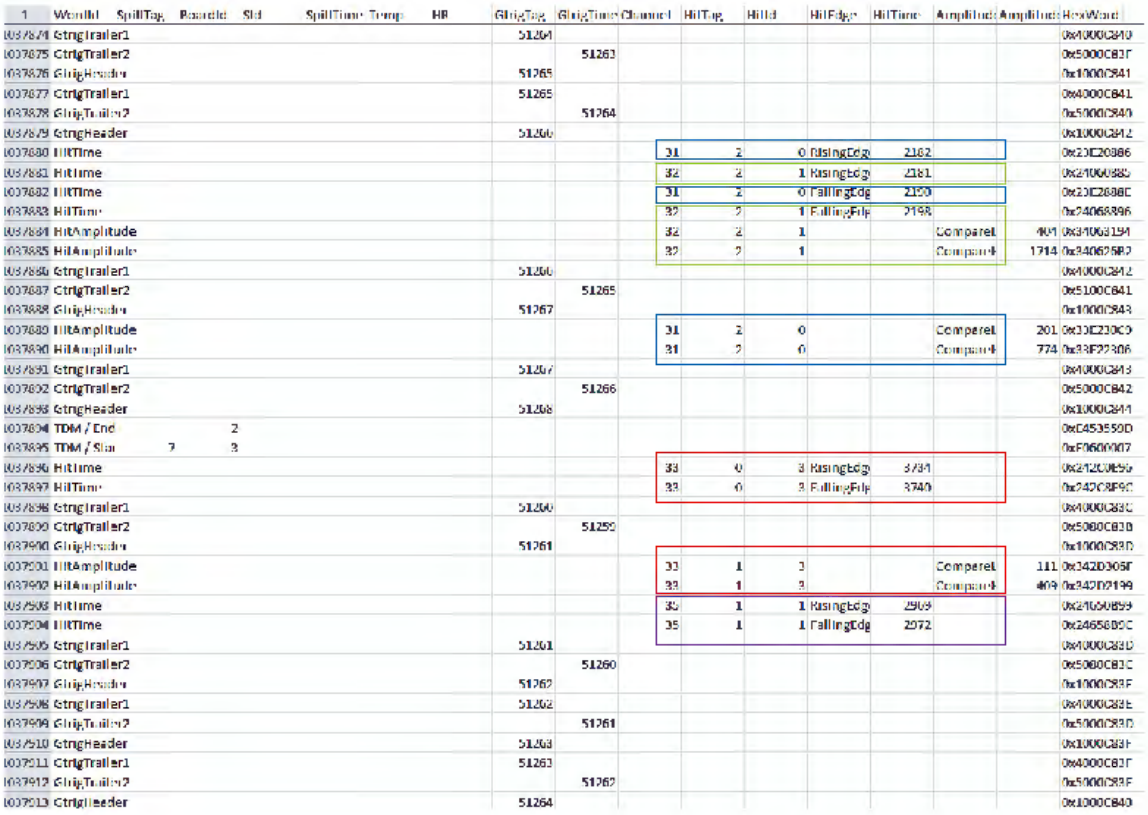

Figure 6-1: An extract of a binary data converted to CSV.

Data unpacking: The first stage of the data processing, shown in figure 6-2, is the TDM unpacking, through which the binary data file is split into separate binary files per FEB. The main unpacking software is then applied to each FEB file to create a root tree per FEB for storing hit information. The branches of the FEB tree are shown in figure 6-3. Each branch is a vector, whose size is equal to the total number of hits on the FEB.

Amplitude matching and calibration: At this stage a correction code is applied to cure the hit amplitude and hit time mis-match which was described in section 4.3.5. Figure 6-4 shows the distribution of the HG amplitude and ToT for one channel, before and after the correction. In the next stage, the calibration is performed which creates new branches in the FEB tree corresponding to calibrated values of the high gain, low gain and time over threshold in units of p.e. and a reconstructed hit charge from the combination of all three signal paths as described in section 5.5.2.

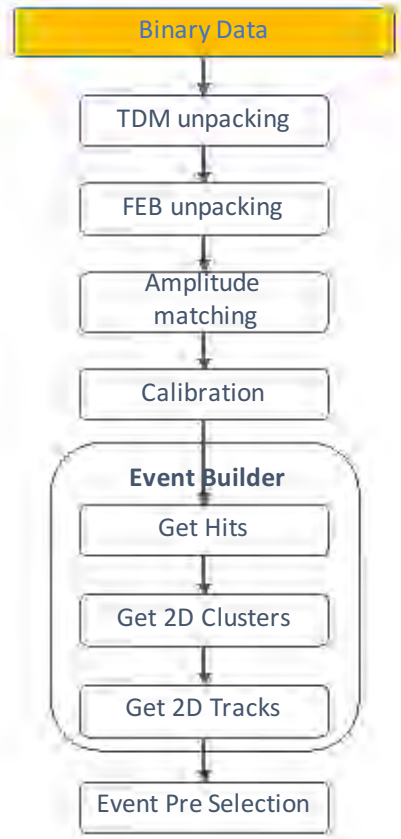

Figure 6-2: The stages of data processing from the binary data to event pre-selection.

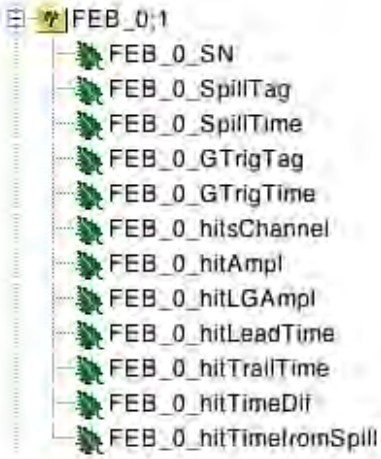

Figure 6-3: Branches of the FEB tree after the unpacking.

6.1.1 Event builder

After the calibration, the event builder block is launched in several stages which creates a new data structure based on an event class, a hit class, a cluster class and a track class (figure 6-5). The properties of each class are defined to make use of all the extractable information from the data.

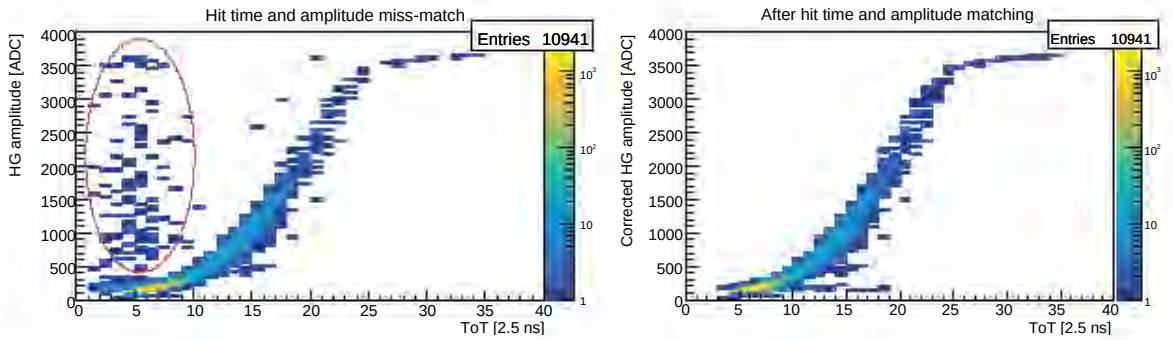

Figure 6-4: Correction of the hit time and hit amplitude miss-match, shown in the left plot by red circle.

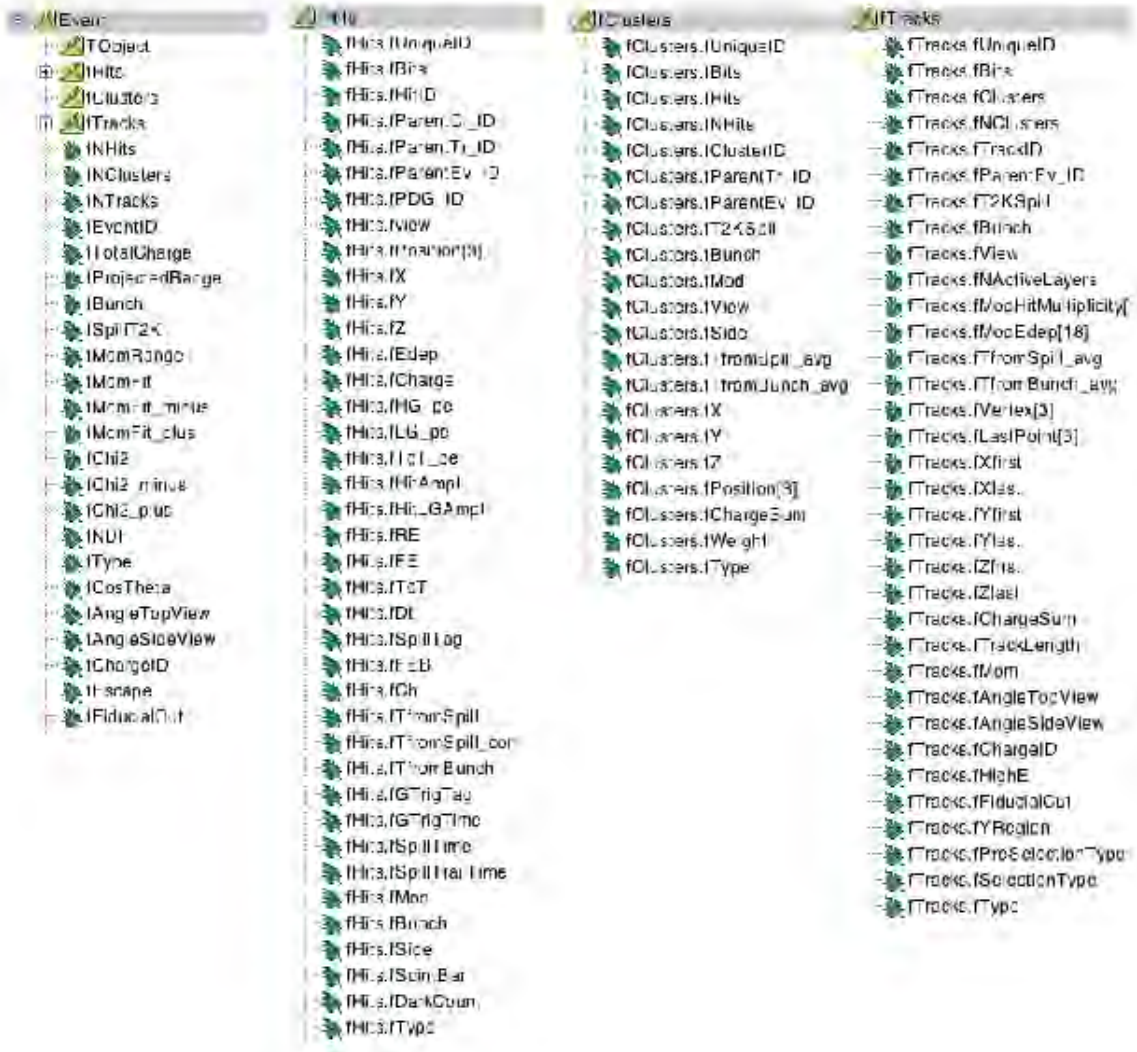

Figure 6-5: Properties of the event class, hit class, cluster class and track class created by the event builder.

Get hits: The first stage of the event builder, creates an event per neutrino bunch by imposing a time window of ±100 ns around the bunch center and recombines the hits from all FEB trees which occurred in that bunch and store them in an event. The

size of the time window is chosen based on the hit time distribution of all the channels of detector around a bunch center shown in figure 6-6.

This is followed by a hit classifier code, which analyses the electronics noise compo-

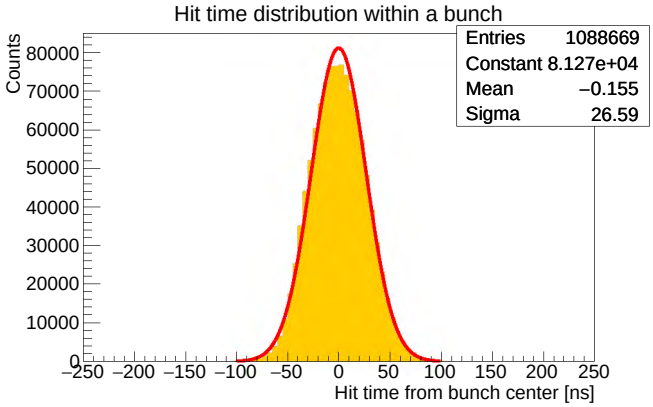

Figure 6-6: Hit time distribution in a T2K neutrino bunch.

nents, discussed in section 5.5.6, to classify the hits based on the hit amplitude and hit delay time with respect to the highest amplitude hit on the same FEB.

Get clusters: At this stage the hits which are created by the passage of a particle and recorded by channels of the overlapping scintillating bars in the same scintillating module are grouped together for the side view and the top view separately into two dimensional clusters. The selection is performed based on the hit rising time, required to be within ±50 ns from the cluster average time.

Get tracks: The last stage of the event builder groups hits and clusters that are within ±50 ns, for the side view and the top view separately into two dimensional track objects. The time window allocated in this stage is smaller than the time window allocated for collection of all the hits in a bunch because the bunch has an intrinsic width from the accelerator.

At this stage the track objects are essentially time separated collections of hits and clusters with no reconstruction performed. These track objects are used for the pre-selection of the events discussed in section 6.3.

6.2 Topology of the neutrino events in Baby MIND

Before proceeding with the event categorization, we need to bring forward a discussion about the types of events we are expecting to witness in Baby MIND. The neutrino

events in Baby MIND are predominantly occurring in the iron modules which constitute more than 90 % of the detector mass. The expected contribution of different ν_μ interaction modes on iron, simulated with the T2K neutrino flux at 1.5° off-axis angle, using NEUT package [126], is presented in table 6.1. In general, events with a certain

Table 6.1: Expected contribution of different ν_μ interaction modes on iron, simulated with the T2K flux at 1.6 ° off-axis angle.

ν_μ **events on Iron**	**CC-QE**	**CC-RES**	**CC-DIS**	**NC**
	37.6 %	21 %	15.5 %	26 %

interaction mode can appear to have different event topologies in the detector. This is shown in the schematics of figure 6-7.

In case of Baby MIND, given the number of iron layers between the scintillating mod-

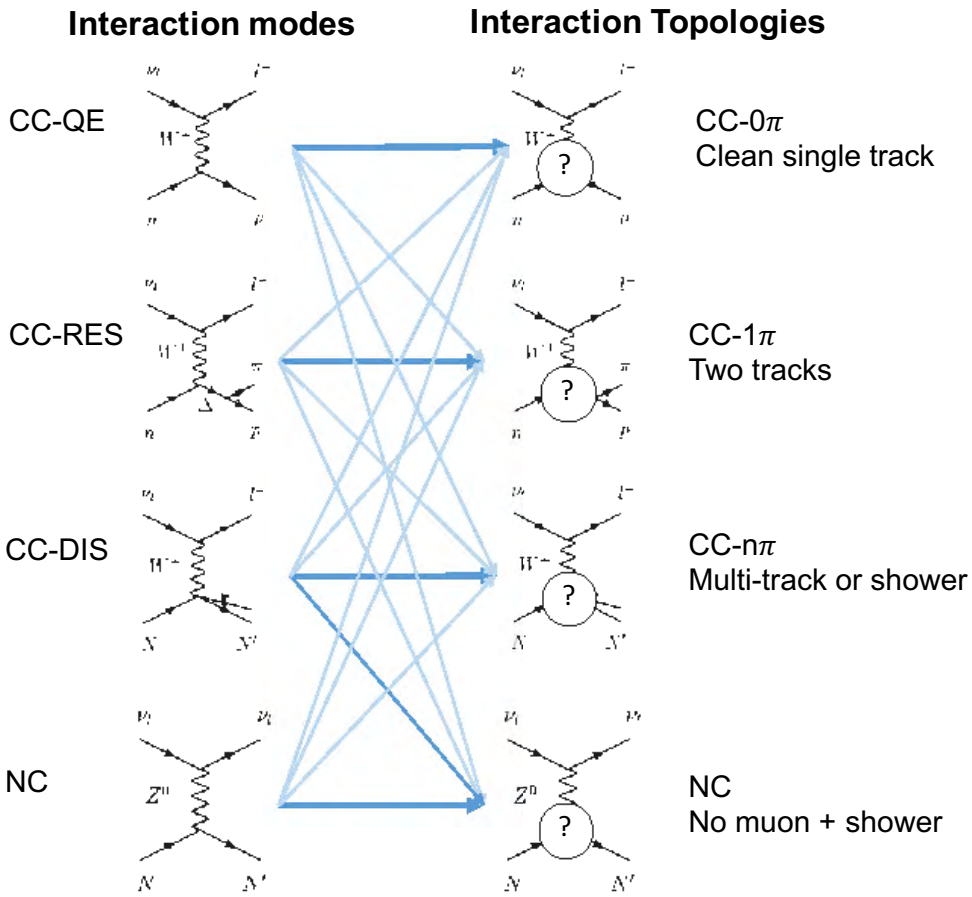

Figure 6-7: Neutrino events with a certain interaction mode can appear to have different event topologies in the detector.

ules, particles such as the low energy pions of the CC-RES events might get absorbed quickly in the iron and appear as a single track event with some activities near the

vertex.

In order to extract a realistic topological criteria for the event selection, thousands of event displays from the real data were inspected. Figure 6-8 shows some representative event displays of the neutrino interactions in Baby MIND, including two clean single track events (a μ^- and a μ^+), a multi-track event with a visible muon and a shower like event.

For the current study, the strategy is to identify and select a sample of clean single track neutrino events and proceed with the stages of analysis.

6.3 Event pre-selection based on topology criteria

The event pre-selection scheme can be described as follows. A pre-selected event is composed of two 2D track objects for the side view (Y-Z) and the top view (X-Z). Each view contains all the hits within ±50 ns from the mean time. The pre-selected events are categorized based on simple topology criteria as described in table 6.2.

Table 6.2: Event pre-selection categories.

Categories	**Description**	**Criteria**
Pre type 0	Short tracks	Less than 3 active layers in at least one view
Pre type 1	Clean single tracks	3 or more active layers in both views & N clusters per layer ≤ 2 & Clusters position spread per layer ≤ 5 cm
Pre type 2	Not clean single tracks	3 or more active layers in both views & $2\leq$ N clusters per layer ≤ 4 & Clusters position spread per layer ≤ 15 cm
Pre type 3	Multi tracks, shower like or pile up events	All the remaining events.

On average, from all the neutrino bunches during a data run, about 40 % contains recorded hits in Baby MIND for which an event is created. About 30 % of these events have less than three active layers and are categorized as short tracks. Figure 6-9 shows the number of active layers for all events in one data run. Of the remaining events with 3 or more active layers, about 30% are categorized as clean single tracks, 24% as not clean single tracks and the remaining 46% are categorized as multi tracks or shower like events.

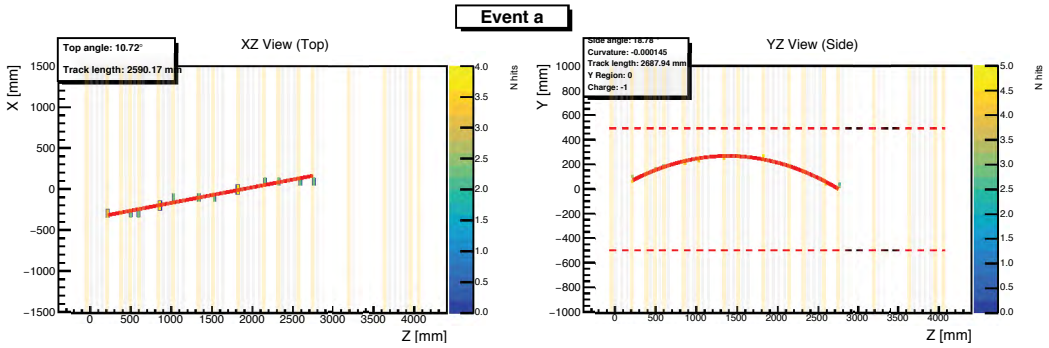

(a) A μ^- candidate.

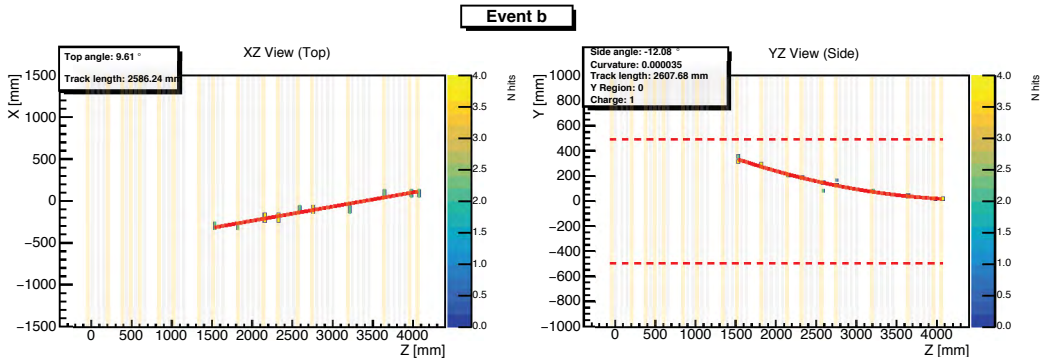

(b) A μ^+ candidate.

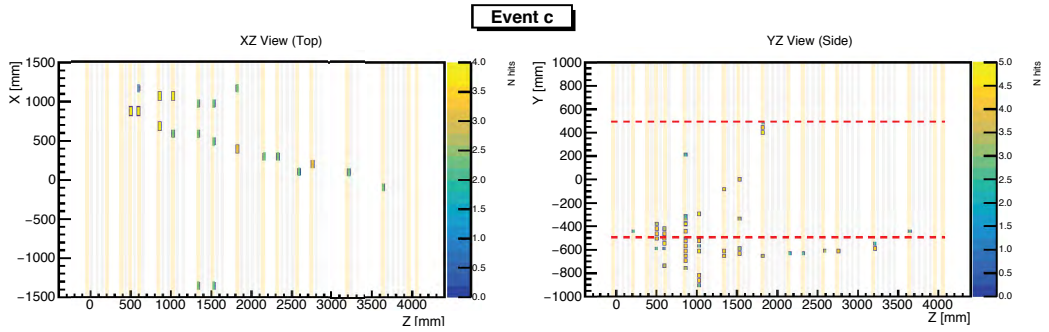

(c) A multi track candidate.

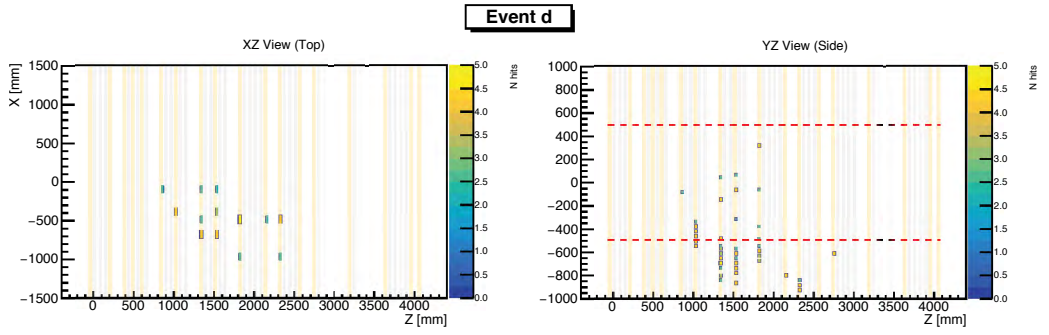

(d) A shower like candidate.

Figure 6-8: Examples of neutrino events with different topologies in Baby MIND detector.

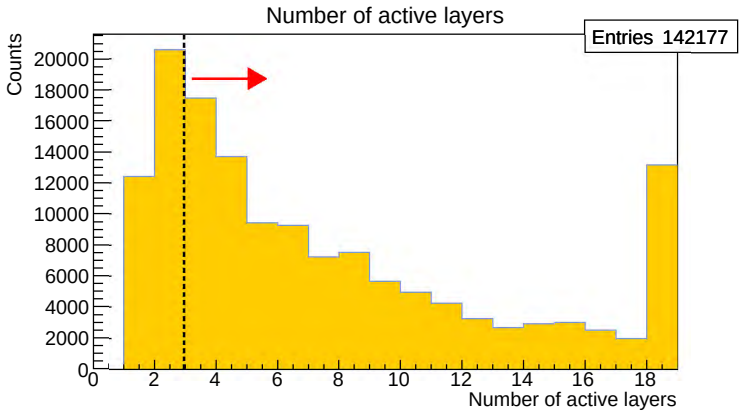

Figure 6-9: Number of active layers in the side view projection of all events in one data run (16 Dec).

6.3.1 Data statistics summary

In order to study the event rate stability over the data runs in the period of December 2019, a subset of the sand muons were chosen. The criteria for selection of sand muon events is to belong to one of the two categories of single tracks, have a hit on the first detector layer and have at least 10 active layers in total i.e. relatively high momentum sand muons (¿ 800 MeV/c). Figure 6-10 shows the rate stability of all pre-selection categories and the sand muons. The average occurrence rate of the sand muons was found to be 0.92 ± 0.07 events per 10^{15} POT in December data runs. The detailed run

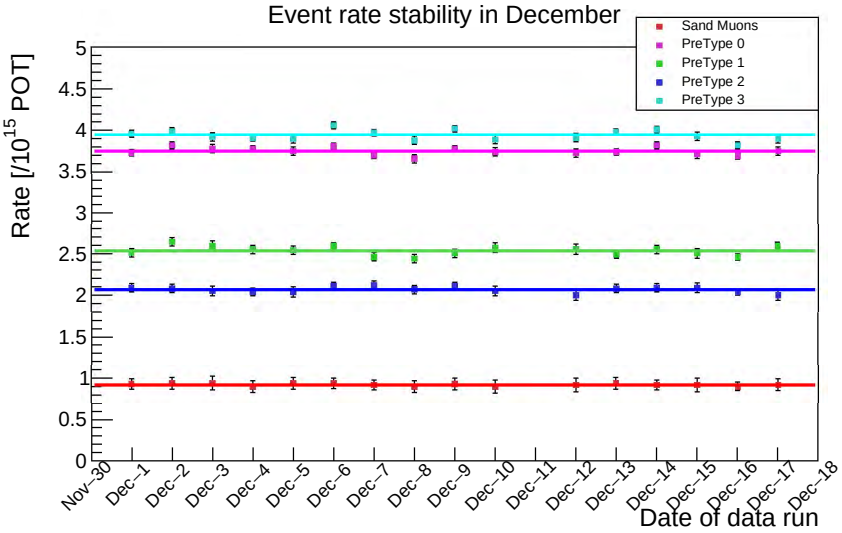

Figure 6-10: Event rate stability during the period of Decemper 2019.

statistics are summarized in table 6.3.

Table 6.3: Summary of pre-selected events in December runs.

Date	N Spills	Pre type 0	Pre type 1	Pre type 2	Pre type 3	Sand Muons	Sand Muons Rate [/10^{15} POT]
1-Dec	33248	32664	21985	18329	34676	8120	0.93 ±0.06
2-Dec	30295	30490	21044	16620	31844	7531	0.94 ±0.07
3-Dec	21697	21626	14830	11730	22387	5376	0.94 ±0.08
4-Dec	30384	30250	20412	16301	31336	7229	0.90 ±0.07
5-Dec	26089	25783	17464	13991	26813	6446	0.94 ±0.07
6-Dec	36417	36541	24826	20291	38937	9004	0.94 ±0.06
7-Dec	33581	32707	21761	18735	35138	8115	0.92 ±0.06
8-Dec	27831	26853	17897	15190	28457	6583	0.90 ±0.07
9-Dec	29015	28882	19090	16127	30770	7139	0.93 ±0.07
10-Dec	22336	22016	15104	12077	22914	5313	0.90 ±0.08
12-Dec	21204	20865	14249	11189	21835	5113	0.92 ±0.08
13-Dec	30605	30172	20059	16810	31922	7463	0.93 ±0.07
14-Dec	31613	31780	21245	17428	33365	7683	0.92 ±0.06
15-Dec	22984	22466	15137	12652	23831	5598	0.92 ±0.08
16-Dec	45086	43748	29243	24129	45381	10711	0.90 ±0.05
17-Dec	26569	26274	18096	13997	27297	6455	0.92 ±0.07

6.4 Study of the single track neutrino events

In this section the results of a basic analysis of the clean single track neutrino events inside the Baby MIND volume is presented. This study is based on simple analysis tools developed independently to treat the raw data, without comparison to simulations, which was not available at the time. These results are expected to be revised once the more sophisticated analysis tools are developed and a full reconstruction package and simulation suit is completed. The purpose of this study was to provide a first glimpse at the momentum and angle distribution from the data collected by the Baby MIND detector during the first physics run with a beam in neutrino mode in order to show the physics capabilities of the detector and its performance under physics running conditions.

6.4.1 Algorithm for track reconstruction

The strategy for track reconstruction was to take the simplest pre-selected event type, clean single tracks, as the starting point, and develop new algorithms for building 3D track objects and momentum reconstruction. The overview of the clean single tracks processing is shown in figure 6-11. During the first stage, the two dimensional track objects of the pre-selected events, categorized as clean single tracks are recombined into three dimensional tracks. The algorithm starts from the last module of the detector and for each layer forms a three dimensional voxel made from all hits of the side view

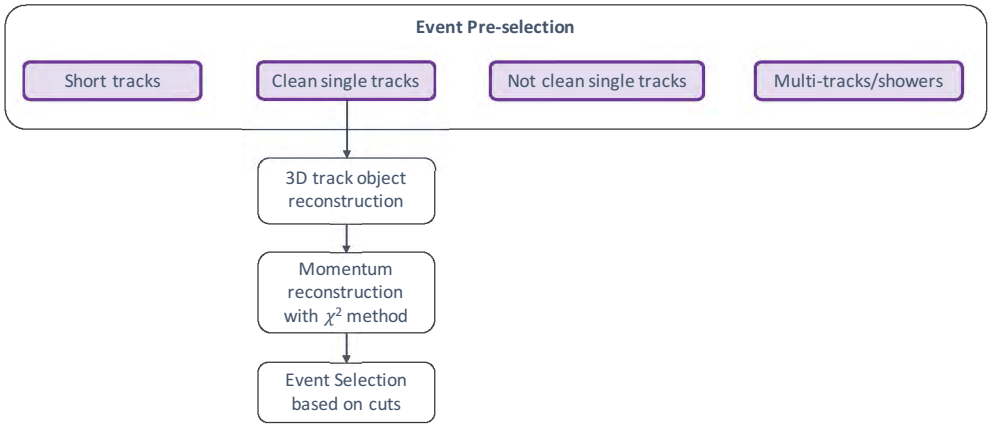

Figure 6-11: Stages of the analysis of pre-selected events of type clean single tracks.

cluster and the top view cluster.

After creation of the three dimensional track, and identification of the event vertex location, a track model is used to generate a track trajectory. The track model requires input track parameters such as the vertex location, a seed momentum estimated from the visible track length, the initial angles in both views, and a seed charge.

The track model considers the detector as having 51 separate layers (18 scintillating layer and 33 magnet layers). For each detector layer, the model calculates the energy loss based on the material density and the value of $\frac{dE}{dx}$ for the given momentum at that layer and the deflection angle due to the magnetic kick, if applied to the layer, and extrapolates the position coordinates of the next layer based on the outgoing angles, and width of the air gap between layers. Given the detector layout is in-homogeneous in the z direction, the calculations at each of the 51 layers are unique and cannot be simplified to one expression for all layers, and therefore the overall trajectory of the particle tracks does not follow an easy to fit well defined function. Trials to fit the events hit points with quadratic or helical fits proved to be inaccurate to describe the particle trajectories in Baby MIND.

The track reconstruction algorithm varies the input parameters of the track model and for each set of parameters generates reconstructed hit points in the detector layers. These reconstructed points are then compared to the data points and a χ^2 value is calculated for each set of the input parameters:.

$$\chi^2 = \sum_{i=1}^{n} (y_{i\,,\mathrm{data}} - y_{i\,,\mathrm{rec}})^2 \,. \tag{6.1}$$

By minimizing the χ^2 value, the best matched group of input parameters are then reported as the reconstructed parameters for the track.

The χ^2, in this content provides a measure of the deviation of the reconstructed

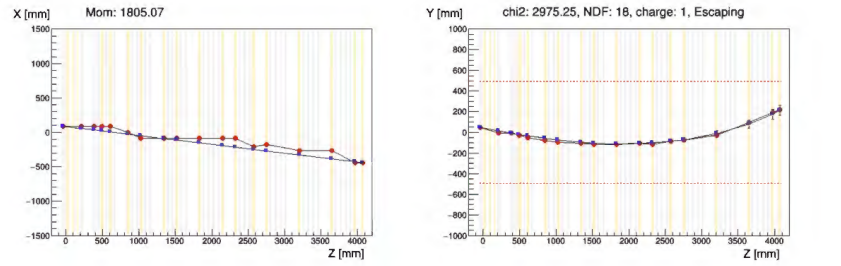

(a)

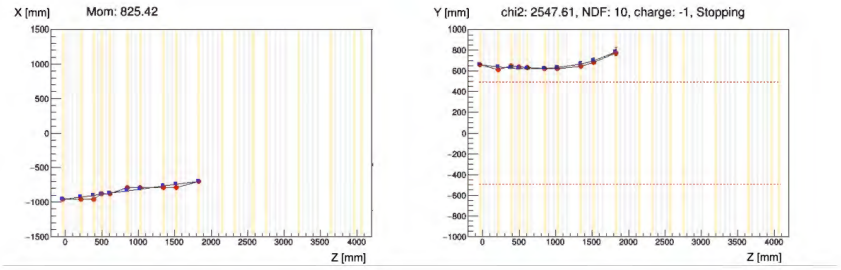

(b)

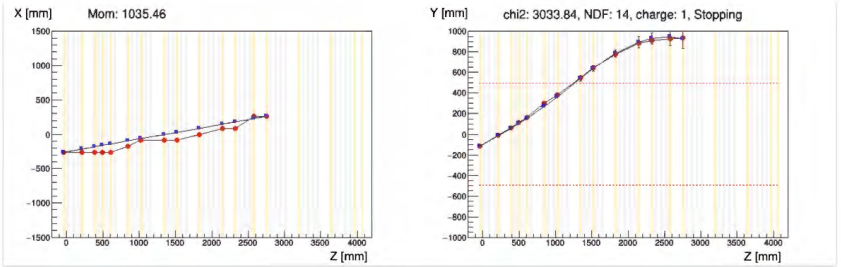

(c)

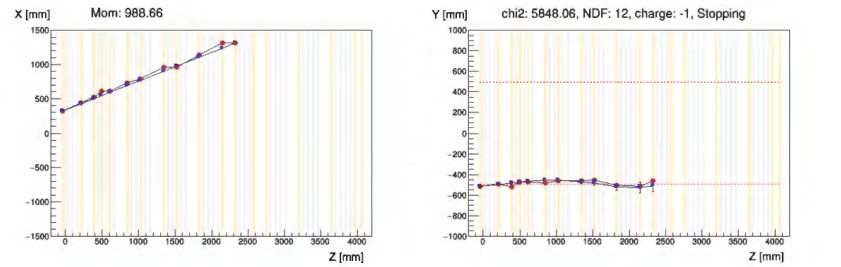

(d)

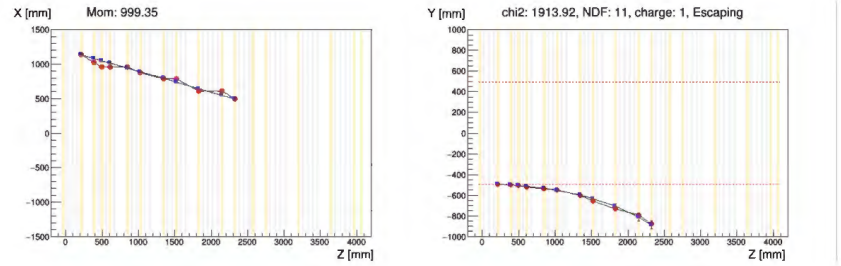

(e)

Figure 6-12: Example of reconstructed tracks. The red points are the data points and the blue points show the generated track points with a minimum χ^2 value.

points from the data points. The number of degrees of freedom (NDF) corresponds to the number of active layers in the detector. We can therefore interpret the $\sqrt{\frac{\chi^2}{NDF}}$ as the average deviation of each data point from the reconstructed point along the track. Figure 6-12 shows examples of the track reconstruction. In these plots the red circles represent the data points and the blue squares show the reconstructed points with the track model. In this figure, event (a) is fully contained in the middle magnetic region, events (b) and (e) are fully contained in the upper and lower magnetic regions, whereas event (c) is a clear case of a track which crosses the magnetic regions and is bent in different directions in each region and finally event (d) represents a special case where the negatively charged track is oscillating around the line where the magnetic field changes sign (attractor region).

6.4.2 Charge identification

The wrong sign contamination of the neutrino mode beam, is negligible. In order to evaluate the capacity of the χ^2 method in determination of the charge of the particle tracks, a sample of clean single tracks events with 5 or more active layers which passed the quality cut $\sqrt{\frac{\chi^2}{NDF}} < 20$ mm, was selected. The χ^2 method identified about 88 % of the cases as negatively charged tracks. A summary of the study is presented in table 6.4 for different sub-categories of the sample. The stopping tracks in the detector had slightly better charge identification efficiency since the curvature of the track is more pronounced towards the end of the track.

This limited study reveals that a simple χ^2 method can achieve charge identification

Table 6.4: The summary of the charge identification study with the χ^2 method.

Sample	**# events**	**# μ^-**	**# μ^+**	**% of μ^+**
All events	7486	6581	905	12.1 %
$p_\mu < 0.5$ GeV	1162	1019	143	12.3 %
0.5 GeV $\leq$ p_μ < 0.7 GeV	1841	1654	187	10.2 %
0.7 GeV $\leq$ p_μ < 1 GeV	1463	1363	100	6.8 %
1 GeV $\leq$ p_μ < 2 GeV	1750	1495	255	14.6 %
2 GeV $\leq$ p_μ	1270	1050	220	17.3 %
Stopping events	3973	3609	364	9.2 %
Escaping events	3513	2972	541	15.4 %

efficiency of 88 %. This value is expected to improve with a more sophisticated reconstruction package.

One aspect, that might impact the efficiency of charge identification is the presence of an attractor and a reppeller zones in the detector volume. These zones are created as

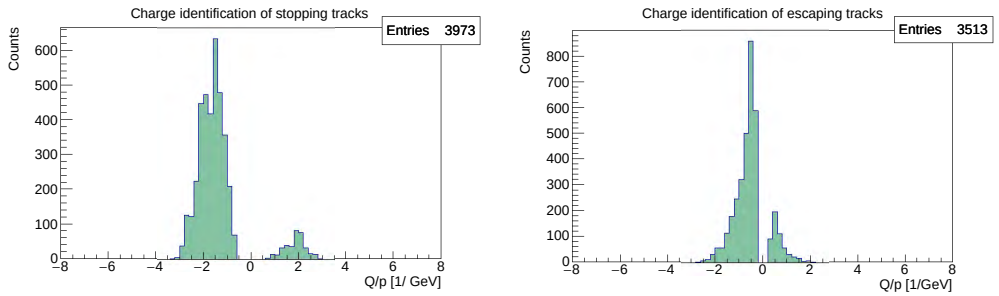

(a) Stopping tracks (b) Escaping tracks

Figure 6-13: Charge sign of muons from χ^2 method.

a result of the magnetic scheme of Baby MIND around the horizontal planes where the magnetic field changes sign at $Y = \pm 500$ mm. Figure 6-14-a shows these zones as a

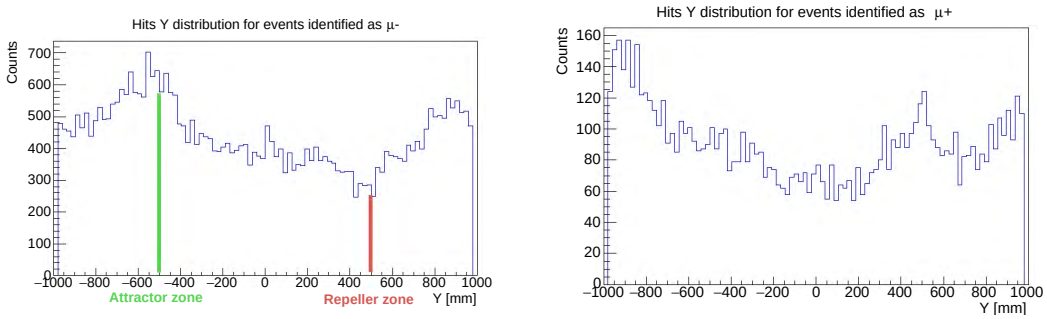

(a) Reconstructed as μ^- (b) Reconstructed as μ^+

Figure 6-14: Attractor and reppeller zones of the Baby MIND detector for negatively charged particles on the Y axis (left). Events mis-identified as μ^+ have concentration of hits at the repeller zone or the boundaries of the detector (right).

depleted and an over populated regions in hits Y position distribution, for negatively charged identified tracks. The tracks that were positively charged or mis-identified as one, have concentration of hits at the repeller zone (for negative tracks) or at the boundaries of the detector (escaping cases).

Other distributions such as the polar angle (figure 6-15) or azimuthal angle (figure 6-16) does not show any difference between the tracks reconstructed as negative or positive. The sensitivity of the χ^2 method for charge separation can be reflected as the difference of the best fit $\sqrt{\frac{\chi^2}{\text{NDF}}}$ for both charge scenarios. If the difference is large the charge separation is clear, on the contrary if the difference is close to zero, it reveals that the χ^2 method has little to no sensitivity for charge separation. The plot in figure 6-17 shows the distribution of the charge identification sensitivity for the same data sample. In this asymmetric distribution, the tracks identified as μ^+ have a low charge identification sensitivity.

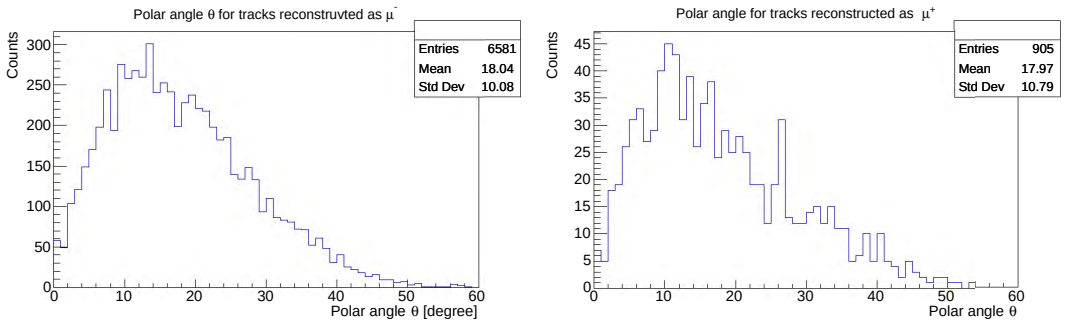

Figure 6-15: Distribution of the polar angle θ.

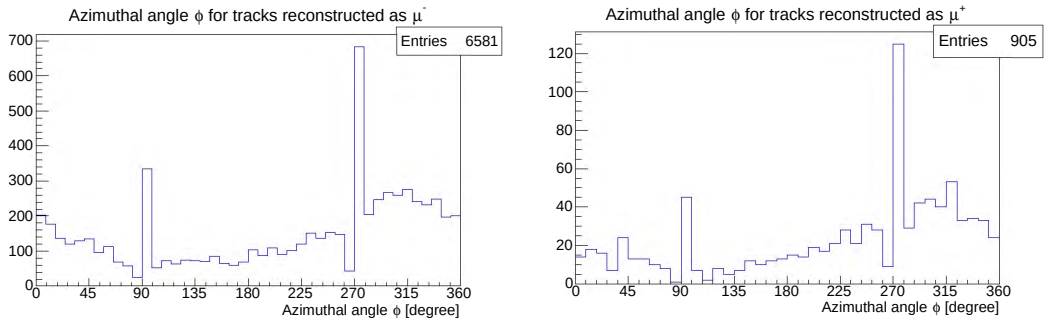

Figure 6-16: Distribution of the azimuthal angle ϕ (The spikes at $\pi/2$ and at $3\pi/2$ represent an excess of tracks with top view angle 0).

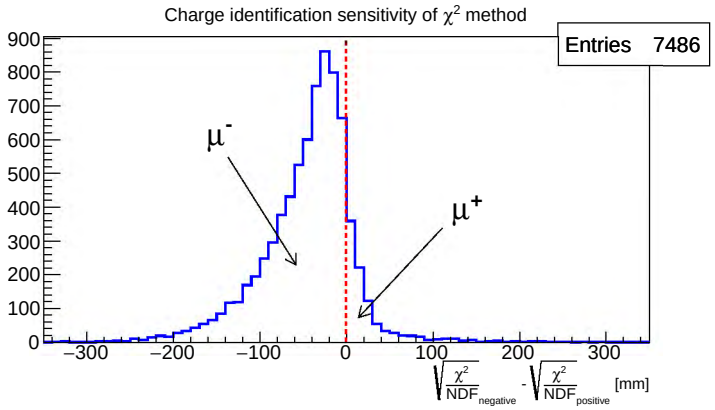

Figure 6-17: Charge identification sensitivity of the χ^2 method.

6.4.3 Results of the reconstruction of muon momentum and scattering angle

In order to visualize the distributions of the muon momentum and scattering angle of the neutrino interaction events in Baby MIND, a strict sample selection is required to eliminate the trajectories entering the Baby MIND volume from either sides. The selection is based on the quality cuts and the vertex fiducial volume cuts as shown in table 6.5.

The quality cut $\sqrt{\frac{\chi^2}{NDF}} < 20$ mm is chosen somehow arbitrarily with the only function

Table 6.5: Neutrino events selection criteria in Baby MIND volume.

Type	**Condition**
Quality cuts	N active layers > 4
	$\sqrt{\frac{\chi^2}{NDF}} < 20$ mm
Fiducial volume cuts	$Z_{\text{mod2}} \leq Z_{\text{vertex}} \leq Z_{\text{mod14}}$
	$\lvert X_{\text{vertex}} \rvert < 1300$ mm
	$\lvert Y_{\text{vertex}} \rvert < 800$ mm

to improve the quality of the track. This average deviation of the reconstructed points from the data points is comparable with the width of horizontal bars which is 30 mm. The cuts on the vertex position are applied to ensure a full and effective removal of any particle entering the detector volume from upstream. The vertex position distribution

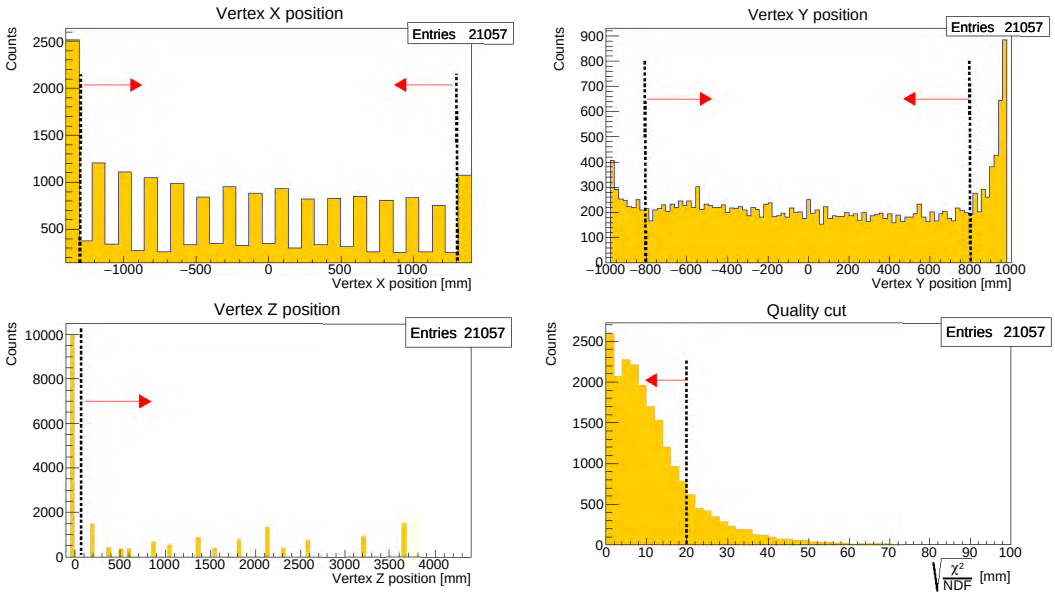

Figure 6-18: Selection cuts based on vertex location and fit quality.

plots shown in figure 6-18 demonstrate a clear excess at lower X detector boundary (left side of the detector) and the upper Y boundary (top of the detector), which is caused by the asymmetric beam profile at the detector location.

The distributions of the reconstructed momentum and the scattering angle of the muons are shown in figure 6-19. Using the muon's momentum and scattering angle θ, the neutrino energy can be reconstructed assuming the quasi-elastic interaction

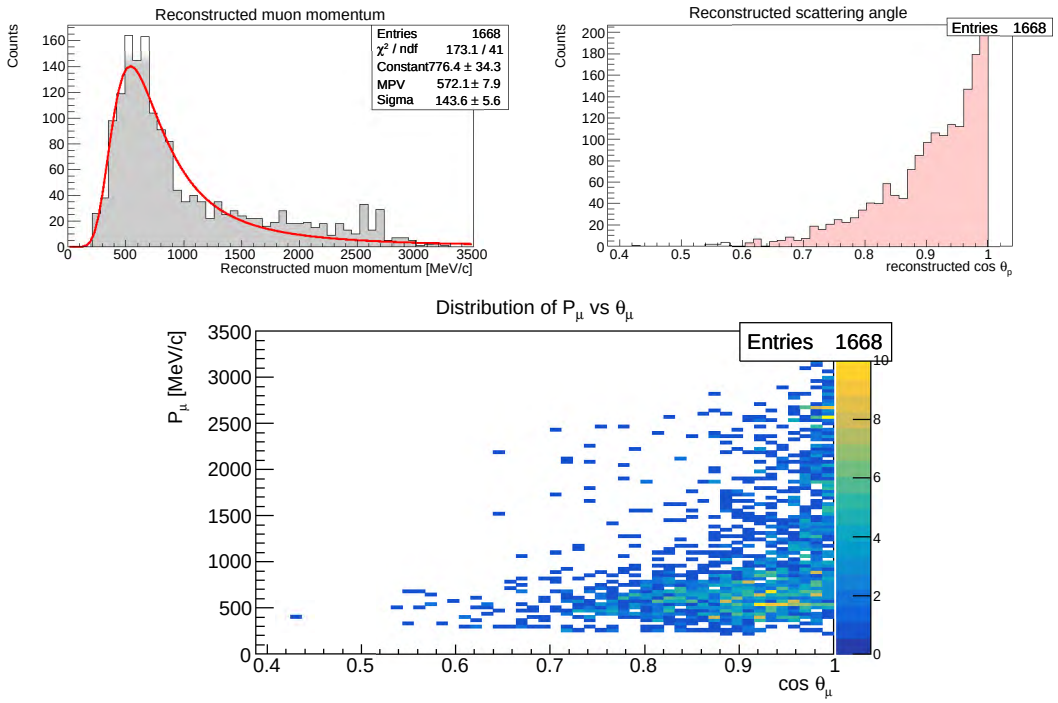

Figure 6-19: Reconstructed momentum and scattering angle of the muons from a sample of clean single track neutrino events.

kinematics with target nucleon at rest. The relation is given by

$$E_\nu^{QE} = \frac{2(M_n - E_B)E_\mu - [(M_n - E_B)^2 + m_\mu^2 - M_p^2]}{2[M_n - E_B - E_\mu + p_\mu \cos\theta_\mu]}\,. \tag{6.2}$$

The result of the reconstructed neutrino energy is shown in figure 6-20. The distribu-

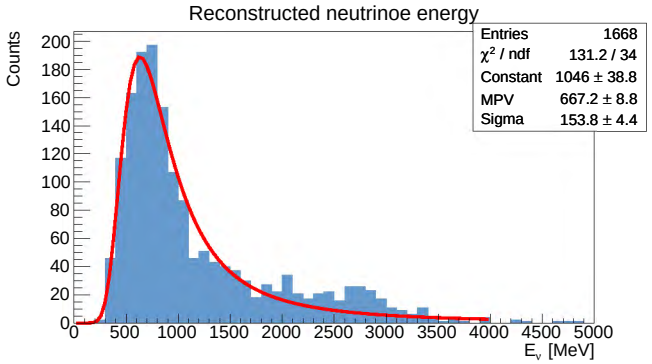

Figure 6-20: Reconstructed neutrino energy, assuming a quasi-elastic interaction kinematics with target nucleon at rest.

tion has a peak at 667.2 MeV, which is in agreement with the expected peak of the T2K neutrino flux at an off-axis angle of 1.5 °. Given the fact the selected sample is likely to be contaminated by some CC-RES and CC-DIS interaction modes, correct interpretation of these results would require comparison with MC.

Chapter 7

Conclusion

Baby MIND is the downstream magnetized muon range detector for the WAGASCI experiment at J-PARC. The detector systems of Baby MIND were designed, prototyped, constructed, tested at a beam test at CERN, shipped to Japan, commissioned on the T2K beamline and took the first physics run with an extremely compressed schedule, between 2016 and 2020.

This thesis covers the description of Baby MIND detector systems and presents activities carried out during all stages of the project.

Baby MIND has a modular design with a novel magnetization system where iron plates are all individually magnetized as opposed to the traditional monolithic magnetized iron detectors such as MINOS. This design is the result of the requirement to lower the detector segments through a narrow shaft down to the B2 floor of the ND280 building. The full layout of the detector is composed of 18 scintillating modules interleaved with 33 magnet modules.

The newly developed Front-End electronics of Baby MIND is based on CITIROC ASICs and was extensively tested and characterized throughout the project. This electronics was also used for the SuperFGD prototype beam test at CERN in 2018 and is currently being upgraded and adapted for the future SuperFGD, which is the new target-tracker sub-detector of the T2K near detector upgrade project.

The first physics run of Baby MIND together with other WAGASCI sub-detectors was a successful data taking campaign with 97 % data collection efficiency.

The detector performance studies such as the scintillating bars light yield measurements, timing studies, electronics noise investigations and data corruption instances are reported. The synchronization system of the detector was validated and this is demonstrated by an accurate representation of the T2K bunch structure

The data processing flow from raw binary data to event creation and the scheme of the event pre-selection, based on the topology criteria are discussed and some examples of the neutrino interactions events on iron are presented.

For the analysis of the clean single track neutrino events, a track reconstruction algorithm based on a χ^2 method is developed. The final distributions of the reconstructed muon momentum and the muon scattering angle as well as the reconstructed neutrino energy are shown in figures 7-1 and 7-2.

This study can be continued with a complementary MC study in order to determine

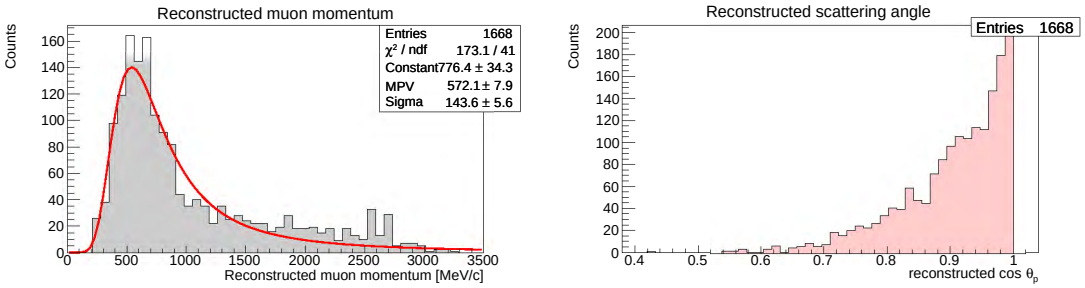

Figure 7-1: Reconstructed momentum and scattering angle of the muons from a sample of clean single track neutrino events.

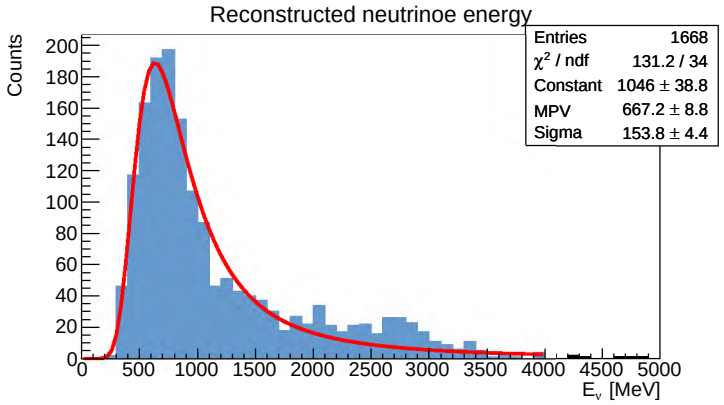

Figure 7-2: Reconstructed neutrino energy, assuming a quasi-elastic interaction kinematics with target nucleon at rest.

the momentum reconstruction efficiency and the charge identification efficiency of the χ^2 algorithm. The data collected by Baby MIND in the first physics run can be used to perform neutrino cross-section studies on iron. Such a study can illustrate the potential of Baby MIND to be used as a magnetized beam monitor for the T2K beam, with the capability of measuring the wrong sign component of the (anti)neutrino beam.

The WAGASCI collaboration is currently developing a full reconstruction package and MC suit based on the INGRID analysis environment in order to combine the

data from all WAGASCI sub-detectors, including Baby MIND, and perform neutrino cross-section measurement studies on water and hydrocarbon.

Bibliography

[1] J. Chadwick, "The intensity distribution in the magnetic spectrum of beta particles from radium (B+C)", *Verh.phys.Gesell* **16**, 383-391, 1914

[2] W. Pauli, "Dear radioactive ladies and gentlemen", *letter to the Physical Institute of the Federal Institute of Technology, Zurich*, 1930

[3] E. Fermi, "An attempt on the theory of beta radiation", *Z.phys* **88**, 161-177, 1934

[4] H. Bethe, R. Peierls, "The Neutrino", *Nature* **133**, 532-532, 1934

[5] C. Cowan, F. Rienes, F. Harrison, H. Kruse, A. McGuire, "Detection of a free neutrino: A confirmation", *Science* **124**, 103-104, 1956

[6] C. Sutton, "Ghosts in the machine", *CERN Courrier*, **56**:,17-19 ,2016

[7] T. D. Lee and C. N. Yang, "Question of parity conservation in weak interactions", *Phys.Rev* **104**, 254-258, 1956

[8] C. Wu, E. Ambler, R. Hayward, D. Hoppesc and R. Hudson, "Experimental test of parity conservation in beta decay", *Phys.Rev* **105**, 1413-1414, 1957

[9] M. Goldhaber, L. Grodzins and A. Sunyar, "Helicity of neutrinos", *Phys.Rev* **109**, 1015-1017, 1958

[10] G. Danby, J. Gallard, K. A. Goulianos, L. Lederman, N. B. Mistry, *et al.*, "Observation of high energy neutrino reaction and existence of two kinds of neutrinos", *Phys.Rev.lett* **9**, 36-44, 1962

[11] J. Bahcall, W. A. Fowler, J. Iben and R. Sears, "Solar neutrino flux", *Astrophys.J.* **137**, 344-346, 1963

[12] R. Davis Jr. *et al.*, "Search for Neutrinos from the Sun", *Phys. Rev. Lett.* **20**, 1205, 1968

[13] B. Cleveland, T. Daily, R. Davis Jr, J. R. Distel, K. Lande, *et al.*, "Measurement of the solar electron neutrino flux with the Homestake chlorine detector", *Astrophys.J.* **496**, 505-526, 1998

[14] K. S. Hirata *et al.*, 'Observation of ^{8}B solar neutrinos in the Kamiokande-II detector", *PhysRevLett.* **63**, 16, 1989

[15] V. F. Hess, "Über Beobachtungen der durchdringenden Strahlung bei sieben Freiballonfahrten", *Physikalische Zeitschrift* **13**, 10841091, 1912

[16] C. V. Achar *et al.*, "Detection of muons produced by cosmic ray neutrinos deep underground", *Phys. Lett.* **18**, 196, 1965

[17] F. Rienes *et al.*, "Evidence for high energy cosmic ray neutrino interactions", *Phys. Rev. Lett.* **15**, 429, 1965

[18] Y. Fukuda *et al.*, "Atmospheric Neutrino Background and Pion Nuclear Effect for KAMIOKA Nucleon Decay Experiment", *J. Phys. Soc. Jap.* **55**, 3786-3805, 1986

[19] T. J. Haines *et al.*, "Calculation of Atmospheric Neutrino-Induced Backgrounds in a Nucleon-Decay Search", *Phys. Rev. Lett.* **57**, 1986

[20] B. Pontecorvo, "Mesonium and anti-mesonium", *Sov.Phys.JETP* **6**, 429, 1957

[21] Z. Maki, M. Nakagawa, S. Sakata, "Remarks on the Unified Model of Elementary Particles", *Progress of Theoretical Physics* **28**, 870-880, 1962, doi:10.1143/PTP.28.870

[22] B. Pontecorvo, "Inverse beta processes and non-conservation of lepton charge", *Zh. Eksp. Teor. Fiz* **34**, 247, 1957 reproduced and translated in *Soviet Physics JETP* **7**, 172, (1958)

[23] Y. Fukuda *et al.*, "Evidence for oscillation of atmospheric neutrinos", *Phys. Rev. Lett.* **81**, 1562-1567, 1998

[24] Y. Fukuda *et al.*, "Solar ^{8}B and hep neutrino measurements from 1258 days of Super-Kamiokande data", *Phys. Rev. Lett.* **86**, 5651-5655, 2001, doi:10.1103/PhysRevLett.86.5651

[25] Q. Ahmed *et al.* "Direct evidence for neutrino flavour transformation from neutral current interactions in the Sudbury Neutrino Observatatory", *Phys. Rev. Lett.* **89**, 011301, 2002

[26] M. Rayner, "Tuning in to neutrinos", *CERN courier*, July/August, 2020

[27] R. B. Patterson, "Prospects for Measurement of the Neutrino Mass Hierarchy", *Ann. Rev. Nucl. Part. Sci* **65**, 177-192, 2015, doi:10.1146/annurev-nucl-102014-021916

[28] K. Abe *et al.*, "Constraint on the matter-antimatter symmetry-violating phase in neutrino oscillations", *Nature* **508**, 339-343, 2020, doi:10.1038/s41586-020-2415-5

[29] M. Tanabashi *et al.* (Particle Data Group), "Neutrino mixing", *Phys.Rev. D* **98**, 030001, 2018

[30] Z. Chacko, A. Dev, P. Du *et al.*, "Cosmological limits on the neutrino mass and lifetime", *JHEP* **4**, 20, 2020, doi:10.1007/JHEP04(2020)020

[31] M. Akar *et al.*, "Improved upper limit on the neutrino mass from a direct kinematic method by KATRIN", *Phys. Rev. Lett* **123**, 221802, 2019 doi:10.1103/PhysRevLett.123.221802

[32] A.N. Aseev *et al.*, "An upper limit on electron antineutrino mass from Troitsk experiment", *phys. Rev. D* **84**, p 112003, 2011, doi:10.1103/PhysRevD.84.112003

[33] A. Ashtari Esfahani, "Electron Radiated Power in Cyclotron Radiation Emission Spectroscopy Experiments", *Phys. Rev. C* **99**, 5, 055501,2019, doi:10.1103/PhysRevC.99.055501

[34] A. Nucciotti, "Neutrino mass calorimetric searches in the MARE experiment", *Nucl. Phys. B*, 229-232, p 155, 2012, doi:10.1016/j.nuclphysbps.2012.09.025

[35] Faessler *el al.*, "Determination of the neutrino mass by electron capture in ^{163}Ho and the role of the three-hole states in ^{163}Dy", *Phys. Rev. C* **91**, 064302, 2015, doi:10.1103/PhysRevC.91.064302

[36] R. M. Bionta *et al.*, "Observation of a neutrino burst in coincidence with supernova 1987A in the Large Magellanic Cloud", *Phys. Rev. Lett.* **58**, 14, 14941496, 1987, doi:10.1103/PhysRevLett.58.1494

[37] K.Hirata *et al.*, "Observation of a neutrino burst from the supernova SN1987A", *Phys. Rev. Lett.* **58**, 14, 14901493, 1987, doi:10.1103/PhysRevLett.58.1490

[38] E. N. Alekseev *et al.*, "Possible detection of a neutrino signal on 23 February 1987 at the Baksan underground scintillation telescope of the Institute of Nuclear Research", *JETP Lett.* **45**, 589, 1987

[39] IceCube collaboration, "First observation of PeV-energy neutrinos with IceCube", *Phys. Rev. Lett.* **111**, 021103, 2013

[40] A. Plavin, "Observational evidence for the origin of high-energy neutrinos in parsec-scale nuclei of radio-bright active galaxies.", *The Astrophysical Journal* **894**, 2, 101, 2020, doi:10.3847/1538-4357/ab86bd

[41] E. Vitagliano *et al.*, "Grand unified neutrino spectrum at Earth: Sources and spectral components", *Rev. Mod. Phys.* **92**, 045006, 2020, doi:10.1103/RevModPhys.92.045006

[42] M. Messina, "The PTOLEMY project: from an idea to a real experiment for detecting cosmological relic neutrinos", *Frascati Phys. Ser.* **66**, 286-293, 2018

[43] T. Asaka, M. Shaposhnikov, "The νMSM, Dark Matter and Baryon Asymmetry of the Universe", *Phys. Lett. B* **620**, 17-26, 2005, doi:10.1016/j.physletb.2005.06.020

[44] J. Kopp, "Theoretical Neutrino physics", *Lecture Notes at Johannes Gutenberg University*, 2015

[45] E. Amaldi, "L'opera scientifica di Ettore Majorana", *Physis*, 10, 173187, 1968

[46] R.N. Mohapatra and G.Senjanovic, "Neutrino mass and spontaneous parity nonconservation", *Phys. Rev. Lett.* **44**, 912, 1980

[47] B. Meszna, "Neutrino Oscillations", *Wolfram Demonstrations Project*, 2011 https://demonstrations.wolfram.com/NeutrinoOscillations/

[48] L. Wolfenstein, "Neutrino oscillations in matter", *Physical Review D* **17**, 9, 23692374, 1978, doi:10.1103/Phys.Rev.D.17.2369.

[49] S. P. Mikheyev, A.Y. Smirnov, "Resonance enhancement of oscillations in matter and solar neutrino spectroscopy", *Soviet Journal of Nuclear Physics* **42**, 6, 913917, 1985

[50] R. N. Mohapatra *et al.*, "Theory of Neutrinos: A White Paper", *Rept. Prog. Phys* **70**, 1757-1867, 2007

[51] C. H. Llewellyn Smith, "Neutrino reactions at accelerator energies", *Phys. Rept.* **3**, 261-379, 1972, doi:10.1016/0370-1573(72)90010-5

[52] R.A. Smith, E.J. Moniz, "Neutrino reactions on nuclear targets", *Nucl. Phys. B* **43**, 605 ,1972, doi:10.1016/0550-3213(75)90612-4

[53] D. Rein and L. M. Sehgal, "Neutrino excitation of baryon resonances and single pion production", *Annals Phys.* **133**, 79-153, 1981, doi:10.1016/0003-4916(81)90242-6

[54] J.A. Formaggio and G.P. Zeller, "From eV to EeV: Neutrino cross sections across energy scales" *Rev. Mod. Phys* **84**, p 1307, 2012, doi:10.1103/RevModPhys.84.1307

[55] K. Abe *et al.* [T2K Collaboration], "The T2K experiment", *Nucl. Instrum. Meth. A* **659**, p 106, 2011, doi:10.1016/j.nima.2011.06.067

[56] K. Abe *et al.* (T2K Collaboration), "Observation of electron-neutrino appearance in a muon-neutrino beam", *Phys. Rev. Lett.* **112**, 061802, 2014, doi:10.1103/PhysRevLett.112.061802

[57] K. Abe *et al.* (T2K Collaboration), "Precise Measurement of the neutrino mixing parameter θ_{23} from muon-neutrino disappearance in an off-axis beam", *Phys. Rev. Lett.* **112**, 181801, 2014, doi:10.1103/PhysRevLett.112.181801

[58] K. Abe *et al.*, "Proposal for an Extended Run of T2K to 20×10^{21} POT", 2016, arXiv:1609.04111[hep-ex]

[59] L. Zambelli, "Recent Developments on T2K Flux and Uncertainties", *JPS Conf. Proc.* **12**, 010005, 2016, DOI:10.7566/JPSCP.12.010005

[60] K.Matsuoka *et al.*, "Design and performance of the muon monitor for the T2K neutrino oscillation experiment", *Nucl. Instrum. Meth. A* **624**, 591, 2010, doi:10.1016/j.nima.2010.09.074

[61] K. Abe *et al.*, "Measurements of the T2K neutrino beam properties using the INGRID on-axis near detector", *Nucl. Instrum. Meth. A* **694**, p211, 2012, doi:10.1016/j.nima.2012.03.023

[62] K. Abe *et al.* (T2K collaboration), "J-PARC Neutrino Beamline Upgrade Technical Design Report", 2019 arXiv:1908.05141v1.

[63] S. Assylbekov *et al.*, "The T2K ND280 Off-Axis Pi-Zero Detector", *Nucl. Instrum. Meth. A*, 686, p48, 2012, doi:10.1016/j.nima.2012.05.028

[64] N.Abgrall *et al.*, "Time projection chambers for the T2K near detectors", *Nucl. Instrum. Meth. A*, 637, 25, 2011, doi:10.1016/j.nima.2011.02.036

[65] P.-A.Amaudruz *et al.*, "The T2K Fine-Grained Detectors", *Nucl. Instrum. Meth. A*, 696, 1, 2012, doi:10.1016/j.nima.2012.08.020

[66] D. Allan *et al.*, "The Electromagnetic Calorimeter for the T2K Near Detector ND280" *JINST* **8**, P10019, 2013, doi:10.1088/1748-0221/8/10/P10019

[67] S. Aoki *et al.*, "The T2K Side Muon Range Detector (SMRD)", *Nucl. Instrum. Meth. A* **698**, 135, 2013, doi:10.1016/j.nima.2012.10.001

[68] K. Abe *et al.* (T2K Collaboration), "Neutrino oscillation physics potential of the T2K Experiment", *Prog. Theo. Exp. Phys.* **4**, 043C01, 2015, doi:10.1093/ptep/ptv031

[69] L. Fields, "Neutrino cross sections", arXiv:1212.0060[hep-ex], 2012

[70] M. Tanabashi *et al.* (Particle Data Group), "Neutrino Cross Section Measurements - PDG", *Phys. Rev. D* **98,** 030001 2019 update.

[71] K. Abe *et al.* (T2K), "Measurement of the inclusive ν_μ charged current cross section on carbon in the near detector of the T2K experiment", *Phys. Rev. D* **87**, 9, 092003 (2013), arXiv:1302.4908.

[72] K. Abe *et al.* (T2K), "Measurement of inclusive double-differential ν_μ charged-current cross section with improved acceptance in the T2K off-axis near detector", *Phys. Rev. D* **98**, 012004 (2018), arXiv:1801.05148.

[73] K. Abe *et al.* (T2K), "Measurement of the ν_μ charged-current cross sections on water, hydrocarbon, iron, and their ratios with the T2K on-axis detectors", *Prog. Theor. Exp. Phys.* **9**, 093C02, 2019, arXiv:1904.09611.

[74] K. Abe *et al.* (T2K), "Measurement of the inclusive ν_μ charged current cross section on iron and hydrocarbon in the T2K on-axis neutrino beam", *Phys. Rev. D* **90**, 5, 052010 (2014), arXiv:1407.4256.

[75] K. Abe *et al.* (T2K), "Measurement of the muon neutrino inclusive charged-current cross section in the energy range of 13 GeV with the T2K INGRID detector", *Phys. Rev. D* **93**, 7, 072002 (2016), arXiv:1509.06940.

[76] K. Abe *et al.* (T2K), "Measurement of the inclusive electron neutrino charged current cross section on carbon with the T2K near detector", *Phys. Rev. Lett.* **113**, 24, 241803 (2014), arXiv:1407.7389.

[77] K. Abe *et al.* (T2K), "Measurement of the electron neutrino charged-current interaction rate on water with the T2K ND280 π^0 detector", *Phys. Rev. D* **91**, 112010 (2015), arXiv:1503.08815.

[78] K. Abe *et al.* (T2K), "Measurement of $\overline{\nu}_\mu$ and ν_μ charged current inclusive cross sections and their ratio with the T2K off-axis near detector", *Phys. Rev. D* **96**, 5, 052001, arXiv:1706.04257.

[79] K. Abe *et al.* (T2K), "Measurement of double-differential muon neutrino charged-current interactions on C_8H_8 without pions in the final state using the T2K off-axis beam", *Phys. Rev. D* **93**, 11, 112012, 2016, arXiv:1503.08815.

[80] K. Abe *et al.* (T2K), "First measurement of the ν_μ charged-current cross section on a water target without pions in the final state", *Phys. Rev. D* **97**, 1, 012001, 2018, arXiv:1708.06771.

[81] K. Abe *et al.* (T2K), "First measurement of the charged current $\overline{\nu}_\mu$ double differential cross section on a water target without pions in the final state", *Phys. Rev. D* **102**, 1, 012007 (2020), arXiv:1908.10249 doi:10.1103/PhysRevD.102.012007

[82] K. Abe *et al.* (T2K), "Measurement of the ν_μ charged current quasielastic cross section on carbon with the T2K on-axis neutrino beam", *Phys. Rev. D* **91**, 11, 112002 (2015), arXiv:1503.07452.

[83] K. Abe *et al.* (T2K), "Measurement of the ν_μ charged-current quasielastic cross section on carbon with the ND280 detector at T2K", *Phys. Rev. D* **92**, 11, 112003 (2015), arXiv:1411.6264.

[84] K. Abe *et al.* (T2K), "Characterization of nuclear effects in muon-neutrino scattering on hydrocarbon with a measurement of final-state kinematics and correlations in charged-current pionless interactions at T2K", *Phys. Rev. D* **98**, 3, 032003 (2018), arXiv:1802.05078.

[85] K. Abe *et al.* (T2K), "Measurement of the neutrino-oxygen neutral-current interaction cross section by observing nuclear deexcitation γ rays", *Phys. Rev. D* **90**, 7, 072012 (2014), arXiv:1403.3140.

[86] K. Abe *et al.* (T2K), "First measurement of the muon neutrino charged current single pion production cross section on water with the T2K near detector", *Phys. Rev. D* **95**, 1, 012010 (2017), arXiv:1605.07964.

[87] K. Abe *et al.* (T2K), "Measurement of coherent π^+ production in low energy neutrino-carbon scattering", *Phys. Rev. Lett.* **117**, 19, 192501 (2016), arXiv:1604.04406.

[88] K. Abe *et al.* (T2K), "T2K ND280 Upgrade - Technical Design Report", arXiv:1901.03750v2.

[89] C. Ahdida *et al.*, "The experimental facility for the Search for Hidden Particles at the CERN SPS", *JINST* **14**, P03025, 2019. doi:10.1088/1748-0221/14/03/P03025

[90] S. Parsa, "Development of a 3D highly granular scintillator neutrino detector for the T2K experiment", *Nucl. Instrum. Meth. A* **958**, 162165, 2020. doi:10.1016/j.nima.2019.05.006

[91] A. Blondel, *et al.*, "The SuperFGD Prototype charged particle beam tests", *JINST* **15**, 12, P12003, 2020. doi:10.1088/1748-0221/15/12/P12003

[92] S. Fukuda, *et al.*, "The Super-Kamiokande detector", *Nucl. Instrum. Meth. A* **501**, 418462, 2003. doi:10.1016/S0168-9002(03)00425-X.

[93] P. A. Cherenkov, "Visible emission of clean liquids by action of γ radiation", *Doklady Akademii Nauk SSSR* **2**, 451, 1934.

[94] J. F. Beacom and M. R. Vagins, "GADZOOLS! Anti-neutrino spectroscopy with large water Cerenkov detectors", *Phys. Rev. Lett.* **93**, 171101, 2004. doi:10.1103/PhysRevLett.93.171101.

[95] Xu, Chenyuan, "Current status of SK-Gd project and EGADS". *J. Phys. Conf. Ser.* **718**, 062070, 2016. doi:10.1088/1742-6596/718/6/062070

[96] N. Truong, *et al.*, "Study of neutrino-nucleus interaction at around 1 GeV using cuboid lattice neutrino detector, WAGASCI, muon range detectors and

magnetized spectrometer, Baby-MIND, at J-PARC neutrino monitor hall (E69, WAGASCI/Baby-MIND)", *J-PARC PAC*, 2018

[97] T. Ovsiannikova *et al.*, "The new experiment WAGASCI for water to hydrocarbon neutrino cross section measurement using the J-PARC beam", *Journal of Physics Conference*, S675(1), p 012030, 2016

[98] S. Bhadra, *et al.*, "Proposal for the NuPRISM Experiment in the J-PARC Neutrino Beamline", *J-PARC PAC* , 2015.

[99] S. Geer, "Neutrino beams from muon storage rings: Characteristics and physics potential", *Phys. Rev. D* **57**, 6989-6997, 1998

[100] A. Bross *et al.*, "A Toroidal magnetized iron neutrino detector (MIND) for a neutrino factory", *Phys.Rev. ST Accel. Beams* **16**, 081002 , 2013, arXiv:1306.5327 [physics.ins-det]

[101] A. Cervera *et al.*, "Performance of the MIND detector at a Neutrino Factory using realistic muon reconstruction", *Nucl.Instrum.Meth.A* **624**, 601-614, 2010

[102] F. Dydak *et al.*, "A search for ν_μ oscillations in the Δm^2 range 0.3 to 90 eV^2", *Phys. Lett. B* **134**, no. 3-4: 281286, 1984

[103] I. Ambats *et al.* (MINOS Collaboration), "MINOS Technical Design Report", *NUMI-L-337, FERMILAB-DESIGN*, 1998

[104] P. Adamson, *et al.* (MINOS Collaboration), "Charge-Separated Atmospheric Neutrino-Induced Muons in the MINOS Far Detector", *Phys. Rev. D* **75**, p 092003, 2007

[105] AK Steel International, "ARMCO Pure Iron", `https://www.aksteel.eu/products/armco-pure-iron/`

[106] G. Rolando *et al.*, "A new magnetization scheme for the Baby Magnetized Iron Neutrino Detector at J-PARC", *IEEE Trans. Magnetics* **53**, no 5, pp. 1-6, 2017 `doi:10.1109/TMAG.2017.2664053`

[107] Y. Kudenko *et al.*, "Extruded plastic counters with WLS fibers readout", *Nucl. Instrum. Meth. A* **469**, 340-346, 2001 `doi:10.1016/S0168-9002(01)00780-X`.

[108] O. Mineev *et al.*, "Scintillator detectors with long WLS fibers and multi-pixel photodiodes", *JINST* **6**, P12004, 2011, `doi:10.1088/1748-0221/6/12/P12004`

[109] KURARY CO. LTD., "Plastic Scintillating Fibers", http://Kuraraypsf.jp

[110] W. Baldini *et al.*, "Measurement of parameters of scintillating bars with wavelength-shifting fibres and silicon photomultiplier readout for the SHiP Muon Detector", *JINST* **12**, P03005, 2017, doi:10.1088/1748-0221/12/03/P03005.

[111] M. Antonova *et al.*, "Baby MIND: a magnetized segmented neutrino detector for the WAGASCI experiment", *JINST* **12**, C07028, 2017.

[112] Hamamatsu Photonics K.K., "MPPC modules", *Cat. No. KAPD0002E11 Jan. 2014 DN.*

[113] A. Blondel *et al.* "Readout scheme for the Baby-MIND detector" *PoS photodet 2015* 031, 2015.

[114] E. Noah *et al.*, "Baby MIND Readout Electronics Architecture for Accelerator Neutrino Particle Physics Detectors Employing Silicon Photomultipliers", *JPS Conf. Proc.* 27, 011011, 2019, doi:10.7566/JPSCP.27.011011.

[115] A. Mefodiev *et al.*, "The design, construction and testing of Totally Active Scintillator Detector", *PoS PhotoDet 2015* 067, 2015. doi:10.22323/1.252.0067.

[116] J. Fleury, *et al.*,"CITIROC data sheet", *JINST* **9**, C01049, 2014. doi:10.1088/1748-0221/9/01/C01049.

[117] G. Mitev *et al.*, "Synchronization of the distributed readout frontend electronics of the Baby MIND detector", *Proceedings, 2017 XXVI International Scientific Conference Electronics (ET)*, pp. 1-4, doi:10.1109/ET.2017.8124369.

[118] L. Durieu, O. Ferrando. "Design of T9 (Atlas/CMS) for EHNL", *CERN Notes PS/PA*, 96-39, 1996.

[119] Y. Shafranovich, "Common Format and MIME Type for CSV Files", *IETF* p. 1, 2005, doi:10.17487/RFC4180.RFC4180.

[120] Microsoft Corporation, "An Introduction to C# Generics". Microsoft, 2005

[121] Dassault Systemes Simulia Corporation, "Abaqus unified FEA", https://www.3ds.com

[122] IETF, "The JavaScript Object Notation (JSON) Data Interchange Format", 2017, https://www.json.org

[123] T. Teranishi,"Tera Term Project", 1994. https://ttssh2.osdn.jp

[124] Free Software Foundation, "Packet Sender", 1989. https://packetsender.com

[125] J. Rosado and S. Hidalgo, "Characterization and modeling of crosstalk and afterpulsing in Hamamatsu silicon photomultipliers", *JINST* **10**, P10031,2015. doi:10.10.1088/1748-0221/10/10/P10031.

[126] Y. Hayato, "A neutrino interaction simulation program library NEUT", *Acta Phys. Polon. B* **40** (2009), 2477-2489